Diamonds and Their Inclusions From the Koffiefontein Mine

By

Nicole Anne Meyer

A thesis in partial fulfilment of the requirements for the degree of

Doctor of Philosophy

Department of Earth and Atmospheric Sciences
University of Alberta

Abstract

Diamonds, due to their inert and robust nature, encapsulate and preserve minerals, recording the mantle substrate in which they form. Forming in the subcontinental lithospheric mantle over a protracted period, diamonds provide snapshots of craton formation and mantle evolution over much of Earth's history. The Kaapvaal Craton in southern Africa, the archetypical craton, defines our understanding of craton formation and evolution. The Koffiefontein kimberlite is located on this craton close to an ancient craton suture, allowing for a transect through the craton. Here, rare lower mantle (LM) diamonds have been recovered and provide insight into the deepest regions (~660 km) of the accessible sublithospheric mantle.

The objective of this thesis is to characterise Koffiefontein diamonds and their mineral inclusions to better understand the formation and evolution of the Kaapvaal Craton and how it has been influenced by subduction processes. In this thesis, I use various geochemical techniques to analyse ~200 diamonds and ~200 liberated mineral inclusions and compare the data to other locales worldwide.

Koffiefontein diamonds have a main $\delta^{13}C$ mode for both peridotitic and eclogitic diamonds similar to mantle carbon. Relationships of $\delta^{15}N$-[N] and $\delta^{13}C$-$\delta^{15}N$ indicate that nitrogen was derived from subducted sources and suggests that formation of not only eclogitic but also peridotitic diamonds involved fluids derived from altered oceanic crust. The nitrogen source of a small portion of ^{15}N-depleted peridotitic diamonds remains unknown but could relate to reduced fluids, which can fractionate nitrogen more strongly.

The presence of calcite and former coesite in three diamonds containing an otherwise peridotitic inclusion assemblage is evidence for diamond formation by reduction of carbonate melts. The low intra-diamond variability and general mantle-like $\delta^{13}C$ does not allow to distinguish between diamond formation by redox reactions or isochemical precipitation.

Based on mineral inclusion chemistry, the Koffiefontein diamonds are predominantly peridotitic (~57 %), of which the majority are from highly depleted substrates (~80 % of all garnet is harzburgitic). The very high median $Mg\#_{ol}$ (93.6) and high proportion of low-Ca, peridotitic garnet indicate extremely high levels of melt extraction prior to craton assembly; whereas the high Cr/Al of garnet indicates that melt depletion occurred in the spinel facies. This agrees with the two-stage model of craton formation but does not account for the extremely high Mg# of some olivine (>94.5) and the presence of orthopyroxene in diamond. These findings could be explained by infiltration of silicate melts, perhaps similar to high-Mg andesites in sub-arc settings, before craton thickening and garnet formation.

The strong LREE enrichment in garnet is indictive of metasomatism by high density fluids, which can readily percolate depleted substrates and produce REE_N profiles with peaks at Ce or Nd, attributed to variations in fluid composition. Metasomatism can also result in the formation of new minerals and at Koffiefontein that culminated in goldschmidtite ($KNbO_3$) and a Ta-K-rich oxide.

Geothermobarometry of mineral inclusions shows that Koffiefontein diamond formation conditions are 1100-1300 °C and 4-7 GPa. The similarity of the Koffiefontein diamond and xenolith geotherms, both at 38 $mW \cdot m^{-2}$, suggests that the Kaapvaal Craton either has not

experienced thermal perturbation since its formation in the Archean or that heat from any tectonothermal event had been completely dissipated by the time of Cretaceous kimberlite eruption.

Three LM diamonds were recovered. Coexisting ferropericlase and orthopyroxene (with very low Ni and elevated Al), representing retrogressed bridgmanite, indicate diamond formation at pressures of 23 GPa (~660 km) or higher. The high bulk Mg# of the assemblage (ferropericlase Mg# 83-88 and bridgmanite Mg# ~95) is consistent with the diamond substrate originating from depleted peridotite (harzburgite to dunite), a setting found within the depleted lithospheric mantle portion of an oceanic slab. The presence of magnesite within a LM diamond indicates diamond formation may have proceeded by reduction of carbonate, most likely sourced from the subducted slab; however, the presence of a water-rich inclusion within a ferropericlase assemblage does not preclude other mechanisms that, e.g., involve hydrous melting.

Thus, this study of Koffiefontein diamonds shows that while formation dominantly takes place in depleted peridotite at both lithospheric and lower mantle depths, it can involve carbonate-rich media with a subducted origin. The $\delta^{13}C$-$\delta^{15}N$ systematics and carbon source suggest the same subducted source for both peridotitic and eclogitic diamonds. Subduction has played an important role in the formation and evolution of the Kaapvaal Craton and subsequent diamond formation.

Preface

This thesis is original work by Nicole Meyer and is composed of four separate manuscripts based on the findings of the author's Ph.D. research supervised by Prof. Thomas Stachel and Prof. D. Graham Pearson. The samples for this project were provided by Dr. Jeff Harris, collected from mines operated by De Beers and Petra Diamonds. This project was funded in part by a doctoral scholarship abroad, awarded to N.A. Meyer (grant 94626), by the National Research Foundation of South Africa, a Natural Sciences and Engineering Research Council (NSERC) Discovery Grant to T. Stachel, and a NSERC CREATE grant to D.G. Pearson.

Chapters 1, 2, and 7 are original work produced by the author.

Modified versions of Chapters 3, 4, and 6 will be submitted to peer-reviewed journal. Sample preparation and analytical work was completed by N.A. Meyer, except for C-N-O isotopes which were completed by R.A. Stern. Assistance for EPMA data acquisition was provided by A.J. Locock and Y. Luo for LA-ICP-MS. T. Stachel and D.G. Pearson supervised the project and provided valuable discussions and manuscript edits.

Chapter 5 of this thesis is published in AMERICAN MINERALOGIST as: *Goldschmidtite, $(K,REE,Sr)(Nb,Cr)O_3$: A new perovskite supergroup mineral found in diamond from Koffiefontein, South Africa.* Analytical work was completed by N. Meyer, M.D. Wenz, J.P.S. Walsh, and S.D. Jacobsen. Co-authors S.D. Jacobsen, A.J. Locock and J.W. Harris provided valuable contributions to the discussion and interpretation of results. Additional funding for this project was provided to S.D. Jacobsen from the U.S. National Science Foundation, grant EAR-1853521.

Acknowledgements

With any large body of work there are many people who have shaped not only the science on these pages but the mind behind the work. Thank you to Thomas Stachel and Graham Pearson for designing a challenging project that has made me grow into the scientist I am today. Thank you to my committee members Jeff Harris and Bob Luth for being available to discuss science and passing on your unique knowledge. Profs Karlis Muehlenbachs, Long Li, Tom Chacko, and Chris Herd have given their time and resources to help with aspects of this project that although may be small, have made a significant impact in my understanding of the science.

A project with this amount of analytical resources relies heavily on those who run the labs. Andrew Locock and Richard Stern have provided reliable and precise data. Research staff in the Arctic Resources lab, Chiranjeeb Sakar, Sarah Woodland and Yan Luo helped with data acquisition, chemistry procedures, and anything lab related. Mark Labbe, Martin von Dollen, and Robert Dokken were immensely helpful in sample preparation and passing on their knowledge. Mike Xia at the National Research Council Canada labs graciously organised access on the Raman instrument.

The graduate students in the Diamond Research Group and the Tory offices were the first to welcome me. They were – and still are – my source of knowledge and provided years of fruitful geological and graduate life discussions. Thank you to Matthew, Mandy, Pedro, Janina, Yannick, Margo, Theetso, and Sarah and postdocs Chiara and Suzette. When not working, my running and squash friends have shown me the best parts of Edmonton and Alberta.

Those that have made the greatest sacrifice for me are my husband, family, and friends in South Africa. I miss them every day but am grateful for the opportunities they have given me to prepare me for this adventure. This thesis is dedicated to them.

Table of contents

List of tables

List of figures

Glossary

%B	Percentage of nitrogen in B-centre
[N]	Nitrogen concentration in at.ppm
‰	Per mill
AOC	Altered oceanic crust
at.ppm	Atomic ppm
Brd	Bridgmanite
CL	Cathodoluminescence
Cpx	Clinopyroxene
EPMA	Electron probe micro analysis
FMQ	Fayalite-magnetite-quartz buffer
fO_2	Oxygen fugacity
fPer	Ferropericlase
FTIR	Fourier transform infrared
G9, G10	Class of garnet: lherzolite and harzburgite, respectively
Ga; Gyr	Giga-annum; billion years
GPa	Gigapascal
Grt	Garnet
HDFs	High density fluids
HREE	Heavy rare earth elements
IW	Iron-wüstite buffer
LA-ICP-MS	Laser-ablation inductively coupled plasma mass spectrometry
LM	Lower mantle
LREE	Light rare earth elements
Ma; Gyr	Mega-annum; million years
Mg#	100 x molar Mg/(Mg+Fe)
MORB	Midocean ridge basalt
Ol	Olivine
Opx	Orthopyroxene
P	Pressure in GPa
ppm	Parts per million
-pvk	Perovskite structured mineral
REE	Rare earth elements
SCLM	Subcontinental lithospheric mantle
T	Temperature in °C
Type IaA, IaB, IaAB	Nitrogen in the A- or B-centre, respectively, or a combination
Type II	Nitrogen concentration below detection, <10 ppm
TZ	Transition zone
vol%	Volume percent
VPDB	Vienna-Pee-Dee-belemnite
VSMOW	Vienna-standard-mean-ocean-water
wt%	Weight percent
$\delta^{13}C$, $\delta^{15}N$, $\delta^{18}O$	Isotopic composition of carbon, nitrogen, and oxygen, respectively

Chapter 1. Introduction

1.1. The study of diamonds

Diamonds have proved not to be the quintessential form of investment in times of global financial instability, but for the study of Earth they are an investment that continues to be scientifically profitable long after they have been mined. Much of what scientists know about Earth – its structure and composition – comes from global-scale seismic studies (e.g., PREM; Dziewonski and Anderson, 1981) and chemical models based on solar nebula compositions derived from meteorites (e.g., McDonough and Sun, 1995). Whereas seismic models are representative of today's Earth, chondritic models are representative of an early primitive Earth before it became differentiated. In between is a tumultuous history punctuated by discreet events and processes that may no longer occur but have led to heterogeneous domains in bulk silicate Earth, including both the crust and mantle. Physical samples from the mantle in the form of basalts, derived from midocean spreading ridges or deeply-derived ocean island basalts, have been used to constrain the composition of the convecting upper mantle. Suboceanic and subcontinental lithospheric mantle is sampled less commonly, in obducted oceanic lithosphere (ophiolites) and xenoliths of subcontinental lithosphere and as mineral inclusions within diamonds brought to the surface in highly-explosive kimberlite eruptions.

The strong carbon-carbon covalent bonds in diamond produce a chemically robust tetrahedral structure that can survive drastic changes in temperature and pressure occurring over short time scales, when diamonds are brought to the surface by kimberlite eruptions. Diamonds form in the lithospheric mantle at great pressures and temperatures – 4.0-6.5 GPa and 900-1350 °C (Boyd and Gurney, 1986; Stachel and Luth, 2015). In addition, rare examples from the lower regions of the upper mantle, the transition zone, and top of the lower mantle exist, indicating diamond formation at pressures >8 GPa (Harte and Harris, 1994; Moore and Gurney, 1985; Scott Smith et al., 1984). Encapsulated within ~1 % of monocrystalline diamonds (Stachel and Harris, 2008) are minerals that were either present or formed when the diamond formed. Included minerals are protected from subsequent chemical changes due to the rigid carbon structure surrounding it, thus preserving their original chemistry, and giving us direct evidence of Archean to Phanerozoic tectonothermal processes (Gurney et al., 2010).

1.2. What can diamonds tell us about the mantle

1.2.1. Lithosphere formation and evolution

Diamonds hosted in kimberlite deposits are found on cratons, the long-lived and stable nuclei of many continents. Cratons are long-term stable crustal features of generally Archean age (Janse, 1994), underpinned by a rigid lithospheric mantle of typically similar age. This thick and cold lithosphere gives rise to a lower geothermal gradient (<45 $mW \cdot m^{-2}$) compared to regions of continental crust underpinned by thinner lithospheric mantle (~50 $mW \cdot m^{-2}$; see Figure 1-1; De Wit et al., 1992). The conductive geotherms characteristic of the lithosphere eventually intersect the mantle adiabat, the convective geotherm of the asthenosphere and underlying deeper mantle. The low geothermal gradients in subcratonic lithospheric mantle (SCLM) increase the stability of diamond over graphite at lower pressures. Lithospheric mantle occurs beneath both oceanic and continental crust as residues of its formation (Frey and Green, 1974). These residues are depleted in basaltic compositions, notably Al_2O_3 and CaO, and have high bulk rock Mg# (Ringwood, 1969).

The mechanism for SCLM formation is still actively debated. For oceanic lithosphere, midocean spreading ridges create new crust, leaving a residue that is significantly depleted (Green and Ringwood, 1969). This can occur at a range of depths, with $Mg\#_{ol}$ increasing with depth of initiation of melt depletion: <3 GPa melting results in $Mg\#_{ol}$ 91-92 from 25-38 % melting, whereas 38-50 % melting at 3-6 GPa results in $Mg\#_{ol}$ 92-94 (Herzberg, 1999). For subcontinental lithospheric mantle, two competing models of formation as melting residues are (1) deep, plume-assisted melting (e.g., Aulbach et al., 2011) or (2) shallow melting creating depleted lithospheric mantle that is subsequently thickened (Jordan, 1978). Thick, residual peridotite has a lower density, a higher solidus temperature, and increased viscosity, which limits its recyclability into the mantle and promotes stable lithosphere formation (Jordan, 1978). The processes that formed cratons occurred early in Earth's history and at a time of higher mantle potential temperatures, enabling processes that possibly no longer occur today (e.g., Sossi et al., 2016).

What can mineral inclusions in diamond tell us about lithosphere formation? A study of ~5000 mineral inclusions in diamonds from global localities have shown that diamond principally forms

in two distinct substrates: peridotite and eclogite (Stachel and Harris, 2008). The most abundant mineral inclusions come from peridotite, an ultramafic assemblage of olivine, orthopyroxene, clinopyroxene, and garnet, with minor chromite and sulphide. Residual peridotite is the primary component of the subcontinental lithospheric mantle and is separated from the convecting mantle (i.e., the asthenosphere, composed of mildly depleted peridotite that constitutes the MORB source) by a thermal and chemical boundary.

Peridotitic inclusions within diamond can vary based on the degree of substrate depletion – e.g., lack of clinopyroxene for very depleted peridotites (harzburgites-dunites). Mineral inclusions within diamonds are small (generally <200 μm) and usually not representative of the complete mineralogy of the diamond substrate; thus, mineral inclusion chemistry is usually employed to determine the substrate paragenesis (e.g., Gurney, 1984). The chemistry of mineral inclusions in diamond is also compared with that of minerals in mantle xenoliths recovered from kimberlites. Notable features of peridotitic inclusions from diamond versus mantle nodules are that they record a higher level of depletion: higher Mg# (modal Mg/Mg+Fe) of olivine and sometimes lower CaO and/or higher Cr_2O_3 in garnet (Stachel and Harris, 2008). The depleted nature of lithospheric peridotite has important consequences for the formation of the SCLM and diamonds, which will be discussed in Section 1.2.2.

The second principle diamond substrate, contributing ~33 % of lithospheric diamonds, is eclogite: a low-Cr_2O_3, bimineralic garnet-omphacite assemblage (Desmons and Smulikowski, 2007; Stachel and Harris, 2008). Mantle eclogite is interpreted as metamorphosed basaltic oceanic crust that has been subducted into the mantle and makes up <1 vol% of the SCLM (Jacob, 2004). Although volumetrically minor, eclogite plays an important role in geodynamics as it is acts as a driving force for subduction due to an increase in density of the basalt/gabbro to eclogite transition (Ringwood and Green, 1966). Evidence provided by mineral inclusions in diamond for a subduction origin of eclogite comes from sulphur isotopes on sulphides showing a sedimentary recycled component (Eldridge et al., 1991), oxygen isotopes showing high- and low-temperature seawater alteration (Lowry et al., 1999), and Eu anomalies indicative of low-pressure fractionation in the presence of plagioclase (Stachel et al., 2004a).

A second stage of lithosphere formation is modification of the mantle root by metasomatism (Frey and Green, 1974). Consequently, a trait of the subcontinental lithospheric mantle (SCLM) is the juxtaposition of intense levels of depletion – documented by high Mg# of olivine – with an increase in LREE and other incompatible trace element contents, most visible in garnet (Gurney and Harte, 1980). This enrichment is attributed to mantle metasomatism (Menzies and Hawkesworth, 1987). The source of metasomatic fluids is unclear as multiple phases of enrichment can be envisioned. Subduction of oceanic crust is a plausible mechanism for the formation of metasomatic melts or fluids that are enriched in incompatible elements compared to depleted peridotite (Green and Wallace, 1988). Deep subduction may also cause the generation of carbonated metasomatic fluids (Weiss et al., 2013). Regardless of the source, metasomatism allows for the chemical re-enrichment, reintroduction or increase in abundance of typical peridotitic minerals (e.g., garnet or clino- and orthopyroxene) and the formation of new minerals (e.g., phlogopite or hawthorneite; Haggerty et al., 1989).

Volatiles, in particular water, entering the mantle via subduction will be released into the surrounding mantle due to the limited stability of host minerals (Luth, 2003). When water is released from a slab, it can exist as a fluid, as the hydrous component of a melt, or dissolved into nominally anhydrous mantle minerals (Bell and Rossman, 1992; Wyllie and Ryabchikov, 2000). The released fluids can interact with surrounding rock, mobilising incompatible elements such as K (Kennedy et al., 1962), or causing flux melting of the infiltrated peridotite by reducing its solidus (Kushiro et al., 1968). It is within these scenarios that the thick cratonic lithosphere can be metasomatised.

Water can be introduced into the mantle on a subducting slab via fractures, sediment, hydrous minerals such as serpentine, and in nominally anhydrous minerals such as silicates. Water in fractures is expelled due to confining pressure (Korenaga, 2020) and sediments can be scraped off by the overriding plate (Poli and Schmidt, 2002; cf. Kerrick and Connelly, 2001). The oceanic crust can bring water into the mantle in the form of hydrous minerals, with lawsonite, chlorite, and amphibole in the basaltic crust (5-6 wt% H_2O) and chlorite, talc, and clay (1-2 wt% H_2O) in the gabbroic portion; however, this water is lost during devolatilisation of the slab (Poli and Schmidt, 2002; Schmidt and Poli, 1998). The peridotitic portion of the slab, containing

serpentine and chlorite, can carry significant amounts of water (up to ~13 wt% H_2O) much deeper into the mantle, which is only lost at temperatures of 500-800 °C (Schmidt and Poli, 1998). Serpentine that remains in the slab undergoes multiple phase transitions, up to 18 GPa, to hydrous Mg-silicates, which have not yet been recorded in natural samples (Liu, 1986). Additionally, water stored as OH^- ions in nominally anhydrous minerals – such as olivine, garnet, and pyroxene – can amount to 1-500 ppm H_2O, with garnet and olivine having lower concentrations compared to pyroxenes (Bell and Rossman, 1992).

1.2.2. Mechanism of diamond formation and the source of diamond-forming fluids

Lithospheric diamonds are predominantly peridotitic (~66 %), among which harzburgitic diamonds dominate (Stachel and Harris, 2008). A sizable component (~⅓) of lithospheric diamonds comes from eclogitic substrates, which make up <1 vol% of the SCLM, (see above and Schulze, 1989; Stachel and Harris, 2008). The concentration of carbon in the ambient mantle is low (20-300 ppm) and towards the lower end of the range for depleted lithologies (Dasgupta and Hirschmann, 2010). Thus, to precipitate diamond, carbon in the mantle must be enriched and/or mobilised.

The classical model for diamond formation is via redox reactions, involving the reduction or oxidation of carbon in a peridotite – harzburgite or lherzolite – or an eclogite (Deines, 1980). Carbon in the mantle is speciated – based on oxygen fugacity (fO_2), temperature, and pressure – as carbonate (CO_3^{2-}) or carbonate-rich fluids, or as methane (CH_4) or methane-rich fluids (Luth, 1999). In eclogite the presence of CO_2 rich fluids is also possibly due to a limited buffering capacity of the garnet-clinopyroxene assemblage (Luth, 1999). Pressure-temperature data for mineral inclusions in diamonds globally show that peridotitic diamonds mostly form below the wet harzburgite solidus and above the wet lherzolite solidus. Eclogitic diamonds form below the carbonated solidus and above the hydrous solidus of metabasalt (Stachel and Harris, 2008). Thus for movement of carbon in the lithospheric mantle, particularly through the most important harzburgitic substrates, C-rich fluids are the most likely medium, due to the high solidus temperature of depleted peridotite (Wyllie, 1987a). The ability of C-bearing hydrous fluids to entrain significant amounts of dissolved solids ("high density fluids"; Kessel et al., 2015; Schrauder and Navon, 1994) also establishes them as excellent agents of mantle metasomatism.

Precipitation of diamond through redox reactions, involving mobile, reduced or oxidized carbon species and peridotitic wall rock, has recently been challenged based on a very low buffering capacity of depleted peridotitic, especially harzburgitic substrates (Luth and Stachel, 2014). In these regions, diamond can precipitate isochemically, due to a decrease in C solubility in a C-rich fluid as the fluid cools or moves upward along a continental geotherm (Luth and Stachel, 2014). This method is preferential in harzburgitic substrates and could explain the overabundance of harzburgitic versus lherzolitic diamonds (Stachel and Luth, 2015). Diamond formation by this mechanism produces equal amounts of diamond and water, which can be taken up in the C-rich fluid or into nominally anhydrous minerals (Luth and Stachel, 2014). A further advantage of this model is that at the water maximum (the pressure, temperature and fO_2 condition where a COH fluids consists mostly of water), where diamond precipitation usually occurs, multiple carbon species are present (mostly CH_4 and CO_2), thus precipitating diamond within the canonical mantle $\delta^{13}C$ range (discussed next; Stachel et al., 2017).

Due to the heterogenous nature of the SCLM and of the fluids or melts produced in the mantle, a number of additional possible diamond-forming reactions and mechanisms are available. It is important to relate mineral inclusions, such as rare carbonates, to these reactions. Additionally, carbon and nitrogen isotopes, being controlled by the carbon and nitrogen speciation, can give additional information to these processes.

Stable isotopes are widely used to trace and track mineral formation and evolution, even within the mantle, and diamonds are no exception. Carbon and nitrogen isotopes ($\delta^{13}C$ for $^{13}C/^{12}C$ and $\delta^{15}N$ for $^{15}N/^{14}N$) are important tracers for the source and evolution of diamond forming fluids. Mantle-derived carbon and nitrogen isotopic values are well constrained to -5 ±2 ‰ ($\delta^{13}C$; Cartigny et al., 2014; Javoy et al., 1986) and -5 ±3 ‰ ($\delta^{15}N$; Marty, 1995), respectively. Two important aspects that are responsible for variations from canonical mantle values are input from non-mantle sources and isotopic fractionation. Large global datasets of $\delta^{13}C$ of diamond have shown a dichotomy in distribution: peridotitic diamonds have a single mode at ~-5 ‰, whereas eclogitic diamonds have a strong mode at ~-5 ‰, a second, broad mode at -19 to -8 ‰, a significant ^{13}C-depleted tail (down to -41 ‰), and a minor ^{13}C-enriched component up to +3 ‰

(Cartigny, 2005; Galimov, 1991; Stachel and Harris, 2009). The ^{13}C-depleted values prominent in eclogitic diamonds are attributed to input of subducted carbon in the diamond-forming fluids (Sobolev and Sobolev, 1980). Nitrogen – a trace impurity in diamond – typically ranges between below detection (<~10 at.ppm) and up to ~1400 at.ppm, with higher values being very rare (Stachel et al., 2009). The concentration of nitrogen in the mantle is low (~8 ppm; Johnson and Goldblatt, 2015) and thus ambient mantle as a source for nitrogen is not likely. Nitrogen is introduced into the mantle in subducted slabs in the form of NH_4^+, which substitutes for K^+ in clay minerals in sediments (Honma and Itihara, 1981). Once in the mantle, it is subjected to prograde metamorphism that – if coupled to a hot/fast slab – can effectively remove significant amounts of nitrogen; along a cold subduction geotherm, nitrogen, however, can survive further into the mantle (Busigny et al., 2003). Nitrogen isotopes in diamond add a second dimension to tracing the source and evolution of diamond-forming fluids. Prograde metamorphism of subducted sediment enriches it in ^{15}N (Haendel et al., 1986), which can be seen in the high proportion of diamond with $\delta^{15}N > 0$ ‰. Rare ^{15}N-depleted sediment can also produce diamond-forming fluids with $\delta^{15}N$ down to -12 ‰ (Li et al., 2007).

An important observation is that altered oceanic crust has a mantle-like averaged $\delta^{13}C$ signature (Shilobreeva et al., 2011), which allows formation of diamonds with mantle-like carbon from fluids introduced into the mantle via subduction. Below the sedimentary cover, oceanic crust consists of basaltic igneous rocks – consisting of pillow lavas, sheeted dykes, and gabbro (~7 km thick) – overlying depleted peridotite (up to ~80 km thick) of mixed dunitic, harzburgitic, or lherzolitic composition (Green et al., 1979). With age, the oceanic crust is chemically altered – by carbonate mineralisation in the upper basaltic lavas and low-grade metamorphism and hydration (Alt and Teagle, 1999) – and, through cooling, the lithosphere becomes less buoyant and subducts. Slow spreading ridges ($<50\ mm \cdot a^{-1}$) produce oceanic crust with a significant component of serpentinised lithospheric mantle, in addition to lithospheric peridotite exposed along deep faults (Poli and Schmidt, 2002). Although water may be lost early to the mantle wedge (Kerrick and Connelly, 2001), carbonated metabasalt will only start to lose carbonatitic melt at the base of the upper mantle, sequestering much of the surficial carbon into the deeper mantle (Dasgupta et al., 2004).

1.2.3. The deeper upper mantle, transition zone, and lower mantle

The deeper regions of the mantle, encompassing the transition zone and lower mantle, are poorly constrained compared to the upper mantle. Much of our understanding in terms of modal mineralogy comes from seismic models and experimental studies, but uncertainty within these models can have a significant impact on mineral proportions, affecting large-scale mantle convection (Ballmer et al., 2017). Although most of the phase transitions occurring in the mantle were determined in the 1960-1980s, modern studies have focused on improved accuracy and fine-scale mantle heterogeneities (Houser et al., 2020).

In the transition zone (410 to 660 km depth, see Figure 1-2), olivine – the volumetrically most important component of peridotite – first transforms to wadsleyite (13.5 GPa or 410 km, with a spinel-like structure) and then to ringwoodite (18 GPa or 520 km; with a true spinel structure; Irifune and Ringwood, 1987). Within the lower mantle, bridgmanite – the perovskite structured $MgSiO_3$ – is modally the most abundant, followed by ferropericlase – (FeMg)O – and perovskite-structured $CaSiO_3$ (Figure 1-2; Ringwood, 1991). Oceanic slabs, both the basaltic and peridotitic portions, also undergo these phase transitions when descending through the mantle (Irifune and Ringwood, 1987). Subducting slabs can reintroduce volatiles such as water into the transition zone and the topmost lower mantle, which play an important role for deep mantle melting, e.g., the formation of plumes (Kuritani et al., 2019). The journey of water in hydrous and nominally anhydrous minerals through the mantle (described in Section 1.2.1) has been experimentally determined for the transition zone (e.g., Ohtani et al., 1995), but only confirmed with the discovery of hydrous ringwoodite inside a diamond (Pearson et al., 2014). Thus, the movement of volatiles from the upper to the lower mantle could have important consequences for deeply-derived magmas such as kimberlites and ocean island basalts.

Lastly, most of the samples for studies on lower mantle diamonds have come from Brazil and Guinea, where the lower mantle diamonds contain an inclusion assemblage with a partially meta-basaltic affinity with a high proportion of Ca-rich minerals, either as $CaSiO_3$ or retrogressed versions (Hutchison, 1997; Stachel et al., 2000b). Koffiefontein is one of the few localities with an exclusively peridotitic lower mantle suite (Moore et al., 1986; Scott Smith et al., 1984).

1.3. The specific case of the Kaapvaal Craton

The Kaapvaal Craton along with the Zimbabwe Craton and various Palaeoproterozoic terranes – e.g., Limpopo Belt, Kheis-Okwa-Magondi Belt, Namaqua-Natal Belt, and Rehoboth Subprovince (not shown) – make up the larger Kalahari Craton in southern Africa – the southern cornerstone of the African continent (Figure 1-3). Forming towards the end of the Archean, the Kaapvaal Craton combines two distinct domains: the Witwatersrand block on the east and the Kimberley block on the west, separated by a series of granites and minor greenstone belts and tonalite-trondhjemite-granodiorite terranes (De Wit et al., 1992; Schmitz et al., 2004). The formation of the Witwatersrand block began at approximately 3.7-3.2 Ga with the amalgamation of small, discrete blocks through a combination of magmatic and tectonic accretion (Eglington and Armstrong, 2004; Lowe, 1994; Poujol et al., 2003; Schmitz et al., 2004). The Kimberley block formed in the same manner almost 600 Myr after, at around 3.1 Ga (Eglington and Armstrong, 2004), with N-S trending greenstone belts of 3.1-3.0 Ga and younger granitic gneisses of 3.0-2.8 Ga (Anhaeusser and Walraven, 1999). A convergent margin – on the eastern edge of the Kimberley block and the western edge of the Witwatersrand block – sutured the blocks between 2.97-2.93 Ga, resulting in overriding of the Kimberley block on the Witwatersrand block (Schmitz et al., 2004). The subduction margin is imaged on the Kaapvaal craton as a magnetic anomaly: the Colesberg lineament.

Multiple models have been put forward for the formation of the Kaapvaal Craton nucleus. Although some plume models exist for its formation (e.g., Griffin et al., 1999; Haggerty, 1986), it is generally accepted to have formed by shallow processes. The lithosphere formation model of Jordan (1978) described craton formation by significant degrees of extraction of basaltic melt in the mantle wedge to produce a depleted peridotite that is too buoyant to subduct. Since then, multiple revisions have been made to modify this craton formation model. Notably, Pearson and Wittig (2008) included a two-stage peridotite depletion model at low pressure, first at a spreading ridge and then in a mantle wedge. With radiogenic dates of mineral inclusions in some Kimberley-block diamonds, Shirey et al. (2004a) related these ages to important craton formation and evolution stages of the Kaapvaal, e.g., 3.3 Ga garnet ages in diamond date the oldest, depleted lithosphere; 2.9 Ga eclogitic sulphides date the merger and accretion of the Kimberley and Witwatersrand blocks; and later Proterozoic magmatism and marginal subduction

enriched the craton, forming lherzolitic diamonds. Later thickening of these depleted peridotitic terranes by lateral accretion, facilitated by collision of building blocks, built up the cratonic lithosphere (Jordan, 1988). This process is matched on the surface by the expression of the crustal rocks, which show accreted terranes (De Wit et al., 1992).

Since stabilisation, the Kaapvaal Craton has experienced many chemical and structural disruptions. Large-scale, craton-wide disturbances in the form of intracontinental rifting culminated in the eruption of the Vendersdorp lavas at 2.72-2.67 Ga soon after craton amalgamation (Schmitz et al., 2004), intrusion of the almost 10 km-thick, mafic Bushveld Complex on the western part of the craton at 2.1 Ga (Walraven et al., 1990), and more recently the Karoo continental flood basalts at 183 Ma (Duncan et al., 1997). For the western Kaapvaal Craton, the formation of the Kheis-Okwa-Mogondi accretionary orogenic belt to the west at 2.1-1.8 Ga, followed by the Namaqua Natal orogeny to the south at 1.4-0.9 Ga caused widespread modification of isotopic signatures in the mantle (Nixon et al., 1987; Shu et al., 2013).

1.4. The Koffiefontein kimberlite

Kimberlite pipes are eruptive, ultramafic, Si-undersaturated magmas derived from the sublithospheric mantle that entrain mantle xenoliths during their volatile-aided fast ascent to the surface (Scott Smith et al., 2013). Globally, kimberlite magmatism occurred during discrete time intervals with peaks at 1200-1050 Ma, 600-480 Ma, 400-320 Ma, and 170-50 Ma (Griffin et al., 2014; Heaman et al., 2019). The Kaapvaal Craton is host to numerous (>150) archetypal kimberlite pipes (Group I) and variously carbonate-rich lamproites (also known as Group II kimberlites or orangeites) that erupted episodically (e.g., Field et al., 2008). The younger Group I kimberlites (~95 Ma) have an ocean island basalt (OIB) signature, evidenced by their unradiogenic Sr and radiogenic Nd isotope ratios and trace element signatures consistent with derivation from the deep mantle, i.e., the transition zone or lower mantle. The older carbonate-rich lamproites (Group II, >110 Ma) have trace element signatures suggesting significant phlogopite in the source, corresponding to the involvement of subduction-associated sediment and subduction-derived fluid, and likely derive from the lithosphere (Becker and le Roex, 2006).

Many of these eruptions occur as fissures and dykes, resulting in multiple diamond-bearing "kimberlite" deposits in the same area.

The Koffiefontein kimberlite – an archetypal kimberlite – is located approximately 80 km SSE of Kimberley in the Free State (Figure 1-3). The kimberlite erupted very close to the Colesberg lineament, providing a glimpse of the cratonic root in this location. Koffiefontein has been a focus for diamond exploration and recovery since its first recorded diamond discovery in 1870 (Field et al., 2008), being the first kimberlite to be mined in southern Africa. The Koffiefontein pipe (90.4 Ma, U-Pb zircon; Davis, 1978) was emplaced into Archean basement and overlying Phanerozoic sediments of the Karoo basin. The mine includes the related pipes of Koffiefontein, Ebenhaezer, and Klipfontein in a SE-NW trending structure presumably related to an underlying fissure complex (Naidoo et al., 2004). The main pipe is steep-sided and precursor intrusions in the west and east created an irregular shape, becoming wider with depth (Clement, 1982).

1.5. Objectives

Since the first chemical studies of mineral inclusions within diamonds began, a unified understanding of the formation and evolution of the cratonic lithosphere and the chemistry of the mantle has emerged. However, questions remain to be answered regarding metasomatic reactions in the mantle, the source of diamond-forming fluids in the mantle, and the formation of rare lower mantle diamonds. For these answers, we continue to study diamonds and utilise both well-established and new geochemical techniques that provide precise results on small, sub-millimetre sized minerals where the elements being analysed are only present in trace amounts. This dissertation builds on decades of research on diamonds and their inclusions and provides answers and insight into these important questions through the study of diamonds from the Koffiefontein pipe on the Kaapvaal Craton. In this study I utilise new and existing techniques to trace the source of diamond forming fluids and the formation history of the diamond substrates within the upper and lower mantle beneath the Kaapvaal Craton.

The objectives of this PhD thesis are summarised as follows:

(i) Identify the diamond-forming reaction(s) occurring in the upper mantle and fingerprint the source of diamond-forming fluids using carbon and nitrogen isotopes. Comment on the origin of ^{15}N-depleted diamonds from the Koffiefontein kimberlite.

(ii) Characterise the levels of melt-depletion and enrichment recorded by mineral inclusions in peridotitic and eclogitic diamonds from Koffiefontein. Using the most up-to-date geothermobarometric techniques, produce an accurate representation of the geothermal gradient in the mantle lithosphere beneath the Koffiefontein kimberlite at the time of eruption.

(iii) Document extreme metasomatism in the upper mantle leading to the formation of goldschmidtite – a new mineral discovered in a Koffiefontein diamond.

(iv) Combine mineral chemistry with lower mantle compositional models to understand the origin of lower mantle diamond substrates and the fate of deeply subducted oceanic slabs.

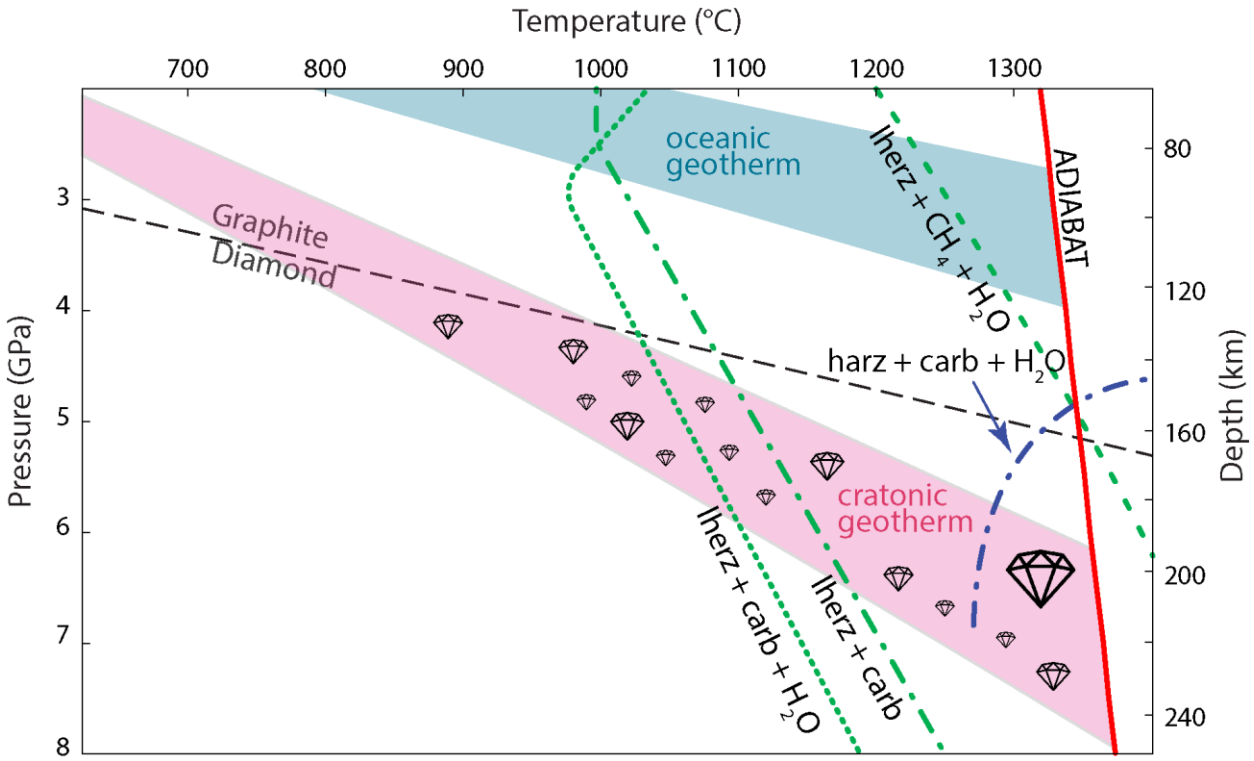

Figure 1-1: Pressure-temperature diagram showing the range of model continental (Hasterok and Chapman, 2011) and oceanic lithosphere geothermal gradients in relation to the graphite-diamond transition (Day, 2012) and the convecting mantle adiabat. For colder continental geothermal gradients, the diamond window (indicated with diamond symbol) increases. In addition, the solidi for carbonate-bearing (± H_2O) lherzolite (lherz; Litasov et al., 2014; Wyllie and Ryabchikov, 2000) and harzburgite (harz; Wyllie, 1987b) are shown.

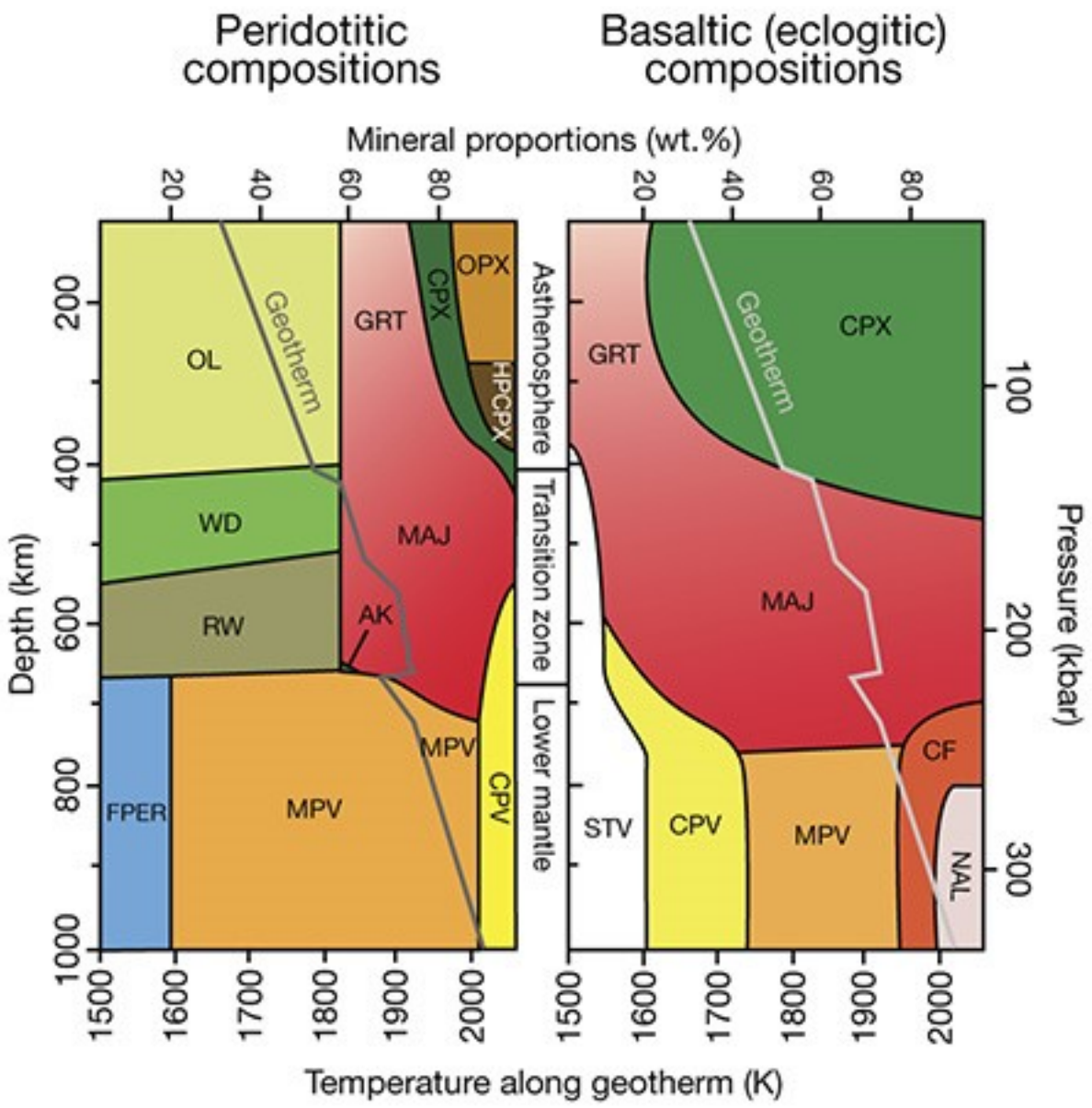

Figure 1-2: Mineralogy and mineral proportions of a (left) pyrolytic and (right) basaltic mantle with an increase in depth. With increasing depth, minerals adopt more compact structures. Phase transitions are determined from high pressure experiments (referenced in text). Geotherm for each bulk composition is shown. Diagram from Harte (2010), adapted from Ringwood (1991).

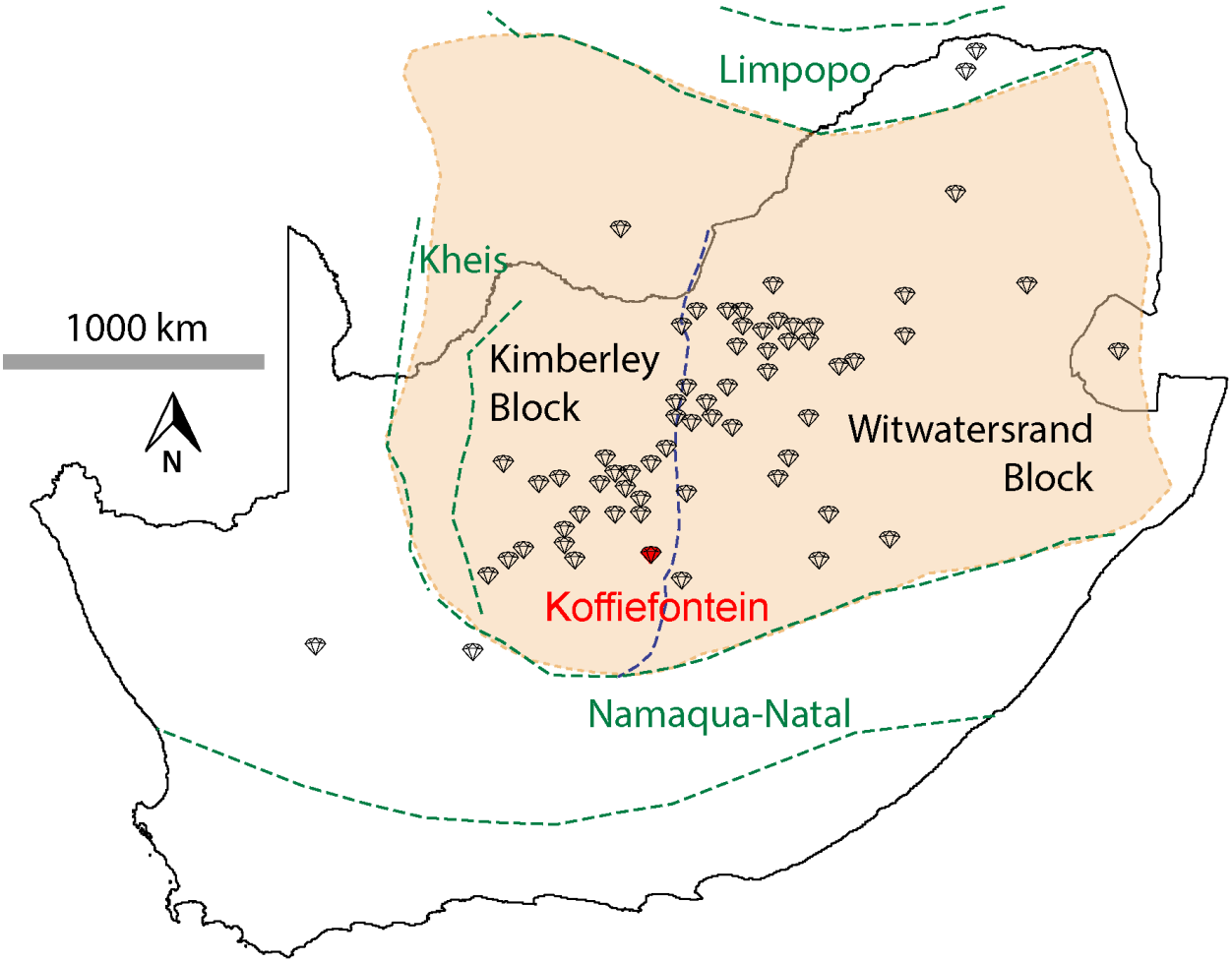

Figure 1-3: Geological map of the Kaapvaal Craton within the context of southern Africa (adapted from Eglington and Armstrong, 2004; Griffin et al., 2003; Schmitz et al., 2004). Indicated on the map: location and extent of the Kimberley and Witwatersrand blocks (orange shaded region), the domains of selected regional-scale mobile belts (green dashed lines), and the Colesberg lineament (blue dashed line). The location of diamond-bearing kimberlite pipes is shown with diamond symbols and the Koffiefontein pipe highlighted in red. Kimberlite locations are from Council for Geosciences (Vorster, 2002).

Chapter 2. Materials and methods

2.1. Sample selection and characterisation

The Koffiefontein diamonds in this study comprise of a parcel of 192 inclusion-bearing diamonds supplied by J.W. Harris and collected during mining operations by De Beers Consolidated Mines since ~1980. The colour, shape, and visible surface features of all diamonds were described. Photographs of each diamond and any notable features were taken with a Nikon D90 DSLR camera attached to a Leica MZ APO binocular microscope. Raw images from the camera were processed with Adobe Photoshop and a scale affixed. A collection of these images is provided as an additional online resource available at the University of Alberta Library's institutional repository, ERA.

The diamonds host an array of inclusion types (number of diamonds in each group): silicate and oxides (145 diamonds), sulphide and silicate (5), sulphide-only (39 diamonds), sublithospheric (3). The diamonds were assigned to the peridotitic, eclogitic, or websteritic suite based on inclusion colour for unbroken diamonds (e.g., orange for eclogitic garnet, purple for peridotitic garnet, and colourless for orthopyroxene and olivine). A representative number of diamonds were selected for further study of the included minerals: 91 silicate-included, 5 sulphide-only, and 3 sublithospheric. The Koffiefontein pipe is known for a subpopulation of diamonds containing large sulphide inclusions only. Based on low Ni contents, these sulphides derive from eclogitic substrates, but they are treated here as a separate group from silicate-included eclogitic diamonds due to their high nitrogen concentrations. Sulphides with coexisting silicate inclusions, however, were grouped into the regular P- or E-type suites.

Inclusions selected for Raman spectroscopic analysis had a “window” polished using a scaife. Diamonds were broken with a steel cracker and the inclusions released were mounted in epoxy, ground with corundum paper, and polished with 1 μm diamond solution on a nylon cloth.

2.2. Fourier transform infrared spectroscopy

Nitrogen abundance and aggregation of diamonds were determined by Fourier transform infrared spectroscopy (FTIR) using a Thermo Nicolet Nexus 470 FT-IR Spectrometer combined with a Continuum infrared microscope. The detector was cooled with liquid nitrogen and the bench and microscope purged with dried and CO_2-free air during analysis. Analyses were performed using a 50x50-µm spot size for ~200 s at a spectral resolution of 2 cm^{-1}. A background spectrum was taken every four hours. Where available, two fragments from each diamond, representing the core and rim, were analysed, otherwise whole diamonds were used. Sample spectra were processed using the DiaMap Excel spreadsheet (Howell et al., 2012b, 2012a) for spectral deconvolution and the concentration (at.ppm) of nitrogen in A- and B-centres was calculated using the absorption strength at 1282 cm^{-1} for A (16.5 ±1; Boyd et al., 1994) and B centres (79.4 ±8; Boyd et al., 1995). Due to the poor quality of spectrum for naturally curved diamond faces, a lower cut-off of 10 at.ppm was used.

2.3. Raman spectroscopy

Prior to diamond breakage and again after being mounted in epoxy, selected minerals of interest were analysed by Raman spectroscopy. For samples with multiple crystalline phases (e.g., pure SiO_2), a Raman spectrum was collected to confirm mineral identification. Spectra were collected with a Thermo-Scientific DXR Raman microscope at the Nanotechnology Research Centre, National Research Council Canada, University of Alberta. A 532 nm laser excitation source was used, with the power varying between 6 to 10 mW, and a 50X objective at with a spatial resolution of 1.1 µm. The Raman system was configured with 1800 lines·mm grating and a 50 µm pinhole. Spectra were recorded between 100 to 3500 cm^{-1} for 30 s and collected five times to maximize the signal-to-noise ratio, producing an estimated spectral resolution of ~1.6-2.0 cm^{-1}. Resulting spectra were compared to known minerals using the RRUFF database (Lafuente et al., 2016).

2.4. Electron probe microanalysis (EPMA)

Major element analyses of polished inclusions from diamond was conducted by electron probe microanalysis (EPMA) at the University of Alberta on either a CAMECA SX100 or a JEOL 8900R, and data reduced using the Probe for EPMA software (Donovan et al., 2015). Operating

conditions for both machines comprised an accelerating voltage of 20 kV and a fully-focused beam (<1 μm diameter or <2 μm for sublithospheric inclusions) at a current of 20 nA. On-peak acquisition times were 40 s for Na_2O and 30 s for SiO_2, TiO_2, ZnO, Al_2O_3, V_2O_3, Cr_2O_3, FeO, NiO, MnO, MgO, CaO, K_2O, P_2O_5, with a combined background time of 30 s. Analytical accuracy and drift were monitored by analysing a selection of well-characterised minerals as secondary standards before and after every analysis run. Due to the Mg-Fe-rich nature of the lower mantle mineral inclusions, synthetic and endmember standards were used to accurately measure the high-Mg samples. Where possible, three spots were analysed and averaged for each mineral inclusion, with each accepted individual analysis having an oxide total between 98.5 to 101.5 wt.%.

For analysis of trace Al, Ca, and Cr in olivine, the CAMECA SX100 was used and the beam current increased to 200 nA. Count times for Al, Ca, and Cr were 300 s for both the on-peak and the combined off-peak (background) measurements. Olivine major element data for each sample (method as described above) was entered into the Probe for EPMA software before data processing. Accuracy was verified using an in-house secondary standard (San Carlos olivine SC-GB) with a previously determined Al concentration of 85 ±4 ppm (Bussweiler et al., 2017). Repeat analyses on the secondary standard resulted in averaged concentrations of (in ppm): Al 82 ± 4, Cr 156 ± 2, Ca 528 ± 0.6; and detection limits of (in ppm): Al 8, Cr 5, Ca 6.

2.5. Laser ablation inductively coupled plasma mass spectrometry (LA-ICP-MS)

Silicate mineral inclusions were analysed for trace elements at the Arctic Resources Laboratory, University of Alberta using a sector-field Thermo Element II XR coupled with a Resonetics M-50 LR 193 nm excimer laser ablation system and 2-volume Laurin_Technic ablation cell. Elements analysed were: Ca, Sc, Ti, Ni, Pb, Sr, Y, Zr, Nb, Ba, La, Ce, Pr, Nd, Sm, Eu, Gd, Tb, Dy, Ho, Er, Tm, Yb, Lu, Hf for garnet and clinopyroxene at spot sizes of 50 or 75 μm; plus Na, Rb for orthopyroxene at a spot size of 90 or 130 μm; and Li, Al, Na, V for olivine at 130 μm. NIST SRM 612 glass was the primary calibration standard and a well-characterised, in-house reference garnet (PN1), clinopyroxene (GP13), and olivine (SC-GB) were used as secondary standards, at the same range of analytical spot sizes. A laser repetition rate of 10 Hz and a fluence of ~ 3.8 $J \cdot cm^{-2}$, measured at the ablation site, were used. Backgrounds were measured

for 250 s followed by sample ablation for 70 s; and a pre- and post-wash-out of 60 s and 40 s, respectively, was used. Ablated material was carried by helium gas and the rare earth elements analysed for 30 cycles, with ^{139}La at 50 ms. The ICP-MS was operated in low mass-resolution mode (~400 M/DM) and the ThO/Th signal was monitored to ensure the oxide ratio and hence oxide production in general, remained low (below 0.5 %). Data was processed offline using Iolite v3.32 (Paton et al., 2011) with ^{29}Si as the internal standard.

2.6. Stable isotopes by secondary ion mass spectrometry (SIMS)

Samples for stable isotope analysis were prepared and measured at the Canadian Centre for Isotopic Microanalysis. One fragment from each broken diamond was selected, and emphasis was placed on selecting fragments that represented a core-rim transect through the diamond. Fragments from 99 diamonds were selected and mounted in epoxy for $\delta^{13}C_{VPDB}$, $\delta^{15}N_{AIR}$, and nitrogen abundance determination. To expose internal growth structures in the diamonds, cathodoluminescence (CL) images were taken prior to analysis on a Zeiss EVO MA15 (15 kV and 3-5 nA beam current) employing a grey-scale CL system composed of a parabolic mirror coupled to a high-sensitivity, broadband photomultiplier detector. For diamond, C-isotopes ($^{13}C/^{12}C$), nitrogen abundances, and N-isotopes ($^{15}N/^{14}N$) were determined on a CAMECA IMS-1280 multi-collector ion microprobe with a primary beam of $^{133}Cs^+$ ions at 20 keV focused to ~12 µm and a current of 0.6-2.9 nA. For $MgSiO_3$ inclusions, O-isotopes ($^{18}O/^{16}O$) were measured under the same conditions but with 1.5 nA and a ~10 µm diameter probe. An initial 20 x 20 µm area was rastered before analysis, principally to remove surface contamination. Total spot-to-spot time was 250 s for C-isotopes, 210 s for N abundance, 540 s for N-isotopes, and 240 s for O-isotopes. The reference materials used were natural diamond (S0270, $\delta^{13}C_{VPDB}$ = -8.84 ‰; Stern et al., 2014) and enstatite (S0170 $\delta^{18}O_{VSMOW}$ = +5.64 ‰; Regier et al., 2020).

Chapter 3. Multiple fluid sources for diamond formation at Koffiefontein, Kaapvaal Craton: a $\delta^{13}C$-$\delta^{15}N$-[N] study

3.1. Introduction

Diamond encapsulates mantle minerals that contain important information about the formation history of early Earth and the chemical environment of its mantle. Beyond that, diamond itself can provide insights into the primordial reservoir of carbon in the mantle (Deines et al., 1987) and the recycling of surficial carbon into the mantle via both ancient and modern subduction processes (Dasgupta, 2013; Sobolev and Sobolev, 1980). Diamonds principally form in subcontinental lithospheric mantle (SCLM) at great pressures and temperatures – 4.5 to 6.5 GPa and 950 to 1350 °C (Boyd and Gurney, 1986; Meyer, 1986) – by redox reactions that involve the oxidation of CH_4 or the reduction of CO_2 (Deines, 1980). Depleted peridotite and subducted oceanic slabs in the mantle provide two different substrates and sources of fluid that both can result in diamond formation.

The rigid carbon lattice structure of diamond maintains its longevity and stability in the mantle but limits the inclusion of molecular impurities. Although diamond is overwhelmingly carbon, minor amounts of nitrogen (parts per million) provide additional information on the source of diamond-forming fluids and their evolution in the mantle. Nitrogen substituted in the diamond lattice aggregates from single nitrogen atoms, to doubly-bonded nitrogen atoms, then to four nitrogen atoms surrounding a vacancy (Davies, 1976; Loubser and Van Wyk, personal communication to Evans and Qi, 1982). The energy required for these processes can be used to evaluate the ambient mantle temperature for a diamond over a specified time interval; however, this can be overwritten by transient heating events, e.g., mantle plume activity (explained in discussion; Taylor et al., 1990).

Isotopic variation of both carbon ($^{13}C/^{12}C$) and nitrogen ($^{15}N/^{14}N$) in diamond can be used to understand the source of diamond-forming fluids. Due to the very large volume of the mantle and trace concentration of carbon therein (30-1100 ppm; Dasgupta, 2013), fluid sources introduced into the mantle, e.g., from dehydrating subducting slabs, can be overwritten,

eliminating the ability to uniquely fingerprint all carbon reservoirs. Small-scale variations and accurate determination of carbon and nitrogen isotopes in-situ made possible by secondary ion mass spectrometry (Wilding, 1990), can provide insight into diamond-forming processes and its fluid evolution during diamond growth (Harte and Otter, 1992).

Mantle-derived rocks have a tightly constrained $\delta^{13}C$ value of -5 ±2 ‰ (Cartigny et al., 2014; Javoy et al., 1986) and $\delta^{15}N$ value of -5 ±3 ‰ (Boyd et al., 1987; Cartigny et al., 1997; Javoy et al., 1986; Marty, 1995). Although a large proportion of global diamonds have $\delta^{13}C$ values within the mantle range, variation between -42 ‰ and +5 ‰ is observed. The same is true for $\delta^{15}N$ values, with a mode at -5 ‰ and a large range from -25 ‰ to +15 ‰ (with a rare minimum value of 40 ‰; Cartigny, 2005; Cartigny et al., 2014). Rayleigh fractionation – the evolution of a fluid during crystallisation – can only account for minor differences in $\delta^{13}C$ and $\delta^{15}N$ (see review of Kirkley et al., 1991). Therefore, the large range in isotopic values most likely relates to either (1) parental fluid composition, possibly related to input of subducted crustal material (Sobolev and Sobolev, 1980; cf. Cartigny et al., 1998a) or (2) fractionation effects arising from differences in C- and N-species in oxidising and reducing environments during diamond formation (Deines, 1980; Petts et al., 2015).

Diamonds, transported from the mantle to the surface by kimberlite eruptions, are located on Archean cratons such as the Kaapvaal Craton in southern Africa. The craton is host to numerous diamond deposits of which the Koffiefontein diamonds are among the most well-studied. A study on diamond physical characteristics by Harris et al. (1975) based their seminal classification on diamonds from Kaapvaal kimberlites, including Koffiefontein. A notable outcome of their investigation was the high proportion of twinned (macles) and irregular-shaped diamonds and the general colourless and translucent nature of the Koffiefontein diamonds (Harris et al., 1975). In addition, the Koffiefontein diamond production contains a sizable cloudy diamond component (~20 %; Harris and Gurney, 1979; Timmerman et al., 2018). Koffiefontein diamonds are unique in their mineral inclusions by having a large proportion of sulphide inclusions (Harris and Gurney, 1979), which provided Archean (2.9-2.7 Ga) and Proterozoic (1.2-1.1 Ga) diamond ages for eclogitic diamonds and Phanerozoic ages (90 Ma) for peridotitic diamonds (Re-Os of sulphide inclusions; Pearson et al., 1998). Early silicate and oxide inclusion

studies on Koffiefontein diamonds indicated a range of lithospheric to sublithospheric paragenesis (Cardoso, 1980), but a modern study on these diamonds has not been completed.

This study reports the content and aggregation state of nitrogen in 189 diamonds from the Koffiefontein pipe combined with SIMS $\delta^{13}C$-$\delta^{15}N$-[N] compositions for fragments from 97 diamonds. The findings reveal that that Koffiefontein diamonds (1) have a complex growth history with multiple stages of growth and resorption, (2) formed from fluids with a mantle-like carbon isotopic signature for both peridotitic and eclogitic diamonds, and (3) likely formed in reduced environments to produce extremely ^{15}N-depleted diamonds.

3.2. Results

3.2.1. Diamond characterisation

The Koffiefontein diamonds were characterised by physical attributes (colour and shape), primary growth features (stacked growth layers), resorption indicated by surface features (e.g., trigons, laminae, hillocks), plastic deformation (striations and coarse plastic deformation), and late-stage alteration (e.g., breakage during transport – ruts – or processing; Table A1).

The inclusion-bearing Koffiefontein diamonds are generally colourless (Figure 3-1; 88 P-type and 63 E-type) and transparent, with no visible clouds or fibrous growth. The yellow diamonds were generally light to very light in colouration (8 P-type and 7 E-type). The brown colours varied from an intense, dark brown to a lighter brown colour (13 P-type and 7 E-type; Figure 3-2D&H). The resorbed, dodecahdral form is the most common with 27 peridotitic and 52 eclogitic diamonds having this shape (Figure 3-2F&G). Twinned forms are common among peridotitic diamonds, 42 diamonds, and present as mainly contact (spinel twin/macle) or less commonly as penetration twins as shown in Figure 3-2E and Figure 3-2C, respectively. Twinned diamonds are less common in the eclogitic and websteritic group (7 diamonds). Irregular diamonds are those that do not conform to a specific shape or are broken, and a primary shape cannot be identified. Irregularly-shaped diamonds are more common in the eclogitic group (12 diamonds) compared to the peridotitic group (11 diamonds; e.g. Figure 3-2D). Two diamonds are pseudohemimorphic (7/14 and 14/01; Table A1), likely being due to one half of the diamond

being unresorbed while embedded in a mantle rock during subsequent fluid influx, possibly associated with kimberlite sampling and ascent.

The majority of the Koffiefontein diamonds exhibit some level of resorption, except for five of the peridotitic octahedral diamonds (Figure 3-2B). Diamond surface features for the inclusion suites are tabulated in Table 3-1. For octahedral-shaped diamonds, stacked growth layers are common (P-type = 15, E-type = 4); whereas for dodecahedral diamonds, terraces are common (P-type = 25, E-type = 35). The most common surface feature is hillocks with varying forms from elongated to elongated drop-shaped, and less commonly shield-shaped. Diamond 12/06 has trigonal-shaped hillocks (Figure 3-2H). Trigons are mostly common as negative, flat-bottomed trigons, some negative terraced trigons are present. Two peridotitic diamonds have octagons and hexagons but their shape is indetermined. In Figure 3-2G, the diamond surface shows a very shallow unevenness not apparently linked to a specific surface feature and is present on all diamond faces. Diamond 40/01 has a bubble-shaped corrosion texture with circular negative relief (Figure 3-2F), which possibly indicates a surface texture distinct to microdisks which have a positive relief. Lastly, plastic deformation lines are visible on 25 diamonds, commonly in the form of striations (single or multiple directions; Figure 3-2D) and less common as coarse lines (Figure 3-2E; Titkov et al., 2012).

3.2.2. Nitrogen abundance and aggregation by FTIR

The nitrogen abundance ([N]) of Koffiefontein diamonds is generally low (Figure 3-3A) with ~19 % of diamonds having no detectable nitrogen (Type II). For peridotitic diamonds, there is a sharp decrease in the numbers of diamonds with increasing nitrogen abundance. A quarter of the peridotitic diamonds have no detectable nitrogen by FTIR (<10 at.ppm). The eclogitic diamonds have a large range in nitrogen abundance with a broad mode between 350 to 750 at.ppm, which is especially prominent in the sulphide-only population in which none of these diamonds are Type II and 97 % have [N] > 100 at.ppm (N = 34). Peridotitic diamonds have a maximum [N] concentration of 1145 at.ppm and eclogitic diamonds extend to 1234 at.ppm. Three websteritic diamonds were analysed with two being Type II and the other having a [N] = 365 at.ppm.

Nitrogen, when above the detection limit in all the Koffiefontein diamonds, is in the aggregated state (Type Ia) and is further categorised according to the degree of aggregation based on %B (Table 3-2). For all suites, Type IaAB aggregation state is the most common. The peridotitic suite has the most diamonds that are fully aggregated – 10 of 79 N-bearing diamonds. During the nitrogen aggregation process, a platelet peak arises that is directly proportional in area (B' peak; cm^{-2}) to the abundance of nitrogen in the B-centre (N_B; at.ppm): classified by Woods (1986) as regular diamonds. Most of the Koffiefontein diamonds with [N] >50 at.ppm are classified as regular diamonds except for three of the eclogitic sulphide-only diamonds (40/12, 40/19, 40/21; Table A2).

3.2.3. Cathodoluminescence

Cathodoluminescence (CL) images of diamond show growth patterns, provided there is a significant change in the nitrogen concentration of the different diamond growth layers or zones. Figure 3-4 shows CL images of selected Koffiefontein diamonds (all diamonds analysed in Figure A1). The majority of the peridotitic diamonds have little to no detectable nitrogen and thus CL images cannot distinguish multiple diamond growth events (e.g., 10/06). For the diamonds with variable nitrogen, growth patterns can be simple-continuous (e.g., 6/02, 8/09, 11/03) or complex (e.g., 7/04, 12/05). For example, the zig-zag pattern of diamond 8/17 is typical for cuboid growth whereas diamond 10/07 reveals a core that was resorbed before octahedral growth started again. Diamond 10/04 clearly displays its twin line (re-entrant twin; indicated in Figure 3-4) and oblique sectioning can be attributed to the complicated pattern of 12/05.

3.2.4. Carbon and nitrogen isotopic compositions

A total of 77 peridotitic, 19 eclogitic, 5 sulphide-only eclogitic, and 3 websteritic diamonds were analysed for carbon and nitrogen isotopes (three spots analysed per diamond; Table A3). Isotopic ratios are expressed as $\delta^{13}C = (^{13}C/^{12}C)_{sample}/(^{13}C/^{12}C)_{standard} - 1$, or $^{15}N/^{14}N$ for $\delta^{15}N$. $\delta^{13}C$ ranges from -18.0 to -2.0 ‰ with a mean of -5.7 ‰ and median of -5.5 ‰ (n = 320). Peridotitic diamonds have mean and median $\delta^{13}C$ values of -5.8 ‰ and -5.5 ‰, respectively; and the majority of analyses fall within the $\delta^{13}C$ composition of the mantle at 5 ±2 ‰. An appreciable number of diamonds have carbon isotope compositions that are less than -10 ‰ (Figure 3-5A),

with two samples having strongly negative values of ~-15 ‰ (12/06) and ~-17 ‰ (6/01). The eclogitic diamonds have a slightly lower mean and median of -6.4 ‰ and -5.8 ‰, respectively, with a range from -12.0 to -4.0 ‰. The sulphide-only eclogitic diamonds have a mean and median of -4.4 ‰ and range between -5.5 to -3.2 ‰. The three websteritic diamonds have a range of $\delta^{13}C$ values from -9.1 to -2.0 ‰. The majority of the eclogitic diamonds plot within the mantle range and some analyses cluster around -10 ‰ and -12 ‰ (Figure 3-5C).

The nitrogen isotope compositions of Koffiefontein diamonds are extremely variable for both peridotitic and eclogitic diamonds, with $\delta^{15}N$ ranging from -25.6 to +13.2 ‰, with a mean of -0.8 ‰ and median of -1.4 ‰ (n = 140). The peridotitic diamonds (n = 70) have a wide range from -25.6 to +13.2 ‰ with a mean of -0.4 ‰ and median of -1.6 ‰; whereas the eclogitic diamonds (n = 39) range from -8.4 to +12.6 ‰ with a mean and median of ~0 ‰. The sulphide-only diamonds (n = 22) have a range in $\delta^{15}N$ of -8.6 to +0.3 ‰ and the three websteritic diamonds fall between -15.2 and +9.4 ‰ (Figure 3-5D).

There are no discernible trends between $\delta^{13}C$ or $\delta^{15}N$ and nitrogen concentration (Figure 3-5E&F). Diamonds with high nitrogen concentrations – [N] > 1000 at.ppm – have mantle-like $\delta^{13}C$ and $\delta^{15}N$ values, whereas diamonds with nitrogen concentrations between 100 to 1000 at.ppm have $\delta^{15}N$ values within and outside of the mantle range. Comparison of the variation of $\delta^{13}C$ and $\delta^{15}N$ within individual diamonds indicates that $\delta^{13}C$ values change by only 0.8 ‰ on average (maximum of 6 ‰), whereas $\delta^{15}N$ varies on average by ~3.3 ‰ (maximum range of 19.1 ‰).

From the SIMS analyses of the Koffiefontein diamonds, four important observations can be made: Nitrogen concentrations and carbon or nitrogen isotopes appear uncorrelated. The carbon isotope composition changes by ~1 ‰ from core to rim. While $\delta^{13}C$ has a narrow range within samples, $\delta^{15}N$ for the same samples may vary dramatically. $\delta^{13}C$ values below the mantle range are not restricted to eclogitic diamonds but also occur in peridotitic diamonds.

3.3. Discussion

3.3.1. Mantle environment: temperature and residence times

Nitrogen aggregation from doubly bonded nitrogen pairs (A-centre; Type IaA) to four singly bonded nitrogen atoms around a vacancy (B-centre; Type IaB) follows a temperature-, concentration-, and time-dependent reaction (Taylor et al., 1990). Although either temperature or age can be calculated, nitrogen aggregation is more sensitive to temperature than to changes in mantle residence (Evans and Harris, 1989): e.g., for time periods >1 Gyr, changing the residence time from 1 to 3 Gyr only changes the temperature by ~30 °C (Figure 3-6A). Thus, an average residence time of 2 Gyr was selected based on the ~3 Ga Kaapvaal diamond ages (Richardson et al., 1984), and the 2.9-2.7 Ga, 1.2-1.1 Ga, and the ~90 Ma Koffiefontein diamond ages (Pearson et al., 1998). The regularity of the Koffiefontein diamonds (i.e., the lack of platelet degradation) rules out any transient heating events (Evans et al., 1995).

Figure 3-6 shows the distribution of the Koffiefontein diamond data across a range of mantle isotherms. Time averaged (2 Gyr) mantle residence temperatures (T_{NA}; Leahy and Taylor, 1997) calculated for all Koffiefontein diamonds range from 1037 °C to 1411 °C, with a dominant peak between 1125 °C to 1250 °C, and median at 1151 °C (Figure 3-6B). The interquartile range, from 1119 °C to 1189 °C, is within the range of temperatures calculated from mineral-exchange thermometry of silicate mineral inclusions in Koffiefontein diamonds (Chapter 4.3). Peridotitic diamonds extend to very high residence temperatures, up to 1410 °C. Although the majority of the Koffiefontein diamonds are either Type IaA or IaAB, a small proportion of fully aggregated (100 %B) peridotitic diamonds accounts for the high mantle-residence temperatures, >1200 °C, which suggest derivation from near the base of the lithosphere or even below.

3.3.2. Growth and resorption in Koffiefontein diamonds: multiple formation events

The suite of inclusion-bearing Koffiefontein diamonds in this study has a higher proportion of twinned diamonds (26 %) and fewer irregular-shaped diamonds (14 %) compared with run-of-mine diamonds studied by Harris et al. (1975; 12 % and 52 %, respectively). As the diamonds for this study were selected based on being inclusion-bearing, the high proportion of twinned diamonds is most likely a sampling bias as twinned diamonds are more commonly inclusion-bearing (Harris and Gurney, 1979; Navon et al., 1988). The generally high levels of resorption,

evidenced by the high proportion of rounded or dodecahedroid-shaped diamonds and the abundant resorption features visible on almost every diamond (e.g., trigons, hillocks; Table 3-1), indicate that the Koffiefontein diamonds experienced at least one, but likely multiple, diamond-destructive events. This is in agreement with the CL images that indicate complex growth patterns and resorbed cores (e.g., 10/07 in Figure 3-4). Up to five different resorption and growth events can be determined for diamonds 8/03 and 8/07, as evidenced by the rounded (resorbed) internal growth zones and the change in direction of the growth zones. Thus, multiple carbon-bearing fluids may have passed through the host rocks to the Koffiefontein diamonds before kimberlite eruption. At least one growth event of <10 Ma (established by low nitrogen aggregation and U-He constraints) before kimberlite eruption, created an abundance of coated diamonds, making up almost one third of the diamonds recovered (Harris and Gurney, 1979; Izraeli et al., 2004; Timmerman et al., 2018). Multiple resorption and re-growth events are consistent with the three ages of diamond formation found in a small number of diamonds studied by Pearson et al. (1998).

3.3.3. Diamond forming fluids: isotopic characteristics and nitrogen incorporation

Source of mantle-like $\delta^{13}C$ for both peridotitic and eclogitic diamonds

The Koffiefontein peridotitic diamonds, with a median $\delta^{13}C$ of -5.6 ‰, have a general within-diamond $\delta^{13}C$ range of 0.8 ‰ even for diamonds that have a significant within-diamond [N] variation of ~1300 at.ppm (e.g., 7/03; Table A3). The single exception is the unusual moissanite-bearing diamond 2/05, which has a $\delta^{13}C$ range of 4.2 ‰ and a nitrogen concentration range of 2090 at.ppm. The small within-diamond variance of these Koffiefontein diamonds is consistent with a worldwide value of ±2 ‰ (Howell et al., 2020). This result is not surprising as the carbon isotopic fractionation factor for diamond growth from CO_3^{2-} or CH_4 is small at mantle temperatures: $\Delta^{13}C_{diam\text{-}CO3}$ = -1.73 ‰ and $\Delta^{13}C_{diam\text{-}CH4}$ = +1.21 ‰ (calculated using β values compiled by Tom Chacko for calcite of Chacko et al., 1991 and CH_4 of Richet et al., 1977). Rayleigh fractionation during diamond formation in the lithospheric mantle produces a maximum diamond $\delta^{13}C$ range of 6.4 ‰ or 4.5 ‰ from CO_3^{2-}- or CH_4-rich fluids, respectively, provided complete, closed system exhaustion of the fluid occurs. A larger fractionation factor exists for diamond-CO_2 but due to the lack of stability of CO_2 in the mantle, carbonate or methane in a carbon bearing fluid is more likely (Stachel and Luth, 2015). In reality, a

harzburgitic SCLM like that beneath Koffiefontein is deficient in Fe^{3+} and unable to buffer interacting C-rich fluids (Luth and Stachel, 2014). This minimal oxygen buffering capacity of the host peridotitic mantle allows for mixed species fluids and diamond formation from mixed CO_2-CH_4 fluids. Multiple-component diamond formation modelling by Stachel et al. (2017; based on modelling the Rayleigh isotopic fractionation from a multicomponent source of Ray and Ramesh, 2000) showed that a diamond with an average $\delta^{13}C$ of -5.7 ‰ and an internal variation of ~1 ‰ can be achieved by ~50% crystallisation of fluids with equal proportions of CO_2 and CH_4 and an initial $\delta^{13}C$ of -5.0 ‰. Applying this model to the Koffiefontein peridotitic diamond substrate, a within-diamond $\delta^{13}C$ range of 0.8 ‰ can be achieved in a diamond with an initial $\delta^{13}C$ of -5 ‰ if the fluid is reducing, i.e. CO_2:CH_4 ≤1.

Averaged $\delta^{13}C$ values of Koffiefontein diamonds range from -18.0 to -2.0 ‰, and both peridotitic and eclogitic diamonds have a population of $\delta^{13}C$ <-10 ‰ (Figure 3-5). A long-standing observation of the $\delta^{13}C$ values of worldwide eclogitic diamonds is their large $\delta^{13}C$ range and strongly negatively skewed distribution compared with those of a peridotitic paragenesis (Galimov, 1991). The ^{13}C-depleted nature of eclogitic diamonds is typically interpreted to arise due to the subduction of crustal material (Sobolev and Sobolev, 1980). In the subduction model, low $\delta^{13}C$ values, below -8 ‰ down to -25 ‰, are ultimately derived from either organic matter or biogenic carbonate in subducted sediment (Mattey et al., 1984; Schidlowski, 2001; Sobolev and Sobolev, 1980; Veizer and Hoefs, 1976). However, mantle-like $\delta^{13}C$ compositions can be incorporated during subduction, attributed to the $\delta^{13}C$ signature of altered oceanic crust (AOC; Shilobreeva et al., 2011). As an alternative to the subduction model, incorporation of primordial mantle heterogeneities related to the accretion of Earth, has been suggested to explain the varied isotopic ranges observed in diamonds (Deines, 1980; Deines et al., 1987) or some very depleted C- and N-isotopic signatures (Palot et al., 2014). This model has fallen out of favour for lithospheric diamonds due to questions on the long-term preservation of mantle heterogeneities in a mixed mantle model; for example, nitrogen isotope compositions of ocean island basalts – originating from the lower mantle – indicate a mixed primordial and subducted signature (Labidi et al., 2020). Fractionation effects are a third alternative for ^{13}C-depleted diamond formation. Rayleigh fractionation can occur during diamond growth or during fluid evolution (e.g., by loss of CO_2; Cartigny et al., 1998a). As shown previously, Rayleigh fractionation can only account

for a ~4.5 ‰ difference from an CH_4-rich fluid and only $\Delta^{13}C_{diam\text{-}fluid}$ >0 ‰ will result in more negative $\delta^{13}C$ values; thus, a parental fluid of <-13 ‰ would be needed to generate diamond with a $\delta^{13}C$ of -17 ‰ (e.g., for diamond 6/01; Table A3). Hence, even if Rayleigh fractionation affects the C isotope composition of diamond during its formation, a source is required for fluid with an anomalously low $\delta^{13}C$ value. Diamond formation from reduced carbides, e.g., Fe_3C, has a much more positive fractionation factor ($\Delta^{13}C_{diam\text{-}Fe3C}$ = +8.9 ‰; Horita and Polyakov, 2015), which could produce ^{13}C-depleted diamonds (Jacob et al., 2004; Mikhail et al., 2014b). Although this requires very reduced mantle environments, the occurrence of moissanite in diamond 2/05 ($\delta^{13}C$ = -8.5 to -4.6 ‰) suggests this as a possibility in the Koffiefontein diamond-forming environment.

From the above discussion, a subduction scenario seems most plausible as a mechanism to generate the C-rich fluids, with varied C isotope compositions, for eclogitic diamond formation at Koffiefontein and elsewhere. A Wilcoxon test – a ranked, nonparametric statistical test – does not allow rejection, at the 95% confidence level, of the null hypothesis that the mean C isotope composition of the Koffiefontein peridotitic and eclogitic diamonds are the same (Figure 3-5). Although both peridotitic and eclogitic diamond populations have strong, similar modes, the eclogitic distribution has a prominent second population at ~-12 ‰ to -9 ‰ whereas the peridotitic distribution has a greater variance with an extension to higher values and very negative values. The strong mode at -5.5 ‰ for both peridotitic and eclogitic diamonds suggests that, for these diamonds, the carbon source for both the peridotitic and eclogitic diamonds could be the same. A possible carbon source for the Koffiefontein diamonds with C isotope compositions close to the modes of ~-5 ‰ is a purely mantle-derived fluid. However, fluids/melts extracted from subducted hydrothermally AOC, which contains carbon with a mean $\delta^{13}C$ of -4.7 ‰ (Li et al., 2019; Shilobreeva et al., 2011) is also a plausible source for these diamonds.

Trends in nitrogen incorporation and $\delta^{15}N$-[N] coupling

Greater than 50 % of the global nitrogen budget resides in the mantle but due to the sheer size of the mantle, its concentration is low at ~8 ppm (Johnson and Goldblatt, 2015). The primary method of nitrogen re-entry into the mantle is by substitution of NH_4^+ for K^+ in subducted

sediment (Busigny et al., 2003; Honma and Itihara, 1981). How much sediment is subducted remains a subject of active debate. In cold subduction settings, <10 °C/km gradient, slowly descending slabs effectively transport nitrogen into the mantle to depths of ~100 km compared to warmer subduction settings, >13 °C/km gradient, where significant nitrogen is lost (Busigny et al., 2003; Dasgupta, 2013).

World-wide, both peridotitic and eclogitic diamonds have a similar distribution of nitrogen concentrations, tapering off at ~1200 at.ppm, but peridotitic diamonds have a much higher proportion of Type II (Cartigny, 2005). The nitrogen concentration range of Koffiefontein peridotitic diamonds has a single mode (~50 at.ppm) with the distribution being skewed towards a significant tail of diamonds with low nitrogen abundances. Compared to global peridotitic diamonds, the Koffiefontein peridotitic suite has a similar proportion of Type II diamonds (24 % versus 18 %, respectively; Stachel and Harris, 2009). Eclogitic diamonds from Koffiefontein generally have [N] >100 at.ppm (Figure 3-3A), and form a bimodal distribution, with a narrow peak at ~50 ppm and a second, broad peak between 400 to 800 at.ppm. A noticeable component of this second, broad peak is that it consists predominantly of eclogitic sulphide-only diamonds (Figure 3-3A).

Sulphide is the most common inclusion in diamonds, especially at Koffiefontein (Boyd and Gurney, 1986; Bulanova, 1995; Harris and Gurney, 1979). The Koffiefontein sulphide-only diamonds are generally colourless and sharp-edged dodecahedroids with high nitrogen concentrations and mantle-like $\delta^{13}C$ and $\delta^{15}N$ signatures. It was suggested by Meyer (1987), due to their overabundance at some Kaapvaal mines and because of their restricted $\delta^{13}C$ range, to treat these sulphide-only diamonds as a paragenesis that is distinct from eclogitic and peridotitic diamonds (Deines et al., 1987). Cartigny et al. (2014, 2009) also noted that the sulphide-included diamonds, that contain no silicate component, display a distinct $\delta^{13}C$ distribution and more restricted pressure-temperature range when compared to their silicate-included counterparts; but no reason for these observed differences was presented. Trace element analysis of sulphide-included peridotitic gem diamonds from the Victor pipe, Superior Craton, suggest that its sulphide-only diamond population formed deeper in the lithosphere where diamond-forming fluids were less fractionated (Krebs et al., 2019). This could account for the high nitrogen and

mantle-like $\delta^{13}C$-$\delta^{15}N$ signature of the Koffiefontein eclogitic sulphide-only diamonds; however, a more thorough investigation is needed. At this stage, it is not clear if these sulphide-bearing eclogitic diamonds do represent a distinct paragenesis.

Globally, the main modes of $\delta^{15}N$ values for peridotitic and eclogitic diamonds are <0 ‰, with peridotitic diamonds having a broad peak between -10 ‰ to +4 ‰ and eclogitic diamonds having a narrow peak centred at -6 ‰ (Cartigny et al., 2014). The Koffiefontein diamonds have a wide range in $\delta^{15}N$ from -25.6 ‰ to +13.2 ‰. The $\delta^{15}N$ distribution for peridotitic diamonds is a bimodal distribution with widely spaced peaks at -5 ‰ and +8 ‰, compared to eclogitic diamonds which have a prominent mode at ~0 ‰ (Figure 3-5E&F). Although no distinct trend, there is less variability between [N] and $\delta^{15}N$ for peridotitic diamonds whose $\delta^{15}N$ values range between -5 and +10 ‰ (Figure 3-5B). How can correlations between [N] and $\delta^{15}N$ be generated? During subduction, prograde metamorphism results in the devolatilisation of nitrogen and an increase in $\delta^{15}N$ (Haendel et al., 1986). Two dominant sources of nitrogen enter the mantle that may have distinct N isotope signatures: metamorphosed sediment with $\delta^{15}N$ of ~+6 ‰ at [N] up to ~2000 ppm, or serpentinised peridotite with more positive $\delta^{15}N$ values of +4-+15 ‰ at lower [N] of 1.4-15 ppm (Busigny et al., 2003; Busigny and Bebout, 2013). High-temperature clay minerals within altered oceanic crust can contribute $\delta^{15}N$ of ranging from -11.6-8.3 ‰ at low [N] of 1.3-18.2 ppm (Li et al., 2007). Regardless of how nitrogen enters the mantle on a subducting slab – sediment, carbonate, or altered oceanic crust – the result is lower $\delta^{15}N$ where nitrogen concentration is high or more positive $\delta^{15}N$ where nitrogen concentration is low. Thus, both input sources are attribute to the slight negative correlation observed for $\delta^{15}N$ values between -5 ‰ and +10 ‰ in these peridotitic and eclogitic Koffiefontein diamonds.

Paired $\delta^{13}C$-$\delta^{15}N$ variations and the source of Koffiefontein diamond-forming fluids

Variations in $\delta^{13}C$ or $\delta^{15}N$ alone cannot be used to unequivocally fingerprint carbon reservoirs as the signatures are often non-unique but coupled $\delta^{13}C$-$\delta^{15}N$ analyses offer more insight into possible reservoir and fluid mixing. Figure 3-7 shows Koffiefontein diamond $\delta^{13}C$-$\delta^{15}N$ analyses for diamonds with [N] >100 at.ppm. Also shown are carbon and nitrogen components present in oceanic slabs with either normal or biogenic carbonate and ^{15}N-enriched clay (Li et al., 2019). Mixing of these reservoirs with the "normal" mantle reservoir characterised by $\delta^{13}C$ and $\delta^{15}N$

≈ -5 ‰ produces diamonds with $\delta^{13}C$-$\delta^{15}N$ compositions within a specific envelope (dashed coloured lines in Figure 3-7). For example, diamonds that have $\delta^{13}C$ of ~-5 ‰ but more positive $\delta^{15}N$ values could be produced from mantle fluids mixed with a small amount of carbonate, either normal or biogenic and a ^{15}N-enriched clay component that has a high N:C ratio to more lever the $\delta^{15}N$ values in a positive direction. These C-N isotope systematics and the invoked mixing scenario are the most common for the Koffiefontein diamonds (Figure 3-7). For diamonds with $\delta^{13}C$ of <-8 ‰, they have a clear biogenic carbonate input, as shown by the group of eclogitic diamonds which grew from a fluid that has ~1:1 mantle plus biogenic carbonate and ^{15}N-enriched clay component (Figure 3-7).

For peridotitic diamonds, the large variation and positive trend of $\delta^{15}N$ with an almost-constant $\delta^{13}C$ of -5 ‰ could also be explained by mixing of purely mantle carbon and nitrogen-rich metamorphosed pelagic sediment (Bebout and Fogel, 1992; Busigny et al., 2003). A third alternative is Rayleigh fractionation. Rayleigh fractionation has a much larger effect on N isotopes than C isotopes due to the much larger $\Delta^{15}N_{diam\text{-}fluid}$ and it is a minor constituent of C-rich fluids (Petts et al., 2015). Rayleigh fractionation modelling of diamond $\delta^{15}N$ shows that variations of ~10 ‰ are achievable after <70 % crystallisation while retaining a $\delta^{13}C$ signature that is within mantle bounds (initial conditions: $\delta^{13}C$ and $\delta^{15}N$ = -5 ‰, $\Delta^{13}C_{diam\text{-}fluid}$ = -1.33 ‰, $\Delta^{15}N_{diam\text{-}fluid}$ = -3.5 ‰, [N] = 5000 at.ppm). Such a fractionation effect is thus potentially capable of generating the weak correlation of decreasing [N] and increasing $\delta^{15}N$ in a sub-population of the Koffiefontein diamonds (Figure 3-5B).

The origin of ^{15}N-depleted diamonds ($\delta^{15}N$ <-10 ‰) is less clear compared to ^{15}N-enriched diamonds. Although the $\delta^{15}N$ values of most lithospheric and sublithospheric diamonds lie between -5 ‰ and +18 ‰, values as low as -25 ‰ exist in both lithospheric and lower mantle diamonds (Cartigny et al., 2014; Palot et al., 2012). The ^{15}N-depleted nature of diamonds has been attributed to source characteristics arising from mantle-derived heterogeneity (Deines, 1980) or abiotic production in subducted oceanic slabs (Li et al., 2007), or from Rayleigh fractionation (Cartigny et al., 1998b). An oft-favoured explanation is formation from mantle fluids with a residual “primordial” signature (Deines, 1980; Deines et al., 1987; Javoy et al., 1986, 1984). For instance, Javoy et al. (1984) linked these highly depleted ^{15}N signatures to

diamond formation from a primitive, un-degassed reservoir, minimally contaminated by subduction, such as the lower mantle. Such a primitive reservoir was thought by these authors to have a parental $\delta^{15}N$ akin to chondrites, specifically enstatite chondrites, which have $\delta^{15}N$ values as low as -40 ‰ (Javoy et al., 1986; Sephton et al., 2003). Models of the evolution of mantle $\delta^{15}N$ from 4.5 Ga to the present show that the mantle, including the lower mantle, likely had a consistent $\delta^{15}N$ of -6 ‰ (Labidi et al., 2020) with long-term crustal nitrogen cycling evident in high $^{3}He/^{4}He$ plumes demonstrating that the deep-mantle stores recycled carbon, with effective mixing of subducted material (Barry and Hilton, 2016). This means that any extreme vestigial low ^{15}N signatures from Earth's accretion are likely to be over-printed and hence unlikely to be sampled by diamond growth events. A second potential source of ^{15}N-depleted fluids is AOC that is subducted into the mantle (Li et al., 2019). $\delta^{15}N$ values of -12 ‰ are produced abiotically by mantle derived N_2 that is converted to NH_3 and incorporated into the sediment (Li et al., 2007). However, the formation of Archean kerogens – as the most ^{15}N-depleted residues of biotic systems, only record $\delta^{15}N$ values down to -7 ‰ (Ader et al., 2016; Beaumont and Robert, 1999) and possibly even as low as -12.6 ‰ (Nishizawa et al., 2007). Additionally, only cold subduction geotherms would allow a subducted AOC to retain these low $\delta^{15}N$ signatures into the mantle due to lower temperature (Dasgupta and Hirschmann, 2010). Therefore, abiotically- or biotically mediated depletion in ^{15}N is not sufficient to produce the very low $\delta^{15}N$ Koffiefontein diamonds.

Like the origin of ^{13}C-depleted diamonds, ^{15}N-depletion has also been attributed to Rayleigh fractionation (Cartigny et al., 1998b). Unlike carbon, the nitrogen species in C-rich fluids is dependent on both oxidation state and pH: N_2 versus NH_3 (Li and Keppler, 2014) and NH_3 versus NH_4^+, respectively (Mikhail and Sverjensky, 2014). However, the $\Delta^{15}N_{diam\text{-}fluid}$ is negative for N_2, NH_3, and NH_4^+, which results in diamond $\delta^{15}N$ values increasing during diamond crystallisation (Petts et al., 2015). For what fluid compositions could $\Delta^{15}N_{diam\text{-}fluid}$ be positive? N isotope fractionation factors involving diamond are only positive for very reduced species such as nitrides: e.g., $\Delta^{15}N_{diam\text{-}BN}$ = +1.29 ‰ (calculated using β values compiled by Tom Chacko for BN of Hanschmann, 1981). Modelling Rayleigh fractionation of a diamond formed from a BN-rich fluid, where BN is analogous for a reduced N species, with initial $\delta^{15}N_{fluid}$ = -5 ‰ can produce diamond with of $\delta^{15}N$ < -26 ‰ but only when most of the fluid has crystallised and [N] ≈ 0 at.ppm. Further, the resulting diamond would have $\delta^{13}C$ < -26 ‰, which is not seen in the

^{15}N-depleted Koffiefontein diamonds. Decreasing the initial $\delta^{15}N_{fluid}$ to -12 ‰ would still require >80 % crystallisation to produce a diamond with $\delta^{15}N$ = -26 ‰. Hence, as shown by Petts et al. (2015), Rayleigh fractionation is unlikely to be responsible for the extremely ^{15}N-depleted signature of some diamonds. Instead, a more positive $\Delta^{15}N_{diam\text{-}fluid}$ factor from reduced species may be responsible, but a likely fluid species has yet to be identified.

The three most ^{15}N-depleted diamonds with $\delta^{15}N$ <-10 ‰ are one websteritic diamond (12/02) which has a large range in $\delta^{15}N$ from +4 to -15‰ and two inclusions of green diamonds – the colour likely produced from radiation damage (Vance et al., 1973) – that have $\delta^{15}N$ of +8 to +9 ‰; and two peridotitic diamonds which have regions of high [N] corresponding to low $\delta^{15}N$ as well as nitrogen-free regions. The websteritic diamond is highly unusual with its goldschmidtite-bearing inclusions chemistry, and thus could have formed in rather exotic conditions. The two peridotitic diamonds having regions of high to little [N] could invoke very separate diamond forming fluids, whereby the $\delta^{13}C$ of the two growth regions are decoupled to [N] with a constant supply of mantle-like carbon, thus Rayleigh fractionation for these two diamonds could explain the very ^{15}N-depleted nature. The more moderately ^{15}N-depleted peridotitic diamonds may in fact derive from the unusually ^{15}N-depleted AOC described by Li et al. (2007) or in reduced environments where nitrogen is more readily fractionated.

3.4. Conclusions

Inclusion-bearing Koffiefontein diamonds record a complex history of growth, resorption, and subsequent growth – often multiple episodes – within the Kaapvaal SCLM. Based on nitrogen aggregation constraints, diamond formation occurred predominantly between 1125 °C and 1250 °C for these lithospheric diamonds, although some diamonds record higher mantle residence temperatures (>1250 °C) indicating that they could have formed near the base of the lithosphere or are older than the main population. These results broadly agree with constraints from geothermobarometry of included silicates in these diamonds. The $\delta^{13}C$ signature of the peridotitic and eclogitic diamonds is very similar and the values are within the mantle range. There is no clear origin for these diamond-forming fluids, however either purely mantle-derived carbon or the addition of carbon from altered oceanic crust are possible sources. In a sub-set of diamonds, the trend of decreasing nitrogen concentration with increasing $\delta^{15}N$ for both

peridotitic and eclogitic diamonds can be explained by nitrogen incorporation from subducted material mixing with a mantle endmember. The Koffiefontein diamond suite also contains diamonds with anomalously light nitrogen isotope compositions whose origins are very difficult to explain. Recent models of bulk mantle nitrogen isotopic evolution appear to rule out a primordial signature for these diamonds. Their origins may be more readily explained by diamond formation in a reduced environment where nitrogen fractionation factors between the reduced species of nitrogen and diamond are responsible for the large ^{15}N-depletion.

Table 3-1: Summary of surface features of Koffiefontein diamonds, separated by inclusion suite, with the eclogitic diamonds divided into silicate and sulphide and sulphide-only ($Sulphide_E$) inclusions. Numbers are diamonds exhibiting the feature and the percentage in brackets is of the total 189 diamonds.

	n	Stacked growth layers	Terraces	Shield-shaped Laminae	Trigons	Hillocks	Plastic def.	Ruts
Peridotite	109	15 (8 %)	25 (13 %)	17 (9%)	52 (28 %)	67 (35 %)	11 (6 %)	13 (7 %)
Websterite	3	0	0	0	0	3 (2 %)	1 (<1 %)	1 (<1 %)
Eclogite	39	2 (1 %)	17 (9 %)	1 (<1 %)	5 (3 %)	31 (16 %)	8 (4 %)	8 (4 %)
$Sulphide_E$	39	2 (1 %)	18 (10 %)	0	3 (2 %)	20 (11 %)	5 (3 %)	2 (1 %)

Table 3-2: Nitrogen content and aggregation state of Koffiefontein diamonds by FTIR. Samples are divided by inclusion suite, with sulphide-only eclogitic suite diamonds labelled as $Sulphide_E$. The total number of diamonds measured in each suite is indicated. Numbers in brackets are percentages of the total 181 diamonds measured.

	Type II [N] = 0 at.ppm	Type IaA [N] >0 at.ppm %B <10 %	Type IaAB [N] >0 at.ppm 10 % < %B <90 %	Type IaB [N] >0 at.ppm %B >90 %
Peridotite (108)	29 (16 %)	12 (7 %)	57 (31 %)	10 (6 %)
Websterite (3)	2 (1 %)	1 (<1 %)	0	0
Eclogite (3)	4 (2 %)	7 (4 %)	23 (13 %)	1 (<1 %)
$Sulphide_E$ (35)	0	9 (5 %)	26 (14 %)	0

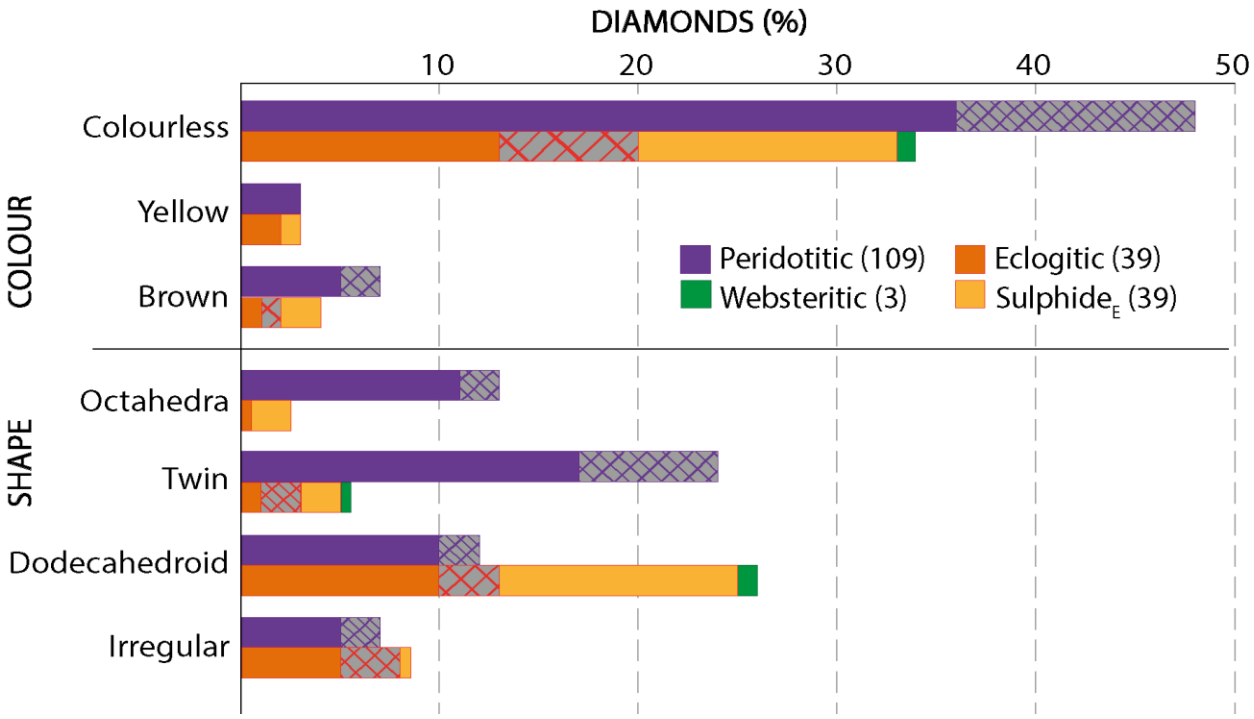

Figure 3-1: Koffiefontein diamond colour and shape distribution, this study (n = 190) and literature data (hatched pattern) from Deines et al. (1991; n = 62). Numbers in legend are the total number of diamonds in each inclusion suite for this study.

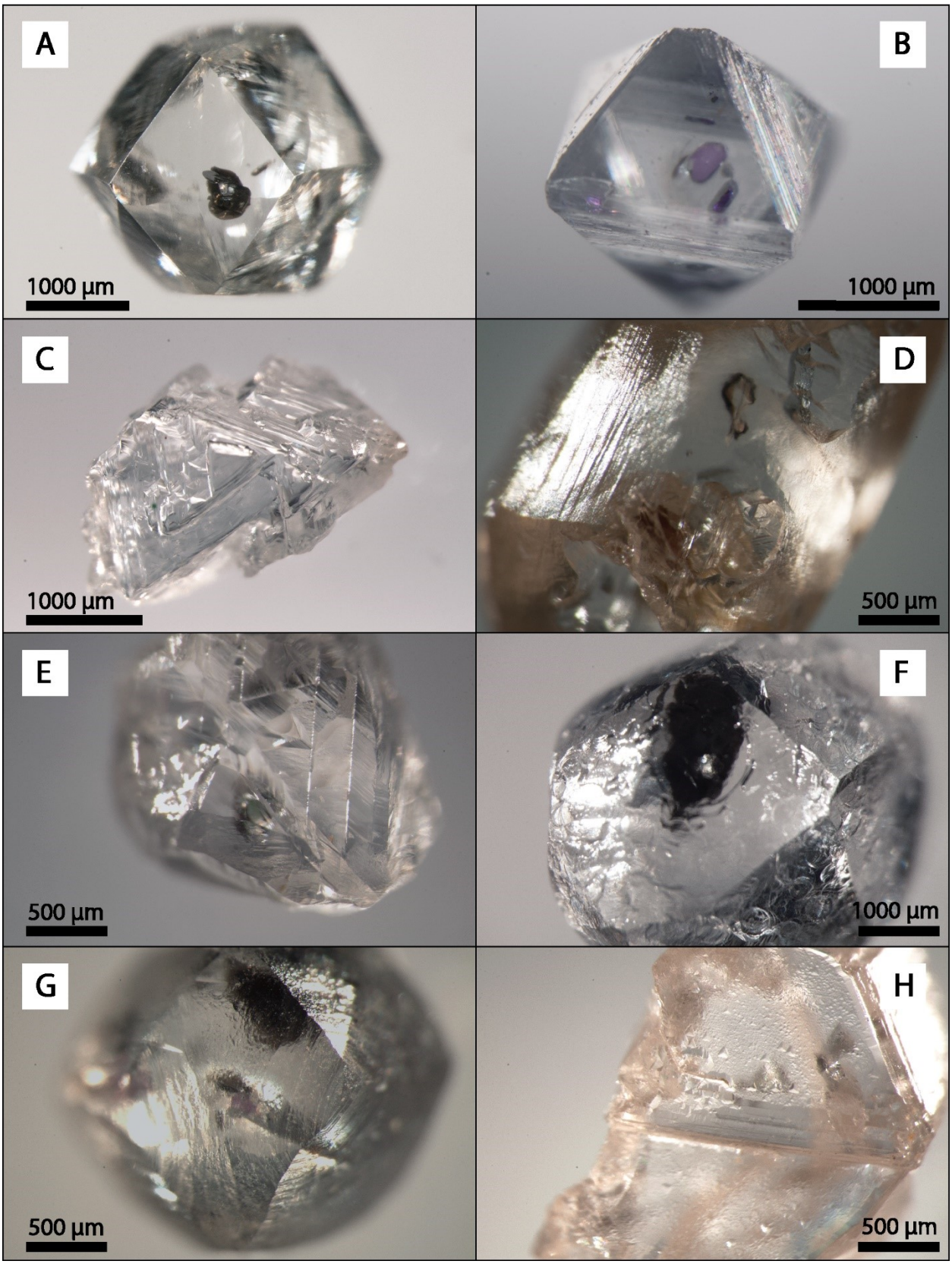
A
1000 µm
B
1000 µm
C
1000 µm
D
500 µm
E
500 µm
F
1000 µm
G
500 µm
H
500 µm

Figure 3-2 (previous page): Photographs of selected Koffiefontein diamonds displaying specific surface features, shapes, or colours: (A) sulphide-only, colourless dodecahedroid with sharp edges; (B) multiple purple garnet and colourless olivine inclusions in a colourless octahedron; (C) colourless, parallel interpenetration twin; (D) light brown, irregular-shaped diamond with striations on the left edge, indicative of plastic deformation; (E) coarse plastic deformation lines in a colourless twinned dodecahedroid; (F) bubble-shaped, negative-relief corrosion on a colourless, octahedroid eclogitic sulphide-only included diamond; (G) hillocks and terraces on a colourless dodecahedroid; and (H) fine positively-oriented, raised trigons on a broken octahedron.

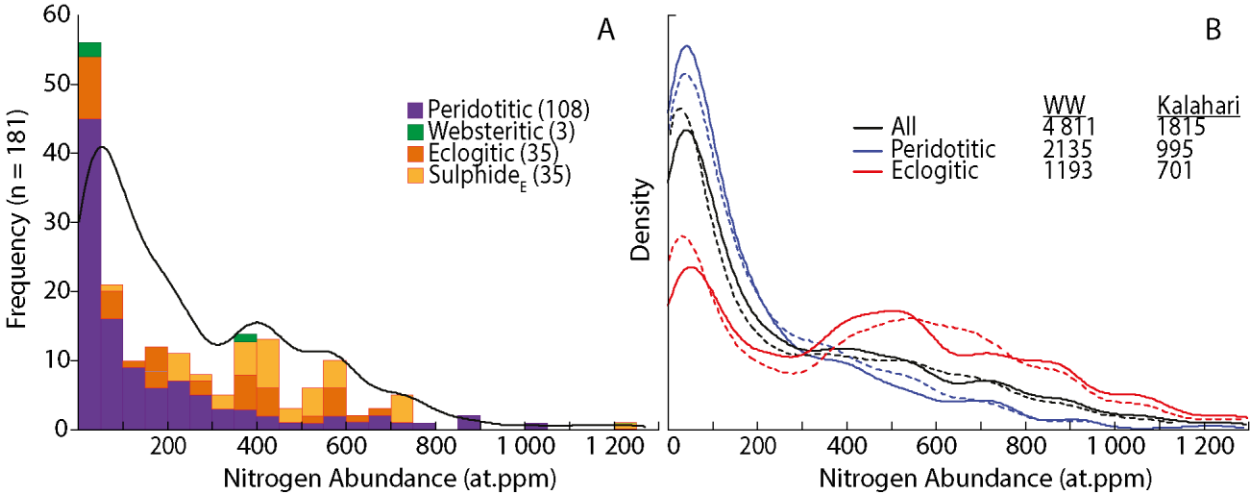

Figure 3-3: Nitrogen abundance ([N]; at.ppm) in diamond determined by FTIR. (A) Histogram of nitrogen abundance in all Koffiefontein diamonds separated by inclusion suite (n = 181; this study) with kernel density plot of all Koffiefontein [N] data (>10 at.ppm), including Koffiefontein literature data of Deines et al. (1991a). (B) Kernel density plot of [N] in diamonds (>10 at.ppm, i.e. only Type I diamonds) from the Kalahari Craton (dashed lines) and world-wide (solid line) separated by inclusion suite from the database of Stachel et al. (2009).

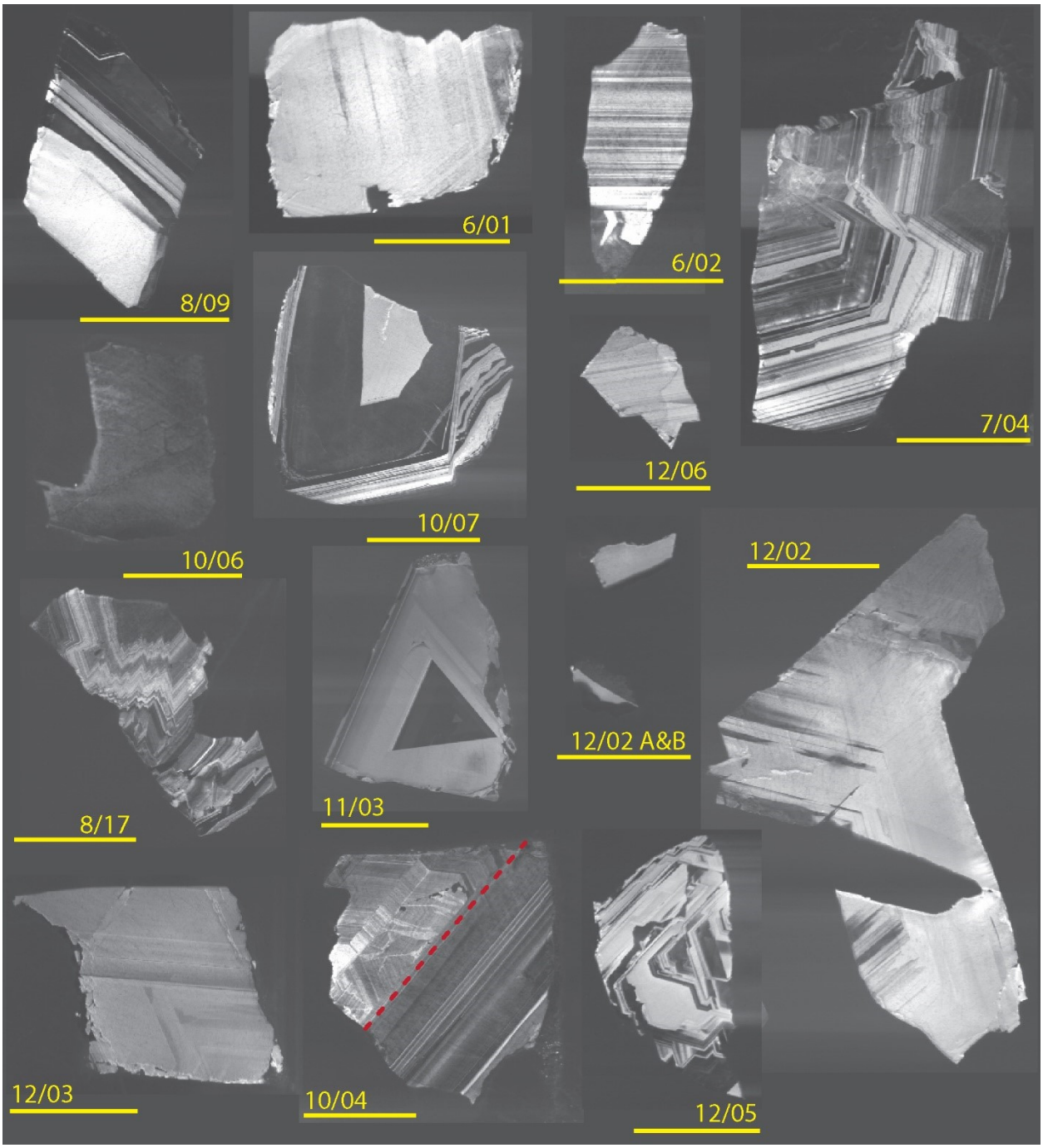

Figure 3-4: Cathodoluminescence images of selected diamonds analysed in this study (all samples in Figure A1 and Table A3). Lighter regions on each diamond fragment indicate a higher concentration of nitrogen. Numbers indicate sample number and scale bars represent 500 µm. Red dashed line on 10/04 is the twin plane. Each diamond fragment is discussed in the text.

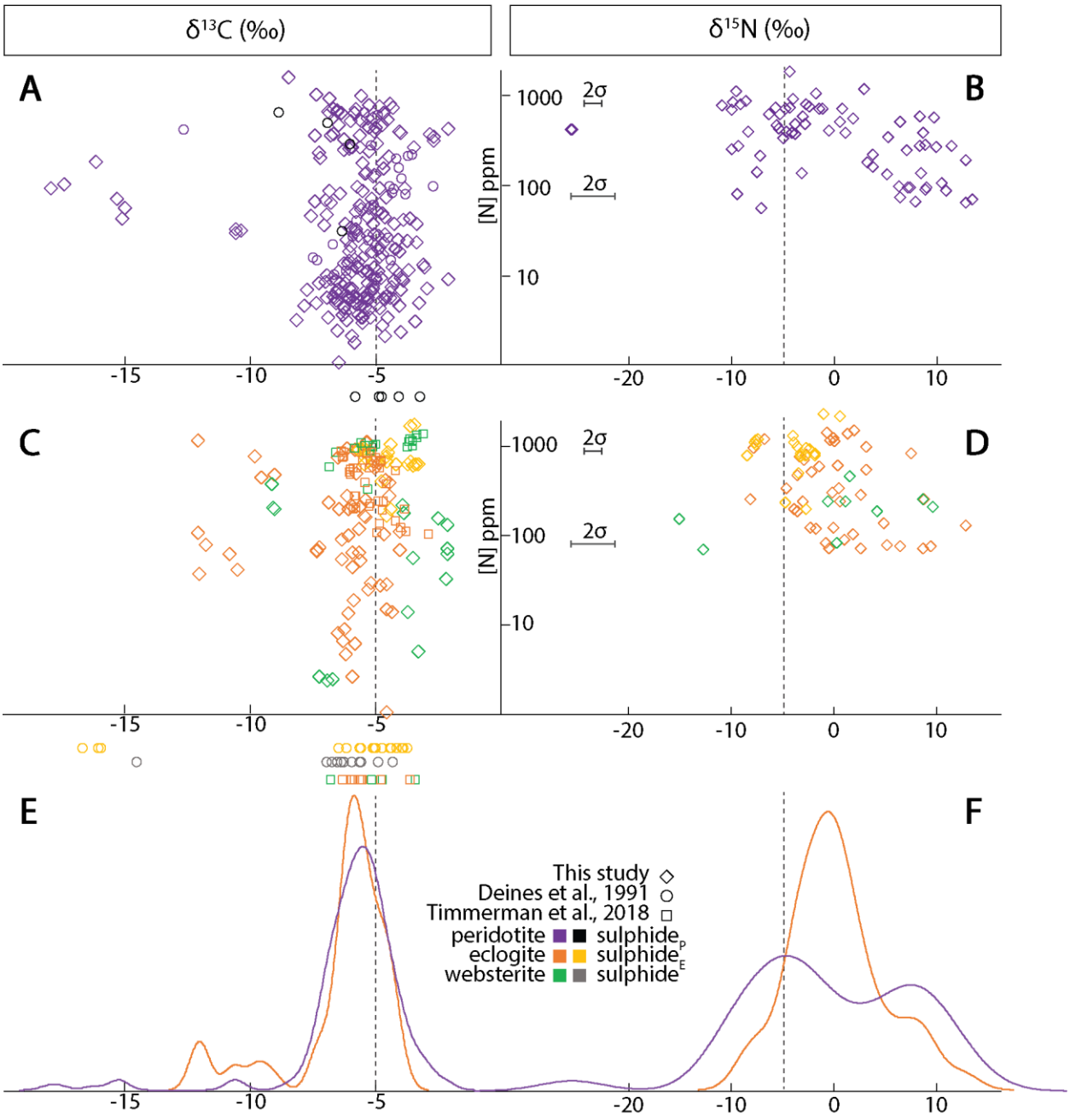

Figure 3-5: Plots of $\delta^{13}C_{VPDB}$ (‰) and $\delta^{15}N_{AIR}$ (‰) versus nitrogen concentration (at.ppm) and density plot (this study only). Literature data with no nitrogen concentration is added below the x-axis of its respective graph. Dashed line represents the mantle average for $\delta^{13}C$ and $\delta^{15}N$ at -5 ‰. Average error bars (2 σ) are plotted for $\delta^{15}N$ at 100 and 1000 ppm; error in $\delta^{13}C$ is smaller than symbol.

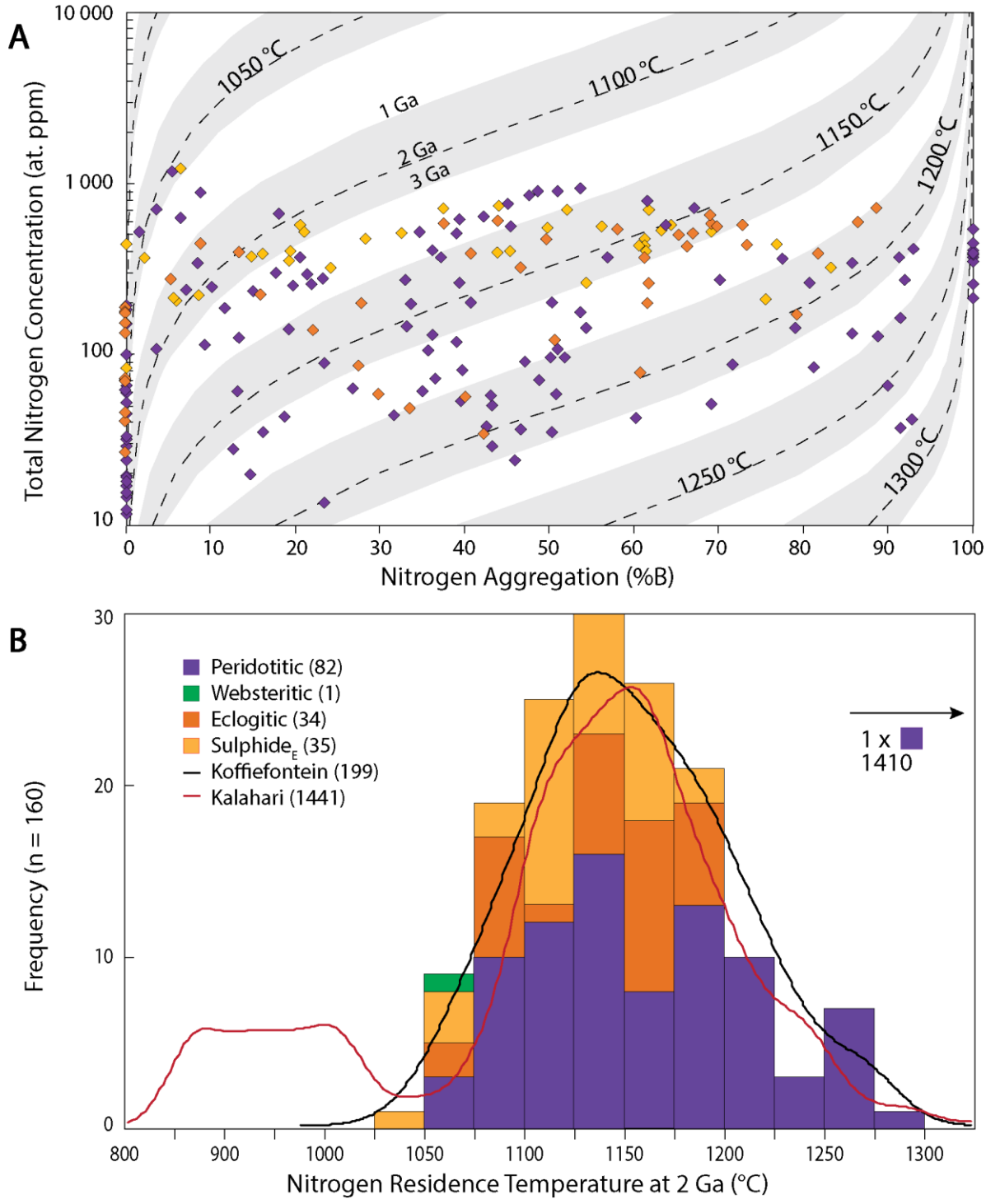
A
Total Nitrogen Concentration (at. ppm)
10 000
1 000
100
10
1050 °C
1100 °C
1150 °C
1200 °C
1250 °C
1300 °C
1 Ga
2 Ga
3 Ga
0
10
20
30
40
50
60
70
80
90
100
Nitrogen Aggregation (%B)
B
Frequency (n = 160)
30
20
10
0
Peridotitic (82)
Websteritic (1)
Eclogitic (34)
Sulphide$_E$ (35)
Koffiefontein (199)
Kalahari (1441)
1 x
1410
800
900
1000
1050
1100
1150
1200
1250
1300
Nitrogen Residence Temperature at 2 Ga (°C)

Figure 3-6 (previous page): (A) Total nitrogen content by FTIR versus %B component of Koffiefontein diamonds. Isotherms are shown for a 2-Gyr mantle residence time calculated from Taylor et al. (1990) and Leahy and Taylor (1997). Shaded regions represent the 1- and 3-Gyr bounds of the upper and lower range of the temperature isotherm. (B) Histogram of mantle residence temperatures calculated for 2-Gyr residence time (bins = 25 °C) with kernel density plot for Kalahari and Koffiefontein diamonds for a 2-Gyr residence time from the database of Stachel et al. (2009). For diamonds with >99 %B or <1 %B, a value of 99 %B and 1 %B, respectively, was used to attain an approximate temperature. Numbers in parentheses indicate number of diamonds analysed in this study.

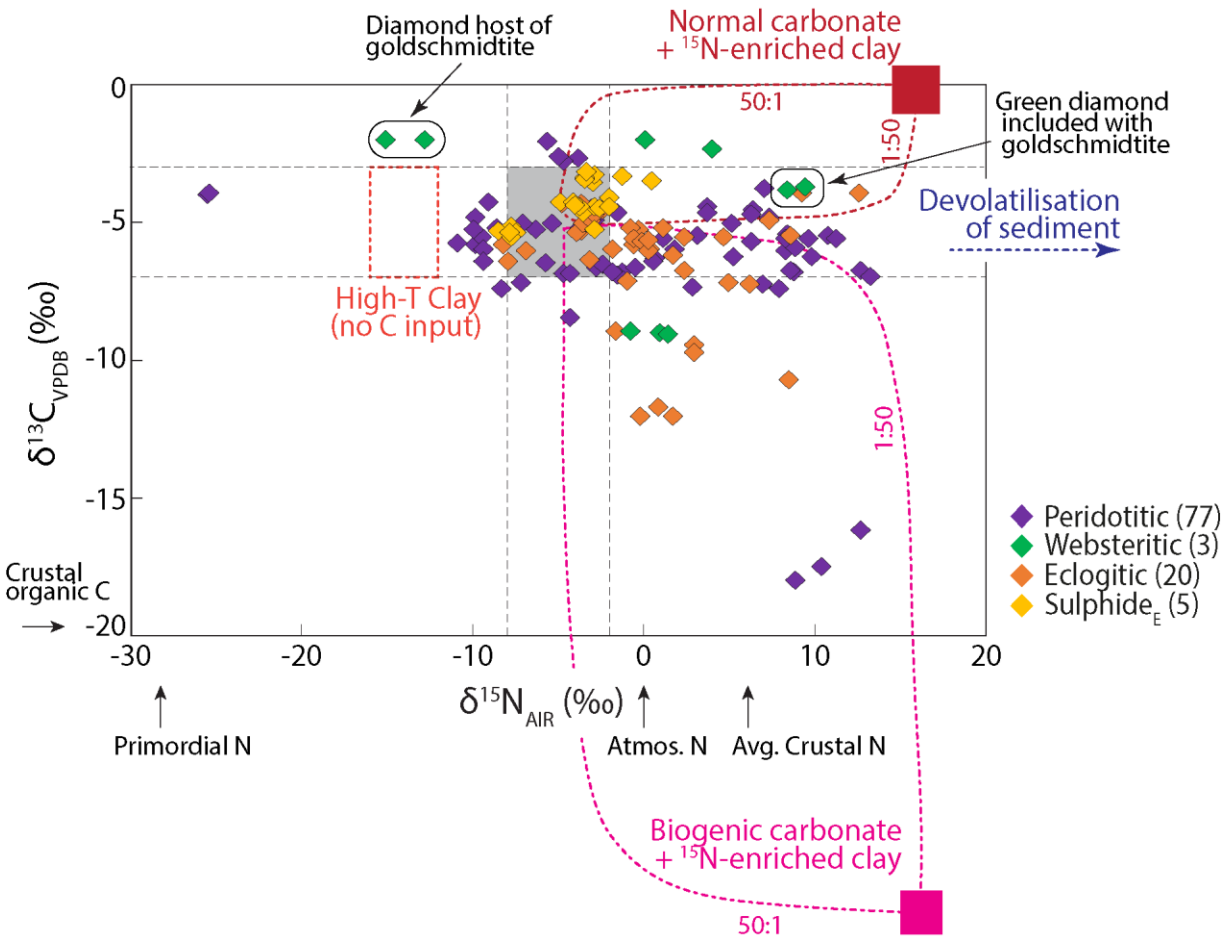

Figure 3-7: $\delta^{13}C$ versus $\delta^{15}N$ (‰) of Koffiefontein diamonds for [N] > 100 at.ppm (~3 analysis spots per diamond). Mantle ranges of $\delta^{13}C = -5 \pm 2$ ‰ and $\delta^{15}N = -5 \pm 3$ ‰ delimited by black dashed lines. Isotopic compositions of potential and conceptual reservoirs indicated with arrows and referenced in text: crustal organic carbon (Schidlowski, 2001), crustal nitrogen (Bebout and Fogel, 1992), primordial lower mantle nitrogen (Cartigny and Marty, 2013). Carbon and nitrogen components of altered oceanic slab (high-temperature clay, low-temperature clay with either normal carbonate or biogenic carbonate) with mantle-derived carbon and nitrogen mixing envelopes in dashed lines (50:1 and 1:50 refer to the proportion of nitrogen from mantle and altered oceanic slab; Li et al., 2019).

Chapter 4. Melt depletion and deep peridotite carbonation in the Kaapvaal Craton lithospheric root – a window from inclusions within diamond

4.1. Introduction

The Kaapvaal Craton in South Africa is the archetype locale for the formation of continental lithosphere from Archean mantle and its subsequent evolution; and this history is preserved as mineral inclusions in diamond (Shirey et al., 2004a). Two processes dominate the formation and evolution of the subcratonic lithospheric mantle (SCLM): melt depletion events to create buoyant lithospheric mantle (Ringwood, 1962a), and metasomatic re-enrichment events that may form new minerals or only chemically modify the craton (Bailey, 1982; Dawson, 1984; Grütter et al., 1999). Diamonds, brought to the surface by kimberlite magma from deep in the mantle, carry minerals which preserve evidence of these processes by virtue of their physical and chemical robustness (Harris and Gurney, 1979).

Numerous studies of minerals included in diamonds from cratons globally have demonstrated that cratonic roots are comprised of varying degrees of depleted peridotite consisting of olivine plus orthopyroxene, with minor clinopyroxene and garnet (Gurney, 1984; Haggerty, 1986). The majority of cratonic peridotites have experienced melt extraction up to the point of orthopyroxene exhaustion, evident by the high magnesium number (Mg#; 100x molar Mg/[Mg+Fe]) of the olivine (Bernstein et al., 2007). These depletion processes must have occurred at relatively low pressures, evident from the Cr-rich nature of the peridotitic garnets, which require melt depletion in the spinel stability field (Shu et al., 2018; Stachel et al., 1998b). Subsequent mantle metasomatism is notable in the formation of garnet, orthopyroxene and clinopyroxene (Rudnick et al., 1993; Simon et al., 2007) and light rare earth (LREE) enrichment in peridotitic garnets (i.e. cryptic metasomatism; Dawson, 1984). Because mantle rocks represent an open system, the samples available as xenoliths in kimberlite can reflect numerous metasomatic events, including late-stage infiltration by the host kimberlite. As such, mineral inclusions within diamond – a rigid, inert barrier protecting encapsulated minerals – provide a more robust signal of craton formation and its early, chemical and mineralogical evolution (Stachel and Harris, 2008).

A variety of silicate and oxide minerals included in diamonds from the Koffiefontein kimberlite are analysed to further our understanding of the formation and evolution of the Kaapvaal Craton. A new palaeogeotherm is defined for the Koffiefontein lithosphere from silicate mineral inclusions in diamond (interpreted to be old, likely Archean in age) and in comparison, compared to the Cretaceous-aged xenolith palaeogeotherm, provides insights into craton stability since the Archean.

4.2. Results

Mineral inclusions released from diamonds were all non-touching (multiple inclusions denoted by letters after sample number) except for two diamonds that contained touching grt-opx (8/11B*, 10/02A*). Inclusion mineral species were assigned based on their mineral chemistry and then divided into suites as follows: peridotitic (P-type) – olivine, high Cr-garnet (Cr_2O_3 >1 wt%), orthopyroxene, and clinopyroxene (augite or diopside); and eclogitic-websteritic (E-type and W-type) – low-Cr garnet (Cr_2O_3 <1 wt%) and clinopyroxene (omphacite or augite). A detailed chemical discrimination for mineral classification is described in Section 4.2.1. Table 4-1 lists the total number of diamonds that released a specific mineral(s), grouped by suite: peridotitic and eclogitic-websteritic (low-Cr).

4.2.1. Major-element composition of mineral inclusions

Major element data for each mineral analysed by EPMA are listed in Table B1. Plotted data are supplemented with unpublished thesis data of mineral inclusions from diamond (Cardoso, 1980) and xenoliths (Cardoso, 1980; Hanrahan, 2003) from Koffiefontein to compare with the data in this study.

Garnet

Garnet is the most common mineral liberated in this study (as classified by Grütter et al., 2004; Figure 4-1A): 70 peridotitic, 8 eclogitic, and 1 websteritic garnets. 89 % of garnet inclusions are classified as deriving from peridotite with over 90 % of the peridotitic garnets classifying as harzburgitic (G10 = 62; lherzolite, G9 = 9). Furthermore, one third of the harzburgitic garnets have CaO <1.8 wt% (n = 21), classifying as low-Ca peridotitic and are likely dunitic in origin

(Grütter et al., 1999). The average Mg# for the peridotitic garnets is 88.6. One garnet (14/03A) classifies as being derived from pyroxenite (G5; Grütter et al., 2004). Low-Cr garnets (Cr_2O_3 <1 wt%; n = 8) span a wide range of CaO compositions and classify as either high-Ca garnet (G3 = 2) or low-Ca garnet/pyroxenite (CaO <6 wt%; G4 = 6). The average Mg# for the eclogitic garnets is 63.1. No garnets show a majoritic component indicated by an increase in Si cations exceeding analytical uncertainty (i.e. Si >3.03).

Olivine

Olivine is the second-most abundant silicate inclusion in Koffiefontein diamonds, with 55 discrete olivine grains being released from 30 diamonds, of which 16 diamonds contained only olivine and liberated 29 olivine grains. Olivine Mg# ranges from 91.5 to 95.0, with a mean and median of 93.5 and 93.4, respectively (Figure 4-1B). For garnet-bearing inclusion assemblages (all non-touching), the olivine inclusions classify almost exclusively as harzburgitic, with one diamond having an olivine and lherzolitic garnet (39/01). Due to the overlap of harzburgitic and lherzolitic olivine Mg# distributions, the remaining olivine inclusions can only be classified as peridotitic (Stachel and Harris, 2008).

Orthopyroxene

A total of 31 orthopyroxene inclusions were released from 21 diamonds. All orthopyroxenes are enstatites with Mg# ranging from 93.4 to 97.3 (mean and median values of 94.9 and 94.8, respectively). Enstatites are generally similar in major element chemistry with only small variances in FeO (1.87 to 4.48 wt.%) and Cr_2O_3 (0.12 to 0.28 wt.%). The exceptions are an orthopyroxene touching garnet, which has Cr_2O_3 of 0.53 wt.% (10/02A), and one outlier with Cr_2O_3 of 0.43 wt.% (21/02E). Where co-existing garnet(s) is present, its chemistry permits classification of 16 orthopyroxene grains as harzburgitic (two of which are touching inclusions) and one as lherzolitic (non-touching). For those orthopyroxenes without coexisting minerals, Mg#-CaO permits classification of nine orthopyroxenes as harzburgitic and three as lherzolitic (Stachel and Harris, 2008).

Clinopyroxene

A total of 27 clinopyroxene inclusions were released from 14 diamonds. First-order discrimination is based on the Na# ($2Na/[2Na+Ca+Mg+Fe^{2+}]$), with Na# >0.2 corresponding to omphacite and <0.2 corresponding to diopside/augite; Morimoto, 1988). Low-Na# clinopyroxenes (n = 7) were classified based on molar Ca-Mg-Fe, with 6/07A classifying as a diopside and the remainder classifying as augites. To distinguish between peridotitic and pyroxenitic associations, Mg# was employed due to peridotitic clinopyroxenes generally having Mg# >90 (Stachel and Harris, 2008). Thus 16/01A, 16/02A, and 12/06A are peridotitic and 12/02C, 12/03A&B classify as websteritic based on an intermediate Mg# of ~86 and moderate Cr_2O_3 content of 1.2 wt%, transitional to the peridotitic suite. In total, 20 clinopyroxenes classified as omphacite with Na# ranging from 0.25 to 0.46, and Cr# <2 (Cr# = Cr/[Cr+Al]).

Mg-chromite

Five Mg-chromite inclusions were recovered from three separate diamonds. All chromite inclusions have similar chemistry with a narrow range in Cr# of 83.3 to 84.1. The major element range is within the bounds of Mg-chromite released from diamonds world-wide (Stachel and Harris, 2008).

Additional minerals

Several non-typical lithospheric mantle minerals were found during the course of this study, with at least one representing a new mineral. In the peridotitic suite, diamond 2/05 contained moissanite (SiC) with olivine and enstatite. Two separate peridotitic diamonds contained SiO_2 as quartz – interpreted to be regressed coesite – in combination with harzburgitic garnet + olivine + enstatite (8/03) and harzburgitic garnet + olivine (10/04). Diamond 39/02 yielded olivine + calcite but no exterior fractures were visible, indicating that the calcite inclusions are likely primary. Diamond 9/01 contained three harzburgitic garnets as well as one each of olivine, orthopyroxene, sulphide, and an Mg-silicate (SiO_2 = 64.34 wt.%, FeO = 2.88 wt.%, MgO = 18.16 wt.%) that has yet to be classified. Diamond 12/02 contained inclusions of Cr-rich augite (websteritic), two green diamonds, a $(K,REE,Sr)(Nb,Cr)O_3$ perovskite (now named goldschmidtite; Meyer et al., 2019), and an intergrowth of a Mg-silicate, chromite, and a Ta-rich oxide (in wt%: Ta_2O_5 = 82.27; K_2O = 17.69) that probably also represents a new mineral. Two

minerals of uncertain paragenesis were recovered from two separate diamonds: corundum was released from diamond 1/01 and is assumed to be eclogitic (Table 1-2 of Stachel, 2014), and a solitary calcite was released from diamond 12/04.

4.2.2. Trace-element composition of silicate inclusions in diamond

The trace element concentration of selected elements for garnet, olivine, orthopyroxene, and clinopyroxene are listed in Table B3. Olivine trace element analysis includes both LA-ICP-MS and EPMA (Table B2).

Garnet

Trace elements analyses of 31 garnets are listed in Table B3 and the REE are plotted in Figure 4-2. C1-chondrite normalised ($_N$; McDonough and Sun, 1995) patterns are shown for all peridotitic garnets analysed (G10 = 22; G9 = 2) in Figure 4-2A, superimposed on the interquartile range of Kaapvaal harzburgitic garnets in diamond (grey; database of Stachel et al., 2004a). Normalised patterns of eclogitic and websteritic garnets (G3 = 2; G4 = 4; G5 = 1) in Figure 4-2B, are superimposed on the interquartile range of Kaapvaal eclogitic garnets from diamond.

All peridotitic garnets (except 39/01B) show sinusoidal patterns with a peak at Ce-Sm and a trough at Dy-Er (Figure 4-2A). Figure 4-2C and D (J4-normalised; approximately equivalent to normalization to a primitive mantle garnet, see Stachel et al., 1998b) show a condensed view of the major harzburgitic patterns and other discernible trends. Lherzolitic garnet (10/06B) shows the greatest enrichment in LREE with a broad maximum at Sm and a minimum at Tm; and the other lherzolitic garnet (39/01B) shows a distinct U-shape with a depletion in the MREE (Nd to Dy) at about 0.1 times chondritic abundance. Garnet 8/17A forms an almost horizontal REE pattern with most LREE to HREE enriched between 2 to 3x chondrite, except for La, which is approximately chondritic. Two garnets (8/08I, 8/09A) from different diamonds both show an identical, strongly sinusoidal trend, which has the most significant LREE enrichment and HREE depletion, which results in Sm/Ho <<1.

The remaining harzburgitic garnets can be grouped into two distinctly different sinusoidal trends, as shown by their respective medians in Figure 4-2C&D. Both trends are sinusoidal but differ in

the maximum LREE enrichment and HREE depletion. The Ce-max pattern peaks at Ce before steeply dropping to a minimum at Ho (garnets: 8/02A, 8/11B, 8/16A, 10/03A, 10/07A, 10/10A, 10/12A, 10/14A, 10/16A), whereas the Nd-max trend drops gently from a maximum at Nd to a less pronounced low at Ho (garnets: 8/01B, 8/12A, 8/14A, 8/15B, 10/04A, 10/08A, 10/15B). The Nd-max suite has higher ΣREE than the Ce-max suite. For all garnets, lower CaO concentrations generally coincide with overall lowered REE_N patterns (dunitic garnets in Figure 4-2A). Besides, there are no clear correlations between REE patterns and garnet major element chemistry or the presence of certain associated minerals.

Eclogitic garnet REE_N patterns in Figure 4-2B are coloured based on their classification as low- and high-Ca. The garnets have a steep increase in the LREE, a more moderate increase in the MREE, followed by a gentle positive MREE-HREE slope. The eclogitic garnet patterns show a large concentration range in the LREE that narrows towards the HREE. HREE abundances are slightly above the Kaapvaal median. Websteritic garnet (14/03A) has a broadly similar REE pattern to the eclogitic garnets, but with a pronounced MREE enrichment (Nd to Tb) peaking at Sm to Gd, followed by a steady decrease in the MREE-HREE to Lu. Two G4 garnets and the websteritic garnet have slight negative Eu anomaly (<0.95); and two G4 and G3 garnet have a slight positive Eu anomaly (>1.05; where Eu/Eu* = 2*Eu/[Sm+Gd]).

Olivine

Some non-typical trace elements (Al, Cr, Ca) were obtained on olivine for geothermometry (Section 4.3.2). Concentrations of Al, Cr, and Ca can be obtained on a greater number of olivine inclusions due to the fully focused beam and small analytical volume of EPMA compared to LA-ICP-MS. Results obtained by EPMA for Al, Cr, and Ca are within uncertainty of those from LA-ICP-MS with a 130 µm spot, the optimal spot size to minimise inter-element fractionation in olivine on our laser system (Bussweiler et al., 2019). Al concentrations range from 11 to 135 ppm with a similar average (67 ppm) and median (64 ppm). Cr concentrations range from 133 to 546 ppm, again with a similar average (323 ppm) and median (332 ppm). Lastly, Ca concentrations range from 16 to 401 ppm an average of 187 ppm and a median of 202 ppm.

Concentrations of HFSE in Koffiefontein olivine inclusions generally approach the lower limit of detection and are below detection for most of the REE (Pr to Lu; dashed lines in Figure 4-3A). Using garnet-olivine partition coefficients for REE (McKenzie and O'Nions, 1991), hypothetical olivine compositions were calculated from the composition of coexisting garnets (shaded region Figure 4-3A), but generally plot below the LA-ICP-MS limit of detection. Calculated and analysed REE concentrations generally agree within one order of magnitude for the REE that were above the limit of detection, except for Ce, where the measured values were 1-2 orders of magnitude lower than calculated.

Orthopyroxene

The concentration of REE in orthopyroxene, like olivine, are low, with abundances of the remaining HFSE analysed only slightly above the limit of detection for LA-ICP-MS (dashed lines; Figure 4-3B). Orthopyroxene compositions calculated from garnets using partition coefficients (McKenzie and O'Nions, 1991; shaded region in Figure 4-3B) showed higher values for La, Ce, Nd, Sm, and Ti than the measured orthopyroxenes. Calculated MREE to HREE concentrations were below detection for Eu to Lu for harzburgitic assemblages but above detection for lherzolitic assemblages.

Clinopyroxene

C1-chondrite normalised and J4-normalised patterns are shown for all clinopyroxenes analysed in Figure 4-4A&B, superimposed on the interquartile range of Kaapvaal clinopyroxene in diamond (grey; database of Stachel et al., 2004a). The lherzolitic diopside has a steep negative MREE-HREE slope with Tm to Lu below detection. The REE abundances for eclogitic clinopyroxenes are typically superchondritic (Figure 4-4A), except for slightly subchondritic HREE in two samples. Including the one websteritic sample, the low-Cr clinopyroxenes (Cr_2O_3 <1 wt.%) show two distinct patterns: a steady, negative slope from La or Ce to Lu, with slight negative europium anomalies (4/01A, 12/01A, 12/02C, and 13/01B); and a flatter, curved pattern with a positive hump centred at Sm to Eu (1/03C, 12/05B, 22/01A).

4.3. Geothermobarometry of Koffiefontein inclusions and mantle xenoliths

Coexisting minerals included within a diamond are not necessarily in chemical equilibrium (Griffin et al., 1988; Rickard et al., 1989; Shimizu and Sobolev, 1995). For touching minerals at mantle temperatures, disequilibrium is not possible and as such, mineral pairs will re-equilibrate to changing ambient pressure-temperature conditions close to the timing of kimberlite eruption (Stachel and Luth, 2015). Out of the 209 minerals liberated in this study, only two pairs of garnet and orthopyroxene inclusions were touching (8/11B, 10/02A). For non-touching pairs, successive occlusion during evolving physical or chemical conditions – i.e. the occurrence of chemical disequilibrium between inclusions – must be considered. If in equilibrium, such non-touching inclusions pairs and all single mineral grains record mantle conditions of diamond formation millions to billions of years before kimberlite eruption. Minerals in mantle xenoliths are expected to continuously re-equilibrate and thus reflect conditions immediately prior to exhumation. Disequilibrium may occur when (1) modal or cryptic metasomatic overprinting occurred in temporal proximity to, or during kimberlite magmatism or (2) when mantle temperatures approach closure temperatures for the relevant exchange equilibria. In the absence of an intergranular exchange medium (e.g., in a dry rock), effective closure may already occur at about 800 °C, especially for thermobarometers involving net-transfer reactions (Pattison and Bégin, 1994); but in optimal cases – small grains in direct contact – diffusive exchange may continue to below 700 °C (Frost and Chacko, 1989).

4.3.1. P-T estimates mineral inclusions from diamond and mantle xenoliths from Koffiefontein

Due to the chemically depleted nature of the lithospheric mantle where Koffiefontein diamonds formed (clinopyroxene mostly absent), and the high proportion of single-species inclusion assemblages, only a limited number of mineral-exchange geothermobarometers can be applied to define a palaeogeotherm. Because of this, pressure and temperature estimates for silicate mineral inclusions from Koffiefontein diamonds (this study and Cardoso, 1980) are supplemented with geothermobarometry data for Koffiefontein mantle xenoliths (Cardoso, 1980; Hanrahan, 2003; Table B4).

Table 4-2 lists the temperature-pressure estimates obtained for this Koffiefontein inclusion suite. For peridotitic clinopyroxene inclusions, the single-grain thermobarometer PT_{NTcpx} (Nimis and

Taylor, 2000) was used, subject to compositional filters and analytical quality checks (Grütter, 2009; Ziberna et al., 2016). For garnet-orthopyroxene pairs, pressure-temperature estimates were calculated iteratively with $T_{Ca\text{-}in\text{-}opx}$ (Brey and Köhler, 1990) for lherzolitic or T_{Harley} (Harley, 1984) for harzburgitic assemblages combined with P_{NG85}* (Nickel and Green, 1985; *with Al in M1 calculated after Carswell and Gibb, 1987). For assemblages that did not allow application of a geobarometer, pressure-dependent temperature estimates were obtained through projection onto a selected geotherm (Table B4). For eclogitic garnet-omphacite pairs, $T_{Krogh88}$ (Krogh, 1988) was employed. Pressure-independent temperature estimates are obtained from the Ni content in peridotitic garnet (Canil, 1999), analysed by LA-ICP-MS, assuming a Ni in olivine content of 3700 ppm (averaged from EPMA results) where co-existing olivines are not present. Lastly, pressure estimates from the Cr content in garnet in equilibrium with spinel (P_{38}; Grütter et al., 2006) are plotted on Figure 4-1A and represent minimum estimates as the actual presence of spinel in the diamond substrate is not established.

4.3.2. Al-in-olivine thermometry

Olivine is abundant in the mantle – in both depleted and fertile peridotites – constituting >75 % of cratonic garnet harzburgites and has a chemical structure that precludes the substitution of mantle incompatible elements. Due to these factors, extreme levels of metasomatism are required to change its chemistry. Garnet, however, may record secondary processes such as cryptic metasomatism or be formed via mantle metasomatism, meaning that in most cases olivine is preferable for study. Analysis of Al in olivine can be performed by EPMA with a spot size of <1 μm and the results are comparable to LA-ICP-MS (Tables B2&B3). The abundance of olivine as inclusions in diamond and the ease of Al analysis by EPMA adds a further dimension to the diamond sampling window of the Kaapvaal lithosphere.

Although the Al-in-olivine thermometer was calibrated on lherzolitic olivines (Bussweiler et al., 2017), it is assumed to be applicable to harzburgitic assemblages because olivine is more sensitive to changes in temperature than bulk rock concentrations (De Hoog et al., 2010). Thus, Al-in-olivine thermometry provides higher precision temperature estimates than those dependant on mineral equilibrium, e.g., diamond 8/14 where a garnet-orthopyroxene pair plots on the high-temperature side of the adiabat (Table 4-2). Exchange thermometers have inherent errors. For

example, Fe-Mg exchange thermometry in garnet-olivine pairs (T_{OW}; O'Neill and Wood, 1979) has an error of ±60 °C, most noticeable at temperatures >1200 °C (Nimis and Grütter, 2010), producing large scatter in calculated temperatures within the calibrated range (Brey et al., 1990). For garnet-orthopyroxene pairs using T_{Harley}, although in good agreement at 1000 °C, systematically under- and overestimates by ~100 °C at low and high temperatures, respectively (Brey and Köhler, 1990). Further uncertainty arises from the Fe^{3+} partitioning between minerals, e.g.: (1) Fe^{3+} in olivine is negligible and thus produces best results when ignored; (2) Fe^{3+} is taken up by garnet and ortho- and clinopyroxene and thus large errors can result for $T_{Krogh88}$ from Fe-Mg exchange in garnet-clinopyroxene (Canil and O'Neill, 1996); (3) and the partitioning systematics for Fe^{3+} between orthopyroxene and garnet is temperature sensitive but its effect is not accounted for in the Fe-Mg exchange thermometers of Harley (1984), also resulting in large errors (Luth et al., 1990). The maximum uncertainty in the $T_{Al\text{-}in\text{-}olivine}$ calculation is ±9 °C, which is an effect of calibration Al concentration and experimental pressure and temperature (Bussweiler et al., 2017). The EPMA method used for Al analysis in this study has relatively small errors, even at low concentrations: the standard SC-GB is 82 ±4 ppm (~5 % error; Section 2.4 due to the extended EPMA count times. The Al-in-olivine thermometer, with a large temperature calibration window between 850 to 1450 °C, has a mean temperature deviation of ±20 °C as calculated against $T_{Ca\text{-}in\text{-}opx}$, making it a robust, accurate thermometer (Bussweiler et al., 2017).

4.3.3. Palaeo-geothermal gradient for Koffiefontein

The diamond mineral inclusion and xenolith data were regressed separately with the programme FITPLOT (Mather et al., 2011; McKenzie and Bickle, 1988). Both datasets produced a geotherm that closely resembles a Hasterock and Chapman (2011) model geotherm with an equivalent surface heat flow of 38 $mW \cdot m^{-2}$ (Figure 4-5), thus, a 38 $mW \cdot m^{-2}$ geotherm was selected to represent the palaeogeotherm at Koffiefontein. This geotherm can be compared to published geotherms for southern Africa. The older studies tended to use the geotherm formulations of Pollack and Chapman (1977). It has been shown more recently (Goes et al., 2020; McKenzie et al., 2005) that the radiative heat conduction component at high temperatures was greatly overestimated. Hence, the ~40 $mW \cdot m^{-2}$ geotherm used by Grütter et al. (2006) for southern Africa is equivalent to the 38 $mW \cdot m^{-2}$ geotherm obtained using the Hasterock & Chapman

(2011) or McKenzie et al. (2005) geotherm formulations, in the pressure range between 4 and 5.5 GPa (inset Figure 4-5). Figure 4-5 represents our new geotherm for the mantle beneath the Koffiefontein pipe and the projected $T_{Al\text{-}in\text{-}olivine}$ and $T_{Krogh88}$ data. The calculated equilibration pressures show a bimodal distribution, with one mode at 2.5 to 3 GPa dominated by xenolith data, and a second mode centred at 5.5 to 6 GPa, represented mainly by olivine inclusions in diamond, corresponding to depths of 180 to 210 km (Figure 4-5). Further, the available xenolith data has a maximum pressure of ~6 GPa, whereas the diamond inclusion data extend to pressures of 7.5 GPa. The 38 $mW \cdot m^{-2}$ model geotherm intersects the mantle adiabat at ~7 GPa, which equates to ~220 km depth. This is comparable to results from the P_{38} barometer (Grütter et al., 2006; Figure 4-1), which gives a minimum maximum thickness of the Koffiefontein lithosphere of ~180 km. The bar chart in Figure 4-5 indicates that the high density of olivine analysis that last equilibrated between 5.5 to 6.5 GPa, corresponding to depths of 180 to 200 km. High-pressure, coexisting grt + opx inclusions imply a lithospheric thickness of ~250 km; however, this could result from the large errors associated with the T_{Harley} thermometry. The errors associated with T_{Harley} are ±40 to 80 °C due to large relative errors in experimental and natural rock data used for its calibration (Harley, 1984). The relative uncertainty in EPMA measurements for the major elements – Fe and Mg for orthopyroxene in addition to Ca for garnet – are small (e.g., <0.03 wt% for CaO in garnet) compared to the error associated with the temperature calculation.

4.4. Evolution of the Kaapvaal Craton

4.4.1. Nature of the Koffiefontein SCLM

The peridotitic silicate inclusions recovered from Koffiefontein diamonds record a complex evolution of the local lithospheric mantle, which spans a range of melt depletion environments as evidenced by: (1) garnet CaO from 0.67 to 8.4 wt% and Cr_2O_3 up to 13 wt.%; (2) olivine Mg# between 91 and 95; and (3) the presence or absence of clinopyroxene indicating a fertile or depleted environment, respectively. These signatures are preserved as mineral inclusions in diamond, which although formed at high pressure and temperature in the mantle, record bulk rock chemical and physical changes. The low abundance of eclogitic inclusions agrees with previous studies on Koffiefontein diamonds (Cardoso, 1980; Rickard et al., 1989); and the

eclogitic garnet chemistry and REE_N is within the bounds of eclogitic inclusions described by Stachel and Harris (2008).

Peridotitic garnet – which accounts for almost half of the minerals released from the Koffiefontein diamonds – forms from either the reaction of spinel and orthopyroxene with increasing pressure or by exsolution from high-temperature orthopyroxene during isobaric cooling (Bulatov et al., 1991; Gibson, 2017; Green and Ringwood, 1967). Experimental studies of Cr_2O_3-Al_2O_3 ratios in spinel, orthopyroxene, and garnet have been used to distinguish between these two pathways (Brey and Shu, 2018). Garnet and orthopyroxene inclusion data from Koffiefontein diamonds (Figure 4-6) indicate that garnet growth could have occurred by both mechanisms based on the range of Cr-contents. The high-Cr nature of the Koffiefontein garnets (Cr_2O_3 up to 13 wt.%) reflects high bulk rock Cr:Al and thus indicates an early stage of peridotite melting in the shallow lithosphere where spinel is stable and garnet is absent (spinel-facies melting; Stachel et al., 1998b). During spinel-facies melting, REE in peridotite is depleted but it is the low concentration of HREE – preserved in later formed peridotitic garnet – that is reminiscent of a residue produced from spinel-facies melting, because melting in the garnet-facies fractionates the HREE due to their compatibility in garnet (Johnson et al., 1990). Based on the very low concentration and inter-element fractionation of HREE in the Koffiefontein garnet inclusions (Figure 4-2), they are consistent with more than 25 % melt extraction in the spinel-facies; and although garnet-facies melting could account for the positive HREE slopes, it cannot account for $HREE_N$ <1, even after 50 % melt extraction (Lazarov et al., 2012). Extensive levels of melt depletion are recorded in peridotitic garnet inclusions with less than 1.8 wt% CaO, likely representing dunitic substrates (Grütter et al., 1999), higher degrees of melt extraction may be unfeasible. Hence, the very high Cr garnets present at Koffiefontein and in the global inclusions in diamond dataset (Figure 4-6) show clearly that a significant fraction of these garnets must have formed by metamorphic reaction from low-pressure spinel peridotite precursors.

For cratonic peridotites, olivine Mg# ($Mg\#_{ol}$) approximates the bulk rock Mg# and for residual rocks is used as a measure for the extent of melt extraction (Boyd, 1989). Cratonic peridotite $Mg\#_{ol}$ between 92.6 and 92.9 requires ~40 % melt extraction at low pressures, which corresponds to the point of orthopyroxene exhaustion (Bernstein et al., 2007; Figure 4-1B).

Worldwide, excluding the Kaapvaal, olivine inclusions from diamond show a $Mg\#_{ol}$ median of 92.6 (n = 876); compared to the Kaapvaal, where the $Mg\#_{ol}$ median is 93.4 (n = 467; see also Stachel and Harris, 2008). As illustrated in Figure 4-1B, a median $Mg\#_{ol}$ of 93.6 – for the Koffiefontein data – would indicate melt extraction either beyond the point of orthopyroxene removal (almost 60 % melt removal at 3 GPa) or at very high pressures (50 % melt extraction at 7 GPa). Even higher olivine $Mg\#_{ol}$, such as those >94.5 seen in the Koffiefontein suite, would require exceedingly high degrees of melt extraction even at high pressure (>65 % melt extraction at 7 GPa), which would imply the thermally implausible continued melting of pure olivine residues (Baker and Stolper, 1994; Bernstein et al., 2007; Pearson and Wittig, 2008; Walter, 1999). Due to the nature of mineral inclusions in diamond not representing the full mineral assemblage, it is impossible to confirm that these olivines – classified compositionally as deriving from dunite – actually derived from a dunite parent rock. However, based on combined chemical and petrological studies of mantle xenoliths, these unusually high $Mg\#_{ol}$ clearly imply that secondary processes must have enhanced the primary melt depletion signature for at least some of the Koffiefontein olivine inclusions.

A process that has been attributed to increasing bulk rock $Mg\#_{ol}$ is carbonate melt metasomatism (Hauri et al., 1993). Experimental investigations on peridotite show that at high pressure and temperature, Fe is partitioned into the silicate phase over carbonate, and preferentially into olivine over orthopyroxene (Dalton and Wood, 1993; Martinez et al., 1998). According to coexisting opx-ol assemblages and the high $Mg\#_{ol}$ and $Mg\#_{opx}$ (Figure 4-7), carbonate melt metasomatism is likely not responsible for the elevated $Mg\#_{ol}$, which is equally elevated in orthopyroxene and olivine.

An alternative mechanism to locally increase $Mg\#_{ol}$ is by melt-rock reaction conduits analogous to dunite formation in ophiolites. Spinel peridotite residues produced at hot mid ocean ridges, once cooled away from the ridge axis, can react with ascending, silica-undersaturated basaltic melts generated at low pressure (>1 GPa) to produce channels of dunite where orthopyroxene is preferentially dissolved and olivine precipitated (Braun and Kelemen, 2002; Kelemen et al., 1995). The residual rock is a spinel harzburgite with zones of laterally progressive depletion and localised channels of dunite up to a few meters in thickness; however, the harzburgite and dunite

both have similar $Mg\#_{ol}$ to residual mantle peridotite (Kelemen et al., 1992). If instead, a high-MgO parental melt – such as a boninite – infiltrates a residual peridotite, the $Mg\#_{ol}$ in the residual dunite can be increased (e.g., Bodinier and Godard, 2013; Rollinson, 2019). Such a process, even infiltrating modern-day oceanic peridotite, is capable of creating $Mg\#_{ol}$ of 93 to 94 (Rollinson, 2019). In the hotter Archean Earth, the residual peridotite and high MgO melts would likely have had a higher Mg#, enhancing this effect. Such a scenario of a boninite parental melt could be accommodated by a move from a spreading ridge to an ocean-ocean subduction setting where the subducting slab interacts with and induces melting of the depleted lithosphere in the overlying mantle wedge (discussion continued in Section 4.4.4). Alternatively, the spreading ridge could be in an arc setting, with melting affecting previously depleted mantle.

4.4.2. Peridotite carbonation during diamond formation recorded by SiO_2-Mg_2SiO_4-$MgSiO_3$ assemblages

Two peridotitic diamonds hosted inclusions of SiO_2 (structurally quartz but interpreted as primary coesite) together with non-touching inclusions of olivine and garnet (10/04; 1300 °C and 7 GPa), and enstatite (8/03; 1184 °C and 5.8 GPa). In diamond 10/04, the garnet is harzburgitic (CaO = 2.33 wt%) and has an $Mg\#_{ol}$ of 93.3. In diamond 8/03, the garnet reflects ultradepleted harzburgitic-dunitic substrates (CaO = 1.14 wt%), consistent with a very high observed $Mg\#_{ol}$ (94.1). Whilst coesite is a fairly common inclusion in eclogitic suite diamonds (constituting nearly 2 % of all eclogitic inclusions; Stachel and Harris, 2008), in the peridotitic suite it is very rare (Stachel et al., 1998a). A significant number of SiO_2 inclusions are, however, associated with the peridotitic inclusion suite at the Renard pipe on the Superior Craton (Hunt et al., 2012). The explanation proposed for the Renard SiO_2 inclusions – extreme carbonation of peridotitic diamond substrates (Hunt et al., 2012) – can be applied to the diamonds from Koffiefontein. Addition of >30 wt.% CO_2 (Schrauder and Navon, 1993) to a peridotitic diamond substrate, carbonates all the available olivine to stabilise free SiO_2 (Wyllie and Huang, 1976). In this process, the olivines must have been occluded before carbonation was completed and carbonation likely would have occurred in localised, vein-like areas (Hunt et al., 2012). This explanation can be extended to diamond 39/02, which liberated calcite and olivine ($Mg\#_{ol}$ 92.5-92.7).

4.4.3. Moissanite – evidence of locally extreme fO_2

Diamond 2/05 hosted moissanite (SiC), orthopyroxene and olivine. The major element chemistry of the orthopyroxene and olivine is within the normal range of such minerals from Koffiefontein diamonds. The $Mg\#_{ol}$ is 94.5 and pressure-temperature conditions indicate formation at 1300 °C and 6.5 GPa. Moissanite is a rare mineral in diamond and its formation requires extremely reducing conditions in the mantle, corresponding to oxygen fugacities far below the iron-wüstite buffer (IW; Schmidt et al., 2014). Experimental studies show that silicate minerals in equilibrium with moissanite will be pure magnesium endmembers, as all iron present will be native metal at such low fO_2 conditions. In a peridotitic system, equilibrium between moissanite and diamond may be described by the reaction:

$$Mg_2SiO_4 + SiC + O_2 \rightarrow Mg_2Si_2O_6 + C, \qquad \text{(Equation 4-1)},$$

which at upper mantle conditions occurs at $\Delta\log fO_2$ of IW-9 to IW-6 (10 GPa; Schmidt et al., 2014). Such reducing conditions do not occur on a regional scale in Earth's mantle, at least not above the core-mantle boundary, and the presence of normal amounts of Fe^{2+} in olivine and orthopyroxene in inclusions within the same diamond further precludes derivation from overall super-reducing substrates. Given the peridotitic paragenesis of the two associated silicate inclusions, moissanite formation during metamorphism of subducting, reduced carbonaceous sediments (Mathez et al., 1995) also is precluded. More likely, the formation of the isolated moissanite inclusion in diamond 2/05 reflects a short-lived, localised, non-equilibrium event where fO_2 conditions have been driven to extremely low levels in a small chemical environment.

4.4.4. Large-scale Si enrichment

The SiO_2 excess in the Kaapvaal peridotites – as evidenced by the low bulk rock Mg:Si – is a well-known phenomena (Bernstein et al., 2007; Boyd, 1989; Kelemen et al., 1998; Kesson and Ringwood, 1989a; Simon et al., 2007; Walter, 1999). The general consensus is that orthopyroxene was added to Kaapvaal cratonic peridotites through metasomatism involving a Si-rich fluid or melt (Bell et al., 2005). The origin of such fluids/melts has been attributed to subduction (Kesson and Ringwood, 1989a), more specifically TTG (tonalite-trondhjemite-granite) produced from the melting of metabasalts/eclogites (Kelemen et al., 1998; Rudnick,

1994), melts derived from metasediments (Zhang et al., 2001), or Si-LREE-LILE-rich hydrous fluids from early crust subduction (Simon et al., 2007). All these processes require pervasive melt/fluid percolation through the deep cratonic lithosphere. If this process took place in already-formed lithospheric mantle and is representative of the whole cratonic root, Walter (1999) notes that: "a volume of liquid equal to or even greater than the volume of cratonic lithosphere would be needed, for example, to crystallize enough opx to enrich the entire southern African lithosphere in SiO_2" (p.235). The very restricted and normal mantle-like O-isotope compositions of olivine and orthopyroxene from these rocks appear to rule out a fluid or melt origin from a crustal precursor such as sediment or eclogite. Alternatively, the orthopyroxene enrichment took place as a product of melt-rock reaction in low-pressure parental oceanic peridotites prior to lithospheric thickening, a process supported by the normal oxygen isotope compositions of the olivine and orthopyroxene from these peridotites (Regier et al., 2018). However, this model cannot account for the high $Mg\#_{ol}$ evident in the Koffiefontein olivine inclusions as the parental rock would only record $Mg\#_{ol}$ of harzburgite.

A source for the necessary high MgO magmas required for the lower pressure melt-rock reaction to enhance orthopyroxene contents in the precursor low-pressure peridotites to the Kaapvaal mantle root can be found in some komatiites from the Barberton Greenstone Belt that are now recognised as boninitic lavas (e.g., Barberton AUK type, BK type, and Commondale type; Sossi et al., 2016; Wilson, 2003). The Commondale Komatiites, on the western margin of the Kaapvaal Craton, are unique in their high SiO_2 contents (46.6-49.8 wt%), low FeO (4.3-6.7 wt%), high $CaO:Al_2O_3$ and $Al_2O_3:TiO_2$, and extreme depletion of incompatible elements (Wilson, 2003). The ultra-high Mg# of the olivine in these rocks (>96) indicate a parental magma composition of 36.1 wt.% MgO and 6.8 wt.% FeO and anhydrous eruption/intrusion temperature of 1670 °C (Wilson, 2019). Interaction of a partial melt derived from a refractory mantle source with shallowly overlying abyssal peridotite is chemically compatible with the SiO_2-metasomatism of the Kaapvaal Craton. Further, the 3.4 Ga age of these "komatiites" (whole rock Re-Os; Wilson et al., 2003) implies an available source for metasomatism before craton amalgamation and the earliest diamond formation. The very high Mg# of the parental melt could further increase the Mg# of the peridotites by melt-rock interaction, increasing both the Mg# of the depleted lithosphere and enriching it in Si, evidenced by orthopyroxene formation.

4.4.5. Large-scale REE enrichment

Mantle garnets record changes in the incompatible trace element budget of their host rocks, in particular through their REE abundances and patterns (Shimizu and Richardson, 1987). By occlusion from the surrounding mantle, garnet inclusions particularly preserve detailed signatures of metasomatic events occurring before or during diamond formation, dating back to over 3 Ga in many cases. The LREE-enrichment documented in garnet included in diamond from some peridotitic xenoliths indicates a metasomatic overprint by a fluid or melt with very high LREE:HREE (Hoal et al., 1994; Shimizu and Richardson, 1987; Stachel et al., 1998b). This metasomatic agent has been attributed to COH fluids (Stachel et al., 1998b; Stachel and Harris, 1997; Weiss et al., 2013, 2009) or a carbonatitic or kimberlitic melt (Rudnick et al., 1993; Shu and Brey, 2015). Following the modelling of Shu and Brey (2015), combining the high garnet LREE:HREE characteristics with variable Ti:Eu and low Zr:Hf (<2500) indicates interaction with a carbonatitic metasomatic agent for the Koffiefontein peridotitic garnets. While the Roberts Victor garnets of Shu and Brey (2015) require only 3 % carbonatitic melt for re-enrichment, the range of Koffiefontein garnets analysed would require 1-20 % of this component to produce their very steep $LREE_N$ slopes (Figure 4-2), but values on the higher end are likely unrealistic unless locally focused enrichment processes are envisaged.

There are several arguments against metasomatic overprint by a carbonatitic melt. (1) In the Archean, oceanic carbonates likely were not subductable (Dasgupta and Hirschmann, 2010) and hence there is no obvious source for sufficient amounts of carbonatitic melts for either craton-scale metasomatic modification of the SCLM or craton-wide but localised regions of diamond formation. (2) The diamond substrates for Koffiefontein diamonds are largely harzburgitic and carbonatite melt cannot percolate through rocks below their solidus temperature. Along a 38 $mW \cdot m^{-2}$ geotherm, only a small number of Koffiefontein diamonds, deriving from pressure-temperature conditions greater than 6 GPa and 1270 °C (Figure 4-5), exceed the solidus of hydrous carbonated harzburgite (Wyllie, 1987a). (3) In a fluid-buffered SCLM (Stachel and Luth, 2015), the percolation of carbonatitic melts with melt-rock ratios >1:100 would constrain ambient fO_2 conditions to the EMOD buffer (which limits carbonate stability in harzburgite) or

above, which then requires subsequent reduction of SCLM by at least 1 log unit to match observed fO_2 values in the xenolith record (Stagno, 2019).

Compared to carbonate melts, high density fluids (HDFs) are water- and carbonate- or silicate-rich fluids elevated in incompatible elements (e.g., K, Na, Zr, Hf, LREE) with a range of end-member compositions, making them highly mobile and reactive (Schneider and Eggler, 1986; Weiss et al., 2013, 2009). H_2O contents can vary from 10-25 wt% as found in fibrous diamonds (Weiss et al., 2010) to 40-65 % based on experimental studies (Adam et al., 2014; Kessel et al., 2015), and up to 98 % at the water maximum of a pure CHO fluid (Luth and Stachel, 2014). Models of HDF-enrichment of a pre-metasomatic garnet (Stachel et al., 2004b) can generate the ranges of LREE-enrichment seen in peridotitic garnets (Weiss et al., 2009). Furthermore, these models predict a change in the position of the garnet REE_N maximum – from Ce to Pr-Nd – with changing concentration of the metasomatic HDFs (Weiss et al., 2009); analogous to the Ce-peak and Nd-peak curves of the garnet REE_N patterns in Figure 4-2C. These HDFs can be either peridotitic, generated from interaction of hydrous saline fluids and carbonated peridotite; or eclogitic, resulting from the interaction of alkali-rich, hydrous fluids with eclogite (Weiss et al., 2009). At high pressure, these COH fluids can transport a significant quantity of dissolved elements; however, large fluid-rock ratios are needed to effect appreciable major-element metasomatism (Adam et al., 2014; Schneider and Eggler, 1986). Furthermore, experiments show that these melts (or fluids) have high Mg:Fe (carbonatitic melt Mg# of 85; (Green and Wallace, 1988), thus not affecting the high Mg# observed in the craton. Thus, the interaction of HDFs in the Kaapvaal Craton before or during diamond formation can produce the pervasive LREE-enrichment present in garnets without the need for significant modal metasomatism or changes to the oxidation state of the cratonic mantle. I therefore suggest that the pervasive REE enrichment in the peridotitic garnet inclusions at Koffiefontein and throughout the Kaapvaal Craton largely reflects the interaction of the thickened mantle root with incompatible element enriched HDFs that, in some cases, crystallised diamond. The involvement of such HDFs in the formation of gem diamonds such as those containing the Koffiefontein inclusions analysed here has recently been documented in terms of major elements (Jablon and Navon, 2016) and trace elements (Krebs et al., 2019).

4.4.6. Palaeogeotherms: indicators of a dynamic SCLM

The thermobarometry of minerals trapped in diamonds from the Kaapvaal Craton are representative of a number of time slices, ranging from Early Archean SCLM formation (~3.3 Ga Sm-Nd ages from various Kaapvaal localities; Richardson et al., 1984), through proto-craton merger (2.7-3.0 Ga Re-Os ages at Koffiefontein; Shirey et al., 2004b) to diamond-formation just before kimberlite emplacement (Re-Os ages at Koffiefontein; Pearson et al., 1998); whereas xenoliths – in an open system – record ambient conditions just before eruption (~90 Ma in the case of Koffiefontein; Davis, 1977). It is expected that mantle xenoliths and minerals included in diamonds should reflect distinct time-integrated physical and chemical environments in the SCLM (Bell et al., 2003) and a case has been made, at Kimberley on the Kaapvaal Craton, for inclusions in diamonds preserving geotherm conditions significantly different from the mantle peridotites from that locality (Weiss et al., 2018). In contrast, at Koffiefontein, diamonds and xenoliths produce identical geotherms, within both analytical error and geotherm model uncertainty (inset Figure 4-5). Although a 90-110 °C difference exists between a 38 and 40 m.W·m^{-2} geotherm between 5-6 GPa, both the xenolith and inclusion-in-diamond geotherms rely on similar mineral-exchange thermobarometers that have inherent errors. A similar example of identical xenolith-based geotherms exists on a 500 Ma timescale for a group of Phanerozoic 550-50 Ma kimberlite pipes on the Slave Craton (Canil, 2008). This indicates that potential cooling from the time of diamond formation in the Archean to the time of kimberlite eruption in the Cretaceous, a more than 2 Ga time period, was unresolvable. This has implications for two aspects of mantle heat flow: (1) secular cooling rates in the convecting mantle and (2) transient heating events in the SCLM.

Secular temperature change of the convecting mantle is controlled by a number of factors that balance out heat production (core heat flow, and radiogenic decay in the mantle and lithosphere) and heat loss (oceanic and continental heat loss) to end up with a net energy loss of 46 TW (TerraWatts; Jaupart et al., 2015). Although heat production models vary (e.g., Vlaar et al., 1994), variations in non-arc basalts indicate a 200 °C change in mantle potential temperature for the Earth's history, or 50 °C·Gyr^{-1} (Herzberg et al., 2010). However, the similarity of the xenolith and diamond-included Koffiefontein geotherms show that there has been no detectable cooling in the SCLM in the past 3 Gyr, assuming earliest diamond formation at 3.3 Ga,

indicating that the continental geotherms are shielded from temperature variations in the convecting mantle.

Lithospheric keel formation of the Kaapvaal Craton from stacking of mature, cold slabs supports a thick, cold lithosphere with a large diamond stability field early in its formation history (Eaton and Perry, 2013), further supported by old, ~3 Ga, diamond ages (Richardson et al., 1984). In reality, it is only the rheological boundary layer – that region of the SCLM adjacent to the convecting mantle, >200 km depth – that is affected by the ambient mantle (Sleep, 2003). This is in contrast to studies of xenoliths, which show protracted cooling of the Kaapvaal SCLM through age differences determined by both the Lu-Hf and Sm-Nd isotopic systems (peridotitic xenoliths of Bedini et al., 2004; and eclogitic and pyroxenitic xenoliths of Shu et al., 2014). Trace element and isotopic studies on minerals in xenoliths suffer from late-stage metasomatic effects – often related to kimberlite infiltration – that can alter trace abundances without significantly impacting the ambient temperature (Sleep, 2003 and discussed below). For example, the negative Sm-Nd ages in the Bedini et al. (2004) study indicate that Sm-Nd systematics had been reset by outside melts or fluids. Additionally, garnet – most often used for isotopic studies due to its affinity for REE – can be both metasomatically altered or reintroduced into a peridotitic assemblage (Simon et al., 2003). Further, errors in pressure-temperature estimates arise from the use of disequilibrium assemblages – discussed in Section 4.3 – and especially for eclogitic assemblages that cannot make use of a mineral barometer.

Some previous studies have related melt or fluid infiltration to thermal perturbations in the mantle (Bell et al., 2003; Kobussen et al., 2009; Weiss et al., 2018). These authors call for large-scale events such as metasomatism or intrusion of large igneous provinces (e.g., the Jurassic-aged Karoo Igneous Province) and more-localised intrusions such as lamproites to appreciably affect the geothermal gradient of the craton. If kimberlite eruption or diamond formation occurred within 500 Myr of transient heating, the time period required to dissipate 95 % of the heat introduced heat from 200 km-thick lithosphere, this would cause xenoliths and young diamond-forming events (e.g., fibrous/cloudy diamonds) to record hotter cratonic geotherms (Jaupart et al., 2016). The apparent consistency of the mantle geotherm recorded over a ~3 Ga time period at Koffiefontein does not indicate that large-scale heating or metasomatic events

changed the thermal regime of the SCLM, at least to a level that can be observed at present. Geothermal modelling (Sleep, 2003) shows that (1) because metasomatising magmas move up a geothermal gradient, there is no change in local temperature; and (2) due to the low volume of a kimberlite magma, there is little latent heat for heating the lithosphere. For larger-scale events, e.g., intrusion of plume-derived Karoo Flood Basalt, its effect on the lithospheric mantle is less constrained with some models requiring only minor amounts (<3 %) of lithospheric mantle to be assimilated (Arndt and Christensen, 1992) and others calling for significant thermal increase of the lithosphere, leading to lithosphere erosion (Saunders et al., 1992). However, a change in heat transfer mechanism at the base of the lithosphere from convective (and advective) to conductive is less efficient (Saunders et al., 1992), and thus may limit the thermal perturbation of the cratonic lithosphere.

Although the Kaapvaal Craton mantle root consists of ancient, melt-depleted peridotites – being stable for billions of years – the depth profile of xenolith versus diamond data thermobarometry could relate to changes in the extent of craton thickness at different times. Grütter et al. (2009) showed that well characterised mantle xenoliths from the western Kaapvaal Craton have an abrupt sample termination at 5.6 GPa, even though the geotherm intersects the adiabat at >7 GPa, indicating a thick boundary layer between the depleted lithosphere and the convecting mantle, in contrast to the mantle sample reflected in the diamond inclusions (maximum pressure of 7.4 GPa). The change in maximum depth of sampling of young kimberlites (~90 Ma) versus old diamonds may relate to a change in the thickness of the craton's mechanical boundary layer over time, but this should also be evident by a distinctly higher xenolith geotherm.

4.5. Summary and conclusions

A new suite of ~200 mineral inclusions from Koffiefontein diamonds provides the basis for an improved understanding of the Kaapvaal SCLM formation and evolution. The chemically highly depleted nature of the SCLM relies heavily on geochemical information from olivine (high Mg#) and low-Ca garnet. Although extensive decompression melting in the spinel-facies can account for the high-Cr, low-Ca garnet and pre-metasomatic steep positive LREE:HREE garnet trends, it cannot fully account for the extremely high $Mg\#_{ol}$, (up to ~95) observed in Koffiefontein diamond inclusion olivines and other olivines included in Kaapvaal Craton diamonds. Instead,

these very high Mg#s could result from the interaction of a refractory, melt-depleted mantle lithosphere protolith with high Mg# melt in conduits in shallow lithosphere, prior to thickening into deep stable cratonic lithosphere. Additionally, the depleted harzburgitic lithosphere is enriched in Si by the formation of orthopyroxene, likely a consequence of interaction with rare Archean boninitic, Mg-, Si-rich magmas that are produced in the mantle wedge, or by other high MgO magmas that achieve orthopyroxene-saturation through melt-rock reaction. These processes occurred early, before the protoliths of SCLM were displaced to greater depths. The very high Cr garnets observed as inclusions in diamonds are subsequently formed through the reaction of orthopyroxene and spinel in protoliths with relatively high Cr/Al. The occurrence of calcite inclusions in lherzolitic assemblages and retrogressed coesite in harzburgitic assemblages is direct evidence for diamond formation from the reduction of carbonatitic magmas or carbonate-rich fluids, respectively. The low abundance and very normal eclogite suite at Koffiefontein does not point towards any unusual trends or settings that have not been documented at other Kaapvaal locales. However, the introduction of a unique pyroxenitic mineral, in the form of goldschmidtite, does indicate some unusual metasomatic fluids. Prior to diamond formation, ubiquitous LREE metasomatism occurs through the interaction of high-density fluids originating deeper in the convecting mantle. HDFs are also linked to diamond formation and thus REE enrichment and diamond formation could occur simultaneously. Lastly, calculated geotherms for xenoliths and diamonds indicate that the SCLM shields the lithospheric mantle within from secular changes in the convecting mantle over time scales of ~3 Gyr.

Table 4-1: Mineralogy and abundance of inclusions from diamonds by suite liberated from 91 Koffiefontein diamonds. Numbers outside of parentheses are the total number of diamonds that contain specified inclusions and the numbers in parentheses are the total number of specified inclusions recovered.

Peridotitic		**Eclogitic-Websteritic (Low-Cr)**	
Single-species assemblages		*Single-species assemblages*	
olivine (29)	16	low-Cr garnet (6)	5
enstatite (5)	2	omphacite (17)	7
Cr-rich garnet (32)	21	websteritic garnet (1)	1
clinopyroxene (4)	4	websteritic augite (2)	1
chromite (5)	3	Other: corundum[1] (1), calcite[1] (1)	
Bimineralic assemblages		*Bimineralic assemblages*	
olivine (7) + enstatite (6)	4	garnet (2) + omphacite (4)	2
olivine (12) + garnet (15)	5		
enstatite (15) + garnet (18)	11		
olivine (3) + calcite (1)	1		
Polymineralic – 1 diamond each			
olivine (1) + enstatite (2) + moissanite[1] (1)			
garnet (1) + olivine (1) + SiO_2[1] (1)			
augite (1) + goldschmidtite[2] (1) + intergrowth (Mg-silicate, chromite, Ta-K-oxide[3]) (1)			
garnet (2) + olivine (1) + enstatite (1) + SiO_2[1] (1)			
garnet (1) + enstatite (1) + sulphide (1)			
garnet (1) + enstatite (1) + sulphide (1) + olivine (1) + Mg-silicate[3] (1)			

[1]Checked by Raman spectroscopy;
[2]New, approved mineral with formula $(K,REE,Sr)(Nb,Cr)O_3$ (Meyer et al., 2019)
[3]Yet to be identified

Table 4-2: Geothermobarometry for Koffiefontein mineral inclusions in diamond. Thermobarometers used are explained in the text.

Diamond	Minerals	Thermometer/ Barometer	T (°C)	P (GPa)	Comments
6/07	cpx	NTcpx	783	2.49	Passes Grütter (2009) but fails Ziberna et al. (2016) tests
7/01	2opx, 4gt	Harley/NG85*	1285	6.84	
7/04	opx, gt	Harley/NG85*	1233	6.59	
8/01	opx, gt	Ca-in-opx/NG85	986	4.75	
8/03	ol, opx, 2gt, SiO_2	Harley/NG85*	1239	7.13	
8/10	opx, 3gt	Ca-in-opx/NG85	1101	4.95	
8/11	opx, gt	Harley/NG85*	1144	5.98	Touching gt-opx
8/12	4opx, 2gt	Harley/NG85*	1222	6.83	
8/13	opx, gt	Harley/NG85*	1160	6.33	
8/14	opx, gt	Harley/NG85*	1437	7.96	Plots on other side of adiabat, thus not in chemical equilibrium
8/16	opx, 2gt	Harley/NG85*	1255	5.90	
9/01	ol, opx, 3gt	Harley/NG85*	1342	7.40	
9/02	opx, gt	Harley/NG85*	1305	6.28	
10/02	opx, gt	Harley/NG85*	1151	5.31	Touching gt-opx
16/01	cpx	NTcpx	1159	5.21	
12/02	cpx	NTcpx	1190	5.32	
12/03	cpx	NTcpx	1202	5.35	
12/06	cpx	NTcpx	1517	8.12	Passes Grütter (2009) but fails Ziberna et al. (2016) tests
			1434	5.00	Calculated at fixed pressure of 5 GPa

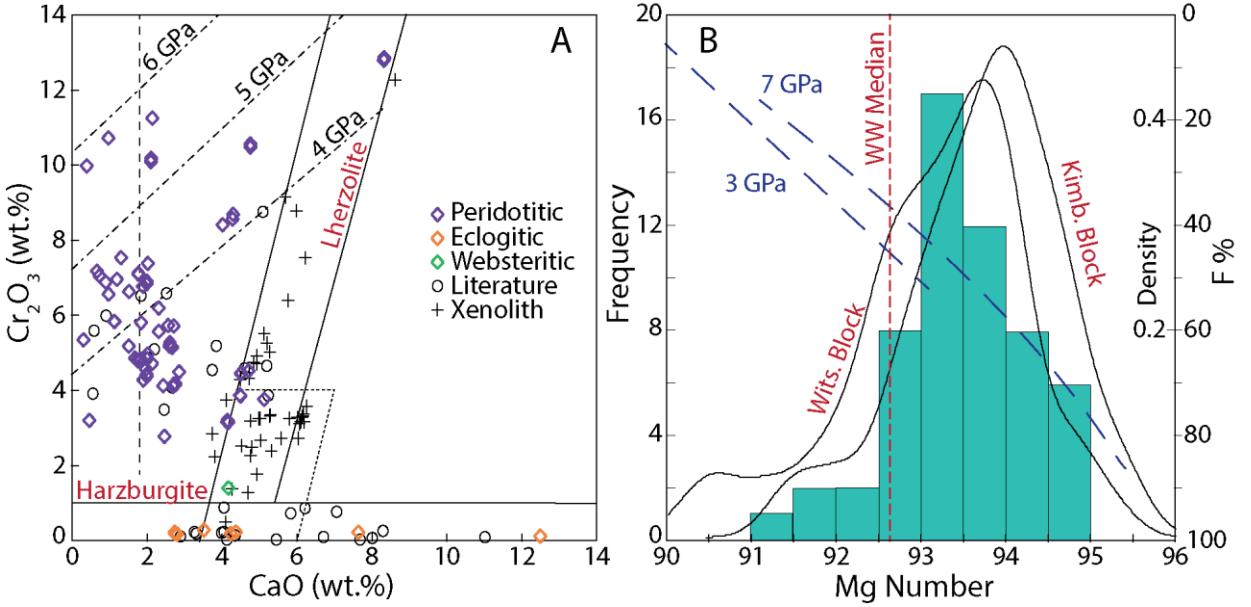

Figure 4-1: (A) CaO vs. Cr_2O_3 of garnets from diamond and xenolith (Bell, 1981; Meyer and McCallister, 1984 and unpub from Cardoso, 1980; Hanrahan, 2003) from Koffiefontein. Outline of garnet compositional fields from with the vertical dashed line (CaO < 1.8 wt%) delimitating harzburgitic garnets from the ultra-depleted dunitic compositions Grütter et al. (2004). Dashed lines are the isobars of the P38 barometer of Grütter et al. (2006) and represent minimum pressure estimates if coexistence of spinel is not observed (as is the case for almost all samples plotted). (B) Histogram of diamond-liberated olivine Mg# for Koffiefontein (this study) overlain with kernel density distributions for the Kimberley block (Koffiefontein, De Beers Pool, Finsch, Roberts Victor, and Jwaneng) and the Witwatersrand block (Dokolwayo, Helam, Jagersfontein, Klipspringer, Letseng, Klipsringer, Monastery, and Cullinan/Premier), and the world-wide median from the database of Stachel and Harris (2008). Melting experiments (dashed lines) at 3 GPa and 7 GPa show the extent of melt extraction (F %) in relation to the Mg# of olivine in the residual peridotite (Pearson and Wittig, 2008; based on experimental data of Baker and Stolper, 1994; Walter, 1998).

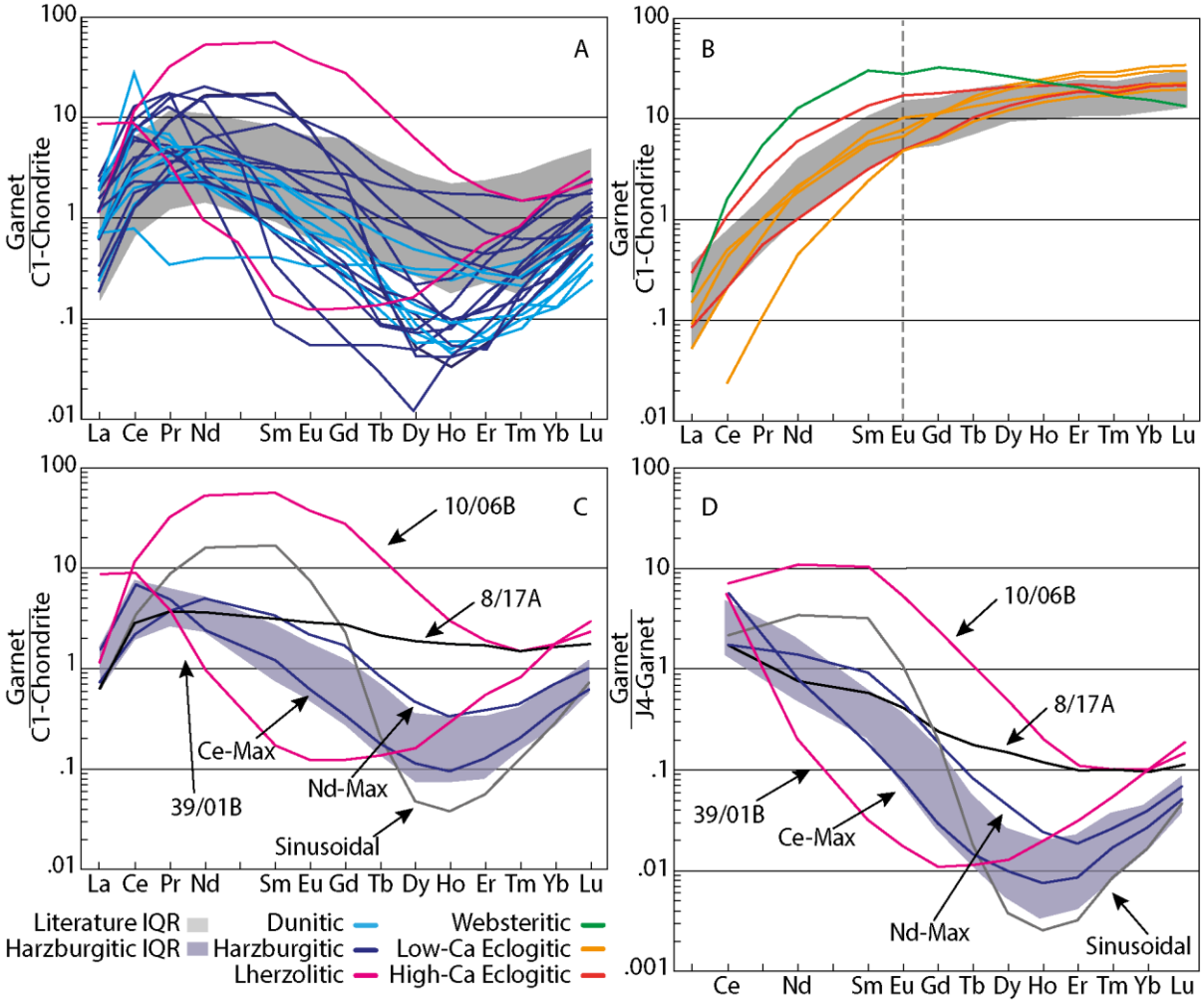

Figure 4-2: Rare earth element concentrations of Koffiefontein garnets, normalised to C1-chondrite (A, B, C; McDonough and Sun, 1995) and J4 (D; primitive garnet of Jagoutz and Spettel (unpub) in Stachel et al., 1998). A: peridotitic garnets (lines) and the interquartile range of harzburgitic garnet inclusions from the Kaapvaal Craton (grey band; database of Stachel et al., 2004). B: Low-Cr (eclogitic-websteritic) garnet inclusions from Koffiefontein and the interquartile range of eclogitic garnet inclusions the Kaapvaal Craton (database of Stachel et al., 2004). C: Range of Koffiefontein harzburgitic garnet inclusions (shaded) and selected patterns described in the text. D: Same as C but normalised to J4.

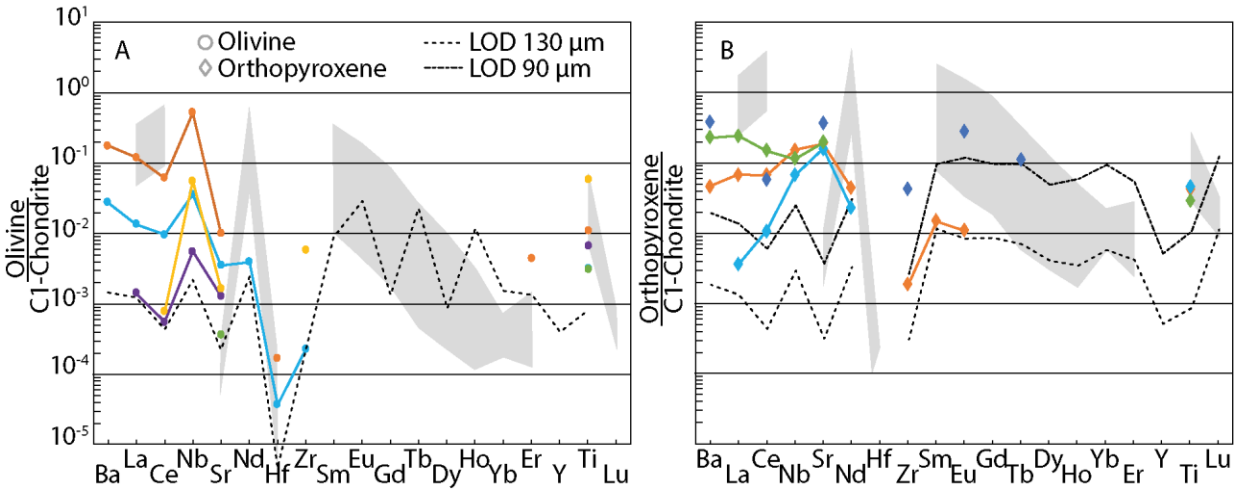

Figure 4-3: Extended trace element pattern, normalised to C1-chondrite (McDonough and Sun, 1995) for (A) olivine and (B) orthopyroxene mineral inclusions from Koffiefontein diamonds by LA-ICP-MS. Solid symbols are mineral analysed in this study and the dashed line is the limit of detection based on spot size. Shaded region indicates the range of predicted values based on Koffiefontein garnets (from Figure 4-2) using the partition coefficients of McKenzie and O'Nions (1991).

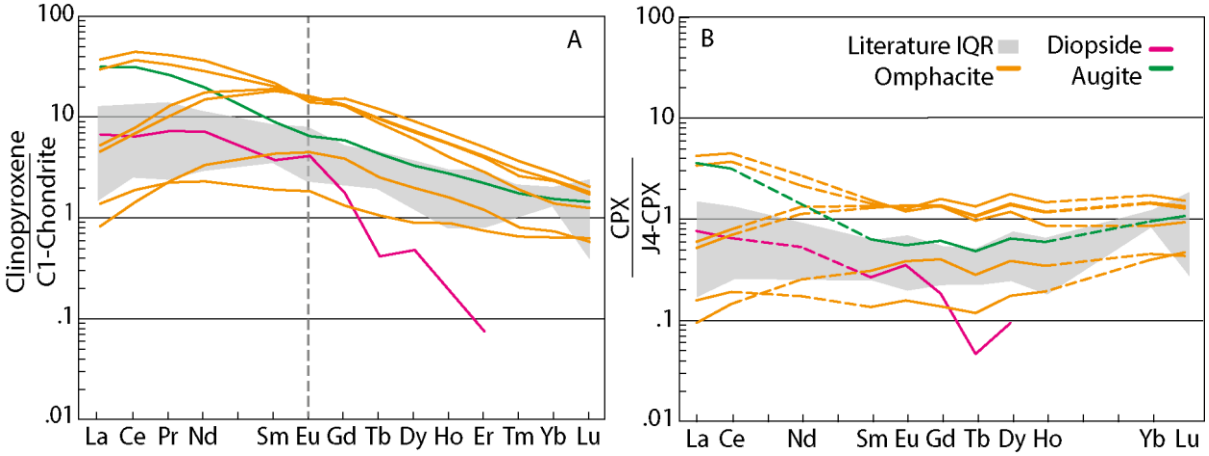

Figure 4-4: Rare earth element concentrations of selected Koffiefontein clinopyroxene parageneses, normalised to C1-chondrite (A, B, C; McDonough and Sun, 1995) and J4 (D; primitive garnet of Jagoutz and Spettel (unpub) in Stachel et al., 1998). The interquartile range of literature Kaapvaal, lherzolitic clinopyroxene (database of Stachel et al., 2004) is shown as a grey band.

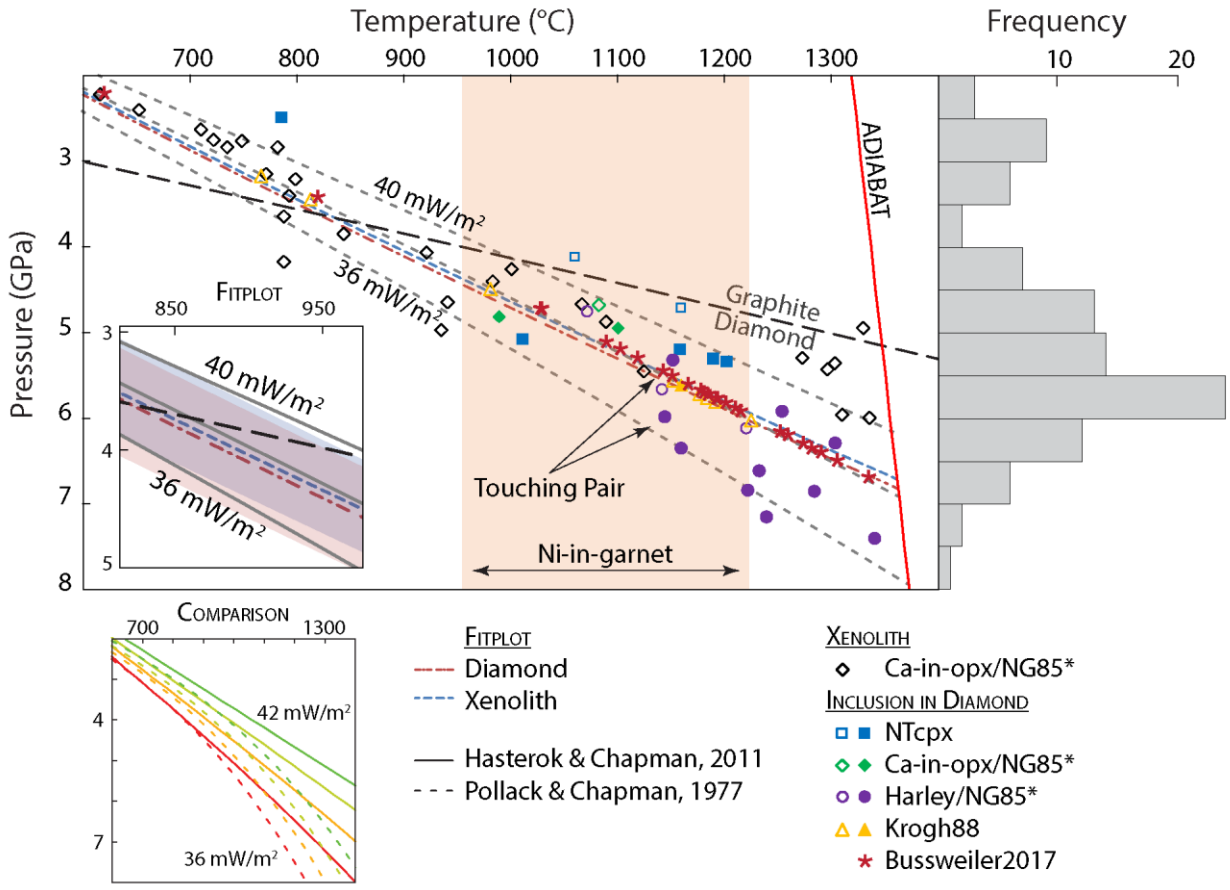

Figure 4-5: Pressure-temperature estimates for Koffiefontein xenoliths and mineral inclusions in diamonds using the geothermobarometers referenced in the main text. Data from this study are listed in Table 4-2 and recalculated unpublished data from Cardoso (1980; xenolith and mineral inclusions) and Hanrahan et al. (2003; xenolith) are shown with open symbols. Data define a 38 $mW \cdot m^{-2}$ model palaeogeotherm for the Koffiefontein pipe. Eclogite and Al-in-olivine PT data are calculated as a projection onto this geotherm. Temperature range determined by Ni-in-garnet thermometry (Canil, 1999) is indicated by the orange shaded region. Calculated palaeogeotherms for Koffiefontein xenolith and diamond data using FITPLOT (Mather et al., 2011; McKenzie and Bickle, 1988) are shown by coloured, dashed lines, which closely follow the model 38 $mW \cdot m^{-2}$ geotherm. A close-up of the fit is shown as an inset. The graphite-diamond transition of Day (2012) and mantle adiabat are indicated. The inset in the bottom left highlights the deviation of the Hasterok and Chapman (solid lines; 2011) from the Pollack and Chapman (dashed line; 1977) model geotherms for 36, 38, 40, and 42 $mW \cdot m^{-2}$. Inset graphs have the same axes and values as the larger graph. A histogram of all calculated pressure-temperature points is shown to the right and indicates a bimodal distribution, with the majority of diamonds being sampled at ~6 GPa.

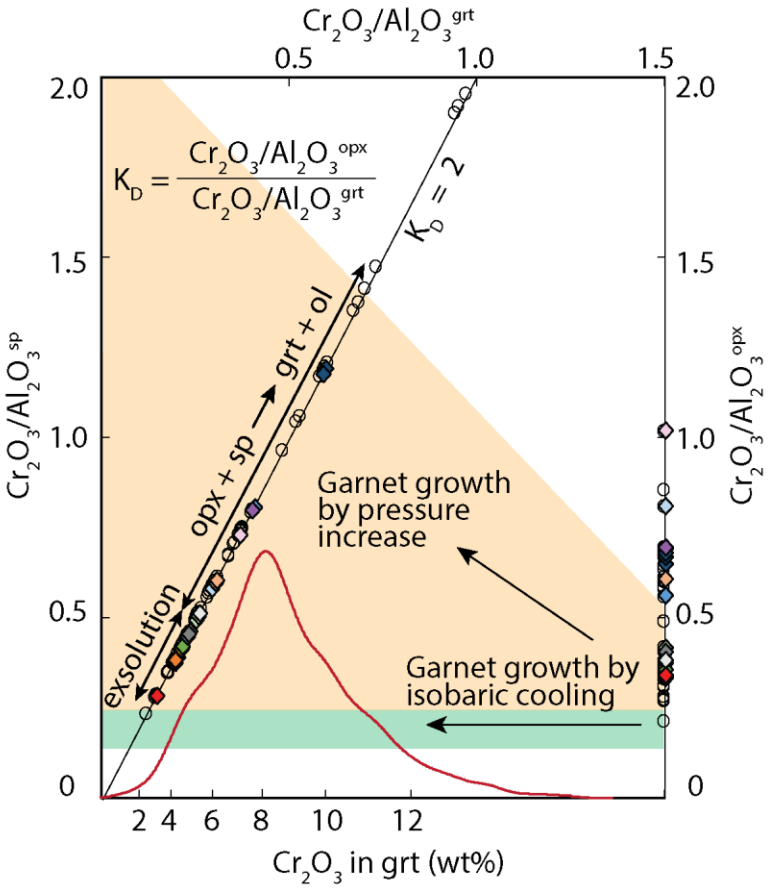

Figure 4-6: Cr_2O_3-Al_2O_3 ratios of experimental spinel and orthopyroxene compositions of Brey and Shu, (2018). Regions on the diagram distinguish garnet growth from pressure increase (reaction of orthopyroxene + garnet; line of K_D =2) or isobaric cooling (exsolution; indicated by horizontal arrow). Garnet and orthopyroxene compositions for the Koffiefontein suite (this study) are projected onto the K_D = 2 line, and right y-axis, respectively. Coexisting garnet and orthopyroxene have the same colour symbol and the remaining garnet and orthopyroxene inclusions are shown in open symbols. A kernel density plot (red line) is show for all garnet inclusions. $Cr_2O_3/Al_2O_3^{opx}$ data is plotted on the right and a value of 0.13 represents the transition from spinel- to garnet-facies.

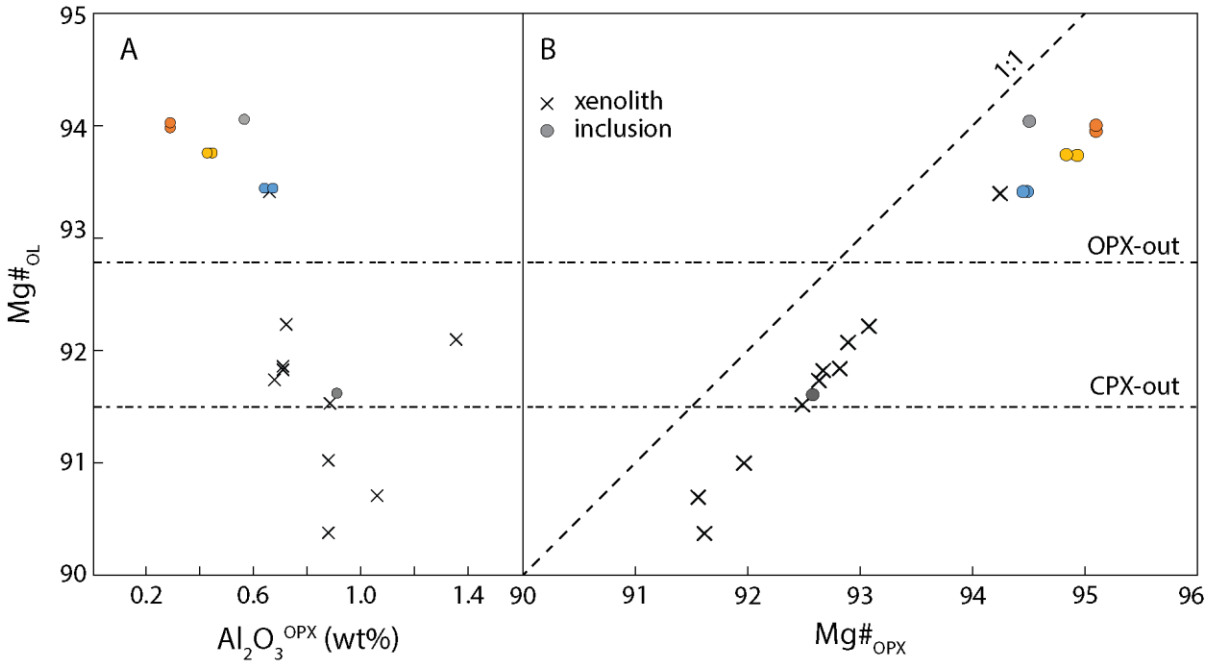

Figure 4-7: Mg# of olivine versus (A) Mg# of orthopyroxene and (B) Al_2O_3 in orthopyroxene of coexisting olivine-orthopyroxene pairs in xenoliths (Cardoso, 1980) and diamond (this study). Vertical dashed lines indicate the idealised clinopyroxene out (91.5) and orthopyroxene out (92.8) reactions, respectively from Bernstein et al. (2007; based on experiments at 3 GPa of Baker and Stolper, 1994). Colours refer to individual diamond samples.

Chapter 5. Metasomatism of the Kaapvaal Craton and the formation of goldschmidtite

5.1. Introduction

Diamonds are carriers of minerals from the lithospheric mantle underpinning cratons (Harris and Gurney, 1979; Helmstaedt et al., 2010; Meyer, 1987), the mantle transition zone (Kiseeva et al., 2013b; Pearson et al., 2014; Tschauner et al., 2018), and the lower mantle (Harte et al., 1999; Nestola et al., 2018; Palot et al., 2016; Tschauner et al., 2014). As a chemically inert and rigid host, diamond can preserve included minerals for billions of years, and thus provide a snapshot of ancient chemical conditions in cratonic keels or deep-mantle regions.

The Kaapvaal craton in South Africa is host to many diamondiferous kimberlites that have been intensively mined and studied since the 1970s (e.g., the International Kimberlite Conferences held since 1973). Large-scale mining, large inclusion-bearing diamonds, and the efforts of geochemists globally, have made it the most-studied craton from the perspective of diamond formation.

We report the first natural occurrence of (K,REE,Sr)(Nb,Cr)O_3, now named goldschmidtite (IMA No. 2018-034), included in a websteritic diamond from the Koffiefontein kimberlite, Kaapvaal craton, South Africa. The holotype specimen is deposited in the Royal Ontario Museum, accession number M58208. It is the fifth perovskite-structured mineral to occur in Earth's mantle, along with perovskite sensu stricto ($CaTiO_3$), bridgmanite (Harte et al., 1999; Tschauner et al., 2014), $CaSiO_3$-perovskite (Nestola et al., 2018), and K-REE-Cr-rich tausonite, which previously recorded the highest Nb- and K-content in a perovskite mineral-inclusion from diamond (Kopylova et al., 1997).

Goldschmidtite is the natural analogue of the well-known ferroelectric material $KNbO_3$, which has the perovskite structure type with orthorhombic symmetry at room temperature (coexisting with a metastable monoclinic phase: Lummen et al. (2017), and whose symmetry increases to cubic above ~400 °C (Skjærvø et al., 2018). Solid solution of $LaFeO_3$ in $KNbO_3$, at molar

amounts of 20 % or more, also has the effect of increasing the symmetry to cubic at room temperature (Kakimoto et al., 2003).

Endmember $KNbO_3$ was first synthesized by Joly (1877), as discussed by Holmquist (1897). Thomas F.W. Barth, a member of Victor Moritz Goldschmidt's research group, was the first to determine the crystal structure of perovskite, $CaTiO_3$ (Barth, 1925). In the following year, Goldschmidt and his group reported that $KNbO_3$ was effectively isostructural, and simultaneously introduced the famous tolerance factor for prediction of the perovskite structure type (Goldschmidt, 1926).

Goldschmidtite is named in honour of the eminent scientist Victor Moritz Goldschmidt (born Zürich, 27 January 1888; died Oslo, 20 March 1947). Goldschmidt made very wide-reaching contributions in geology, chemistry, mineralogy, crystallography, and petrology (Bastiansen, 1962; Kauffman, 1997; Mason, 1992; Suess, 1988; Tilley, 1948). He is widely recognized as the "founder of modern geochemistry" (Bastiansen, 1962; Kauffman, 1997), and as stated by Laves (1962): "The influences of V. M. Goldschmidt's work on the development of mineralogy and crystallography cannot be overestimated."

The name goldschmidtite was briefly used (Hobbs, 1899) for a supposed gold-silver telluride, Au_2AgTe_6, that was shown later to be sylvanite (Palache, 1900). Similarly, goldschmidtine was used (Peacock, 1939) for a supposed antimonide of silver, Ag_2Sb, that was shown subsequently to be stephanite (Peacock, 1940). Both of these names had been intended to honour the celebrated crystallographer Victor Mordechai Goldschmidt (born 10 February 10, 1853; died 8 May 1933).

Following the recently revised nomenclature for minerals of the perovskite supergroup (Mitchell et al., 2017), goldschmidtite is a member of the perovskite subgroup and is the potassium-analogue of isolueshite, $(Na,La)NbO_3$ (Chakhmouradian et al., 1997).

5.2. Occurrence

The 90.4 Ma Koffiefontein kimberlite pipe is located about 80 km SSE of Kimberley, South Africa and was emplaced in the Archean basement of the Kaapvaal Craton and overlying Phanerozoic sediments of the Karoo basin (Clement, 1982; Davis, 1978; Field et al., 2008; Naidoo et al., 2004). This diamondiferous kimberlite was discovered in 1870 (Field et al., 2008) and has been mined for diamonds intermittently.

The diamonds from Koffiefontein are dominantly peridotitic (determined from silicate inclusions: Harris and Gurney, 1979; Rickard et al., 1989). Goldschmidtite was found in a websteritic assemblage in association, but not in direct contact, with Cr-rich augite, and an intergrowth of chromite, Mg-silicate, and an unidentified K-Sr-REE-Nb-oxide. In this region of the diamond surface there was both green and brown radiation damage (Figure 5-1). The Cr-content (1.19 wt% Cr_2O_3) and Mg# (86) of the included augite suggests that the host diamond formed in websterite (Gurney et al., 1984). From single-clinopyroxene geothermobarometry (Nimis and Taylor, 2000), an equilibration pressure of 53 kbar (about 170 km depth) and temperature of formation of 1190 °C can be calculated.

5.3. Experimental details

The goldschmidtite inclusion was released from its host diamond by mechanical fracturing of the diamond with a steel diamond cracker. The released mineral was mounted in epoxy, roughly ground with corundum paper, and polished with 1 μm diamond suspension on a nylon cloth.

A Cameca SX100 electron microprobe at the University of Alberta was used to examine a polished and carbon-coated (25 nm thickness) epoxy mount of goldschmidtite. In addition to secondary-electron and back-scattered electron images, quantitative spot analyses were acquired using wavelength-dispersive spectrometry and Probe for EPMA software (Donovan et al., 2015). Nineteen elements were measured (Na, Mg, Al, Si, K, Ca, Ti, Cr, Fe, Sr, Zr, Nb, Ba, La, Ce, Nd, Pr, Sm, and Th) with the following conditions: 20 kV accelerating voltage, 30 nA probe current, and <1 μm beam diameter (5 μm was used for the standards). Total count times of 40 s were used for both peaks and backgrounds. The X-ray lines, diffraction crystals, and standards were: Na Kα, TAP (thallium hydrogen phthalate), albite; Mg Kα, TAP, pyrope; Al Kα, TAP, Gore

Mountain garnet; Si Kα, TAP, diopside; K Kα, PET (pentaerythritol), sanidine; Ca Kα, PET, diopside; Ti Kα, PET, $SrTiO_3$; Cr Kα, LIF, Cr_2O_3; Fe Kα, LIF (lithium fluoride), fayalite; Sr Lα, PET, $SrTiO_3$; Zr Lα, PET, zircon; Nb Lα, PET, niobium metal; Ba Lγ, PET, sanbornite; La Lα, LIF, $LaPO_4$; Ce Lα, LIF, $CePO_4$; Nd Lβ, LIF, $NdPO_4$; Pr Lβ, LIF, $PrPO_4$; Sm Lβ, LIF, $SmPO_4$; Th Mα, PET, ThO_2. The X-ray intensity data were reduced following Armstrong (1995) with the mass-absorption coefficients of Chantler et al. (2005). For elements found above the detection limits interference corrections (Donovan et al., 2011) were applied to: Al for interference by Th; Ti for interference by Ba; Cr for interference by La; Fe for interference by Th; Sr for interference by Cr; Ce for interference by Ba; and Th for interference by Cr. The following elements were not found above the limits of detection (as element in weight percent in parentheses): Na (0.01), Si (0.01), Zr (0.04), Pr (0.08), Nd (0.05), and Sm (0.05).

The crystal of goldschmidtite was extracted from the epoxy block and mounted on to a glass fibre with isocyanoacrylate adhesive. High-precision unit-cell parameters were determined by single-crystal X-ray diffraction by the eight-position centring method (King and Finger, 1979) on the Huber four-circle diffractometer at Northwestern University equipped with an SMC9300 controller and sealed-tube Mo Kα radiation source. A 360° phi-rotation image was collected on a MAR345 image plate detector. Full-profile peak fitting was performed with the software package SINGLE (Angel and Finger, 2011). In total, 46 reflections were cantered using omega scans (rocking curves) in their eight-equivalent positions with a point detector 40 cm from the crystal at 2θ angles between ±30°. Intensity data used to produce a crystallographic information file (.cif) were collected from -15 to +60 degrees 2θ also using the point detector on the four-circle diffraction system at Northwestern University.

Confocal Raman spectroscopy was carried out at Northwestern University using a custom-built system with an Olympus BX microscope with a Mitutoyo 100X objective. A Melles-Griot (Model 85-BLS-601) solid-state, diode-pumped laser with 200 mW output and wavelength of 458.5 nm was used as the excitation source. The output power was reduced with neutral density filters to achieve an ~8 mW focused beam of ~1-2 μm diameter at the sample surface. Unpolarized Raman spectra were collected in back-scatter geometry through a confocal aperture into a 0.5 m focal-length Andor Shamrock 303i spectrograph with 1200 lines-per-mm diffraction

grating. Spectra were collected on an Andor Newton DU970 CCD camera cooled to -90 °C with a thermoelectric cooler. Spectra were obtained for 10 s, averaged over 12 accumulations for a total of two minutes per spectrum.

5.4. Results and discussions

5.4.1. Physical and properties

Only a single grain of goldschmidtite, about 100 μm in maximum dimension, was recovered. The mineral is dark green with an adamantine lustre, non-fluorescent under longwave UV illumination, and is not cathodoluminescent. The small size of the solitary mineral grain precluded determination of its streak and hardness, and the tenacity, fracture, and cleavage were not observed. From the average chemical composition determined by EPMA and the unit cell parameters, the calculated density is 5.32(3) $g \cdot cm^{-3}$. The refractive index was calculated to be: n_{calc} 2.16(2), with the use of the Gladstone-Dale constants of Mandarino (1976), the calculated density, and the average chemical composition. Stacked optical images of goldschmidtite acquired with a Tagarno Prestige FHD digital microscope are shown in Figure 5-2.

5.4.2. Chemical composition

The average composition of goldschmidtite, for elements above detection, is given in Table 5-1; the iron content is reported as total Fe_2O_3 by analogy with latrappite, $(Ca,Na)(Nb,Ti,Fe)O_3$ (Mitchell et al., 1998). The empirical formula, calculated on the basis of three anions, is:

$$(K_{0.504}La_{0.150}Sr_{0.133}Ba_{0.092}Ce_{0.078}Ca_{0.002}Th_{0.001})_{\Sigma 0.960}$$
$$(Nb_{0.695}Cr_{0.192}Fe_{0.051}Al_{0.014}Mg_{0.036}Ti_{0.011})_{\Sigma 0.999}O_3,$$

which can be simplified to: $(K,REE,Sr)(Nb,Cr)O_3$. The various elements were assigned to the two cation sites (Wyckoff positions 1b and 1a, respectively) in the aristotypic perovskite formula based on size considerations and following the IMA nomenclature (Mitchell et al., 2017). A back-scattered-electron image of goldschmidtite is shown in Figure 5-3.

5.4.3. Crystal structure

The method of eight-position centring on a Huber four-circle diffractometer was used to centre 46 reflections from ±30° 2θ, resulting in 368 total rocking curves. The diffraction spots can be

described as very sharp, with a full-width at half-maximum averaging 0.07° in the final omega scan. Unconstrained least-squares fitting to all 46 reflections gives unit-cell parameters: a = 3.98757(20) Å, b = 3.98751(22) Å, c = 3.98756(20) Å, α = 89.999(4)°, β = 89.997(4)°, and γ = 89.999(4)°, indicating that goldschmidtite is cubic. Cubic-constrained least squares refinement gives a = 3.98755(12) Å and V = 63.404(6) $Å^3$.

Single-crystal intensity data were collected in the range of -15 to +60 degrees 2θ, resulting in 753 total reflections in a sphere of reciprocal space from ±5 *h*, ±5 *k* and ±5 *l*, of which 33 are unique with a merging *R*-factor (R_{int}) of 0.0636. From the intensity data, the space group was determined to be $Pm\bar{3}m$ (No. 221 in the *International Tables for Crystallography*), being the only space group with zero observed symmetry violations. Although all atoms are on special positions in $Pm\bar{3}m$ (Figure 5-4), a refinement was carried out to produce anisotropic displacement parameters and a list of reflections and structure factors provided in the crystallographic information file (CIF), yielding a final *R*-factor of 0.0181. In addition, the powder diffraction pattern was calculated using PowderCell version 2.4 for Windows (Kraus and Nolze, 1996) for Cu$K\alpha_1$, 1.540598 Å, and is presented in Table 5-2. The atom assignments for the powder diffraction calculation were:

Wyckoff 1b – $(K_{0.504}La_{0.15}Sr_{0.133}Ba_{0.092}Ce_{0.078})_{\Sigma 0.957}$;
Wyckoff 1*a* $(Nb_{0.695}Cr_{0.201}Fe_{0.051}Mg_{0.038}Al_{0.014}Ti_{0.011})_{\Sigma 0.999}$;
Wyckoff 3d – O.

Figure 5-5 shows an unfiltered X-ray diffraction image taken with a MAR345 image plate, demonstrating sharp diffraction spots and the absence of twinning. Goldschmidtite is most similar to isolueshite, (Na,La,Ca)(Nb,Ti)O_3 (Krivovichev et al., 2000), which has the identical space group and similar cell dimensions (in the range 3.90-3.91 Å).

Although synthetic $KNbO_3$ is orthorhombic at room temperature, goldschmidtite is cubic. This may be a result of the cation occupancies: the A-site is only 50 % filled by K and the B-site is 70 % filled by Nb atoms. The balance is filled by smaller-sized cations (e.g., La on the A-site, Cr

on the B-site), which results in goldschmidtite adopting a cubic structure as shown for the analogous synthetic system by Kakimoto et al. (2003).

5.4.4. Raman spectrum

Goldschmidtite possesses cubic symmetry, space group $Pm\bar{3}m$, with A site (K, REE, Sr), B site (Nb, Cr), and O all lying on inversion centres with site symmetry O_h, O_h, and D_{4h}, respectively. Consequently, by selection rules, there are no Raman-active modes. As shown in Figure 5-6A, the as-measured (uncorrected) Raman spectrum of goldschmidtite exhibits many weak, broad bands from 100-700 cm^{-1} and a large peak at ~815 cm^{-1}, similar to a spectrum of natural perovskite in the RRUFF database (sample R050456) from Magnet Cove, Arkansas, USA, with composition $(Ca_{0.82}Fe_{0.09}Na_{0.07}Ce_{0.01}La_{0.01})(Ti_{0.95}Nb_{0.05})O_3$. In $CaTiO_3$ solid solutions with $Sr(Mg,Nb)O_3$ and $NdAlO_3$, a strong, broad Raman band at ~820 cm^{-1} has been attributed to partial and local ordering of multiple cations on the B site (Zheng et al., 2004, 2003), suggesting that the 815 cm^{-1} band in goldschmidtite and some $CaTiO_3$ perovskites results from non-random B-site ordering, characteristic of complex perovskites. The broad nature of the 815 cm^{-1} band in goldschmidtite suggests that ordering is short range and weak, which would therefore not be detectable in the single-crystal X-ray diffraction data.

In Figure 5-6, the Raman spectrum of goldschmidtite is also compared with natural tausonite from the type locality and synthetic, cubic $SrTiO_3$ from the RRUFF database (sample X090004). Since $SrTiO_3$ also has the $Pm\bar{3}m$ space group, no first-order Raman is expected and the observed bands are second-order features (Nilsen and Skinner, 1968; Schaufele and Weber, 1967). Second-order Stokes Raman scattering involves the addition or difference combination of phonons from different longitudinal-optical (LO), transverse-optical (TO), or transverse-acoustic (TA) modes (Nilsen and Skinner, 1968). In Table 5-3, the second-order Raman band positions and assignments in $SrTiO_3$ from Nilsen and Skinner (1968) are listed along with the observed bands in goldschmidite from a deconvolution of the baseline-corrected spectrum, shown in Figure 5-6B. Thus, most of the features in the measured Raman spectrum of goldschmidtite are either attributed to weak, local cation ordering or second-order Raman scattering.

5.5. Implications

Potassium and niobium are not common elements in the typical suite of mantle-derived minerals included in diamonds but indicate mantle metasomatism (Dawson, 1982; Erlank and Rickard, 1977). Several Nb-rich minerals were found in the heavy mineral concentrate from Jagersfontein and from a metasomatic vein in a peridotite from Bultfontein (both kimberlite pipes are in close proximity and age to the Koffiefontein pipe): Nb-rich perovskite (21-28 wt% Nb_2O_5), Nb-rich rutile (~13 wt% Nb_2O_5), Nb-rich titanite (11.9 wt% Nb_2O_5); and were believed to form by the interaction of metasomatic fluids with peridotite at 20 to 30 kbar and 900 to 1000 °C (Haggerty et al., 1983). The existence of goldschmidtite indicates that perovskite-structure oxides have the potential to be significant hosts for K and Nb in the mantle, along with other lithophile elements such as La and Ce, and high-field-strength elements such as Ti and Ta. However, the precipitation of a mineral with such high concentrations of LILE (K, Ba) and strongly incompatible HFSE (Sr, LREE, Nb) requires an extremely fractionated metasomatic fluid that is much more enriched in incompatible elements than has been observed for "normal" mantle metasomatism (Allègre et al., 1995; Hofmann, 1988). To stabilize such a phase would require that these incompatible elements become major components in the fractionating fluid. Thus, this would likely result from the last drops of an initially much larger volume of metasomatic melt or fluid.

The presence of edgarite, $FeNb_3S_6$, in an unusually reduced fenite (Barkov et al., 2000) has been interpreted recently to indicate that niobium may occur in the trivalent or tetravalent states in the mantle (Bindi and Martin, 2018). However, the occurrence of goldschmidtite in diamond suggests that niobium is more likely in the pentavalent state in the mantle, at least in diamond-forming environments.

Table 5-1: Electron microprobe analysis of goldschmidtite.

Constituent	wt%	Range (n=11)	Stand. dev.
Nb_2O_5	44.82	43.97 – 46.04	0.69
TiO_2	0.44	0.42 – 0.46	0.01
ThO_2	0.1	0 – 0.16	0.06
Al_2O_3	0.35	0.32 – 0.39	0.02
Cr_2O_3	7.07	6.80 – 7.15	0.11
La_2O_3	11.85	11.45 – 12.05	0.17
Ce_2O_3	6.18	6.02 – 6.29	0.08
Fe_2O_3	1.96	1.95 – 1.98	0.01
MgO	0.7	0.67 – 0.78	0.03
CaO	0.04	0.02 – 0.07	0.01
SrO	6.67	6.14 – 6.83	0.21
BaO	6.82	6.48 – 7.30	0.27
K_2O	11.53	11.16 – 11.67	0.14
Total	98.53	97.81 – 99.81	0.58

Table 5-2: Calculated powder diffraction data for goldschmidtite.

Relative intensity, I (%)	$d_{calc.}$ (Å)	hkl
0.61	3.9876	100
100.00	2.8197	110
6.89	2.3022	111
49.93	1.9938	200
0.22	1.7833	210
57.80	1.6279	211
35.82	1.4098	220
0.01	1.3292	300
0.05	1.3292	221
28.15	1.2610	310
2.11	1.2023	311
12.89	1.1511	222
0.02	1.1060	320
37.95	1.0657	321
7.30	0.9969	400
0.02	0.9671	410
0.02	0.9671	322
8.63	0.9399	330
17.25	0.9399	411
1.13	0.9148	331
29.88	0.8917	420
0.03	0.8702	421
20.86	0.8502	332
43.24	0.8140	422

Table 5-3: Raman spectral assignments for second-order modes.

Goldschmidtite (cm^{-1})	$SrTiO_3$ (cm^{-1})[a]	Assignments for $SrTiO_3$[a]
	81	TO_2-TA; TO_2-TO_1
125		
160		
240	251	2TA; $2TO_1$; TO_1+TA
320	308	TO_2+TA; TO_2+TO_1; TO_4-TO_2
	369	TO_4-TA; TO_4-TO_1; $2TO_2$
445		
465		
580		
	629	TO_4+TA; TO_4+TO_1
	684	$2TO_3$
715	727	TO_4+TO_2
750		
815		
850		
	1038	$2LO_2$; $2TO_4$
	1325	LO_4+LO_2
1590	1618	$2LO_4$

[a] Synthetic, pure $SrTiO_3$ (Nilsen and Skinner, 1968).

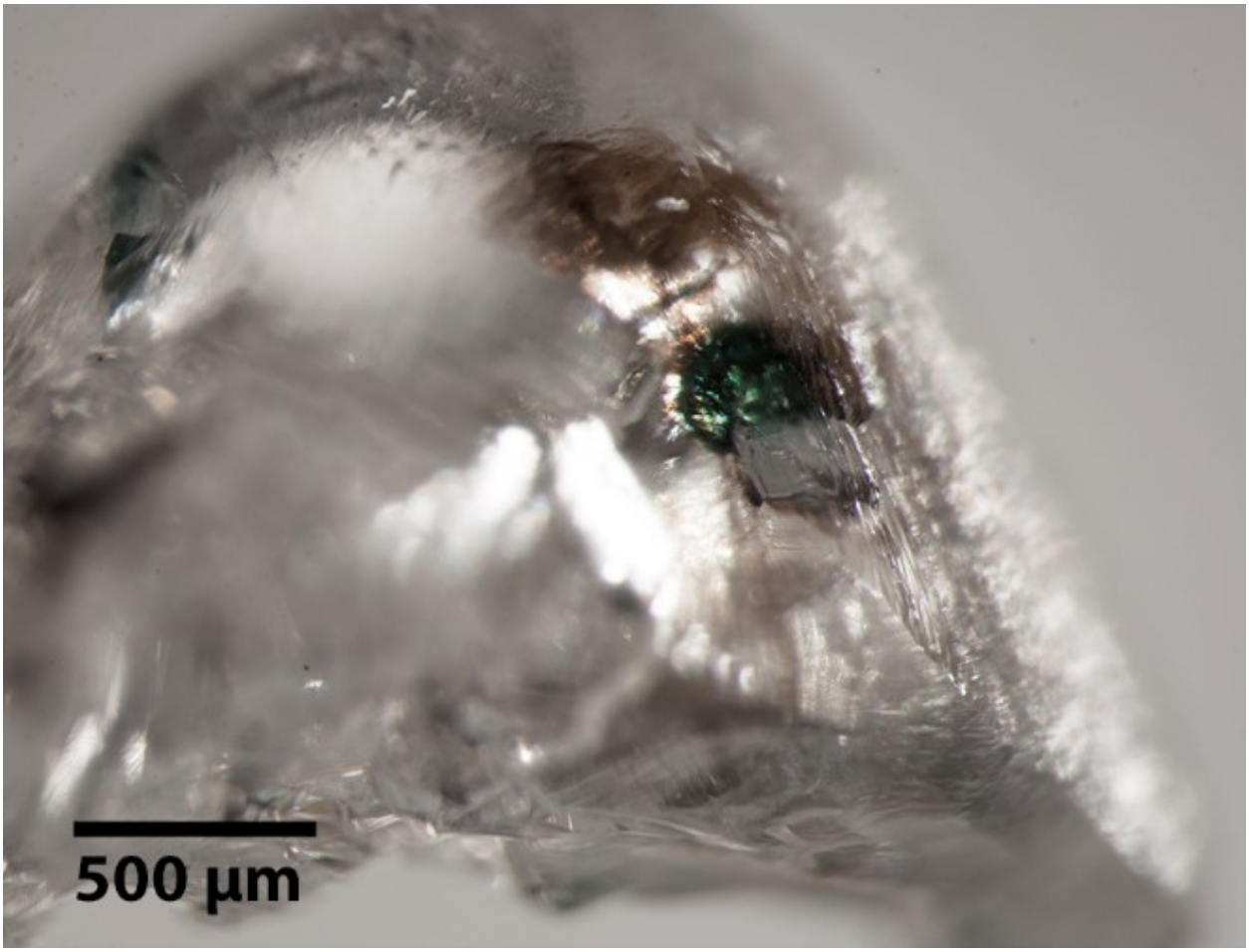

Figure 5-1: Broken and rounded dodecahedral diamond from Koffiefontein that hosted goldschmidtite (before breakage). Goldschmidtite is seen in green and radiation damage of the diamond can be seen by the brown regions.

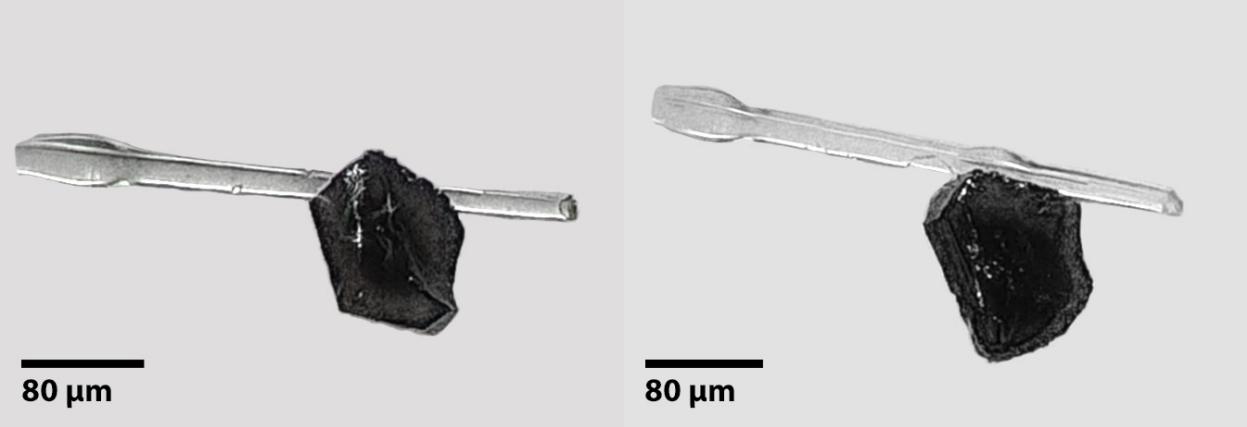

Figure 5-2: Two orientations of the crystal of goldschmidtite adhered to a glass fibre. Crystal shape has been affected by polishing. Background noise due to the digital-image stacking has been removed.

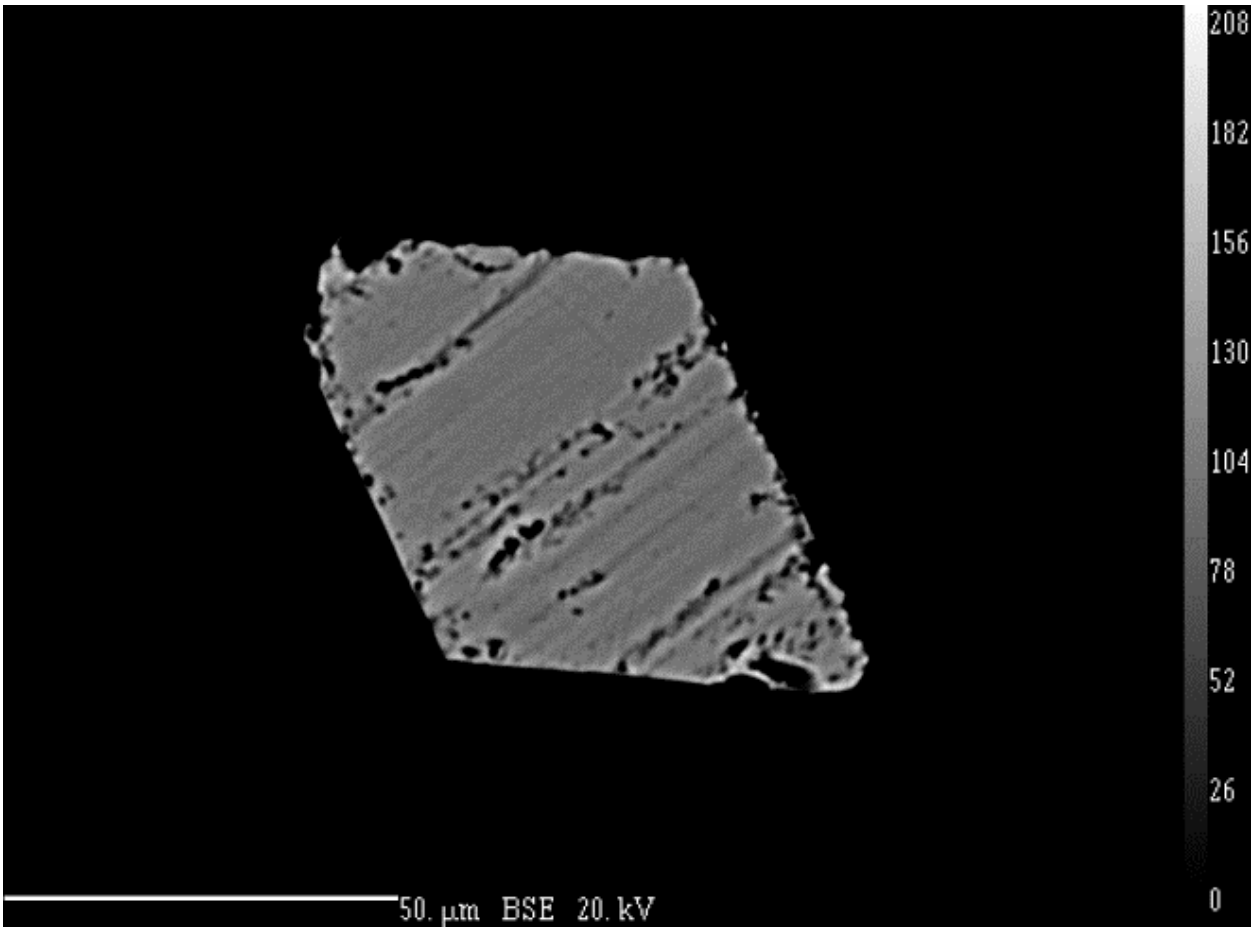

Figure 5-3: Back-scattered-electron image of goldschmidtite. The lamellar structure is probably a result of polishing.

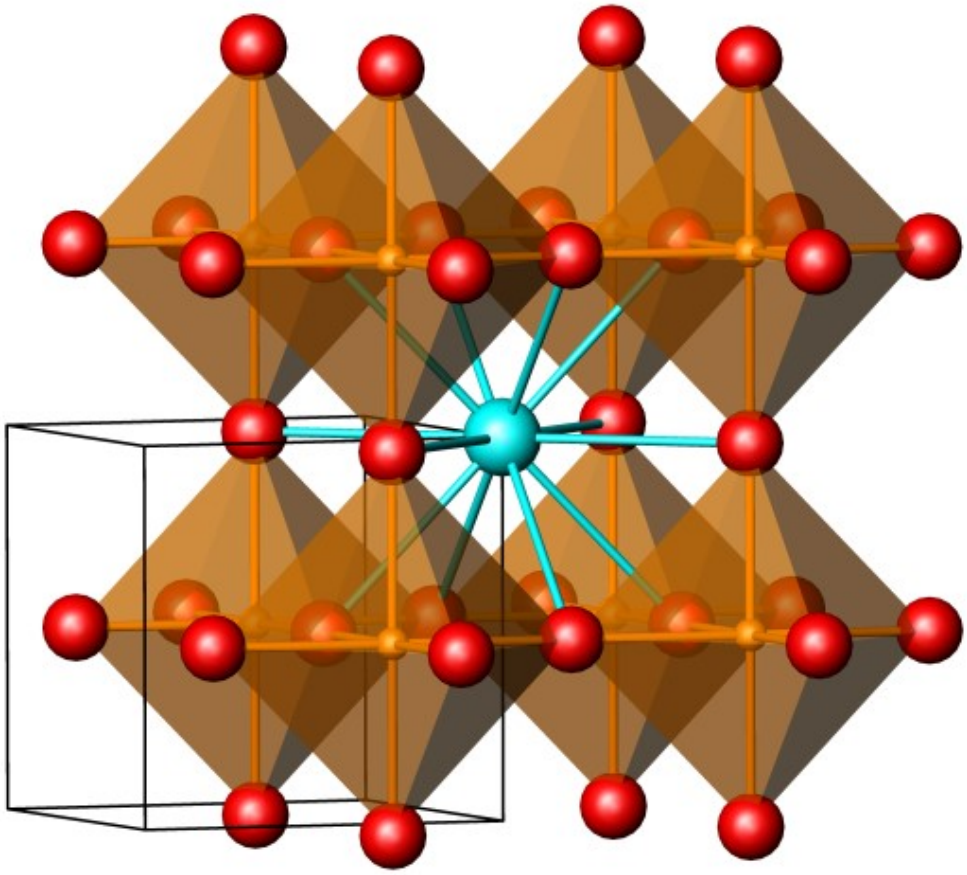

Figure 5-4: Clinographic view of the structure of goldschmidtite: Nb atoms are orange and in 6-fold coordination, K is pale blue and in 12-fold coordination, O atoms are red, and the unit cell is shown in black.

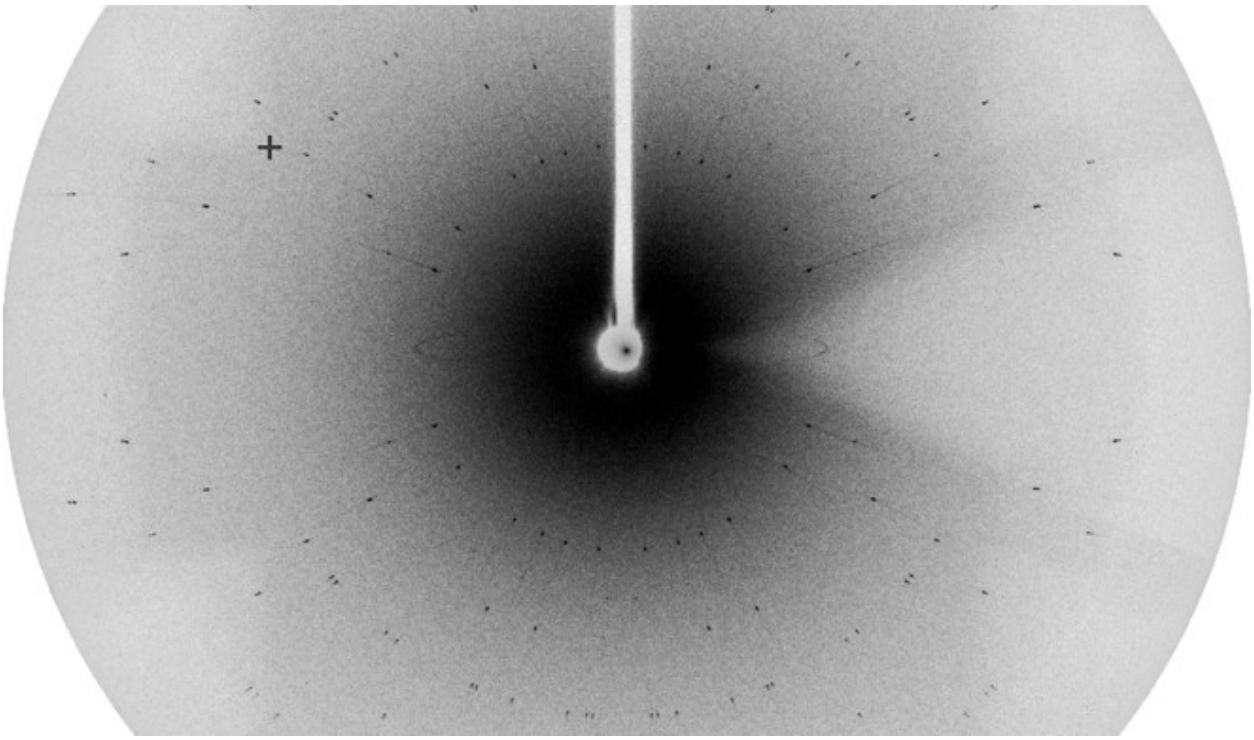

Figure 5-5:Unfiltered X-ray diffraction image (Mo *K*α radiation) taken with a MAR345 image plate showing sharp, single diffraction spots and the absence of twinning.

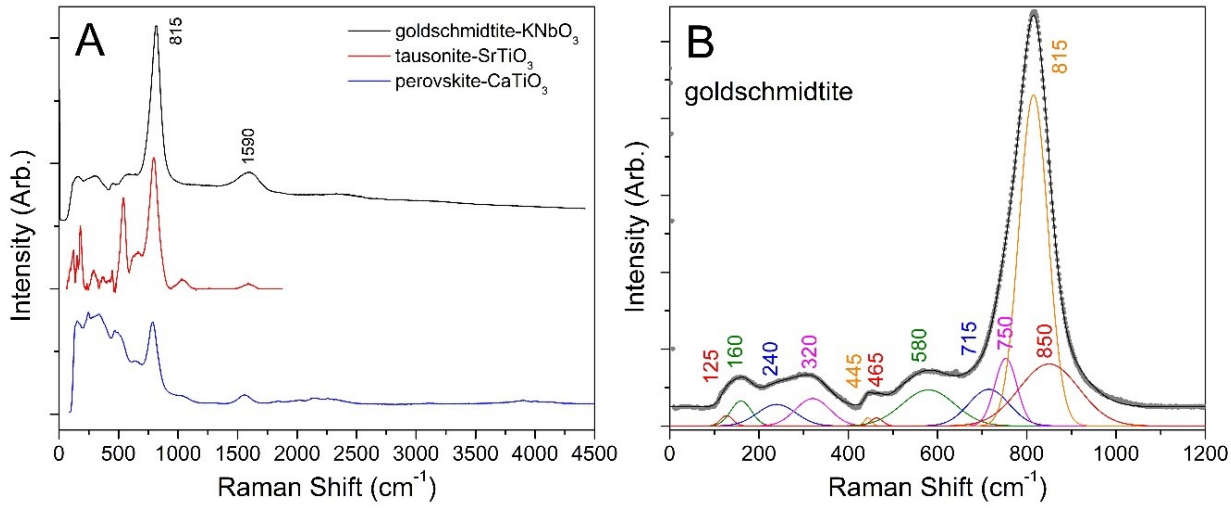

Figure 5-6: (A) Uncorrected Raman spectrum of goldschmidtite (black) using a 458.5 nm excitation laser, compared with natural tausonite (red curve) and perovskite (blue curve, RRUFF sample R050456). Spectra are offset for clarity. Raman features in $SrTiO_3$ are attributed to second-order Raman scattering (Nilsen and Skinner, 1968). The strong band at 815 cm^{-1} is likely due to weak, local ordering of different cations on the B site (Zheng et al., 2003). (B) Deconvolved and baseline-corrected Raman spectrum of goldschmidtite below 1200 cm^{-1}.

Chapter 6. Sublithospheric Diamonds from Beneath the Kaapvaal Craton

6.1. Introduction

The lower mantle is the largest reservoir of the solid Earth, contributing 56 % of its volume (Ballmer et al., 2017). Direct samples of the chemical and mineralogical composition of the lithospheric upper mantle (<250 km) come from xenoliths and mineral inclusions in diamonds that have been brought to the surface through kimberlite and lamproite volcanism (e.g., reviews by Harte (2010) and Harte and Hudson (2013); whereas information on the deeper upper mantle and lower mantle (LM) typically relies on a combination of geophysical data, high pressure-temperature experiments, and magmas such as ocean island basalts and kimberlites that are thought to sample the deeper convecting mantle (e.g., Boyd and England, 1960; Bullen, 1950). In rare cases, we have been provided with direct samples of the deep asthenosphere, transition zone, and lower mantle in the form of sublithospheric diamonds (e.g., Deines et al., 1991a; Harte et al., 1999; Moore and Gurney, 1985; Stachel et al., 2000a, 2000b).

The expected mineralogy of the sublithospheric mantle (see Figure 1-2) can be predicted based on bulk rock chemistry, which is determined from both theory (e.g., Stixrude and Lithgow-Bertelloni, 2007) and phase equilibria (e.g., Frost, 2008), with the variety of minerals expected depending on whether the bulk rock is metaperidotite – either pyrolitic mantle with a primitive major element composition or melting residues thereof – or subducted metabasalt (Irifune and Ringwood, 1993, 1987). In the lower regions of the upper mantle, throughout the lower mantle, and at the core-mantle boundary, minerals adopt increasingly compact structures to accommodate the increasingly high ambient pressures (Ringwood, 1958). Many of these minerals have been found included within sublithospheric diamonds, as either preserved high pressure polymorphs (e.g., Hutchison, 1997; Kaminsky and Wirth, 2017; Moore et al., 1986; Nestola et al., 2018; Pearson et al., 2014; Scott Smith et al., 1984; Stachel et al., 2000b) or their retrogressed equivalents (e.g., Brenker et al., 2002; Harris et al., 1997; Harte et al., 1999; Hutchison, 1997; Joswig et al., 1999; Stachel et al., 2000b). Sublithospheric diamonds can reside at the base of the subcontinental lithospheric mantle (SCLM) where they plasticly deform and some encapsulated minerals (e.g., bridgmanite) retrogress from high-pressure phases to those

commonly associated with upper mantle pressures (Cayzer et al., 2008; Joswig et al., 1999). Thus, for mineral inclusions in diamond, it is commonly the association of multiple mineral phases that confirms a lower mantle paragenesis (e.g., Brenker et al., 2005; Stachel et al., 2000b).

The upper and lower mantle domains are defined by significant increases in shear wave velocity (PREM; Dziewonski and Anderson, 1981) that can be related to specific structural or mineral changes as determined by high pressure experiments (Liu, 1976a). Although the mineralogy of the lower mantle is dominated by perovskite-structured minerals (denoted by -pvk) and the transition zone (TZ; 410–670 km) is the site of two major structural transformations, the boundary between them is a dynamic region that can encompass aspects of both. The transition of olivine to wadsleyite (410 km) and then to ringwoodite (rwd; 520 km) marks the top and middle of the transition zone, respectively (Irifune and Ringwood, 1987). The LM transition (660 km discontinuity) is defined by both the decomposition of ringwoodite to bridgmanite (brd; $MgSiO_3$-pvk) and ferropericlase (fPer) at 22.6 GPa and the instability of majoritic garnet (maj) at ~24 GPa, until its complete disappearance by 25 GPa (Irifune, 1994; Liu, 1976b). Beyond 98 GPa (D" layer), the perovskite structure is no longer stable and transforms into a denser, stacked SiO_6-octahedral sheet structure (Murakami et al., 2004). Detailed, high pressure and temperature experiments on pyrolitic bulk chemistry show that the stable mineral assemblage within the lower mantle is dominantly bridgmanite, just under 10 vol% ferropericlase, ~5 vol% $CaSiO_3$-pvk (CaSipvk Irifune and Ringwood, 1987); but based on seismic models instead, the abundance of ferropericlase decreases to 5 vol% with trace amounts of $CaSiO_3$-pvk (Murakami et al., 2012, 2004).

Sublithospheric mineral inclusions in diamonds are rare and their occurrence is dominated by a few key localities: The Juína area on the Amazon Craton (Brazil) provided the largest number of studied LM and TZ diamonds (Bulanova et al., 2010; Harte et al., 1999; Hayman et al., 2005; Hutchison, 1997; Walter et al., 2011, 2008). Kankan, on the West Africa Craton, has a LM and TZ suite similar to the Brazilian diamonds albeit with higher Mg# ferropericlase (Stachel et al., 2002, 2000a, 2000b). Some of these sublithospheric inclusions are Ca-rich and Fe-poor, providing evidence for carbonated fluids at depth (Brenker et al., 2007; Thomson et al., 2016) or

have compositions indicative of deeply subducted oceanic crust (Stachel et al., 2000b; Walter et al., 2011). A less common, but nevertheless significant occurrence of superdeep diamonds occurs in the Lac de Gras area of the Slave Craton, most prominently at DO27 (Tli Kwi Cho kimberlite complex; Davies et al., 1999) and at two mined localities that were the subject of detailed inclusion studies (Panda, Tappert et al., 2005b; A154, Donnelly et al., 2007). Kimberlites bearing an appreciable abundance of sublithospheric diamonds on other cratons are sparse, with Jagersfontein and Monastery on the Kaapvaal Craton being notable because of a significant number of majorite-bearing diamonds (Deines et al., 1991a; Moore and Gurney, 1985; Tappert et al., 2005a). Despite the higher abundance of sublithospheric diamonds in the abovementioned deposits, the first recorded find of a diamond containing a mineral inclusion indicative of a possible sublithospheric origin – fPer + opx – was at the Koffiefontein mine, South Africa (Cardoso, 1980); however, it was only a few years later that such an assemblage was confirmed as having derived from the sublithospheric mantle (Scott Smith et al., 1984). Since the initial report of potential lower mantle inclusions at Koffiefontein, no systematic study has been conducted on its sublithospheric diamond suite.

Mineral inclusions in asthenospheric and TZ diamonds clearly show that the source of the inclusions are subducted slabs – or its interaction with the ambient mantle – that have sunk into the TZ and possibly even the upper LM. With the known existence of metaperidotitic LM inclusions in Koffiefontein diamonds, my goal is to constrain the source of these LM diamonds in more detail and to examine a potential link to subduction processes. Here we present a detailed study of three sublithospheric diamonds and their inclusions found in a suite of ~200 diamonds selected from Koffiefontein. The mineral inclusions are analysed for major elements and oxygen isotopes, and the host diamonds are analysed for carbon and nitrogen isotopes and nitrogen concentration and aggregation.

6.2. Results

6.2.1. Diamond morphology

Three diamonds from Koffiefontein contained mineral inclusions that were deemed to have come from either the TZ, LM, or the boundary zone between. Diamond 21/01 (Figure 6-1 and Table 6-1) has an octahedral shape with shield-shaped lamellae and negative, flat-bottomed trigons,

and edges that are rounded, indicating resorption. There are no visible deformation lines on the diamond surface (e.g. striations), but the diamond is light brown, a colour that is usually related to plastic deformation (Harris, 1987). Diamond 23/01 is a light brown octahedral twin with shield-shaped lamella and hexagons present (Table 6-1). Resorption is minor on one side with rounding of the octahedral edges while the other side is well rounded, leaving the diamond with a pseudohemimorphic shape (Figure 6-1). Plastic deformation is present in the form of coarse lamination lines in one direction. Diamond 25/01 is a dark brown, irregularly shaped, twinned diamond (Figure 6-1). One side is resorbed and covered with fine elongated hillocks, while the parallel side is broken with slight rounding of the broken edges (Table 6-1). Plastic deformation is visible as striations in two directions.

6.2.2. Diamond nitrogen concentration and aggregation by FTIR

Diamond 25/01 is Type II, with nitrogen concentration ([N]) below detection, diamonds 21/01 and 23/01 have minor amounts of nitrogen ([N] = 8 and 12 at.ppm, respectively) and all the nitrogen is fully aggregated in the B-centre.

6.2.3. Cathodoluminescence and $\delta^{13}C$-$\delta^{15}N$-[N] by SIMS

The cathodoluminescence (CL) images of the sublithospheric diamonds along with their $\delta^{13}C$-$\delta^{15}N$-[N] systematics are shown in Figure 6-1. In the CL image, two different growth regions are visible through a contrast in brightness. CL images of diamonds 21/01, 23/01, and 25/01 show faint streaks in two directions that indicate deformation lines (DeVries, 1975). The $\delta^{13}C$ values of all sublithospheric diamonds range from -3.4 to -6.2 ‰ and are within the canonical mantle range of -5 ±2 ‰ (Cartigny, 2005). The within diamond $\delta^{13}C$ range does not exceed 1.5 ‰. For all diamonds, the nitrogen concentration obtained by SIMS is generally low (<10 at.ppm) except for one spot on diamond 23/01 and two spots on diamond 25/01. In the CL image (Figure 6-1), a distinct contrast in brightness along a sharp boundary in diamond 23/01 indicates two different growth stages. The brightest portion of the diamond corresponds to the highest [N] at 78 at.ppm and the remaining three spots have [N] <4 at.ppm. For diamond 25/01, the region with high nitrogen does not display a brighter CL response, suggesting that the increased luminescence must be caused by other defects. Where possible, $\delta^{15}N$ values were determined for the two "nitrogen-rich" spots in diamond 23/01 and 25/01, which are -14.1 and -14.8 ‰, respectively.

These N-rich regions occur towards the centre of the diamond (Figure 6-1) and thus are not expected to be caused by lithospheric overgrowth.

6.2.4. Metaperidotitic mineral assemblages

Diamond with ferropericlase and retrograde minerals

Four discrete inclusions were liberated from diamond 21/01 and identified by either EPMA and/or Raman spectroscopy (Table 6-2). Two of the inclusions were identified as ferropericlase (A, C) and their Raman spectrum has two broad peaks at ~900 and ~1200 cm^{-1} (Figure 6-2). The two ferropericlase inclusions have Mg# of 88.2 and 88.5 and plot within the range of other Koffiefontein ferropericlase inclusions and those from the literature (Figure 6-3). The remaining two inclusions, B and D, were not Raman active, but were identified as Mg-Fe-silicates by EPMA with low oxide totals (Table 6-3). Inclusion 21/01B is polycrystalline and EPMA totals are consistent throughout the mineral and average (wt%): SiO_2 50.3; MgO 17.7; FeO 6.82; Al_2O_3 2.76. The deficit in the analytical total of ~20 wt% is most likely H_2O because carbonate minerals can be strongly Raman active at ~150 cm^{-1}, which was not seen. The 20 wt% H_2O and Mg:Si ratio of 0.5 is compositionally similar to the water-rich DHMS phase D (Frost, 1999), however additional crystal structure data are required to make this assessment. Inclusion 21/01D has separated into two domains: one Si-rich and the other a Ca-Mg-Fe-silicate (oxide total ~95 wt%). The higher oxide totals (>90 wt%) suggest either limited or no H_2O is present in these phases. The Ca-Mg-Fe-silicate is with within the major element range – albeit slightly Al-deficient – of TZ pyroxenes from Juina area, Brazil (specifically BZ218B of Hutchison, 1997). Because the host diamond had no visible fractures, these silicate inclusions are assumed to be recrystallisation products of primary minerals; however, the lack of structural data and Raman determination cannot clarify either the identification of these minerals or their origin any further.

Diamonds with ferropericlase + orthopyroxene

One inclusion in diamond 23/01 was determined by Raman spectroscopy to be enstatite (23/01A), while the remaining six inclusions were ferropericlase (B, C, D, E, F, G; Table 6-2). The enstatite had a Mg# of 95.1 and low concentrations of Al_2O_3 (1.67 wt%) and Cr_2O_3 (0.37 wt%). Three ferropericlase inclusions were analysed and had similar Mg#, ranging from 82.7 to 83.2 (Table 6-3). The enstatite chemistry is within the range of compositions suggested in previous literature to represent retrogressed bridgmanite (Stachel et al., 2000b) and the

ferropericlase inclusions plot towards slightly more Fe-rich chemistry compared to the other Koffiefontein ferropericlase inclusions (Figure 6-3).

From diamond 25/01, 14 mineral inclusions were liberated: three were enstatite (D, E, J), nine were ferropericlase (A, B, C, D, F, I, K, L, M), one magnesite (G), and one (H) a MgFe-silicate with low oxide totals (82-91 wt%). The ferropericlase inclusions are similar to those of diamond 21/01, with Mg# ranging from 86.6 to 88.0. The enstatite chemistry is similar to diamond 23/01 with an Mg# of 95.0-95.1. Inclusion 25/01G was determined to be magnesite based on a low oxide total of 51.4 wt% and MgO of 40.9 wt%. Magnesite, with a minor silicate component, was found to rim ferropericlase inclusion 25/01M. A MgFe-silicate (25/01H) with low oxide totals (82.6-91.1 wt%) was present. Its mineralogy was not determined as it is not Raman active. EPMA analysis reveals that it is heterogenous in composition, with SiO_2-rich (35.5 wt%), Cr_2O_3-rich (1.93 wt%) and Al_2O_3-rich regions (3.75 wt%). MgO and FeO show substantial compositional variation, from 32.3-69.7 wt% and 6.43-18.8 wt%, respectively (Table 6-3).

Three enstatite inclusions were sufficiently large enough to enable $\delta^{18}O$ determination. Enstatite inclusion 23/01A had a $\delta^{18}O_{avg}$ of 5.8 ‰ from 5 spots that ranged between 5.7 to 5.8 ±0.25 ‰ (2 σ). Enstatite inclusions from 25/01 had a $\delta^{18}O_{avg}$ of 5.5 ‰ (inclusion D, 3 analysis points), 5.7 ‰ (inclusion E, 3 analysis points), and 5.4 ‰ (inclusion J, one analysis). The combined $\delta^{18}O_{avg}$ of all analytical spots for diamond 25/01 is 5.6 ‰. Analyses are shown in Figure 6-4.

6.3. Discussion

At the TZ-LM boundary (~23 GPa), the likely bulk composition of the Earth's mantle means that diamonds can potentially trap an assemblage of brd + fPer + CaSipvk + maj + rwd, where ringwoodite is metastable (Irifune and Ringwood, 1987; Ishii et al., 2018a). At the top of the TZ, majoritic garnet becomes the dominant Ca-phase and makes up ~40 % of the mantle assemblage before $CaSiO_3$-pvk stabilises at ~18 GPa (Irifune, 1994). Crossing into the lower mantle, the decomposition of ringwoodite occurs rapidly over 0.15 GPa (at 23.1 GPa; Ito and Takahashi, 1989) whereas the decomposition of majoritic garnet occurs over a larger pressure range (2-3 GPa; Wood, 2000). Descending into lower mantle depths majorite becomes increasingly depleted in Ca through exsolution of $CaSiO_3$-pvk, and thus pyrope-rich majorite begins to dissolve into bridgmanite at 24 GPa, completely disappearing by 25 GPa (Irifune, 1994; Trønnes

and Frost, 2002; Wood, 2000). In a metabasaltic bulk composition, clinopyroxene is only fully incorporated into majoritic garnet in the mid TZ, where majorite makes up ~90% of the assemblage. Stishovite is stable (>9 GPa) throughout the TZ and LM but $CaSiO_3$-pvk only stabilises at the base of the TZ (~18 GPa; Irifune and Ringwood, 1987). In the LM, the high Al content of metabasalt increases the stability of majorite to greater pressures, up to 28 GPa (Irifune, 1994). Minor phases accommodating minor elements – e.g. Na, K – include $NaAlSiO_4$ with a calcium ferrite structure (Liu, 1977) and NAL (new aluminous phase; Gasparik et al., 2000).

6.3.1. Metaperidotitic lower mantle diamonds from Koffiefontein

The presence of ferropericlase alone does not necessarily signify a LM assemblage as its stability is not pressure but rather chemistry dependent (Brey et al., 2004; Thomson et al., 2016). Ferropericlase can form in the upper mantle where silica activity and oxygen fugacity is low (Stachel et al., 2000b). However, certain characteristics of the host diamonds – plastic deformation and associated brown colour, Type II – also are consistent with a superdeep origin, which makes a lower mantle origin the most likely explanation. In the present case, the best mineralogical evidence of a LM assemblage is coexisting fPer + brd; but bridgmanite is chemically similar to lithospheric orthopyroxene, thus also requiring further interrogation. If the bulk chemistry ratio of Mg+Ca+Fe:Si is above unity, ferropericlase occurs with bridgmanite (i.e. in a pyrolitic composition; Irifune, 1994); but below unity, bridgmanite is in equilibrium with stishovite (i.e. MORB composition; Hirose et al., 2005). Additionally, at $Mg\#_{brd}$ <~90, Fe-rich portions of bridgmanite decompose to Fe-rich ferropericlase (i.e. magnesiowüstite) and stishovite (Fei et al., 1996; Ringwood and Major, 1966).

Samples 23/01 and 25/01 from Koffiefontein contain separate inclusions of ferropericlase and orthopyroxene. Assuming that these separate inclusions are not disequilibrium assemblages, the orthopyroxene inclusions are interpreted as retrogressed bridgmanite because only in the lower mantle can $MgSiO_3$ (bridgmanite) coexist with ferropericlase (Liu, 1976b; Scott Smith et al., 1984). Other chemical indicators of retrogressed bridgmanite are high Al_2O_3 and low CaO and NiO contents compared to lithospheric orthopyroxene (Stachel et al., 2000b). The CaO and NiO ranges of Koffiefontein retrogressed bridgmanite are 0.03-0.05 wt% and below detection to

0.03 wt%, respectively. These values are lower than lithospheric orthopyroxene, which typically contain CaO of 0.05-0.71 wt% and NiO of 0.08-0.16 wt% when included in diamonds (see lithospheric opx analyses in Chapter 4). The Al_2O_3 content of these Koffiefontein retrogressed bridgmanites is 1.17-1.67 wt%, whereas Koffiefontein lithospheric orthopyroxene inclusions are, on average, much lower in Al_2O_3 (0.54 wt%; Chapter 4). Thus, inclusions 23/01A and 25/01D,E,J are assigned as retrogressed bridgmanite and confer LM status.

At lower mantle depths, Al preferentially substitutes into Mg- over Ca-bearing perovskite due to the smaller size of the Mg cation and so the substitution of Al into bridgmanite has been used as a qualitative measure of pressure in lower mantle assemblages (Liu et al., 2017). Although the exact method of Al substitution into bridgmanite is unclear, it can accommodate up to 25 mol% Al_2O_3 (Andrault, 2003). At pressures corresponding to the top of the LM, majoritic garnet – still stable and a major constituent of the mineralogy at ~15 % – is in equilibrium with bridgmanite, ferropericlase, and $CaSiO_3$-pvk (Ringwood, 1991). At this boundary, Al is initially hosted only in majoritic garnet and then in both majoritic garnet and bridgmanite, resulting in bridgmanite with low Al_2O_3 contents and a strong negative correlation between Al_2O_3 and Mg# (Wood, 2000). The relatively low Al_2O_3 content of the Koffiefontein former bridgmanites (1.17-1.67 wt%) suggests formation at the top of the TZ-LM boundary, i.e. in equilibrium with majoritic garnet. High pressure experiments on pyrolitic starting compositions have produced bridgmanite with 3.61-3.91 wt% Al_2O_3 at 23-25 GPa in equilibrium with majoritic garnet, which increased to 4.69-4.94 wt% Al_2O_3 at pressures above 24.5 GPa, beyond majoritic garnet stability (Hirose, 2002; Irifune, 1994; Wood, 2000). In experiments, the lowest bridgmanite Al_2O_3 of 1.22 wt% for fertile compositions had $Mg\#_{brd}$ ≈93 and coexisting $Mg\#_{fPer}$ 86-87 (Wood, 2000); and although the Koffiefontein former bridgmanite has similar Al_2O_3 contents, it has a much higher Mg# for bridgmanite and ferropericlase compared to the pyrolitic TZ-LM boundary bridgmanite produced in experiments. The causes and significance of this will be discussed in Section 6.3.2.

The brd + fPer assemblage in diamond 23/01 plots in a similar compositional space to primitive peridotite composition in the experiments of Wood (2000), whereas assemblages in diamonds 25/01 and A262 have much higher $Mg\#_{fPer}$, 87-88, but similar $Mg\#_{brd}$ (Figure 6-5; Koffiefontein

literature LM inclusions A262, K30, K33, and K34 of Cardoso, 1980). Due to the chemical equivalence of the fPer + brd assemblage to ringwoodite, any fPer + brd ought to be co-linear with rwd in Mg-Fe-Si space (Figure 6-5; Frost and Langenhorst, 2002; Wood, 2000). Hypothetical ringwoodite co-linear with brd + fPer from diamonds 25/01 and A262 does not correspond to primitive, pyrolitic mantle. In this compositional space (Figure 6-5) ferropericlase from 21/01, K30, K33, and K34 plot in the same location as ferropericlase inclusions from other Koffiefontein brd + fPer diamonds 25/01 and A262.

The distribution co-efficient $D^{Fe/Mg}_{brd/fPer}$ increases with increasing depth due to the increased stability of Fe^{2+} in bridgmanite over ferropericlase (Andrault, 2001); however, no geobarometer exists to define an exact pressure but this relationship suggests that the ferropericlase in 21/01 came from deeper than 23/01, and possibly 25/01 and A262, albeit only slightly. Mineral partition experiments on Ni in high pressure mantle phases show that, in the lower mantle, ferropericlase hosts the Ni that is usually sequestered mostly in Mg-silicate phases in the upper mantle (Kesson and Fitz Gerald, 1991; Stachel et al., 2000b). The Koffiefontein $D^{Ni}_{fPer-brd}$ is ~50 for 23/01 and 130-170 for 25/01 and A262. This partitioning appears strongly dependent on bulk chemistry and mineralogy: for example, Kankan diamonds have $D^{Ni}_{fPer-ol}$ >10 and $D^{Ni}_{fPer-brd}$ >>100 (Stachel et al., 2000b), but the latter is much lower in experimental studies of pyrolite, $D^{Ni}_{fPer-brd}$ = 38 (Ishii et al., 2018b), and depleted peridotite, $D^{Ni}_{fPer-brd}$ = 6 (Kesson and Fitz Gerald, 1991). The similarity in major element chemistry, specifically NiO and Mg#, of the ferropericlase in sample 21/01 to the ferropericlase in the fPer + brg assemblages of 25/01 and A262 indicates that ferropericlase inclusions in diamond 21/01 likely were in equilibrium with bridgmanite and thus points to a LM inclusion origin.

6.3.2. Implications for the chemistry of Earth's lower mantle

Major elements

The LM constitutes ~50 % by mass of the Earth. Although geophysical interpretations of the bulk chemistry and mineralogy are widely used, direct samples are rare. Earth, formed from material in the solar nebula – compositionally similar to C1 chondrites – differentiated into a silicate mantle and a metallic core, but the exact proportion of elements entering the core remains unclear, especially for SiO_2. This has led to a debate centring on the chemical composition of the

LM, specifically its SiO_2 content, and implications for chemical layering between the upper and lower mantle (Ringwood, 1959). Pyrolite – a model major element composition of the primitive bulk mantle (Ringwood, 1962b) – is currently the best approximation to geophysical models encompassing the whole mantle (Irifune et al., 2010). In contrast, a chondritic composition for the lower mantle (Javoy et al., 2010) implies a chemically stratified mantle, with a LM that is Si-rich, leading to a perovskitic LM with brd >93 % (Murakami et al., 2012). The pyrolite and chondrite models also differ drastically in their predicted Mg:Si ratios, with ~1 for chondritic and 1.3 for pyrolitic. The uncertainty associated with geophysical interpretations of lower mantle composition cannot readily discriminate these two bulk composition models and recent studies suggests that the lower mantle is not as homogenous as once thought (Ballmer et al., 2017; Houser et al., 2020).

The major element chemistry of the lower mantle can be simplified to the Mg-Fe-Si system. As shown in Figure 6-6A and by the phase proportions of experimentally determined brd + fPer + maj for pyrolitic bulk compositions, majoritic garnet has the same Mg# as coexisting bridgmanite ($D^{Mg/Fe}_{maj\text{-}brd} \approx 1$; Hirose, 2002; Irifune, 1994; Ishii et al., 2018b; Wood, 2000). Thus, even for assemblages lacking majoritic garnet, bulk compositions must fall on the tie line between fPer + brd in Mg-Si-Fe space. Koffiefontein fPer + brd assemblages are plotted on Figure 6-6B with shaded regions for 23/01, 25/01, and A262. Whereas the tie lines for experimental fPer + brd assemblages (inset of Figure 6-6A) show overlap with pyrolitic/lherzolitic compositions (P and Lz), the tie lines for the Koffiefontein inclusions plot towards more depleted chemistries (Figure 6-6B). Closer inspection (inset Figure 6-6B) shows that the inclusion assemblage from diamond 23/01 is chemically between a lherzolitic and harzburgitic bulk composition, whereas the inclusion assemblages from diamonds 25/01 and A262 are compositionally similar to a harzburgite and dunite. If majoritic garnet coexisted with these assemblages, the $D^{Mg/Fe}_{maj\text{-}brd} \approx 1$ (as shown above) implies that it would have the same Mg# as the bridgmanite and thus would plot on the same tie line. The compositions of the Koffiefontein mineral inclusions in Figure 6-5 and Figure 6-6 compared to experimental pyrolitic starting compositions show that these mineral inclusions do not represent fertile mantle, but instead are similar to depleted peridotitic compositions, notably harzburgite and potentially dunite (Kesson and Fitz Gerald, 1991).

Many high-pressure experiments use either pyrolite or MORB as starting materials to emulate the mineralogy of either the lower mantle or the metabasaltic portion of a subducting slab, respectively. Experimental studies on harzburgite at a range of pressures from the base of the lithosphere to the LM – 12.9 to 27.4 GPa – provide detailed phase transitions and mineral chemistry for depleted lithologies (Ishii et al., 2019). For metaharzburgite, past ringwoodite stability (23.2 GPa), very little garnet remains (~1 %) and the coexisting bridgmanite has an Al_2O_3 content of 1.13 wt% (Ishii et al., 2019). The Koffiefontein former bridgmanite, which has an Al_2O_3 content of 1.17-1.67 wt%, is closer to this range than that of a fertile metaperidotite at 4.9 wt% (Ishii et al., 2018b). At higher pressures (27 GPa), majoritic garnet is no longer stable and all of the Al is taken up by bridgmanite, reaching a maximum of 1.39 wt% Al_2O_3, limited by the bulk Al_2O_3 content of the starting harzburgite. Additionally, these metaharzburgites have high $Mg\#_{fPer}$ of 86 and $Mg\#_{brd}$ of 95, which is significantly higher than bridgmanite ($Mg\#_{brd}$ 92-93) when coexisting with metastable ringwoodite at the TZ-LM boundary (Ishii et al., 2019). The Koffiefontein brd + fPer assemblage for 25/01 is high in Mg/Fe, with $Mg\#_{fPer}$ of 87-88 and $Mg\#_{brd}$ 95, compared to 23/01 with $Mg\#_{fPer}$ of 83 and $Mg\#_{brd}$ 95 (Table 6-3). The similarity of Al_2O_3 and Mg# in these bridgmanites produced by experiments on metaharzburgite is consistent with the Koffiefontein low-Al former bridgmanite originating from deeper than the TZ-LM boundary if the original bulk chemistry is a depleted peridotite: i.e. Al-content alone cannot be used to determine bridgmanite depth as bulk chemistry plays an important role. Thus, the Koffiefontein LM diamonds – indicated above to be derived from depleted peridotite – may instead come from any region below the TZ-LM boundary (~23 GPa) and above the post-perovskite D" discontinuity (>98 GPa; Murakami et al., 2004).

Seismology has revealed clear images of subducting oceanic slabs entering the LM (Van Der Hilst et al., 1997), defining high velocity anomalies in the mantle. Seismic heterogeneity observed in the subducting reservoir implies that it may consist of various lithologies, including depleted harzburgite (Houser et al., 2020). Hirose et al., (1999) has shown that subducting slabs only reach temperatures high enough for partial melting at the core-mantle boundary. Both basaltic oceanic crust and depleted peridotitic lithospheric mantle comprising the slab are likely transported to these depths, making them favourable hosts for diamond formation in the lower

mantle (Kesson and Fitz Gerald, 1991; Stachel et al., 2000b). The high Mg#, low Al_2O_3 of depleted peridotites matches the chemistry indicated by the former-brd + fPer assemblage recovered in the Koffiefontein lower mantle diamonds. Additionally, the high solidus of depleted harzburgite favours its survival via subduction into the lower mantle (Kesson and Ringwood, 1989b).

Oxygen isotopes

Oxygen isotopes ($\delta^{18}O$) of mineral inclusions in lithospheric diamonds provide insights into the provenance of their protoliths. Whereas peridotitic rocks un-altered by surface processes retain the $\delta^{18}O$ of the canonical mantle (+5.5 ±0.2 ‰; Mattey et al., 1994), portions of the oceanic crust that have experienced water-rock exchange during hydrothermal alteration have a wide range in $\delta^{18}O$ from +3 to +13 ‰, depending on their original position within the crust and the water-rock ratios and temperatures of alteration that they experienced (Gregory and Taylor, 1981). Shallow basaltic layers subjected to low-temperature seawater alteration have $\delta^{18}O$ values from +7 to +15 ‰ (e.g., pillow basalts); deeper gabbros, subjected to high-temperature seawater alteration, have $\delta^{18}O$ values from 0 to +6 ‰; and towards the base of the gabbro layer and within the ultramafics of the lowermost oceanic crust and peridotites of the suboceanic lithospheric mantle, the $\delta^{18}O$ values typically retain their mantle signature (Eiler, 2001).

The fractionation of $\delta^{18}O$ between upper mantle peridotitic phases is <1 ‰ (Lowry et al., 1999) and large deviations from the canonical mantle range could indicate interaction with an exotic melt or fluid, at high fluid-rock ratios (Deines et al., 1991b). Analyses of mantle-derived minerals indicate, however, that small volumes of fluid cannot significantly change their oxygen isotopic composition because the mantle is an immense reservoir of oxygen that is not readily changed: mantle xenolith assemblages retain mantle $\delta^{18}O$ values even after potentially large-scale metasomatic Si-enrichment (Jacob et al., 2009; Regier et al., 2018), LREE-enrichment (Riches et al., 2016), and interaction with diamond forming fluids (Lowry et al., 1999). This resistance against overprint, however could also be attributed to the mantle-like $\delta^{18}O$ of the interacting fluid (Jacob et al., 2009) or the fact that fluids passing through the mantle with exotic $\delta^{18}O$ will be rapidly equilibrated to mantle values if flow is by percolation. One exception is interaction with fluids produced from hydrothermally altered minerals (e.g., altered oceanic crust

or serpentinites; Li et al., 2019; Taylor et al., 2005). Thus, it is expected that mineral inclusions within diamond – even those from sublithospheric depths – retain their $\delta^{18}O$ signature on their protoliths at lower pressures: i.e. when oceanic lithosphere formation and alteration occurred (Ickert et al., 2015).

Of the minerals included in sublithospheric diamonds, asthenospheric and TZ majoritic garnets have a range in $\delta^{18}O$ from +4.7 to +11.8 ‰ (Figure 6-4; Burnham et al., 2015; Ickert et al., 2015; Regier et al., 2020), likely as a result of the wide range in $\delta^{18}O$ in subducting altered oceanic crust; additionally, metabasaltic TZ to LM inclusions from Brazil have $\delta^{18}O$ >+8 ‰ (coesite and $CaSiO_3$ in Figure 6-4; Burnham et al., 2015). Globally, within the depleted lithospheric mantle, olivine and orthopyroxene have tightly constrained $\delta^{18}O$ medians of 5.26 ±0.22 ‰ and 5.74 ±0.27 ‰, respectively (Regier et al., 2018). The Koffiefontein former bridgmanites in samples 23/01 and 25/01 have $\delta^{18}O_{avg}$ of +5.6 ‰, within the mantle range and similar to other retrogressed bridgmanites recently reported from Kankan (Regier et al., 2020). This implies an origin in a mantle environment that was not affected by alteration processes near Earth's surface but does not permit us to further distinguish between diamond formation in primitive lower mantle substrates or in depleted hosts of harzburgitic bulk composition related to subduction of depleted sub-oceanic lithospheric mantle.

6.3.3. Diamond formation and the source of the fluids they precipitate from

Carbon and nitrogen isotopes

Carbon and nitrogen isotopes can provide insights into the formation of diamond; however, the concentration of nitrogen in asthenospheric and TZ diamonds is generally low (<100 ppm) and generally below detection – i.e. Type II – for LM diamonds (Davies et al., 1999; Harte and Harris, 1994; Hutchinson et al., 1999; Stachel et al., 2002). Metaperidotitic diamonds have mantle-like $\delta^{13}C$ signatures, between -8 ‰ and -2 ‰, but metabasaltic TZ and LM diamonds have a much wider $\delta^{13}C$ range of -25 ‰ to ~0 ‰ (Cartigny et al., 2014). In lithospheric diamonds, the observed highly ^{13}C-depleted signature has been attributed to recycled surficial carbon (Sobolev and Sobolev, 1980); however, in the TZ and LM where reducing conditions prevail, this signature could also be attributed to diamond formation from iron carbides (Jacob et al., 2004; Mikhail et al., 2014a).

The three studied sublithospheric Koffiefontein diamonds have $\delta^{13}C$ values (-3.4 to -6.2 ‰; multiple spots per diamond) within the canonical mantle range of -5 ±2 ‰ (Cartigny, 2005), and the total within-diamond variability in $\delta^{13}C$ is 0.3 to 1.5 ‰ (Figure 6-7; analyses with no [N] plot on y-axis). This is comparable to LM diamonds from worldwide locations, which show a strongly mantle-like $\delta^{13}C$ signature (Figure 6-7; Cartigny et al., 2014). Diamonds – lithospheric and sublithospheric – with $\delta^{13}C$ values below this range, <-7 ‰ and down to -25 ‰, have been thought to indicate kerogenous carbon input from sediment (e.g., Kirkley et al., 1991; Milledge et al., 1983); and values greater than -3 ‰ up to 0 ‰ are thought to indicate normal biogenic carbonate sediment input, transported along with the subducted oceanic slab (e.g., Kirkley et al., 1991). However, homogenised subducted slabs can produce $\delta^{13}C$ fluid ranges within the mantle range of -5 ± 2 ‰ (Figure 6-7; Shilobreeva et al., 2011) while at the same time, carbonate within altered igneous oceanic crust can have $\delta^{13}C$ as low as -25 ‰ (Li et al., 2019). Alternatively, Rayleigh isotope fractionation during diamond formation can produce variations in $\delta^{13}C$ (Deines, 1980). For example, based on a $\Delta^{13}C_{diam\text{-}CH4}$ = 0.81 at 1300 °C, a -1.5 ‰ variation is achieved during precipitation of ~75% of the CH_4 in the fluid as diamond. Elevated temperatures, such as experienced in the ambient LM, reduce this fractionation factor to 0.48 ‰ at 1600 °C (calculated using β values compiled by Tom Chacko for CH_4 of Richet et al., 1977), though fractionation is unlikely to generate the relatively common ^{13}C-depleted values of -10 to -20 ‰ in TZ diamonds.

On the CL images (Figure 6-1) of the Koffiefontein sublithospheric diamonds, the outer edge of the diamond (red line) and the analysis points (yellow dot) are indicated. The core to rim variation on diamonds 23/01 and 25/01 indicates a decrease in $\delta^{13}C$ values (Figure 6-1). A decrease in $\delta^{13}C$ values occurs when diamonds grow from a reduced fluid, likely CH_4, in one stage; but this "trend" could also occur due to discrete pulses of COH fluid with different $\delta^{13}C$ values. During diamond precipitation from an oxidising fluid/melt, e.g., a carbonate-bearing fluid, ($\Delta^{13}C_{diam\text{-}carbonate}$ = -1.69 at 1300 °C) a +1.5 ‰ variation is achieved during precipitation of ~60% of the $MgCO_3$ in the fluid as diamond (calculated using β values compiled by Tom Chacko for magnesite from Schauble et al., 2006).

Due to the reduced nature of the LM, diamond formation via the sequestration of carbon from ambient lower mantle carbides has been proposed for the Kankan LM diamonds (Regier et al., 2020). Additionally, some LM diamonds have indeed encapsulated iron-carbide and -nitride inclusions (Kaminsky and Wirth, 2017). Diamonds with mineral inclusions of carbide can have very ^{13}C-depleted signatures because $\Delta^{13}C_{diam-fluid}$ values are positive for reduced fluids (CH_4-bearing 0.8 ‰ at 1300 °C; Richet et al., 1977) and, ever more so, in iron carbide systems (6.8 ‰ at 1300 °C; Horita and Polyakov, 2015). For example, Jagersfontein diamonds with iron carbide inclusions record $\delta^{13}C$ of -17.3 to -12.7 ‰ (Mikhail et al., 2014a). However, the Koffiefontein LM diamonds do not show significant ^{13}C-depletion associated with formation from carbides.

The low abundance of nitrogen in diamond has been attributed to nitrogen's siderophile nature at LM conditions, preferentially partitioning into metal melts ($D^{N}_{metal-silicate}$ = 14 at fO_2[IW] = -1.4; Dalou et al., 2019; Palyanov et al., 2013; Smith and Kopylova, 2014; Speelmanns et al., 2019). Where nitrogen is present above the detection limit in sublithospheric diamonds, $\delta^{15}N$ ranges from +6 ‰ down to -25 ‰ (Cartigny et al., 1997; Palot et al., 2014, 2012). For $\delta^{15}N$, values >-2 ‰ are attributed to nitrogen recycling by subduction (Haendel et al., 1986); values between -8 and -2 ‰ being consistent with ambient mantle or the incorporation of subducted altered oceanic crust (Bebout and Fogel, 1992); but for $\delta^{15}N$ values <-8 ‰ the interpretations are less obvious.

A complexity with diamond-forming fluids is the source and speciation of nitrogen. The two fPer + former-brd assemblage diamonds (23/01, 25/01) have [N] <100 at.ppm and $\delta^{15}N$ of -14.1 ‰ and -14.8 ‰, respectively. The origin of ^{15}N-depleted signatures in some lithospheric diamonds has been explained through formation in mantle substrates with remnant primordial heterogeneity (Deines, 1980; Deines et al., 1987; Javoy et al., 1986, 1984). Javoy et al. (1986) suggested that ^{15}N-depleted diamonds involved an additional ^{15}N-depleted component in the form of fluids of "deeper origin", derived from un-degassed mantle with an enstatite chondrite-like, strongly ^{15}N-depleted signature. Chondrites have a large range in $\delta^{15}N$, with enstatite chondrites having very low values, down to -40 ‰ (Javoy et al., 1986; Sephton et al., 2003). Recent models of the nitrogen isotope composition of Earth's mantle from 4.5 Ga to the present, however, show that the mantle likely had a constant $\delta^{15}N$ of about -6 ‰ (Labidi et al., 2020). Furthermore, long-term nitrogen cycling is evident in high $^{3}He/^{4}He$ plumes, which show that the

deep mantle stores recycled nitrogen, with effective mixing of subducted material (Barry and Hilton, 2016). Thus, a significant primordial reservoir of strongly ^{15}N-depleted nitrogen in the LM likely does not exist. Other sources of ^{15}N-depleted nitrogen in diamond could include altered oceanic crust. Li et al. (2007) described one sample of altered oceanic crust with $\delta^{15}N$ of -11 ‰ and suggested that ammonium assimilation could produce such ^{15}N-depletion. Archean kerogens – the most ^{15}N-depleted residues of biotic systems – however, only record $\delta^{15}N$ values down to -7 ‰ (Ader et al., 2016). Additionally, only cold subduction geotherms would allow subducting oceanic crust to carry these low $\delta^{15}N$ organic residues into the mantle (Dasgupta and Hirschmann, 2010) and further retain its signature during prograde metamorphism (Bebout and Fogel, 1992).

Due to the lack of nitrogen in LM diamonds, it is difficult to model Rayleigh fractionation effects; but, modelling of $\Delta^{15}N_{diam–fluid}$ factors is important to identify where these fluids might originate. For lithospheric diamonds, NH_4^+ is assumed to be the primary nitrogen species but varies depending on oxidation state (N_2 versus NH_3; Li and Keppler, 2014) and pH (NH_3 versus NH_4^+; Mikhail and Sverjensky, 2014). The $\Delta^{15}N_{diam–fluid}$ is negative for N_2, NH_3, and NH_4^+ (Petts et al., 2015), which results in $\delta^{15}N$ values increasing during diamond crystallisation under fluid-limited conditions. For what species could $\Delta^{15}N_{diam–fluid}$ be positive? Nitrogen speciation in the LM is poorly constrained but may take the form of N^{3-} in nitrides (e.g., boron nitride, iron nitride; Kaminsky and Wirth, 2011); however, new experimental evidence at lithospheric pressures suggests that in N-rich fluids, nitrogen can form minor compounds with carbon and hydrogen (Sokol et al., 2017). In the nitride form, $\Delta^{15}N_{diam–nitride}$ is positive and the modelling approach of Hanschmann (1981) allows the derivation of $\Delta^{15}N_{diam–BN}$ = +1 ‰ at 1300 °C for boron nitride (Stachel et al., 2021). Large positive $\Delta^{15}N_{diam–fluid}$ values in the LM would be able to produce diamonds with $\delta^{15}N << -5$ ‰ from a fluid within the canonical mantle range, but higher $\Delta^{15}N_{diam-fluid}$ values for other nitrogen species in nature have not yet been found. Osbornite (TiN) inclusions in coesite from Tibetan ophiolites are ^{15}N-depleted, further linking nitrides and low $\delta^{15}N$ values (Dobrzhinetskaya et al., 2009). If these phases can be shown to be of natural origin, a further advantage of this model – N supplied from very reduced species – is its applicability to the upper mantle, where ^{15}N-depleted diamonds occur with some frequency, thus not limiting ^{15}N-depleted diamond-forming reactions to the LM.

Diamond-forming reactions

Diamond formation in the lithospheric mantle generally occurs from the precipitation of COH fluids or C-rich melts, where the carbon species can be reduced (CH_4), oxidised (CO_2), or a combination thereof (Deines, 1980; Stachel et al., 2017). The crystal chemical effects reduces the oxygen fugacity of the mantle with depth from above the fayalite-magnetite-quartz buffer (FMQ) in the uppermost mantle to values corresponding to the iron-wüstite buffer (IW) at the TZ (fO_2[FMQ] = -4) and slightly below these levels at the top of the LM (fO_2[FMQ] = -5; Frost and McCammon, 2008; Wood et al., 1990). At the top of the LM, fO_2[IW] <0 conditions favour reduced carbon (e.g., carbides) and native metal (Frost et al., 2004; O'Neill et al., 1993). In a reduced environment, COH fluids are expected to be dominated by CH_4 and due to its insolubility in silicate minerals, CH_4 is mobile (Green, 1990; Luth, 1999). Evidence for diamond formation in reduced environments in the TZ comes from CH_4 and H_2 fluid films surrounding sulphide inclusions (Smith et al., 2016). Diamond formation by oxidation of methane could occur by:

$$2CH_4 + O_2 \rightarrow 2C + 2H_2O + 2H_2 \qquad \text{(Equation 6-1).}$$

The speciation of carbon at LM pressure is poorly constrained. New experimental evidence suggests the occurrence and stability of heavier hydrocarbons (e.g., ethane) and C-N-complexes depend on the fluid composition and oxygen and hydrogen fugacity (Sokol et al., 2020, 2017). Thus, diamond formation in the LM could potentially occur by the oxidation of a heavier hydrocarbon, e.g., ethane, via the reaction (Matjuschkin et al., 2019):

$$C_2H_6 + O_2 \rightarrow C + H_2O + 2H_2 \qquad \text{(Equation 6-2).}$$

The lower mantle does not have free oxygen and for diamond to form by oxidation, an oxidising agent would need to be supplied. Iron, present at ~8 wt% in un-depleted lower mantle can disproportionate, producing Fe^0, Fe^{2+}, and Fe^{3+} (Frost et al., 2004). Oxidation of methane can thus occur via the reaction (Regier, 2020):

$2Fe_2O_3 + CH_4 \rightarrow 4FeO + C + 2H_2O$ (Equation 6-3),

where the ferrous iron is taken up in mantle mineral(s) and the ferric iron is most likely supplied by bridgmanite, which has been shown to have a higher than expected Fe^{3+} concentration when former bridgmanite has been analysed from LM diamonds (Frost et al., 2004; McCammon et al., 2004). The CH_4 is supplied through the interaction of mantle-derived carbon, in the form of carbides, and water supplied from subducting slabs (Zhu et al., 2019). This mechanism was put forward for Kankan diamonds, where slab water destabilised mantle carbides (Regier et al., 2020).

Diamond can also be produced from reduced carbon-rich melts. Above 9 GPa, the stability of diamond in carbide-rich systems increases, producing diamond and Fe_7C_3 where C >8.41 wt% and within the range of temperatures expected in the LM (Lord et al., 2009). This is one mechanism put forward for the formation of Juína LM diamonds based on the occurrence of inclusions of carbides (Kaminsky and Wirth, 2011); however, carbides have not yet been found in Koffiefontein LM diamonds.

In contrast to diamonds forming from reduced fluids/melts, Koffiefontein diamond 25/01 contains magnesite along with a magnesite rim around ferropericlase. Within the LM, magnesite is the stable carbonate, with Ca being partitioned into $CaSiO_3$-pvk (Biellmann et al., 1993). Carbonate inclusions can reflect diamond formation via the reduction of carbonate-bearing fluids in the TZ, e.g., the Juína TZ diamonds (Walter et al., 2011) or diamond formation from carbonatitic melt (Walter et al., 2008). Experimental evidence suggests a maximum of 20 vol% carbonate from the top of the slab is reduced by ambient Fe^0 in the TZ, depending on slab thermal profiles (Martirosyan et al., 2016); whereas other authors suggest that all carbonate is removed as melt from the subducted slab within the TZ, thereby creating a barrier to carbonate influx into the LM (Kiseeva et al., 2013a; Thomson et al., 2016). However, the nature of the TZ-LM boundary during carbonate influx is still debated. Carbonate melts or fluids in the LM – a reduced environment – would freeze immediately except in local oxidising regions which would have to be at log fO_2[IW] = +2 to +3 (Rohrbach and Schmidt, 2011). Carbonatitic melts produced from deeply subducted slabs are reduced by Fe^0 to diamond, forming an intermediary

carbide phase (Rohrbach and Schmidt, 2011). Diamond formation by the reduction of carbonate by metallic iron is given by (Burnham et al., 2015; Dorfman et al., 2018; Ryabchikov and Kaminsky, 2013):

$$3MgCO_3 + 13Fe^0 \rightarrow Fe_7C_3 + 3MgO + 6FeO \quad \text{(Equation 6-4)}$$

$$3MgCO_3 + 2Fe_3C \rightarrow 9Fe_{0.67}Mg_{0.33}O + 5C \quad \text{(Equation 6-5).}$$

The (Fe,Mg)O resulting from these reactions would equilibrate with the bulk Mg# of the rock, thus reflecting the high bulk Mg# of the system. As carbide cannot exist with carbonate, all available carbide – and metallic iron – would be exhausted before a carbonatitic melt or fluid could move through the mantle (Palyanov et al., 2013). Additionally, Fe within Al-bearing bridgmanite can disproportionate to produce Fe^{3+} and Fe^0 to control the redox state of the lower mantle (Frost et al., 2004). This additional control would more easily reduce carbonate in the LM (McCammon et al., 2004; Stagno et al., 2011).

The Koffiefontein diamonds show both possible diamond formation mechanisms. Diamond 21/01, containing a possible water-rich inclusion could have formed from a water-rich, reduced-carbon fluid, where water was supplied by minerals within the subducted slab that mobilised slab-derived carbon with a mantle-like $\delta^{13}C$ signature. Formation from mantle-derived carbides would produce strongly ^{13}C-depleted diamonds, due to the large $\Delta^{13}C$ fractionation factor, unless complete conversion of the carbide occurs. Although diamond 23/01 does not conclusively point to a diamond formation mechanism, diamond 25/01 – containing magnesite and a carbonate alteration rim on ferropericlase – shows evidence for diamond formation by carbonatitic melts or carbonate-rich fluids in the lower mantle. As the Koffiefontein LM inclusions are representative of a depleted host rock, diamond formation would need to have occurred within the subducted slab – i.e. within the depleted peridotitic portion of the subducted slab, or within former slabs accumulated at the TZ-LM boundary. In this model, carbon within the subducted slab survives into the uppermost LM and carbonate-rich fluids can still be produced within the LM but are easily reduced. The mantle-like $\delta^{18}O$ of the included bridgmanite does not necessarily record the oxygen isotopic signature of the carbonate-rich fluid if the melt-rock ratio is low. For instance, modelling the $\delta^{18}O$ evolution of eclogitic garnet subject to melt-rock interaction with a melt

having a non-mantle like $\delta^{18}O$ value shows that significant amounts of fluid are needed to alter the oxygen isotope composition of mantle minerals as they are buffered by a vast oxygen reservoir (Riches et al., 2016).

6.4. Summary and conclusions

The small suite of Koffiefontein sublithospheric diamonds studied here provide insight into the formation of diamonds within the LM from within a deeply subducted lithospheric substrate. The Koffiefontein sublithospheric inclusions include an assemblage of metaperidotitic inclusions that could have formed at the top of the LM or deeper within the LM. The high Mg# of the former-brd + fPer assemblage and low Al_2O_3 contents in bridgmanite suggest formation of diamond within a substrate that is chemically comparable to a depleted peridotite: from a depleted lherzolite to a dunite in composition. Such a bulk composition is indicative of the uppermost lithospheric mantle portion of a depleted oceanic slab (the upper-most portion of oceanic lithosphere being the most depleted as the extent of melting is related to the amount of mantle decompression at ridges).

The formation of diamond in the LM at Koffiefontein and other locations indicates a carbon source with a carbon isotope signature similar to that of the mantle. This signature, however, could also arise from homogenized altered oceanic carbonate ($\delta^{13}C$ of mean altered oceanic crust is -4.7 ‰). The mantle-like character and minor variability of $\delta^{13}C$ values within the three Koffiefontein sublithospheric diamonds indicates that either the diamonds formed from one homogenous fluid with small amounts of Rayleigh fractionation occurring, or subsequent fluids that had very similar $\delta^{13}C$ signatures. Thus, there is no clear indication of reduced or oxidised C species for diamond formation, but the presence of magnesite in one LM diamond suggests diamond formation by the reduction of oxidised fluids/melts. The presence of possibly OH-bearing mineral inclusions in one of the Koffiefontein diamonds, thought to be of LM origin, indicates that H_2O-rich fluids, possibly containing reduced carbon, are important mechanisms for diamond formation in the LM. Thus, multiple mechanisms are conceivable for formation of the Koffiefontein sublithospheric diamonds.

The very low $\delta^{15}N$ (-14.8 to -14.1 ‰) of the former bridgmanite-bearing diamonds is distinctly outside the expected mantle range (-5 ±2 ‰; Cartigny et al., 2014). Instead of calling on poorly constrained primordial heterogeneities or Rayleigh fractionation mechanisms, I suggest nitrogen isotopic fractionation effects involving highly reduced metallic species, such as nitrides and Fe-Ni metal, as the cause of ^{15}N depletion. This formation model has the advantage of being able to occur also in the lithospheric mantle and is not reliant on primordial heterogeneity. More research is needed on nitrogen isotopic fractionation within very reduced environments such as the LM. Resolving the origin of strongly ^{15}N-depleted nitrogen in diamond is further complicated by the theoretical possibility of numerous nitrogen-bearing species within these environments.

The Koffiefontein sublithospheric diamonds could have formed from deeply subducted lithospheric slabs that contained a basaltic portion and depleted peridotite. This agrees with the oxygen isotopic composition of the former bridgmanite, which has a mantle-like signature, indicating that the primary depleted peridotite was unaltered by seawater. While TZ minerals are shown to have formed within or through melting of subducted basaltic lithosphere (e.g., Burnham et al., 2016; Harte et al., 1999; Regier et al., 2020; Stachel et al., 2000a; Tappert et al., 2005a; Thomson et al., 2014; Walter et al., 2011), inclusions in Koffiefontein diamonds show that depleted former oceanic lithosphere and not ambient mantle material is trapped within LM diamonds as suggested by Kesson and Fitz Gerald (1991) and Stachel et al. (2000b).

Table 6-1: Physical characteristics of sublithospheric diamonds from Koffiefontein.

Sample	Colour	Shape	Growth	Plastic Deformation	Resorption Concentric growth rings	Trigons /Hexagons	Overall resorption
21/01	Light brown	Irregular pseudohemimorphic	shield-shape lamella	N	N	N	Resorbed edges
23/01	Light brown	Octahedra	shield-shape lamella	Coarse lamination lines	N	Hexagons	Minor rounding on octahedra edges
25/01	brown	Irregular/twin pseudohemimorphic	Stacked growth layers	Striations x2	N	N	Resorbed; broken during transport

*No hillocks or ruts

Table 6-2: Summary of sublithospheric mineral inclusions and analytical method of determination.

Sample	Mineral	Raman comment	EPMA comment
21/01			
A	fPer	Y	Y
B	Mg-silicate	Not Raman active	Y
C	fPer	Y	Y
D	MgFeCa-silicate + SiO_2 Alt	Not Raman active	Y
23/01			
A	brd	Y	Y
B	fPer	Y	
C	fPer	Y	Y
D	fPer	Y	Y
E	fPer	Y	Y
F	fPer	Y	
G	fPer	Y	
25/01			
A	fPer	Y	Y
B	fPer	Y	Y
C	fPer	Y	N
D	brd	Y	Y
E	brd	Y	Y
F	fPer	Y	Y
G	magnesite	Not Raman active	Y
H	MgFe-silicate	Not Raman active	Y
I	fPer	Y	Y
J	brd	Y	Y
K	fPer	Y	Y
L	fPer + magnesite	Not Raman active	Y
M	fPer	Y	Y

Minerals: fPer – ferropericlase; brd – bridgmanite; chr – chromite; pvk – perovskite ($CaTiO_3$)

Table 6-3: Major element analysis by EPMA of representative averages of Koffiefontein sublithospheric mineral inclusions.

	21/01 **fPer + Mg-silicate + Mg-Fe-Ca-silicate**					**23/01** **fPer + brdg**			
	21/01A	21/01B		21/01C	21/01D	23/01A	23/01C	23/01D	23/01E
	fPer	Mg-silicate		fPer	MgFeCa-silicate	brd	fPer	fPer	fPer
		min	max		Av				
SiO_2	0.01	47.35	54.15	0.01	58.12	57.06	0.01	0.02	0.01
TiO_2	0.00	0.00	0.01	0.00	0.61	0.10	0.00	0.00	0.00
ZnO	0.02	0.24	0.80	0.02	0.06	0.00	0.02	0.02	0.03
Al_2O_3	0.02	2.40	3.46	0.03	1.40	1.67	0.02	0.03	0.02
V_2O_3	0.00	0.00	0.00	0.00	0.04	0.00	0.00	0.00	0.00
Cr_2O_3	0.52	0.03	0.05	0.51	0.00	0.37	0.85	0.84	0.83
FeO	18.79	6.15	7.83	18.45	6.43	3.45	26.04	25.89	25.57
NiO	1.25	0.39	0.55	1.23	0.00	0.03	1.36	1.33	1.34
MnO	0.16	0.02	0.05	0.16	0.28	0.11	0.25	0.24	0.24
MgO	78.86	14.46	21.19	79.65	12.54	37.66	69.76	70.48	71.23
CaO	0.00	0.58	0.84	0.00	13.69	0.03	0.00	0.00	0.00
Na_2O	0.00	0.14	0.25	0.00	1.23	0.00	0.21	0.31	0.13
K_2O	0.00	0.16	0.58	0.00	0.58	0.00	0.00	0.00	0.00
Total	99.62	71.92	89.75	100.06	95.00	100.48	98.53	99.17	99.41
Mg#	88.2	80-85		88.5	~75	95.1	82.7	82.9	83.2

Table 6-3: continued

	25/01 fPer + brd													
	25/01A	25/01B	25/01D	25/01E	25/01F	25/01G	25/01H		25/01I	25/01J	25/01K	25/01L		25/01M
	fPer	fPer	brd	brd	fPer	mgs	MgFe-silicate		fPer	brd	fPer	fPer	mgs	fPer
							min	max						
SiO_2	0.01	0.00	57.02	58.33	0.02	1.81	0.13	35.48	0.01	57.55	0.07	0.03	2.02	0.01
TiO_2	0.00	0.00	0.03	0.04	0.01	0.00	0.00	1.43	0.00	0.03	0.00	0.00	0.00	0.05
ZnO	0.02	0.03	0.02	0.00	0.00	0.01	0.02	0.12	0.01	0.03	0.05	0.02	0.01	0.02
Al_2O_3	0.08	0.06	1.17	1.20	0.11	1.83	0.12	3.73	0.01	1.21	0.14	0.09	0.59	0.14
V_2O_3	0.00	0.00	0.00	0.02	0.00	0.00	0.00	0.10	0.00	0.02	0.01	0.01	0.00	0.01
Cr_2O_3	0.71	0.72	0.34	0.39	0.71	0.05	0.70	1.93	0.58	0.34	0.59	0.71	0.26	0.73
FeO	20.85	21.12	3.50	3.58	18.85	6.30	6.43	18.75	20.76	3.50	19.89	19.29	9.40	20.13
NiO	1.43	1.46	0.01	0.00	1.23	0.11	1.37	3.70	1.38	0.00	1.42	1.44	0.28	1.11
MnO	0.20	0.20	0.10	0.12	0.13	0.04	0.00	0.16	0.15	0.12	0.15	0.18	0.04	0.14
MgO	75.78	77.07	37.48	38.37	77.86	40.94	32.32	69.69	76.62	37.92	76.65	77.88	46.21	75.32
CaO	0.00	0.00	0.04	0.06	0.00	0.22	0.00	0.32	0.01	0.04	0.00	0.00	0.64	0.00
Na_2O	0.08	0.13	0.00	0.00	0.00	0.02	0.00	0.00	0.09	0.00	0.07	0.00	0.00	0.00
K_2O	0.01	0.00	0.00	0.00	0.00	0.02	0.00	0.02	0.00	0.00	0.01	0.00	0.01	0.00
Total	99.18	100.78	99.72	102.10	98.92	51.35	82.64	91.05	99.62	100.75	99.05	99.64	59.46	97.66
Mg#	86.6	86.7	95.0	95.0	88.0	92.0	60-91		86.8	95.1	87.3	87.8	89.8	87.0

Minerals: fPer – ferropericlase; brd – bridgmanite; mgs – magnesite

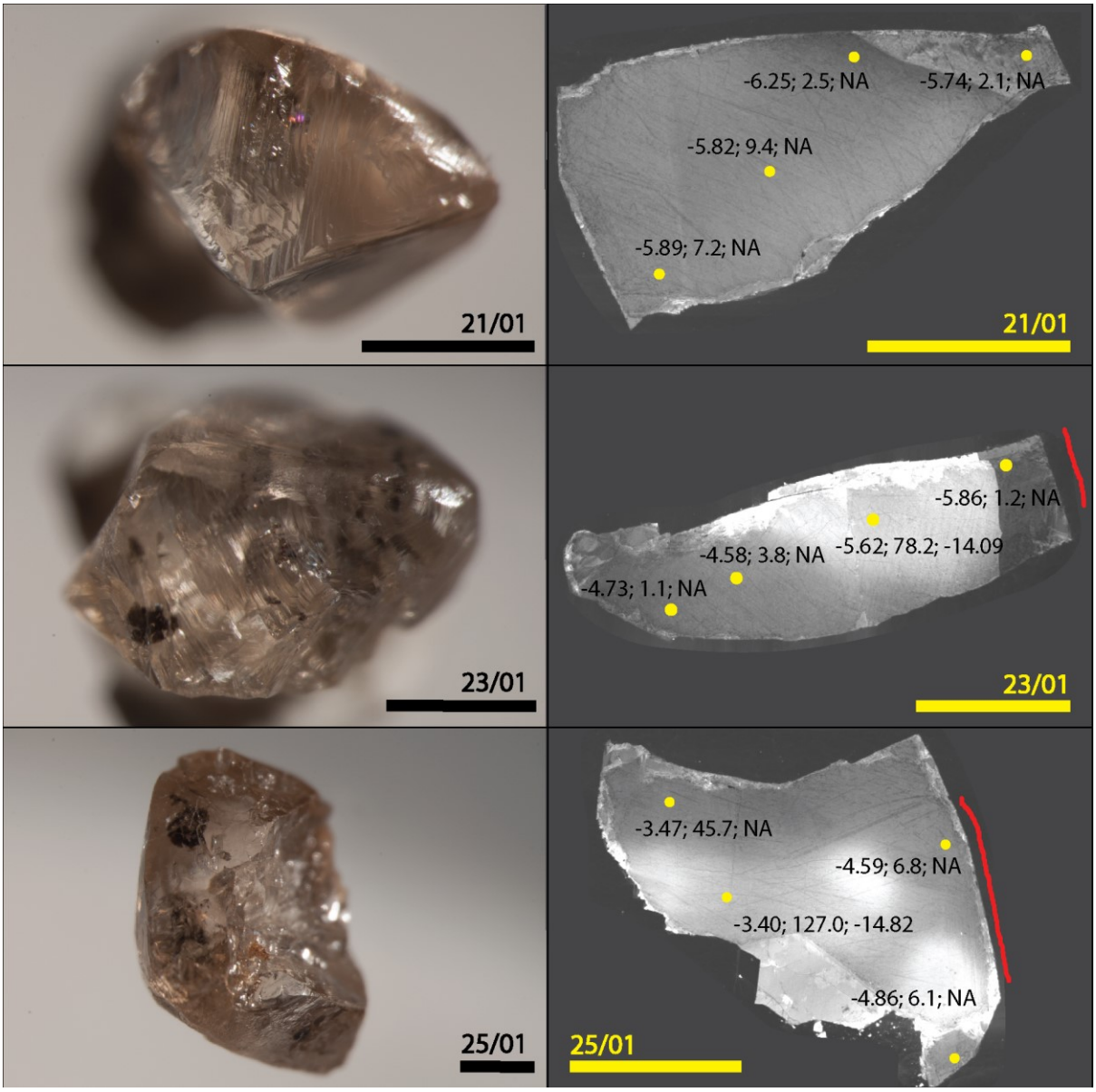

Figure 6-1: Photographs of Koffiefontein sublithospheric diamonds (left; scale bar 1000 µm). 21/01 – irregular and well-rounded light brown diamond, with shield-shaped lamellae visible on the right of the image; 23/01 – light brown octahedral twin with minor resorption on the left side and more moderate resorption on the right, leaving the diamond with a pseudohemimorphic shape; and 25/01 – brown, irregularly shaped twinned diamond fragment, with slight rounding of broken edges. Cathodoluminescence images (right; scale bar 500 µm) of fragments of Koffiefontein sublithospheric diamonds and SIMS analysis points in the order of: $\delta^{13}C_{VPDB}$ (‰), nitrogen concentration (at.ppm), and $\delta^{15}N_{AIR}$ (‰). Solid red lines indicate the outer edge of the diamond fragment.

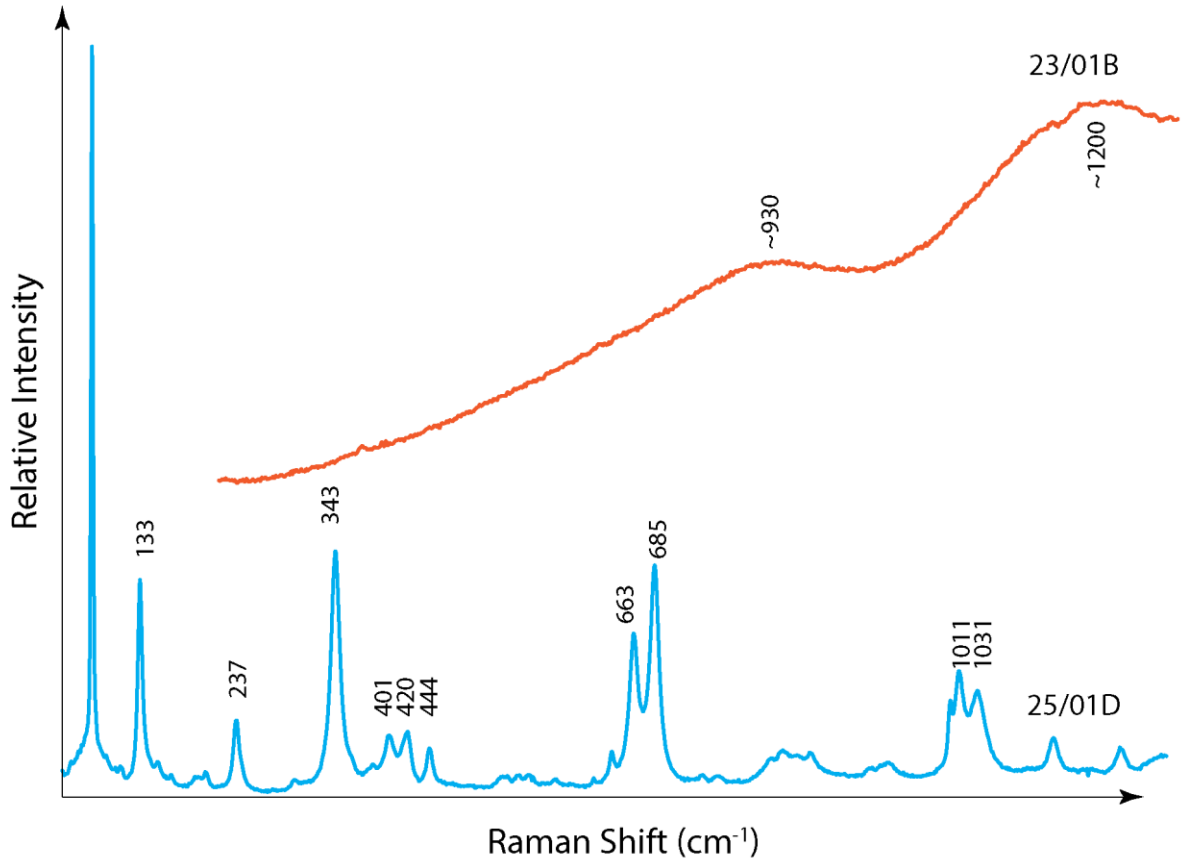

Figure 6-2: Raman spectra representative of former bridgmanite (25/01D) and ferropericlase (23/01B) from the Koffiefontein diamonds. The main peaks used to identify each mineral are labelled. Ferropericlase (orange) has two broad humps, whereas retrogressed bridgmanite (blue) has a single peak at 343 cm^{-1} and double peaks at 663-685 cm^{-1} and 1011-1031 cm^{-1}, all are common to lithospheric orthopyroxene.

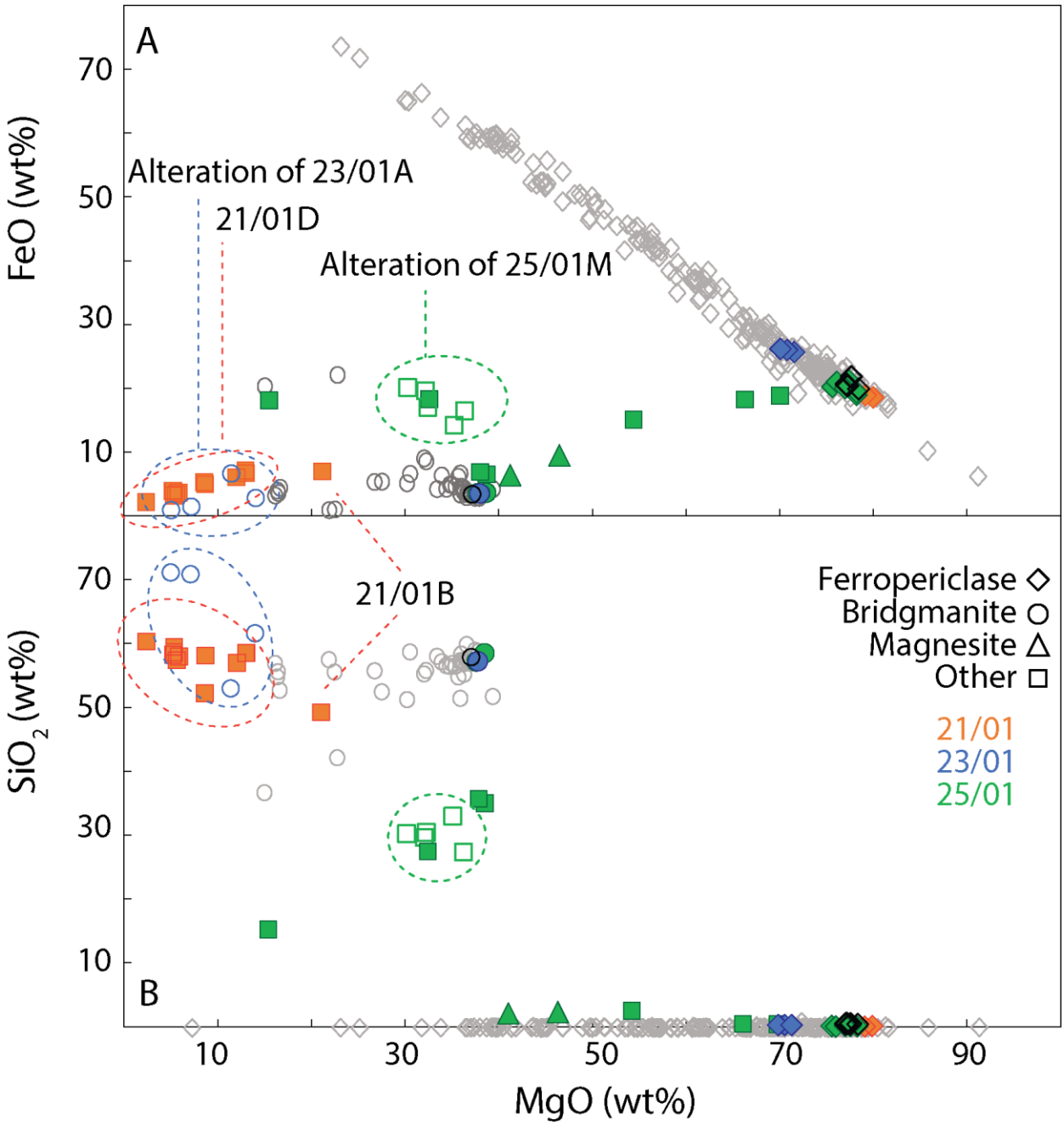

Figure 6-3: FeO (A) and SiO_2 (B) versus MgO of Fe-Mg silicates and oxides from Koffiefontein lower mantle diamonds from this study (coloured symbols) and Cardoso (Cardoso, 1980; black symbols) with literature data from Kankan (Stachel et al., 2000b) and Sao Luis (Hutchison, 1997) lower mantle diamonds (grey). Alteration of enstatite (former bridgmanite; 23/01A) and of ferropericlase (25/01M) in open symbols. Unknown, polyphase and heterogeneous inclusions in solid square symbols (orange 21/01B&D; green 25/01H).

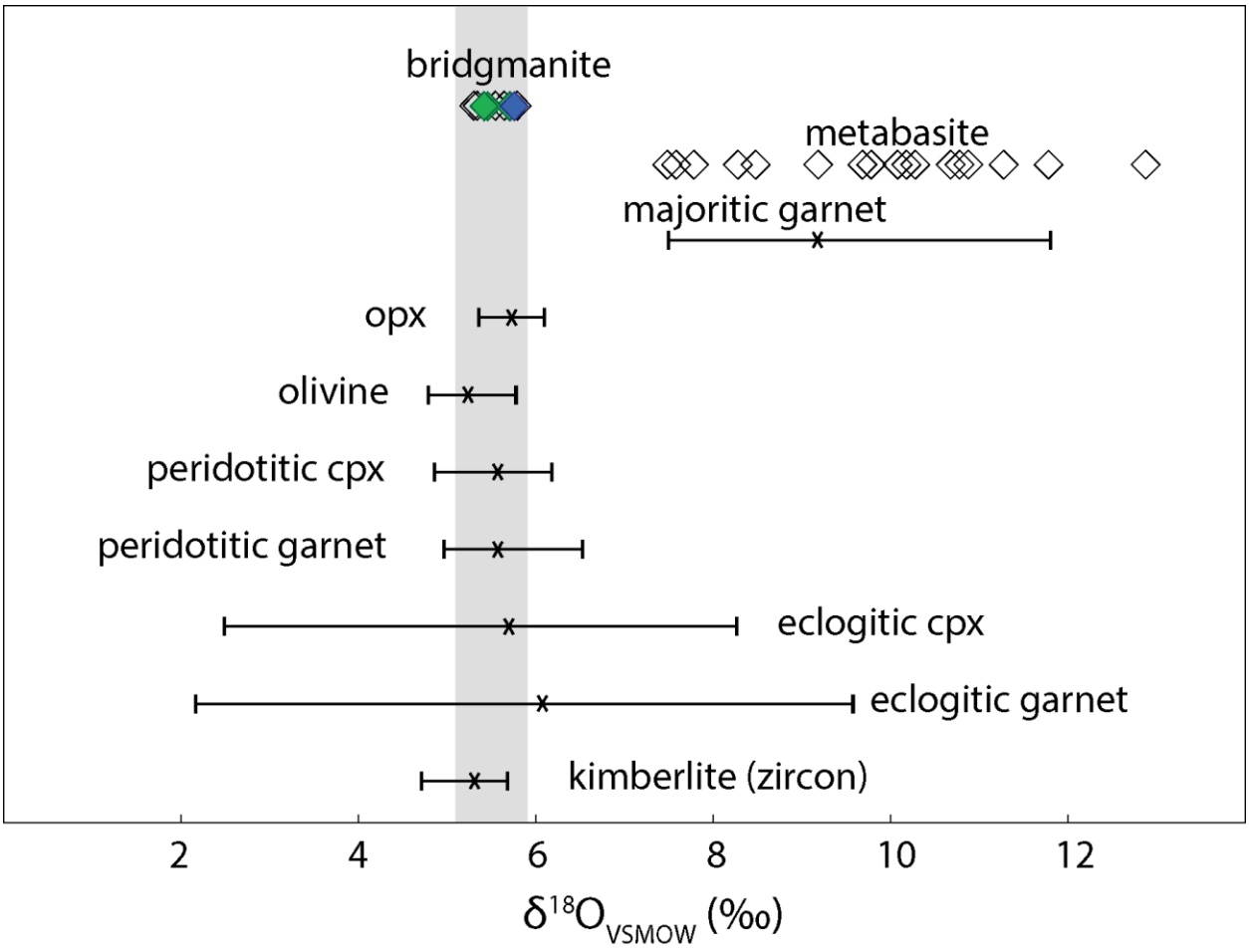

Figure 6-4: Oxygen isotopes of former bridgmanite inclusions from Koffiefontein diamonds (23/01: blue; 25/01: green) and Kankan (Regier et al., 2020) in relation to metabasaltic inclusions from Brazilian sublithospheric diamonds (Burnham et al., 2015) and majoritic garnets from worldwide sources (Burnham et al., 2015; Ickert et al., 2015). $\delta^{18}O$ ranges with median values (x) for specific mantle minerals. Kimberlite oxygen isotope data from Valley et al. (1998). Mantle xenolith data from: Appleyard (2000), Aulbach et al. (2017), Barth et al. (2001), Beard et al. (1996), Deines et al. (1991b), Deines and Haggerty (2000), Garlick et al. (1971), Ionov et al. (1994), Jacob et al. (1994), Malkovets et al. (2003), Mattey et al. (1994), Pernet-Fisher et al. (2014), Regier et al. (2018), Riches et al. (2010), Schulze et al. (2003), Snyder et al. (1995), Spetsius et al. (2008), Taylor et al. (2003), Viljoen et al. (1996), and Williams et al. (2009). Shaded region indicates $\delta^{18}O$ of mantle at +5.5 ± 0.4 ‰ (Mattey et al., 1994).

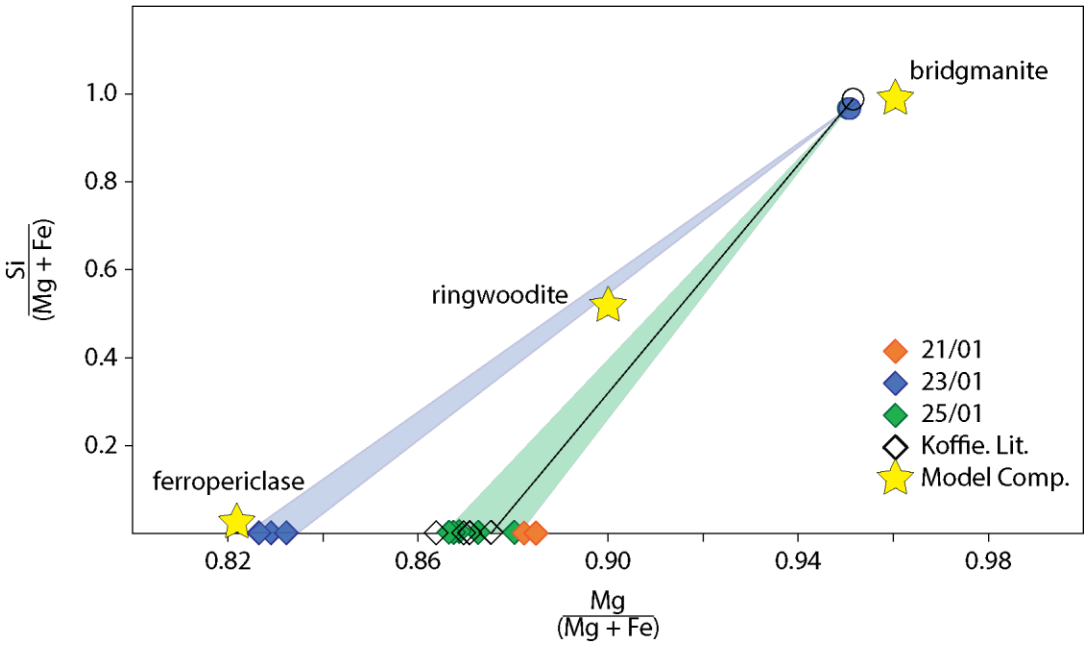

Figure 6-5: Molar Mg versus Si for bridgmanite (circle) and ferropericlase (diamond) inclusions from Koffiefontein sublithospheric diamonds (this study; literature data of Cardoso, 1980). Compositions of bridgmanite for 23/01, 25/01, and A262 plot at the same location. Star symbols indicate the location of coexisting mineral phases at the point of ringwoodite disproportionation (~22.5 GPa and 1627 °C) from experiments of bulk fertile peridotitic of Wood (2000).

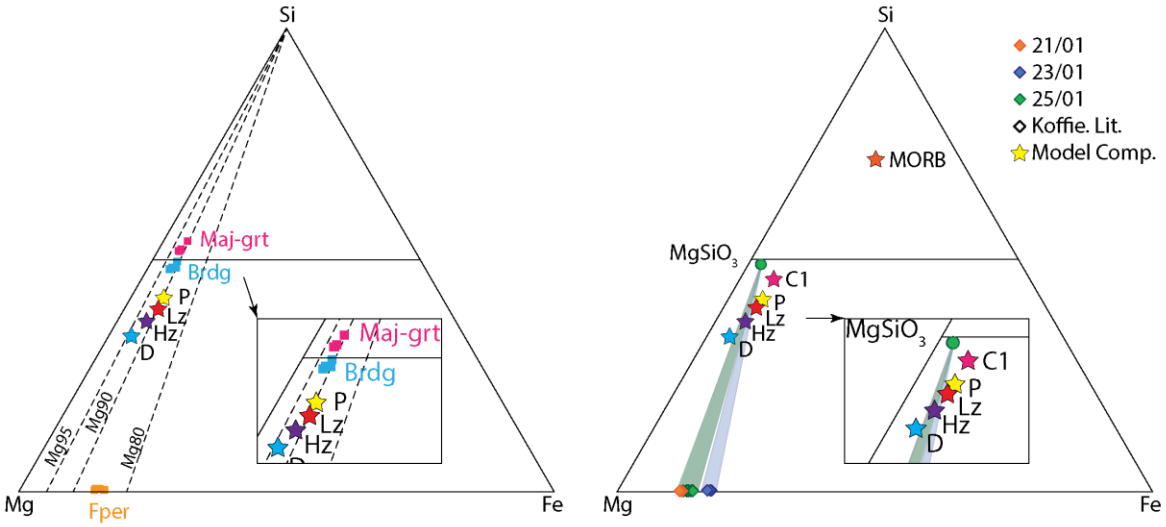

Figure 6-6: Molar Mg-Fe-Si ternary diagram of coexisting phases from the top of the lower mantle and bulk model compositions (stars) for: MORB – mid-ocean ridge basalt (Gale et al., 2013), C1 – chondrite (McDonough and Sun, 1995), P – pyrolite, Lz – cratonic lherzolite, Hz – cratonic harzburgite, D – cratonic dunite (McDonough and Rudnick, 1998). (A) Pyrolitic compositions of bridgmanite + majoritic-garnet + ferropericlase at the 660 km discontinuity – i.e. immediately after ringwoodite transition (Hirose, 2002; Irifune, 1994; Ishii et al., 2018b; Wood, 2000). Dashed lines indicate molar 100Mg/(Mg+Fe). (B) Koffiefontein mineral inclusions in lower mantle diamonds – ferropericlase (diamond) and regressed bridgmanite (circle) – joined with a tie-line for co-existing assemblages. Literature data from Cardoso (1980) for A262 (plotting behind 25/01).

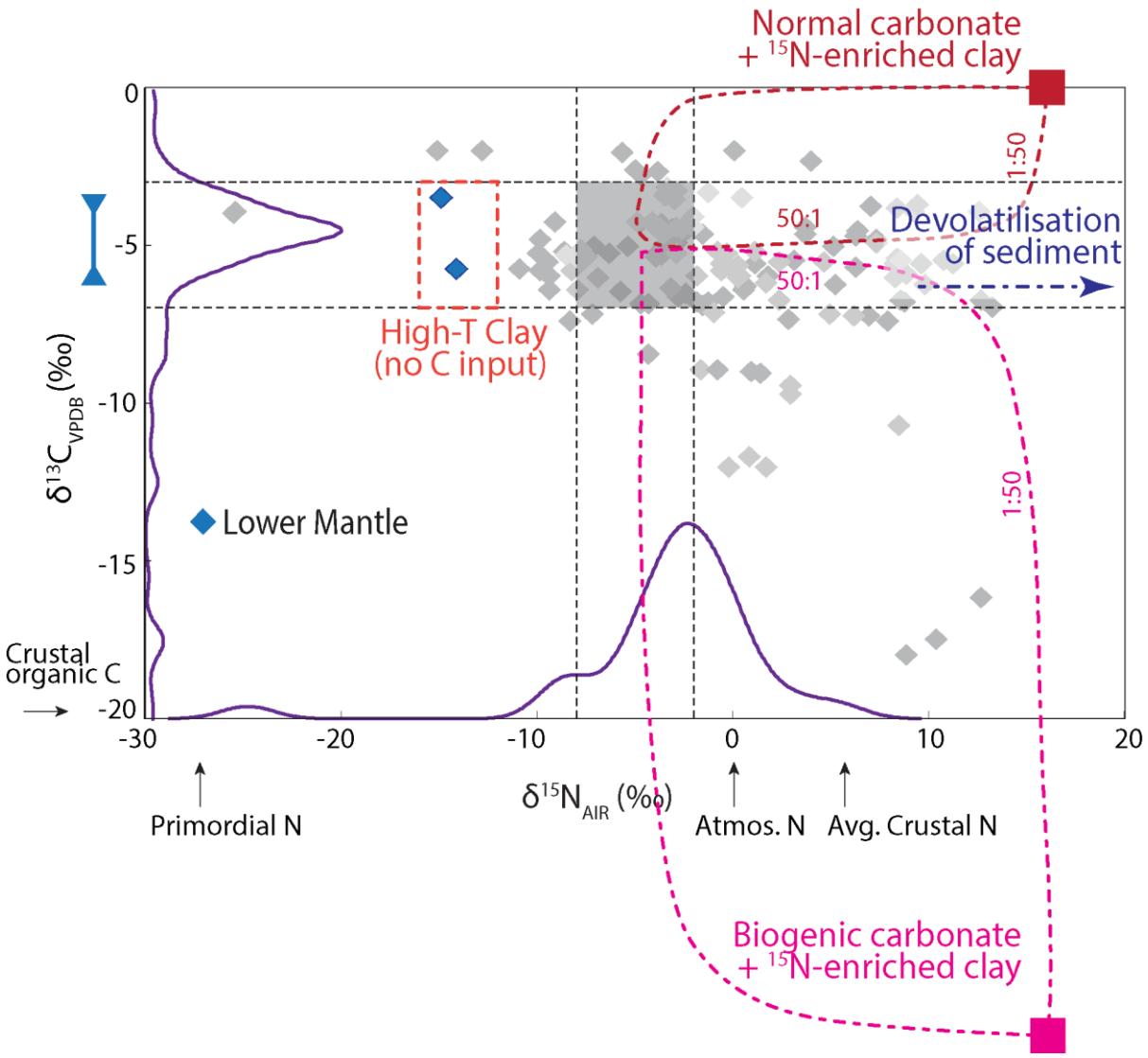

Figure 6-7: $\delta^{13}C_{VPDB}$ versus $\delta^{15}N_{AIR}$ (‰) of Koffiefontein lower mantle (coloured) and lithospheric (grey) diamonds. For diamonds without nitrogen, a range $\delta^{13}C$ values is plotted on the y-axis. Dashed lines delimitate the canonical mantle range and arrows point toward addition of specific reservoirs of Li et al., (2019). Density plots for carbon and nitrogen isotopes of lower mantle diamonds (Cartigny et al., 2014).

Chapter 7. Conclusions

In this thesis, I used a suite of ~200 diamonds and their mineral inclusions from the Koffiefontein kimberlite pipe in southern Africa to further elaborate on how the Kaapvaal Craton mantle root – the substrate for these diamonds – was formed in the Archean and later modified. A significant theme in this thesis is the role of subduction processes in forming depleted peridotitic lithosphere, providing a source, over a large-spatial scale, for metasomatic fluids, and being the source of carbon and nitrogen for diamond formation both in the upper and lower mantle. In this last chapter, I will present the main findings and discussion points that have led to these conclusions.

7.1. Lithosphere formation and evolution

Competing models of cratonic lithosphere formation invoke low- or high-pressure melt depletion. The high Cr_2O_3 content and REE_N patterns of peridotitic garnets in diamond document protolith formation during melt extraction in the spinel-facies (e.g., Stachel et al., 1998b). The generally high Mg# of olivine inclusions corroborates extensive low-pressure melt extraction; but the high bulk Si of cratonic xenoliths on the Kaapvaal Craton does not correlate with the trend expected for melt depletion of peridotite at spreading ridges (Boyd, 1987). The history of the Kaapvaal Craton formation is further complicated by pervasive metasomatic events that enriched the LREE and lead to subsequent diamond formation (Menzies et al., 1987).

Mineral inclusions in the Koffiefontein diamonds are dominated by peridotitic assemblages, especially harzburgitic chemistries, and a significant proportion (approximately one third) of the garnets have very low CaO, being likely of dunitic paragenesis. Cr_2O_3-Al_2O_3 chemistry of garnets indicates that they grew during both the reaction of orthopyroxene and spinel, and exsolution from orthopyroxene. Additionally, the Mg# of the olivine inclusions is high (median $Mg\#_{ol}$ is 93.4 and values extend to 95.0) compared to worldwide sources but within the bounds of other Kaapvaal locales. The significant LREE enrichment and high LREE/MREE in some garnets, combined with their harzburgitic chemistry, are not conducive to melt metasomatism and instead suggest metasomatism by HDFs. Additionally, the Koffiefontein diamonds,

recording an ancient (assumed Paleoarchean) geotherm, plot within error of the xenolith geotherm at ~90 Ma.

The high Cr_2O_3 and positive $HREE_N$ slopes in garnet confirm that depletion occurred in the spinel facies, which is supported by the formation of garnet by the reaction of spinel and orthopyroxene. The low CaO content of garnet, lack of clinopyroxene, and high Mg# of olivine are consistent with extensive levels of melt depletion. The highest $Mg\#_{ol}$, however, would require unfeasibly high levels of melt extraction (>65 %). Such high $Mg\#_{ol}$ can instead be achieved by the infiltration of a high Mg# melt before craton thickening. Such a melt, e.g., a boninite, is hydrous and only available in mantle wedges. The Commondale Komatiite – a newly-recognised boninite (Sossi et al., 2016; Wilson, 2003) – is a Si-, Mg-rich magma that is devoid of incompatible elements and could exemplify a potential source magma. This is a slight modification of previous cratonic lithosphere formation models and retains the initial depletion through extraction of basaltic melts (e.g., Jordan, 1978). But a second stage is invoked that is similar to the melt infiltration model of Kelemen et al. (1998), but instead of the infiltrating melts being broadly of dacitic composition, derived from metabasaltic sources, an infiltrating depleted boninite melt produces significantly higher $Mg\#_{ol}$ and also can reintroduce Si through the formation of orthopyroxene. Garnet and orthopyroxene formation, based on partition coefficients, indicate garnet formation by both reaction of spinel and orthopyroxene and exsolution from orthopyroxene, suggesting that the lithosphere was not completely dunitic before lithosphere thickening, in contrast to what is suggested by high $Mg\#_{ol}$. Later HDFs (e.g., Weiss et al., 2009), carrying dissolved LREE and MREE, enriched the diamond substrate. This fluid-mediated metasomatic event could occur after thickening of lithosphere and/or concurrent to diamond formation. The long-term stability of the geothermal gradient in cratonic lithosphere, as derived from inclusions in diamond and from mantle xenoliths, indicates that the Kaapvaal craton was shielded from secular thermal changes within the mantle and that metasomatic events did not affect the thermal state of the craton in a major way, through advection of heat or addition of heat producing elements. This agrees with the notion that cratons, specifically the Kaapvaal Craton, formed early in Earth's history and remained stable since then. Even the introduction of metasomatic fluids that altered existing minerals (e.g., LREE enrichment in garnet) or formed new minerals (e.g., goldschmidtite, diamond) appears to have had little effect.

7.2. Mechanisms of diamond formation and the source of diamond-forming fluids

Diamonds in the lithospheric mantle are thought to be produced mainly from redox reactions of oxidised or reduced melts or fluids with ambient mantle. Due to the significant over-representation of harzburgitic diamonds (85% of peridotitic diamonds are harzburgitic, but less than 25 % of the peridotitic lithospheric mantle is harzburgite; Griffin et al., 2003; Gurney, 1984), C-rich fluid is favourable because of its mobility in highly depleted subsolidus peridotites (Wyllie and Huang, 1976). However, other mechanisms than wall-rock buffered redox reactions, such as isochemical precipitation from cooling COH-fluid (Luth and Stachel, 2014), can also occur. Modelling of $\delta^{13}C$ trends during diamond precipitation from mixed COH fluids (CO_2 and CH_4 present) is directly comparable to the trends observed in natural diamonds (Stachel et al., 2017). Thus, it is important to utilise both the mineral inclusion chemistry as well as $\delta^{13}C$ variations within diamond to narrow down the possible diamond-forming mechanism. This approach is complicated by diamond's protracted growth history, during which successive pulses of diamond-destructive and diamond-forming fluids/melts may occur, and the source and speciation of diamond-forming fluids. The global diamond $\delta^{13}C$ distribution shows that peridotitic diamonds have a strong mode at ~-5 ‰, whereas the eclogitic distribution is bimodal with a strong mode at ~-5 ‰, and a significant ^{13}C-depleted tail with a secondary mode near -12 ‰ (Cartigny, 2005). Fluids or melts forming eclogitic diamonds can have a strong recycled carbon component, evident in ^{13}C-depleted or ^{13}C-enriched values, whereas the source for peridotitic diamonds is attributed to mantle-derived carbon (Kirkley et al., 1991). However, evidence from carbonates in altered oceanic crust, which is recycled back into the mantle with subducting slabs, shows that both typical recycled and mantle-like carbon isotopic signatures can be produced (Li et al., 2019).

In the studied Koffiefontein lithospheric suite, two diamonds contained former coesite inclusions (retrogressed to quartz) within otherwise typical harzburgitic assemblages. In two other diamonds, one contained calcite within a lherzolitic assemblage, and one contained only calcite. In the sublithospheric diamond suite, one lower mantle diamond contained a magnesite inclusion and magnesite rimming a retrogressed bridgmanite inclusion. Additionally, hydrous alteration was found around a lower mantle ferropericlase inclusion. The presence of carbonate inclusions or retrogressed coesite – interpreted to have formed from extensive carbonation of olivine – is

direct evidence of diamond formation by carbonate reduction in harzburgite. These diamonds likely represent the redox freezing of carbonate melt interacting with a depleted peridotitic substrate. Conversely, the presence of hydrous alteration can be interpreted as the by-product of diamond formation from the oxidation of methane-rich fluids (e.g., Smith et al., 2016; Taylor and Green, 1988). Thus, within the lithospheric mantle, diamonds principally form from both the reduction and oxidation of C-rich fluids or melts.

At Koffiefontein, peridotitic and eclogitic diamonds have statistically similar frequency distributions for $\delta^{13}C$ (Figure 3-5). Mobilising large volumes of carbon from the ambient mantle or depleted lithosphere is not necessary if peridotitic diamonds formed from COH-fluids produced from subducted slabs. Consequently, the mantle-like $\delta^{13}C$ signature of both peridotitic and eclogitic diamonds is attributed to COH-fluids tapping homogenised carbon from subducted altered oceanic crust (mean $\delta^{13}C$ of -5 ‰; Shilobreeva et al., 2011). Some Koffiefontein peridotitic diamonds have $\delta^{15}N$-[N] trends that clearly point to metasedimentary sources. In addition, there are a number of ^{15}N-depleted diamonds. Extensive Rayleigh fractionation cannot account for the wide range in $\delta^{15}N$ and the extreme levels of ^{15}N depletion, and primordial reservoirs or known nitrogen fractionation factors are dismissed as possible scenarios. Diamond formation by isochemical precipitation (Stachel and Luth, 2015) was not tested as the outcome in $\delta^{13}C$ is indistinguishable from the redox reactions involving CO_2 and CH_4.

7.3. Diamond formation in the lower mantle

Physical samples of the transition zone and lower mantle are rare; however, occasionally sublithospheric diamonds are included in a suite of lithospheric diamonds such as at Koffiefontein. The mechanisms of diamond formation in the deep regions of the mantle are not readily understood, especially the source of carbon for the diamonds. Described above are models of diamond formation within the lithosphere; moving towards an understanding of lower mantle diamond formation, additional complications arise from the rarity of lower mantle samples, the unknown speciation of carbon and nitrogen within the lower mantle, and the extent of volatile removal from subducting slabs. Studies of a suite of transition zone diamonds from Brazil have linked diamond formation to carbonate melts, produced from partial melting of subducted oceanic lithosphere (Brenker et al., 2007, 2005; Walter et al., 2008). A similar trend is

seen in West African sublithospheric diamonds (Stachel et al., 2000a, 2000b). These studies point to total removal of slab carbonate during partial melting in the transition zone, producing a barrier to carbon influx into the lower mantle (Thomson et al., 2016). As such, diamond formation in the lower mantle has been attributed to the introduction of water, destabilising carbides and thus liberating carbon (Regier et al., 2020); however, this does not align with the mantle-like $\delta^{13}C$ signature of these diamonds nor does it address the depleted composition of the Koffiefontein lower mantle inclusions compared to experimentally-determined mineral compositions for lower mantle pyrolite. A connection between the depleted mineralogy of lower mantle inclusions in diamond and depleted suboceanic lithospheric peridotite has been made previously but lacked sufficient experimental and diamond data to be conclusive (Kesson and Fitz Gerald, 1991; Stachel et al., 2000b).

The sublithospheric suite of diamonds at Koffiefontein includes metaperidotitic lower mantle inclusions. Two of the lower mantle diamonds contain coexisting ferropericlase plus a $MgSiO_3$ phase interpreted to be retrogressed bridgmanite while one contains ferropericlase only. The retrogressed bridgmanite inclusions have low Al_2O_3 1.17-1.67 wt% and the ferropericlase inclusions had high NiO, all indications of lower mantle phases. Examining the Mg-Fe-Si relations of coexisting ferropericlase and bridgmanite to constrain bulk rock compositions indicates that they are too depleted to be pyrolitic mantle but instead range from slightly depleted lherzolitic to almost dunitic chemistries (Figure 6-6). Further, the mantle-like $\delta^{18}O$ of the retrogressed bridgmanite inclusions indicate no crustal component. The Koffiefontein sublithospheric diamonds all have tightly constrained, mantle-like $\delta^{13}C$ signatures (-3.4 to -6.2 ‰) with little in-diamond variability. Although the lower mantle diamonds had low nitrogen concentrations, two slightly more nitrogen-rich regions within the two bridgmanite-included diamonds have a ^{15}N-depleted signature ($\delta^{15}N$ of -14.1 ‰ and -14.8 ‰).

The Koffiefontein sublithospheric diamonds show indications for diamond formation via growth from both oxidized and reduced fluids or melts. Lower mantle diamond 21/01 likely formed from reduced C-rich fluids – possibly carrying ethane or methane – which left hydrous alteration around ferropericlase inclusions. The former-bridgmanite- and ferropericlase-included diamond 25/01, however, likely formed via growth from carbonate-bearing fluids, indicated by a

magnesite inclusion and alteration rim. A slab source for mantle-like $\delta^{13}C$ could also be extended to sublithospheric diamonds. As discussed above for the lithospheric diamond suite, homogenized slab carbon can form diamonds with a mantle-like $\delta^{13}C$ signature. Although the transition zone-lower mantle boundary can act as a barrier to slab-derived volatiles, the mantle-like $\delta^{13}C$ signature of lower mantle diamonds from Koffiefontein and from other locations is not consistent with formation from carbides, which should lead to precipitation of ^{13}C depleted diamonds. Consequently, carbon would need to be introduced in a localised, either oxidised or slightly reduced (e.g., CH_4) form. Thus, diamonds and their inclusions brought up from lower mantle depths, are not likely to carry carbon and nitrogen isotope signatures representative of ambient mantle, but instead ought to reflect volatile sources from deeply subducted lithosphere. The survival of carbonate in altered oceanic crust or underlying sub-oceanic peridotites into the lower mantle, however, is unknown.

7.4. Future directions

7.4.1. Oxygen isotopes of upper mantle and lower mantle carbonate phases

At Koffiefontein, diamond formation in upper and lower mantle substrates has been shown to likely relate to both reduced, methane-bearing, and oxidised, carbonate-bearing, fluids. Although carbonatitic melts cannot percolate through subsolidus harzburgite, carbonate-rich fluids can due to the lowered CO_2-H_2O-harzburgite solidus (Wyllie, 1978). Direct evidence for diamond formation from carbonate in lithospheric mantle peridotite is uncommon. The source of carbonate in the percolating fluids is not clear and could relate to either subducted altered oceanic crust or mobilisation from previously carbonated peridotite. The $\delta^{18}O$ composition of carbonate-inclusions or carbonate rims around minerals within diamond could relate this carbonate to either crustal or mantle sources. This can be extended into the lower mantle, where one Koffiefontein diamond shows evidence for formation from carbonated fluids/melts. Although a non-mantle-like $\delta^{18}O$ signature of these carbonates would clearly indicate crustal recycling, a mantle-like signature would not necessarily imply an origin from mantle fluids, since the mantle is an extremely large reservoir of oxygen and, therefore, readily capable of buffering external oxygen compositions.

7.4.2. Nitrogen fractionation of reduced species

For nitrogen – the most abundant impurity in diamond – incorporation into diamond is not fully understood and studies are still split between this element being either compatible or incompatible during diamond formation. Further, nitrogen speciation is complex, complicating constraining nitrogen fractionation factors during diamond growth, and increasing the complexity of understanding nitrogen incorporation. A significant difficulty in using N-isotopes to track reservoirs in the mantle – either introduced from subduction or based on heterogeneities in the mantle – is the source or formation of ^{15}N-depleted reservoirs. Since the 1980s, scientific studies on sedimentary rocks (e.g., Bebout, 1995) and subducted oceanic lithosphere (e.g., Li et al., 2007) have shown the evolution of δ^{15}N signatures through subduction-related metamorphism and mixing in the mantle. Although studies show a homogenous δ^{15}N value of ~-5 ‰ for the mantle (Marty, 1995), some diamonds from the lithosphere and the lower mantle, including examples from Koffiefontein, show a distinctly ^{15}N-depleted component. Recent evidence does not support the existence of primordial heterogeneities (Labidi et al., 2020) and thus the ^{15}N-depleted signature of these diamonds might be related to diamond formation. Nitrides or metal-hosted N is an alternative source for nitrogen in diamond. However, there are limited studies on nitrogen isotope fractionation factors for such hosts. As stated in Chapter 3 and 6, the ^{15}N-depleted signature of these diamonds could be produced by formation of COH-fluids, where the nitrogen could be derived from a nitride. This would then imply a decoupled origin of carbon and nitrogen, as the carbon isotopic compositions are not suggestive of highly reduced sources.

7.4.3. New mineral phases at Koffiefontein

During investigation of the Koffiefontein lithospheric diamonds, some unique inclusions were found, one representing a new perovskite group mineral – goldschmidtite (Meyer et al., 2019). Also included with goldschmidtite is an intergrowth of Mg-silicate, chromite, and Ta-K-oxide. The localized exceptional enrichment of K, Nb and Ta in a diamond substrate beneath Koffiefontein warrants further investigation as to how incompatible elements are enriched and move within the mantle. The enrichment of K in this mineral indicates that it has potential for K-Ar dating of diamond formation.

A hydrous Mg-rich silicate phase was also identified in one Koffiefontein diamond. The primary mineral chemistry is compatible with a dense hydrous magnesium silicate (DHMS), a phase that is responsible for hydrating both the upper mantle and transition zone. For mineral identification, crystal structure analyses are needed but this is hindered by the polycrystalline nature of the inclusion. This work is ongoing and once completed, would be unequivocal evidence for the storage of water as DHMS in the lithospheric mantle. Further, the association of this mineral with a sulphide inclusion in the same diamond could allow dating of the timing of its formation, linking water sequestration to an Archean or Proterozoic process, or perhaps a process associated with sulphide-rich fluids.

7.4.4. Sulphide-included diamonds at Koffiefontein as a separate paragenesis

Suggestions of a distinct origin for, specifically, Koffiefontein diamonds included with sulphide only have persisted since the late 1980s (Meyer, 1986). A further anomaly has been the wide range of Re-Os isochron ages that have dated diamond formation at this locality, ranging from the final merger of the Kaapvaal Craton (2.9-2.7 Ga) to as late as concurrent with kimberlite eruption (~90 Ma; Pearson et al., 1998). In addition to the timing of sulphide-included diamond formation, studies show that sulphide formation in the lower mantle proceeds by the oxidation of methane-bearing fluids (Smit et al., 2019). In sublithospheric sulphide melt-included diamonds, $CH_4 + H_2$ films were found surrounding the Fe-Ni-C-S inclusions (Smit et al., 2019). Work on Re-Os dating of additional sulphides in diamonds from Koffiefontein and evidence for H_2- or CH_4-rich fluid films surrounding sulphides is ongoing. With this information, the source of carbon – with mantle-like $\delta^{13}C$ – and nitrogen – high in concentration and mantle-like $\delta^{15}N$ – could shed light onto the reactions that produced these diamonds, which are in high abundance at Koffiefontein.

References

Adam, J., Locmelis, M., Afonso, J.C., Rushmer, T., Fiorentini, M.L., 2014. The capacity of hydrous fluids to transport and fractionate incompatible elements and metals within the Earth's mantle. Geochemistry, Geophys. Geosystems 15, 2241–2253. https://doi.org/10.1002/2013GC005199

Ader, M., Thomazo, C., Sansjofre, P., Busigny, V., Papineau, D., Laffont, R., Cartigny, P., Halverson, G.P., 2016. Interpretation of the nitrogen isotopic composition of Precambrian sedimentary rocks: Assumptions and perspectives. Chem. Geol. 429, 93–110. https://doi.org/10.1016/j.chemgeo.2016.02.010

Allègre, C.J., Poirier, J., Humler, E., Hofmann, A.W., 1995. The chemical composition of the Earth. Earth Planet. Sci. Lett. 134, 515–526. https://doi.org/10.1016/0012-821X(95)00123-T

Alt, J.C., Teagle, D.A.H., 1999. The uptake of carbon during alteration of ocean crust. Geochim. Cosmochim. Acta 63, 1527–1535. https://doi.org/10.1016/S0016-7037(99)00123-4

Andrault, D., 2003. Cationic substitution in $MgSiO_3$ perovskite. Phys. Earth Planet. Inter. 136, 67–78. https://doi.org/10.1016/S0031-9201(03)00023-2

Andrault, D., 2001. Evaluation of (Mg,Fe) partitioning between silicate perovskite and magnesiowustite up to 120 GPa and 2300 K. J. Geophys. Res. Solid Earth 106, 2079–2087. https://doi.org/10.1029/2000jb900362

Angel, R.J., Finger, L.W., 2011. SINGLE: A program to control single-crystal diffractometers. J. Appl. Crystallogr. 44, 247–251. https://doi.org/10.1107/S0021889810042305

Anhaeusser, C.R., Walraven, F., 1999. Episodic granitoid emplacement in the western Kaapvaal Craton: Evidence from the Archaean Kraaipan granite-greenstone terrane, south Africa. J. African Earth Sci. 28, 289–309. https://doi.org/10.1016/S0899-5362(99)00005-6

Appleyard, C.M., 2000. The geochemistry of a suite of eclogite xenoliths from the Rietfontein kimberlite, South Africa. University of Cape Town.

Armstrong, J.T., 1995. CITZAF: a package of correction programs for the quantitative electron microbeam X-ray-analysis of thick polished materials, thin-films, and particles. Microbeam Anal. 4, 177–200.

Arndt, N.T., Christensen, U., 1992. The role of lithospheric mantle in continental flood volcanism: thermal and geochemical constraints. J. Geophys. Res. 97. https://doi.org/10.1029/92jb00564

Aulbach, S., Jacob, D.E., Cartigny, P., Stern, R.A., Simonetti, S.S., Wörner, G., Viljoen, K.S., 2017. Eclogite xenoliths from Orapa: Ocean crust recycling, mantle metasomatism and carbon cycling at the western Zimbabwe craton margin. Geochim. Cosmochim. Acta 213, 574–592. https://doi.org/10.1016/j.gca.2017.06.038

Aulbach, S., Stachel, T., Heaman, L.M., Creaser, R.A., Shirey, S.B., 2011. Formation of cratonic subcontinental lithospheric mantle and complementary komatiite from hybrid plume sources. Contrib. to Mineral. Petrol. 161, 947–960. https://doi.org/10.1007/s00410-010-0573-4

Bailey, D.K., 1982. Mantle metasomatism – continuing chemical change within the Earth. Nature 296, 525–530. https://doi.org/10.1038/296525a0

Baker, M.B., Stolper, E.M., 1994. Determining the composition of high-pressure mantle melts using diamond aggregates. Geochim. Cosmochim. Acta 58, 2811–2827.

https://doi.org/10.1016/0016-7037(94)90116-3
Ballmer, M.D., Houser, C., Hernlund, J.W., Wentzcovitch, R.M., Hirose, K., 2017. Persistence of strong silica-enriched domains in the Earth's lower mantle. Nat. Geosci. 10, 236–240. https://doi.org/10.1038/ngeo2898
Barkov, A.Y., Martin, R.F., Men'shikov, Y.P., Savchenko, Y.E., Thibault, Y., Laajoki, K.V.O., 2000. Edgarite, $FeNb_3S_6$, first natural niobium-rich sulfide from the Khibina alkaline complex, Russian Far North: Evidence for chalcophile behavior of Nb in a fenite. Contrib. to Mineral. Petrol. 138, 229–236. https://doi.org/10.1007/s004100050559
Barry, P.H., Hilton, D.R., 2016. Release of subducted sedimentary nitrogen throughout Earth's mantle. Geochemical Perspect. Lett. 2, 148–159. https://doi.org/10.7185/geochemlet.1615
Barth, M.G., Rudnick, R.L., Horn, I., McDonough, W.F., Spicuzza, M.J., Valley, J.W., Haggerty, S.E., 2001. Geochemistry of xenolithic eclogites from West Africa, part I: A link between low MgO eclogites and archean crust formation. Geochim. Cosmochim. Acta 65, 1499–1527. https://doi.org/10.1016/S0016-7037(00)00626-8
Barth, T., 1925. Die Kristallstruktur von Perowskit und Verwandten Verbindungen. Nor. Geol. Tidsskr. 8, 201–216.
Bastiansen, O.C.A., 1962. Victor Moritz Goldschmidt 1888-1947, in: Ewald, P.P. (Ed.), Fifty Years of X-Ray Diffraction: Dedicated to the International Union of Crystallography on the Occasion of the Commemoration Meeting in Munich July 1962. Springer US, Utrecht, pp. 364–365.
Beard, B.L., Fraracci, K.N., Taylor, L.A., Snyder, G.A., Clayton, R.A., Mayeda, T.K., Sobolev, N. V., 1996. Petrography and geochemistry of eclogites from the Mir kimberlite, Yakutia, Russia. Contrib. to Mineral. Petrol. 125, 293–310. https://doi.org/DOI 10.1007/s004100050223
Beaumont, V., Robert, F., 1999. Nitrogen isotope ratios of kerogens in Precambrian cherts: a record of the evolution of atmosphere chemistry? Precambrian Res. 96, 63–82. https://doi.org/10.1016/S0301-9268(99)00005-4
Bebout, G.E., 1995. The impact of subduction-zone metamorphism on mantle-ocean chemical cycling. Chem. Geol. 126, 191–218. https://doi.org/10.1016/0009-2541(95)00118-5
Bebout, G.E., Fogel, M.L., 1992. Nitrogen-isotope compositions of metasedimentary rocks in the Catalina Schist, California: implications for metamorphic devolatilization history. Geochim. Cosmochim. Acta 56, 2839–2849. https://doi.org/10.1016/0016-7037(92)90363-N
Becker, M., le Roex, A.P., 2006. Geochemistry of South African on- and off-craton, group I and group II kimberlites: Petrogenesis and source region evolution. J. Petrol. 47, 673–703. https://doi.org/10.1093/petrology/egi089
Bedini, R.M., Blichert-Toft, J., Boyet, M., Albarède, F., 2004. Isotopic constraints on the cooling of the continental lithosphere. Earth Planet. Sci. Lett. 223, 99–111. https://doi.org/10.1016/j.epsl.2004.04.012
Bell, D.R., 1981. Ultramafic xenoliths from the Koffiefontein kimberlite pipe, RSA. University of Cape Town.
Bell, D.R., Grégoire, M., Grove, T.L., Chatterjee, N., Carlson, R.W., Buseck, P.R., 2005. Silica and volatile-element metasomatism of Archean mantle: a xenolith-scale example from the Kaapvaal Craton. Contrib. to Mineral. Petrol. 150, 251–267. https://doi.org/10.1007/s00410-005-0673-8
Bell, D.R., Rossman, G.R., 1992. Water in Earth's mantle: the role of nominally anhydrous minerals. Science 255, 1391–1397. https://doi.org/10.1126/science.255.5050.1391

Bell, D.R., Schmitz, M.D., Janney, P.E., 2003. Mesozoic thermal evolution of the southern African mantle lithosphere. Lithos 71, 273–287. https://doi.org/10.1016/S0024-4937(03)00117-8

Bernstein, S., Kelemen, P.B., Hanghøj, K., 2007. Consistent olivine Mg# in cratonic mantle reflects Archean mantle melting to the exhaustion of orthopyroxene. Geology 35, 459–462. https://doi.org/10.1130/G23336A.1

Biellmann, C., Gillet, P., Guyot, F., Peyronneau, J., Reynard, B., 1993. Experimental evidence for carbonate stability in the Earth's lower mantle. Earth Planet. Sci. Lett. 118, 31–41. https://doi.org/10.1016/0012-821X(93)90157-5

Bindi, L., Martin, R.F., 2018. Edgarite, $FeNb_3S_6$, from the Khibina alkaline complex, Russia: solution of the crystal structure. Can. Mineral. 56, 1–6. https://doi.org/10.3749/canmin.1800019

Bodinier, J.L., Godard, M., 2013. Orogenic, Ophiolitic, and Abyssal Peridotites, 3rd ed, Treatise on Geochemistry: Second Edition. Elsevier Ltd. https://doi.org/10.1016/B978-0-08-095975-7.00204-7

Boyd, F.R., 1989. Compositional distinction between oceanic and cratonic lithosphere. Earth Planet. Sci. Lett. 96, 15–26. https://doi.org/10.1016/0012-821X(89)90120-9

Boyd, F.R., 1987. High- and low-temperature garnet peridotite xenoliths and their possible relation to the lithosphere-asthenosphere boundary, in: Nixon, P.H. (Ed.), Mantle Xenoliths. John Wiley & Sons, Inc., pp. 403–412.

Boyd, F.R., England, J.L., 1960. Minerals of the mantle. Carnegie Inst. Washingt. Year B. 59, 47–52.

Boyd, F.R., Gurney, J.J., 1986. Diamonds and the African lithosphere. Science 232, 472–477. https://doi.org/10.1126/science.232.4749.472

Boyd, S.R., Kiflawi, I., Woods, G.S., 1995. Infrared absorption by the B nitrogen aggregate in diamond. Philos. Mag. B 72, 351–361. https://doi.org/10.1080/13642819508239089

Boyd, S.R., Kiflawi, I., Woods, G.S., 1994. The relationship between infrared absorption and the A defect concentration in diamond. Philos. Mag. Part B 69, 1149–1153. https://doi.org/10.1080/01418639408240185

Boyd, S.R., Mattey, D.P., Pillinger, C.T., Milledge, H.J., Mendelssohn, M., Seal, M., 1987. Multiple growth events during diamond genesis: an integrated study of carbon and nitrogen isotopes and nitrogen aggregation state in coated stones. Earth Planet. Sci. Lett. 86, 341–353. https://doi.org/10.1016/0012-821X(87)90231-7

Braun, M.G., Kelemen, P.B., 2002. Dunite distribution in the Oman Ophiolite: implications for melt flux through porous dunite conduits. Geochemistry, Geophys. Geosystems 3, 1–21. https://doi.org/10.1029/2001gc000289

Brenker, F.E., Stachel, T., Harris, J.W., 2002. Exhumation of lower mantle inclusions in diamond: ATEM investigation of retrograde phase transitions, reactions and exsolution. Earth Planet. Sci. Lett. 198, 1–9. https://doi.org/10.1016/S0012-821X(02)00514-9

Brenker, F.E., Vincze, L., Vekemans, B., Nasdala, L., Stachel, T., Vollmer, C., Kersten, M., Somogyi, A., Adams, F., Joswig, W., Harris, J.W., 2005. Detection of a Ca-rich lithology in the Earth's deep (300 km) convecting mantle. Earth Planet. Sci. Lett. 236, 579–587.

Brenker, F.E., Vollmer, C., Vincze, L., Vekemans, B., Szymanski, A., Janssens, K., Szaloki, I., Nasdala, L., Joswig, W., Kaminsky, F. V., 2007. Carbonates from the lower part of transition zone or even the lower mantle. Earth Planet. Sci. Lett. 260, 1–9. https://doi.org/10.1016/j.epsl.2007.02.038

Brey, G.P., Bulatov, V.K., Girnis, A. V., Harris, J.W., Stachel, T., 2004. Ferropericlase – A lower mantle phase in the upper mantle. Lithos 77, 655–663. https://doi.org/10.1016/j.lithos.2004.03.013

Brey, G.P., Köhler, T.P., 1990. Geothermobarometry in four-phase lherzolites 2. New thermobarometers, and practical assessment of existing thermobarometers. J. Petrol. 31, 1353–1378.

Brey, G.P., Köhler, T.P., Nickel, K.G., 1990. Geothermobarometry in four-phase lherzolites 1. Experimental results from 10 to 60 kb. J. Petrol. 31, 1313–1352.

Brey, G.P., Shu, Q., 2018. The birth, growth and ageing of the Kaapvaal subcratonic mantle. Mineral. Petrol. 112, 23–41. https://doi.org/10.1007/s00710-018-0577-8

Bulanova, G.P., 1995. The formation of diamond. J. Geochemical Explor. 53, 1–23. https://doi.org/10.1016/0375-6742(94)00016-5

Bulanova, G.P., Walter, M.J., Smith, C.B., Kohn, S.C., Armstrong, L.S., Blundy, J., Gobbo, L., 2010. Mineral inclusions in sublithospheric diamonds from Collier 4 kimberlite pipe, Juina, Brazil: Subducted protoliths, carbonated melts and primary kimberlite magmatism. Contrib. to Mineral. Petrol. 160, 489–510. https://doi.org/10.1007/s00410-010-0490-6

Bulatov, V., Brey, G.P., Foley, S.F., 1991. Origin of low-Ca, high-Cr garnets by recrystallization of low-pressure harzburgites. Proc. Int. Kimberl. Conf. 5, 29–31.

Bullen, K.E., 1950. An Earth model based on a compressibility-pressure hypothesis. Geophys. J. Int. 6, 50–59. https://doi.org/10.1111/j.1365-246X.1950.tb02973.x

Burnham, A.D., Bulanova, G.P., Smith, C.B., Whitehead, S.C., Kohn, S.C., Gobbo, L., Walter, M.J., 2016. Diamonds from the Machado River alluvial deposit, Rondônia, Brazil, derived from both lithospheric and sublithospheric mantle. Lithos 265, 199–213. https://doi.org/10.1016/j.lithos.2016.05.022

Burnham, A.D., Thomson, A.R., Bulanova, G.P., Kohn, S.C., Smith, C.B., Walter, M.J., 2015. Stable isotope evidence for crustal recycling as recorded by superdeep diamonds. Earth Planet. Sci. Lett. 432, 374–380. https://doi.org/10.1016/j.epsl.2015.10.023

Busigny, V., Bebout, G.E., 2013. Nitrogen in the silicate earth: speciation and isotopic behavior during mineral-fluid interactions. Elements 9, 353–358. https://doi.org/10.2113/gselements.9.5.353

Busigny, V., Cartigny, P., Philippot, P., Ader, M., Javoy, M., 2003. Massive recycling of nitrogen and other fluid-mobile elements (K, Rb, Cs, H) in a cold slab environment: evidence from HP to UHP oceanic metasediments of the Schistes Lustrés nappe (western Alps, Europe). Earth Planet. Sci. Lett. 215, 27–42. https://doi.org/10.1016/S0012-821X(03)00453-9

Bussweiler, Y., Brey, G.P., Pearson, D.G., Stachel, T., Stern, R.A., Hardman, M.F., Kjarsgaard, B.A., Jackson, S.E., 2017. The aluminium-in-olivine thermometer for mantle peridotites - Experimental versus empirical calibration and potential applications. Lithos 272–273, 301–314.

Bussweiler, Y., Giuliani, A., Greig, A., Kjarsgaard, B.A., Petts, D., Jackson, S.E., Barrett, N., Luo, Y., Pearson, D.G., 2019. Trace element analysis of high-Mg olivine by LA-ICP-MS – Characterization of natural olivine standards for matrix-matched calibration and application to mantle peridotites. Chem. Geol. 524, 136–157. https://doi.org/10.1016/j.chemgeo.2019.06.019

Canil, D., 2008. Canada's craton: A bottoms-up view. GSA Today 18, 4–10. https://doi.org/10.1130/GSAT01806A.1

Canil, D., 1999. The Ni-in-garnet geothermometer: Calibration at natural abundances. Contrib. to Mineral. Petrol. 136, 240–246. https://doi.org/10.1007/s004100050535
Canil, D., O'Neill, H.S.C., 1996. Distribution of ferric iron in some upper-mantle assemblages. J. Petrol. 37, 609–635. https://doi.org/10.1093/petrology/37.3.609
Cardoso, P., 1980. A study of mantle inclusions in the Koffiefontein kimberlite pipe, South Africa. University of Cape Town.
Carswell, D.A., Gibb, F.G.F., 1987. Evaluation of mineral thermometers and barometers applicable to garnet lherzolite assemblages. Contrib. to Mineral. Petrol. 95, 499–511.
Cartigny, P., 2005. Stable isotopes and the origin of diamond. Elements 1, 79–84. https://doi.org/10.2113/gselements.1.2.79
Cartigny, P., Boyd, S.R., Harris, J.W., Javoy, M., 1997. Nitrogen isotopes in peridotitic diamonds from Fuxian, China: the mantle signature. Terra Nov. 9, 175–179. https://doi.org/10.1046/j.1365-3121.1997.d01-26.x
Cartigny, P., Farquhar, J., Thomassot, E., Harris, J.W., Wing, B.A., Masterson, A., McKeegan, K., Stachel, T., 2009. A mantle origin for Paleoarchean peridotitic diamonds from the Panda kimberlite, Slave Craton: Evidence from ^{13}C-, ^{15}N- and $^{33,34}S$-stable isotope systematics. Lithos 112, 852–864. https://doi.org/10.1016/j.lithos.2009.06.007
Cartigny, P., Harris, J.W., Javoy, M., 1998a. Eclogitic diamond formation at Jwaneng: No room for a recycled component. Science 280, 1421–1424. https://doi.org/10.1126/science.280.5368.1421
Cartigny, P., Harris, J.W., Phillips, D.L., Girard, M., Javoy, M., 1998b. Subduction-related diamonds? – The evidence for a mantle derived origin from coupled $\delta^{13}C$-$\delta^{15}N$ determinations. Chem. Geol. 147, 147–159.
Cartigny, P., Marty, B., 2013. Nitrogen isotopes and mantle geodynamics: The emergence of life and the atmosphere-crust-mantle connection. Elements 9, 359–366. https://doi.org/10.2113/gselements.9.5.359
Cartigny, P., Palot, M., Thomassot, E., Harris, J.W., 2014. Diamond formation: a stable isotope perspective. Annu. Rev. Earth Planet. Sci. 42, 699–732. https://doi.org/10.1146/annurev-earth-042711-105259
Cayzer, N.J., Odake, S., Harte, B., Kagi, H., 2008. Plastic deformation of lower mantle diamonds by inclusion phase transformations. Eur. J. Mineral. 20, 333–339. https://doi.org/10.1127/0935-1221/2008/0020-1811
Chacko, T., Mayeda, T.K., Clayton, R.N., Goldsmith, J.R., 1991. Oxygen and carbon isotope fractionations between CO2 and calcite. Geochim. Cosmochim. Acta 55, 2867–2882. https://doi.org/10.1016/0016-7037(91)90452-B
Chakhmouradian, A., Yakovenchuk, V.N., Mitchell, R.H., Bogdanova, A., 1997. Isolueshite: a new mineral of the perovskite group from the Khibina alkaline complex. Eur. J. Mineral. 9, 483–490. https://doi.org/10.1127/ejm/9/3/0483
Chantler, C.T., Olsen, K., Dragoset, R.A., Chang, J., Kishore, A.R., Kotochigova, S.A., Zucker, D.S., 2005. X-ray form factor, attenuation and scattering tables, NIST Standard Reference Database 66.
Clement, C.R., 1982. A comparative geological study of some major kimberlite pipes in the Northern Cape and Orange Free State. University of Cape Town.
Dalou, C., Füri, E., Deligny, C., Piani, L., Caumon, M.C., Laumonier, M., Boulliung, J., Edén, M., 2019. Redox control on nitrogen isotope fractionation during planetary core formation. Proc. Natl. Acad. Sci. U. S. A. 116, 14485–14494. https://doi.org/10.1073/pnas.1820719116

Dalton, J.A., Wood, B.J., 1993. The partitioning of Fe and Mg between olivine and carbonate and the stability of carbonate under mantle conditions. Contrib. to Mineral. Petrol. 114, 501–509. https://doi.org/10.1007/BF00321754

Dasgupta, R., 2013. Ingassing, storage, and outgassing of terrestrial carbon through geologic time. Rev. Mineral. Geochemistry 75, 183–229. https://doi.org/10.2138/rmg.2013.75.7

Dasgupta, R., Hirschmann, M.M., 2010. The deep carbon cycle and melting in Earth's interior. Earth Planet. Sci. Lett. 298, 1–13. https://doi.org/10.1016/j.epsl.2010.06.039

Dasgupta, R., Hirschmann, M.M., Withers, A.C., 2004. Deep global cycling of carbon constrained by the solidus of anhydrous, carbonated eclogite under upper mantle conditions. Earth Planet. Sci. Lett. 227, 73–85. https://doi.org/10.1016/j.epsl.2004.08.004

Davies, G., 1976. The A nitrogen aggregate in diamond – its symmetry and possible structure. J. Phys. C Solid State Phys. 9, L537–L542. https://doi.org/10.1088/0022-3719/9/19/005

Davies, R.M., Griffin, W.L., Pearson, N.J., Andrew, A., Doyle, B.J., O'Reilly, S.Y., 1999. Diamonds from the deep: pipe DO-27, Salve Craton, Canada. Proc. 7th Int. Kimberl. Conf. 1, 148–155.

Davis, G.L., 1978. Zircons from the mantle, in: Zartman, R.E. (Ed.), Fourth International Conference, Geochronology, Cosmochronology, Isotope Geology. United States department of the interior geological survey, Colorado, pp. 86–88.

Davis, G.L., 1977. The ages and uranium contents of zircons from kimberlites and associated rocks. Year B. Carnegie Inst. Washingt. 76, 631–635.

Dawson, J.B., 1984. Contrasting types of upper-mantle metasomatism? Dev. Petrol. 11, 289–294. https://doi.org/10.1016/B978-0-444-42274-3.50030-5

Dawson, J.B., 1982. Contrasting types of mantle metasomatism, in: International Kimberlite Conference: Extended Abstracts. pp. 232–233.

Day, H.W., 2012. A revised diamond-graphite transition curve. Am. Mineral. 97, 52–62. https://doi.org/10.2138/am.2011.3763

De Hoog, J.C.M., Gall, L., Cornell, D.H., 2010. Trace-element geochemistry of mantle olivine and application to mantle petrogenesis and geothermobarometry. Chem. Geol. 270, 196–215. https://doi.org/10.1016/j.chemgeo.2009.11.017

De Wit, M.J., Roering, C., Hart, R.J., Armstrong, R.A., de Ronde, C.E.J., Green, R.W.E., Tredoux, M., Peberdy, E., Hart, R.A., 1992. Formation of an Archaean continent. Nature 357, 553–562. https://doi.org/10.1038/357553a0

Deines, P., 1980. The carbon isotopic composition of diamonds: relationship to diamond shape, color, occurrence and vapor composition. Geochim. Cosmochim. Acta 44, 943–961. https://doi.org/10.1016/0016-7037(80)90284-7

Deines, P., Haggerty, S.E., 2000. Small-scale oxygen isotope variations and petrochemistry of ultradeep (>300 km) and transition zone xenoliths. Geochim. Cosmochim. Acta 64, 117–131. https://doi.org/10.1016/S0016-7037(99)00211-2

Deines, P., Harris, J.W., Gurney, J.J., 1991a. The carbon isotopic composition and nitrogen content of lithospheric and asthenospheric diamonds from the Jagersfontein and Koffiefontein kimberlite, South Africa. Geochim. Cosmochim. Acta 55, 2615–2625. https://doi.org/10.1016/0016-7037(91)90377-H

Deines, P., Harris, J.W., Gurney, J.J., 1987. Carbon isotopic composition, nitrogen content and inclusion composition of diamonds from the Roberts Victor kimberlite, South Africa: evidence for 13C depletion in the mantle. Geochim. Cosmochim. Acta 51, 1227–1243. https://doi.org/10.1016/0016-7037(87)90215-8

Deines, P., Harris, J.W., Robinson, D.N., Gurney, J.J., Shee, S.R., 1991b. Carbon and oxygen isotope variations in diamond and graphite eclogites from Orapa, Botswana, and the nitrogen content of their diamonds. Geochim. Cosmochim. Acta 55, 515–524. https://doi.org/10.1016/0016-7037(91)90009-T

Desmons, J., Smulikowski, W., 2007. High P/T Metamorphic Rocks, in: Fettes, D., Desmons, J. (Eds.), Metamorphic Rocks: A Classification and Glossary of Terms. Cambridge University Press, Cambridge, pp. 32–35.

DeVries, R.C., 1975. Plastic deformation and "work-hardening" of diamond. Mater. Res. Bull. 10, 1193–1199. https://doi.org/10.1016/0025-5408(75)90026-4

Dobrzhinetskaya, L.F., Wirth, R., Yang, J., Hutcheon, I.D., Weber, P.K., Green, H.W., 2009. High-pressure highly reduced nitrides and oxides from chromitite of a Tibetan ophiolite. Proc. Natl. Acad. Sci. U. S. A. 106, 19233–19238. https://doi.org/10.1073/pnas.0905514106

Donnelly, C.L., Stachel, T., Creighton, S., Muehlenbachs, K., Whiteford, S., 2007. Diamonds and their mineral inclusions from the A154 South pipe, Diavik Diamond Mine, Northwest territories, Canada. Lithos 98, 160–176. https://doi.org/10.1016/j.lithos.2007.03.003

Donovan, J.J., Kremser, D., Fournelle, J.H., Goemann, K., 2015. Probe for EPMA: acquisition, automation and analysis.

Donovan, J.J., Lowers, H.A., Rusk, B.G., 2011. Improved electron probe microanalysis of trace elements in quartz. Am. Mineral. 96, 274–282. https://doi.org/10.2138/am.2011.3631

Dorfman, S.M., Badro, J., Nabiei, F., Prakapenka, V.B., Cantoni, M., Gillet, P., 2018. Carbonate stability in the reduced lower mantle. Earth Planet. Sci. Lett. 489, 84–91. https://doi.org/10.1016/j.epsl.2018.02.035

Duncan, R.A., Hooper, P.R., Rehacek, J., Marsh, J.S., Duncan, A.R., 1997. The timing and duration of the Karoo igneous event, southern Gondwana. J. Geophys. Res. B Solid Earth 102, 18127–18138. https://doi.org/10.1029/97jb00972

Dziewonski, A.M., Anderson, D.L., 1981. Preliminary reference Earth model. Phys. Earth Planet. Inter. 25, 297–356. https://doi.org/10.1016/0031-9201(81)90046-7

Eaton, D.W., Perry, H.K.C., 2013. Ephemeral isopycnicity of cratonic mantle keels. Nat. Geosci. 6, 967–970. https://doi.org/10.1038/ngeo1950

Eglington, B.M., Armstrong, R.A., 2004. The Kaapvaal Craton and adjacent orogens, southern Africa: a geochronological database and overview of the geological development of the craton. South African J. Geol. 107, 13–32. https://doi.org/10.2113/107.1-2.13

Eiler, J.M., 2001. Oxygen Isotope Variations of Basaltic Lavas and Upper Mantle Rocks. Rev. Mineral. Geochemistry 43, 319–364. https://doi.org/10.2138/gsrmg.43.1.319

Eldridge, C.S., Compston, W., Williams, I.S., Harris, J.W., Bristow, J.W., 1991. Isotope evidence for the involement of recycled sediments in diamond formation. Nature 353, 649–653. https://doi.org/10.1038/246170a0

Erlank, A.J., Rickard, R.S., 1977. Potassic richterite bearing peridotites from kimberlite and the evidence they provide for upper mantle metasomatism, in: International Kimberlite Conference: Extended Abstracts. pp. 93–95.

Evans, T., Harris, J.W., 1989. Nitrogen aggregation, inclusion equilibrium temperatures and the age of diamonds, in: Ross, J. (Ed.), Kimberlites and Related Rocks. Geological Society of Australia, pp. 1001–1006.

Evans, T., Kiflawei, I., Luyten, W., van Tendeloo, G., Woods, G.S., 1995. Conversion of platelets into dislocation loops and voidite formation in type IaB diamonds. Proc. R. Soc. London. Ser. A Math. Phys. Sci. 449, 295–313. https://doi.org/10.1098/rspa.1995.0045

Evans, T., Qi, Z., 1982. The kinetics of the aggregation of nitrogen atoms in diamond. Proc. R. Soc. A Math. Phys. Eng. Sci. 381, 159–178. https://doi.org/10.1098/rspa.1982.0063
Fei, Y., Wang, Y., Finger, L.W., 1996. Maximum solubility of FeO in (Mg,Fe)SiO_3-perovskite as a function of temperature at 26 GPa: Implication for FeO content in the lower mantle. J. Geophys. Res. B Solid Earth 101, 11525–11530. https://doi.org/10.1029/96jb00408
Field, M., Stiefenhofer, J., Robey, J., Kurszlaukis, S., 2008. Kimberlite-hosted diamond deposits of southern Africa: a review. Ore Geol. Rev. 34, 33–75. https://doi.org/10.1016/j.oregeorev.2007.11.002
Frey, F.A., Green, D.H., 1974. The mineralogy, geochemistry and origin of lherzolite inclusions in Victorian basanites. Geochim. Cosmochim. Acta 38, 1023–1059. https://doi.org/10.1016/0016-7037(74)90003-9
Frost, B.R., Chacko, T., 1989. The granulite uncertainty principle: limitations on thermobarometry in granulite. J. Geol. 97, 435–450.
Frost, D.J., 2008. The upper mantle and transition zone. Elements 4, 171–176. https://doi.org/10.2113/GSELEMENTS.4.3.171
Frost, D.J., 1999. The stability of dense hydrous magnesium silicates in Earth's transition zone and lower mantle, in: Fei, Y., Bertka, C.M., Mysen, B.O. (Eds.), Mantle Petrology: Field Observations and High Pressure Experimentation (a Tribute to Francis R. (Joe) Boyd). The Geochemical Society, pp. 283–296.
Frost, D.J., Langenhorst, F., 2002. The effect of Al_2O_3 on Fe–Mg partitioning between magnesiowüstite and magnesium silicate perovskite. Earth Planet. Sci. Lett. 199, 227–241. https://doi.org/10.1016/S0012-821X(02)00558-7
Frost, D.J., Liebske, C., Langenhorst, F., McCammon, C.A., Trønnes, R.G., Rubie, D.C., 2004. Experimental evidence for the existence of iron-rich metal in the Earth's lower mantle. Nature 428, 409–412. https://doi.org/10.1038/nature02413
Frost, D.J., McCammon, C.A., 2008. The Redox State of Earth's Mantle. Annu. Rev. Earth Planet. Sci. 36, 389–420. https://doi.org/10.1146/annurev.earth.36.031207.124322
Gale, A., Dalton, C.A., Langmuir, C.H., Su, Y., Schilling, J.G., 2013. The mean composition of ocean ridge basalts. Geochemistry, Geophys. Geosystems 14, 489–518. https://doi.org/10.1029/2012GC004334
Galimov, E.M., 1991. Isotope fractionation related to kimberlite magmatism and diamond formation. Geochim. Cosmochim. Acta 55, 1697–1708. https://doi.org/10.1016/0016-7037(91)90140-Z
Garlick, G.D., MacGregor, I.D., Vogel, D.E., 1971. Oxygen isotope ratios in eclogites from kimberlites. Science 172, 1025–1027. https://doi.org/10.1126/science.172.3987.1025
Gasparik, T., Tripathi, A., Parise, J.B., 2000. Structure of a new Al-rich phase, $[K, Na]_{0.9}[Mg, Fe]_2[Mg, Fe, Al, Si]_6O_{12}$, synthesized at 24 GPa. Am. Mineral. 85, 613–618. https://doi.org/10.2138/am-2000-0426
Gibson, S., 2017. On the nature and origin of garnet in highly-refractory Archean lithospheric mantle : constraints from garnet exsolved in Kaapvaal craton orthopyroxenes. Mineral. Mag. 81, 781–809. https://doi.org/10.1180/minmag.2016.080.158
Goes, S., Hasterok, D., Schutt, D.L., Klöcking, M., 2020. Continental lithospheric temperatures: A review. Phys. Earth Planet. Inter. 306. https://doi.org/10.1016/j.pepi.2020.106509
Goldschmidt, V.M., 1926. Geochemische Verteilungsgesetze VII. Die Gesetze der Krystallochemie nach Untersuchungen gemeinsam mit T. Barth, G. Lunde, W. Zacharisasen. Skr. Utg. av det Nor. Videnskaps-Akademi i Oslo 1 Mat. Naturvidenskapelig

Klasse 1–117.
Green, D.H., 1990. The role of oxidation-reduction and C-H-O fluids in determining melting conditions and magma compositions in the upper mantle. Proc. Indian Acad. Sci. - Earth Planet. Sci. 99, 153–165. https://doi.org/10.1007/BF02871903
Green, D.H., Hibberson, W.O., Jaques, A.L., 1979. Petrogenesis of mid-ocean ridge basalt, in: McElhinny, M.W. (Ed.), The Earth, Its Origin, Structure, and Evolution. Academic Press, London, pp. 265–300.
Green, D.H., Ringwood, A.E., 1969. The origin of basalt magmas, in: Hart, P.J. (Ed.), Geophysical Monograph Series. William Bryd Press, Richmond, pp. 489–495. https://doi.org/10.1029/GM013p0489
Green, D.H., Ringwood, A.E., 1967. The stability fields of aluminous pyroxene peridotite and garnet peridotite and their relevance in upper mantle structure. Earth Planet. Sci. Lett. 3, 151–160.
Green, D.H., Wallace, M., 1988. Mantle metasomatism by ephemeral carbonatite melts. Nature 336, 459–462. https://doi.org/10.1038/336459a0
Gregory, R.T., Taylor, H.P., 1981. An oxygen isotope profile in a section of Cretaceous oceanic crust, Samail Ophiolite, Oman: Evidence for $\delta^{18}O$ buffering of the oceans by deep (>5 km) seawater-hydrothermal circulation at mid-ocean ridges. J. Geophys. Res. Solid Earth 86, 2737–2755. https://doi.org/10.1029/jb086ib04p02737
Griffin, W.L., Batumike, J.M., Greau, Y., Pearson, N.J., Shee, S.R., 2014. Emplacement ages and sources of kimberlites and related rocks in southern Africa : U–Pb ages and Sr–Nd isotopes of groundmass perovskite. Contrib. to Mineral. Petrol. 168, 1032. https://doi.org/10.1007/s00410-014-1032-4
Griffin, W.L., Jaques, A.L., Sie, S.H., Ryan, C.G., Cousens, D.R., Suter, G.F., 1988. Conditions of diamond growth: a proton microprobe study of inclusions in West Australian diamonds. Contrib. to Mineral. Petrol. 99, 143–158. https://doi.org/10.1007/BF00371457
Griffin, W.L., O'Reilly, S.Y., Natapov, L.M., Ryan, C.G., 2003. The evolution of lithospheric mantle beneath the Kalahari Craton and its margins. Lithos 71, 215–241. https://doi.org/10.1016/j.lithos.2003.07.006
Griffin, W.L., O'Reilly, S.Y., Ryan, C.G., 1999. The composition and origin of sub-continental lithospheric mantle, in: Fei, Y., Bertka, C.M., Mysen, B.O. (Eds.), Mantle Petrology: Field Observations and High Pressure Experimentation (a Tribute to Francis R. (Joe) Boyd). The Geochemical Society, pp. 13–45.
Grütter, H.S., 2009. Pyroxene xenocryst geotherms: Techniques and application. Lithos 112, 1167–1178. https://doi.org/10.1016/j.lithos.2009.03.023
Grütter, H.S., Apter, D.B., Kong, J., 1999. Crust-mantle coupling: evidence from mantle-derived xenocrystic garnets, in: Gurney, J.J., Gurney, J.L., Pascoe, M.D., Richardson, S.H. (Eds.), The J.B. Dawson Volume, Proceedings of the VIIth International Kimberlite Conference. Red Roof Designs, Cape Town, pp. 307–313.
Grütter, H.S., Gurney, J.J., Menzies, A.H., Winter, F., 2004. An updated classification scheme for mantle-derived garnet, for use by diamond explorers. Lithos 77, 841–857. https://doi.org/10.1016/j.lithos.2004.04.012
Grütter, H.S., Latti, D., Menzies, A.H., 2006. Cr-saturation arrays in concentrate garnet compositions from kimberlite and their use in mantle barometry. J. Petrol. 47, 801–820. https://doi.org/10.1093/petrology/egi096
Gurney, J.J., 1984. A correlation between garnets and diamonds in kimberlites, in: Glover, J.E.,

Harris, P.G. (Eds.), Kimberlite Occurrence and Origin: A Basis for Conceptual Models in Exploration. The University of Western Australia, Perth, pp. 143–166.
Gurney, J.J., Harris, J.W., Rickard, R.S., 1984. Silicate and oxide inclusions in diamonds from the Orapa Mine, Botswana. Dev. Petrol. 11, 3–9. https://doi.org/10.1016/B978-0-444-42274-3.50007-X
Gurney, J.J., Harte, B., 1980. Chemical variations in upper mantle nodules from southern African kimberlites. Philos. Trans. R. Soc. A Math. Phys. Eng. Sci. 297, 273–293. https://doi.org/10.1098/rsta.1980.0215
Gurney, J.J., Helmstaedt, H.H., Richardson, S.H., Shirey, S.B., 2010. Diamonds through time. Econ. Geol. 105, 689–712. https://doi.org/10.2113/gsecongeo.105.3.689
Haendel, D., Mühle, K., Nitzsche, H.M., Stiehl, G., Wand, U., 1986. Isotopic variations of the fixed nitrogen in metamorphic rocks. Geochim. Cosmochim. Acta 50, 749–758. https://doi.org/10.1016/0016-7037(86)90351-0
Haggerty, S.E., 1986. Diamond genesis in a multiply-constrained model. Nature 320, 34–38. https://doi.org/10.1038/320034a0
Haggerty, S.E., Grey, I.E., Madsen, I.C., Criddle, A.J., Stanley, C.J., Erlank, A.J., 1989. Hawthorneite, $Ba[Ti_3Cr_4Fe_4Mg]O_{19}$: A new metasomatic magnetoplumbite-type mineral from the upper mantle. Am. Mineral. 74, 668–675.
Haggerty, S.E., Smyth, J.R., Erlank, A.J., Rickard, R.S., Danchin, R. V., 1983. Lindsleyite (Ba) and mathiasite (K): two new chromium-titanates in the crichtonite series from the upper mantle. Am. Mineral. 68, 494–505.
Hanrahan, M., 2003. Garnet peridotite xenoliths from the Koffiefontein mine, South Africa. University of Alberta.
Hanschmann, G., 1981. Berechnung von isotopeneffekten auf quantenchemischer Grundlage am Beispiel stickstoffhaltiger Moleküle. Zitl.-Mitt. 41, 19–39.
Harley, S.L., 1984. An experimental study of the partitioning of Fe and Mg between garnet and orthopyroxene. Contrib. to Mineral. Petrol. 86, 359–373.
Harris, J.W., 1987. Recent physical, chemical, and isotopic research of diamond, in: Nixon, P.H. (Ed.), Mantle Xenoliths. John Wiley & Sons, Inc., pp. 477–500.
Harris, J.W., Gurney, J.J., 1979. Inclusions in diamond, in: Field, J.E. (Ed.), The Properties of Diamond. Academic Press, London, pp. 555–591.
Harris, J.W., Hawthorne, J.B., Oosterveld, M.M., Wehmeyer, E., 1975. A classification scheme for diamond and a comparative study of South African diamond characteristics, in: Ahrens, L.A., Dawson, J.B., Duncan, A.R., Erlank, A.J. (Eds.), Physics and Chemistry of the Earth. Pergamom Press, Oxford, pp. 765–783. https://doi.org/10.1016/0079-1946(75)90050-6
Harris, J.W., Hutchison, M.T., Hursthouse, M.B., Light, M.E., Harte, B., 1997. A new tetragonal silicate mineral occurring as inclusions in lower-mantle diamonds. Nature. https://doi.org/10.1038/387486a0
Harte, B., 2010. Diamond formation in the deep mantle: the record of mineral inclusions and their distribution in relation to mantle dehydration zones. Mineral. Mag. 74, 189–215. https://doi.org/10.1180/minmag.2010.074.2.189
Harte, B., Harris, J.W., 1994. Lower mantle mineral associations preserved in diamonds. Mineral. Mag. 58A, 384–385. https://doi.org/10.1180/minmag.1994.58A.1.201
Harte, B., Harris, J.W., Hutchison, M.T., Watt, G.R., Wilding, M.C., 1999. Lower mantle mineral associations in diamonds from Sao Luiz, Brazil, in: Fei, Y., Bertka, C.M., Mysen, B.O. (Eds.), Mantle Petrology: Field Observations and High Pressure Experimentation (a

Tribute to Francis R. (Joe) Boyd). The Geochemical Society, pp. 125–153.
Harte, B., Hudson, N.F.C., 2013. Proceedings of 10th International Kimberlite Conference. Proc. 10th Int. Kimberl. Conf. 1. https://doi.org/10.1007/978-81-322-1170-9
Harte, B., Otter, M., 1992. Carbon isotope measurements on diamonds. Chem. Geol. 101, 177–183. https://doi.org/10.1016/0009-2541(92)90215-q
Hasterok, D., Chapman, D.S., 2011. Heat production and geotherms for the continental lithosphere. Earth Planet. Sci. Lett. 307, 59–70.
Hauri, E.H., Shimizu, N., Dieu, J.J., Hart, S.R., Hauri, E.H., Shimizu, N., Dieu, J.J., Hart, S.R., 1993. Evidence for hotspot-related carbonatite metasomatism in the oceanic upper mantle. Nature 365, 221–227. https://doi.org/10.1038/365221a0
Hayman, P.C., Kopylova, M.G., Kaminsky, F. V., 2005. Lower mantle diamonds from Rio Soriso (Juina area, Mato Grosso, Brazil). Contrib. to Mineral. Petrol. 149, 430–445. https://doi.org/10.1007/s00410-005-0657-8
Heaman, L.M., Phillips, D., Pearson, G., 2019. Dating kimberlites: methods and emplacement patterns through time. Elements 15, 399–404. https://doi.org/10.2138/gselements.15.6.399
Helmstaedt, H.H., Gurney, J.J., Richardson, S.H., 2010. Ages of cratonic diamond and lithosphere evolution: constraints on Precambrian tectonics and diamond exploration. Can. Mineral. 48, 1385–1408. https://doi.org/10.3749/canmin.48.5.1385
Herzberg, C., 1999. Phase equilibrium constraints on the formation of cratonic mantle, in: Fei, Y., Bertka, C.M., Mysen, B.O. (Eds.), Mantle Petrology: Field Observations and High Pressure Experimentation (a Tribute to Francis R. (Joe) Boyd). The Geochemical Society, pp. 241–257.
Herzberg, C., Condie, K., Korenaga, J., 2010. Thermal history of the Earth and its petrological expression. Earth Planet. Sci. Lett. 292, 79–88. https://doi.org/10.1016/j.epsl.2010.01.022
Hirose, K., 2002. Phase transitions in pyrolitic mantle around 670-km depth: Implications for upwelling of plumes from the lower mantle. J. Geophys. Res. Solid Earth 107, ECV 3-1-ECV 3-13. https://doi.org/10.1029/2001jb000597
Hirose, K., Fei, Y., Ma, Y., Mao, H.K., 1999. The fate of subducted basaltic crust in the Earth's lower mantle. Nature 397, 53–56. https://doi.org/10.1038/16225
Hoal, K.E.O., Hoal, B.G., Erlank, A.J., Shimizu, N., 1994. Metasomatism of the mantle lithosphere recorded by rare earth elements in garnets. Earth Planet. Sci. Lett. 126, 303–313. https://doi.org/10.1016/0012-821X(94)90114-7
Hobbs, W.H., 1899. Goldschmidtite, a new mineral. Am. J. Sci. 357–364.
Hofmann, A.W., 1988. Chemical differentiation of the Earth: the relationship between mantle, continental crust, and oceanic crust. Earth Planet. Sci. Lett. 90, 297–314. https://doi.org/10.1016/0012-821X(88)90132-X
Holmquist, P.J., 1897. Synthetische Studien über die Perowskit- und Pyrochlormineralien. Geol. Inst. Univ. UPSALA 3, 181–268.
Honma, H., Itihara, Y., 1981. Distribution of ammonium in minerals of metamorphic and granitic rocks. Geochim. Cosmochim. Acta 45, 983–988. https://doi.org/10.1016/0016-7037(81)90122-8
Horita, J., Polyakov, V.B., 2015. Carbon-bearing iron phases and the carbon isotope composition of the deep Earth. Proc. Natl. Acad. Sci. U. S. A. 112, 31–36. https://doi.org/10.1073/pnas.1401782112
Houser, C., Hernlund, J.W., Valencia-Cardona, J., Wentzcovitch, R.M., 2020. Discriminating lower mantle composition. Phys. Earth Planet. Inter. 308, 106552.

https://doi.org/10.1016/j.pepi.2020.106552
Howell, D., Stachel, T., Stern, R.A., Pearson, D.G., Nestola, F., Hardman, M.F., Harris, J.W., Jaques, A.L., Shirey, S.B., Cartigny, P., Smit, K. V., Aulbach, S., Brenker, F.E., Jacob, D.E., Thomassot, E., Walter, M.J., Navon, O., 2020. Deep carbon through time: Earth's diamond record and its implications for carbon cycling and fluid speciation in the mantle. Geochim. Cosmochim. Acta 275, 99–122. https://doi.org/10.1016/j.gca.2020.02.011
Howell, D.H., O'Neill, C.J., Grant, K.J., Griffin, W.L., O'Reilly, S.Y., Pearson, N.J., Stern, R.A., Stachel, T., 2012a. Platelet development in cuboid diamonds: insights from micro-FTIR mapping. Contrib. to Mineral. Petrol. 164, 1011–1025. https://doi.org/10.1007/s00410-012-0786-9
Howell, D.H., O'Neill, C.J., Grant, K.J., Griffin, W.L., Pearson, N.J., O'Reilly, S.Y., 2012b. μ-FTIR mapping: distribution of impurities in different types of diamond growth. Diam. Relat. Mater. 29, 29–36. https://doi.org/10.1016/j.diamond.2012.06.003
Hunt, L., Stachel, T., McCandless, T.E., Armstrong, J., Muelenbachs, K., 2012. Diamonds and their mineral inclusions from the Renard kimberlites in Quebec. Lithos 142–143, 267–284. https://doi.org/10.1016/j.lithos.2012.02.022
Hutchinson, M.T., Cartigny, P., Harris, J.W., 1999. Carbon and nitrogen compositions and physical characteristics of transition zone and lower mantle diamonds from Sao Luiz, Brazil., in: Gurney, J.J., Gurney, J.L., Pascoe, M.D., Richardson, S.H. (Eds.), The JB Dawson Volume, Proceedings of the VIIth International Kimberlite Conference. Red Roof Design, Cape Town, pp. 372–283.
Hutchison, M.T., 1997. Constitution of the deep transition zone and lower mantle shown by diamonds and their inclusions. University of Edinburgh.
Ickert, R.B., Stachel, T., Stern, R.A., Harris, J.W., 2015. Extreme ^{18}O-enrichment in majorite constrains a crustal origin of transition zone diamonds. Geochemical Perspect. Lett. 1, 65–74. https://doi.org/10.7185/geochemlet.1507
Ionov, D.A., Harmon, R.S., France-Lanord, C., Greenwood, P.B., Ashchepkov, I. V., 1994. Oxygen isotope composition of garnet and spinel peridotites in the continental mantle: Evidence from the Vitim xenolith suite, southern Siberia. Geochim. Cosmochim. Acta 58, 1463–1470. https://doi.org/10.1016/0016-7037(94)90549-5
Irifune, T., 1994. Absence of an aluminous phase in the upper part of the Earth's lower mantle. Nature 370, 131–133. https://doi.org/10.1038/370131a0
Irifune, T., Ringwood, A.E., 1993. Phase transformations in subducted oceanic crust and buoyancy relationships at depths of 600-800 km in the mantle. Earth Planet. Sci. Lett. 117, 101–110. https://doi.org/10.1016/0012-821X(93)90120-X
Irifune, T., Ringwood, A.E., 1987. Phase transformations in primitive MORB and pyrolite compositions to 25 GPa and some geophysical implications, in: Manghnani, M.H., Syono, Y. (Eds.), High-Pressure Research in Mineral Physics. Terra Scientific Publishing Company, Washington.
Irifune, T., Shinmei, T., McCammon, C.A., Miyajima, N., Rubie, D.C., Frost, D.J., 2010. Iron partitioning and density changes of pyrolite in Earth's lower mantle. Science 327, 193–195. https://doi.org/10.1126/science.1181443
Ishii, T., Huang, R., Fei, H., Koemets, I., Liu, Z., Maeda, F., Yuan, L., Wang, L., Druzhbin, D., Yamamoto, T., Bhat, S., Farla, R., Kawazoe, T., Tsujino, N., Kulik, E., Higo, Y., Tange, Y., Katsura, T., 2018a. Complete agreement of the post-spinel transition with the 660-km seismic discontinuity. Sci. Rep. 8, 6–11. https://doi.org/10.1038/s41598-018-24832-y

Ishii, T., Kojitani, H., Akaogi, M., 2019. Phase relations of harzburgite and MORB up to the uppermost lower mantle conditions: precise comparison with pyrolite by multisample cell high-pressure experiments with implication to dynamics of subducted slabs. J. Geophys. Res. Solid Earth 124, 3491–3507. https://doi.org/10.1029/2018JB016749

Ishii, T., Kojitani, H., Akaogi, M., 2018b. Phase relations and mineral chemistry in pyrolitic mantle at 1600–2200 °C under pressures up to the uppermost lower mantle: Phase transitions around the 660-km discontinuity and dynamics of upwelling hot plumes. Phys. Earth Planet. Inter. 274, 127–137. https://doi.org/10.1016/j.pepi.2017.10.005

Ito, E., Takahashi, E., 1989. Postspinel transformations in the system Mg_2SiO_4-Fe_2SiO_4 and some geophysical implications. J. Geophys. Res. 94, 10637–10646.

Izraeli, E.S., Harris, J.W., Navon, O., 2004. Fluid and mineral inclusions in cloudy diamonds from Koffiefontein, South Africa. Geochim. Cosmochim. Acta 68, 2561–2575. https://doi.org/10.1016/j.gca.2003.09.005

Jablon, B.M., Navon, O., 2016. Most diamonds were created equal. Earth Planet. Sci. Lett. 443, 41–47. https://doi.org/10.1016/j.epsl.2016.03.013

Jacob, D., Jagoutz, E., Lowry, D., Mattey, D., Kudrjavtseva, G., 1994. Diamondiferous eclogites from Siberia: Remnants of Archean oceanic crust. Geochim. Cosmochim. Acta 58, 5191–5207. https://doi.org/10.1016/0016-7037(94)90304-2

Jacob, D.E., 2004. Nature and origin of eclogite xenoliths from kimberlites. Lithos 77, 295–316. https://doi.org/10.1016/j.lithos.2004.03.038

Jacob, D.E., Kronz, A., Viljoen, K.S., 2004. Cohenite, native iron and troilite inclusions in garnets from polycrystalline diamond aggregates. Contrib. to Mineral. Petrol. 146, 566–576. https://doi.org/10.1007/s00410-003-0518-2

Jacob, D.E., Viljoen, K.S., Grassineau, N. V., 2009. Eclogite xenoliths from Kimberley, South Africa – A case study of mantle metasomatism in eclogites. Lithos 112, 1002–1013. https://doi.org/10.1016/j.lithos.2009.03.034

Janse, A.J.A., 1994. Is Clifford's rule stil valid? Affirimitive examples from around the world, in: Meyer, H.O.A., Leonardos, O.H. (Eds.), Diamonds: Characterization, Genesis and Exploration. CPRM Special Publication, Brasilia, pp. 215–235.

Jaupart, C., Labrosse, S., Lucazeau, F., Mareschal, J.C., 2015. Temperatures, heat, and energy in the mantle of the Earth, Treatise on Geophysics: Second Edition. Elsevier B.V. https://doi.org/10.1016/B978-0-444-53802-4.00126-3

Jaupart, C., Mareschal, J.C., Iarotsky, L., 2016. Radiogenic heat production in the continental crust. Lithos 262, 398–427. https://doi.org/10.1016/j.lithos.2016.07.017

Javoy, M., Kaminski, E., Guyot, F., Andrault, D., Sanloup, C., Moreira, M., Labrosse, S., Jambon, A., Agrinier, P., Davaille, A., Jaupart, C., 2010. The chemical composition of the Earth: Enstatite chondrite models. Earth Planet. Sci. Lett. 293, 259–268. https://doi.org/10.1016/j.epsl.2010.02.033

Javoy, M., Pineau, F., Delorme, H., 1986. Carbon and nitrogen isotopes in the mantle. Chem. Geol. 57, 41–62. https://doi.org/10.1016/0009-2541(86)90093-8

Javoy, M., Pineau, F., Demaiffe, D., 1984. Nitrogen and carbon isotopic composition in the diamonds of Mbuji Mayi (Zaïre). Earth Planet. Sci. Lett. 68, 399–412. https://doi.org/10.1016/0012-821X(84)90125-0

Johnson, B., Goldblatt, C., 2015. The nitrogen budget of Earth. Earth-Science Rev. 148, 150–173. https://doi.org/10.1016/j.earscirev.2015.05.006

Johnson, K.T.M., Dick, H.J.B., Shimizu, N., 1990. Melting in the oceanic upper mantle: an ion

microprobe study of diopsides in abyssal peridotites. J. Geophys. Res. B Solid Earth 95, 2661–2678.
Joly, A., 1877. Recherches sur les composés du nobium et du tantale, in: Annales Scientifiques de l'École Normale Supérieure. pp. 125–186.
Jordan, T.H., 1988. Structure and formation of the continental tectosphere. J. Petrol. Special Volume, 11–37. https://doi.org/10.1093/petrology/Special_Volume.1.11
Jordan, T.H., 1978. Composition and development of the continental tectosphere. Nature 274, 544–548. https://doi.org/10.1038/274544a0
Joswig, W., Stachel, T., Harris, J.W., Baur, W.H., Brey, G.P., 1999. New Ca-silicate inclusions in diamonds – tracers from the lower mantle. Earth Planet. Sci. Lett. 173, 1–6. https://doi.org/10.1016/S0012-821X(99)00210-1
Kakimoto, K., Masuda, I., Ohsato, H., 2003. Ferroelectric and piezoelectric properties of $KNbO_3$ ceramics containing small amounts of $LaFeO_3$. Jpn. J. Appl. Phys. 42, 6102–6105.
Kaminsky, F., Wirth, R., 2017. Nitrides and carbonitrides from the lowermost mantle and their importance in the search for Earth's "lost" nitrogen. Am. Mineral. 102, 1667–1676. https://doi.org/10.2138/am-2017-6101
Kaminsky, F. V., Wirth, R., 2011. Iron carbide inclusions in lower-mantle diamond from juina, brazil. Can. Mineral. 49, 555–572. https://doi.org/10.3749/canmin.49.2.555
Kauffman, G.B., 1997. Victor Moritz Goldschmidt (1888-1947): A tribute to the founder of modern geochemistry on the fiftieth anniversary of his death. Chem. Educ. 2, 1–26.
Kelemen, P.B., Dick, H.J.B., Quick, J.E., 1992. Formation of harzburgite by pervasive melt/rock reaction in the upper mantle. Nature 358, 635–641. https://doi.org/10.1038/358635a0
Kelemen, P.B., Hart, S.R., Bernstein, S., 1998. Silica enrichment in the continental upper mantle via melt/rock reaction. Earth Planet. Sci. Lett. 164, 387–406. https://doi.org/10.1016/S0012-821X(98)00233-7
Kelemen, P.B., Shimizu, N., Salters, V.J.M., 1995. Extraction of mid-ocean-ridge basalt from the upwelling mantle by focused flow of melt in dunite channels. Nature 375.
Kennedy, G.C., Wasserburg, G.J., Heard, H.C., Newton, R.C., 1962. The upper three-phase region in the system SiO2-H2O. Am. J. Sci. https://doi.org/10.2475/ajs.260.7.501
Kerrick, D.M., Connelly, J.A.D., 2001. Metamorphic devolatilization of subducted marine sediments and the transport of volatiles into the Earth's mantle. Nature 411, 293–296. https://doi.org/10.1038/35077056
Kessel, R., Fumagalli, P., Pettke, T., 2015. The behaviour of incompatible elements during hydrous melting of metasomatized peridotite at 4-6 GPa and 1000°C-1200°C. Lithos 236–237, 141–155. https://doi.org/10.1016/j.lithos.2015.08.016
Kesson, S.E., Fitz Gerald, J.D., 1991. Partitioning of MgO, FeO, NiO, MnO and Cr_2O_3 between magnesian silicate perovskite and magnesiowüstite: implications for the origin of inclusions in diamond and the composition of the lower mantle. Earth Planet. Sci. Lett. 111, 229–240. https://doi.org/10.1016/0012-821X(92)90181-T
Kesson, S.E., Ringwood, A.E., 1989a. Slab-mantle interactions. 1. Sheared and refertilised garnet peridotite xenoliths – samples of Wadati-Benioff zones? Chem. Geol. 78, 83–96. https://doi.org/10.1016/0009-2541(89)90109-5
Kesson, S.E., Ringwood, A.E., 1989b. Slab mantle interactions. 2. The formation of diamonds. Chem. Geol. 78, 97–118.
King, H.E., Finger, L.W., 1979. Diffracted beam crystal centering and its application to high-pressure crystallography. J. Appl. Crystallogr. 12, 374–378.

Kirkley, M.B., Gurney, J.J., Otter, M.L., Hill, S.J., Daniels, L.R.M., 1991. The application of C isotope measurements to the identification of the sources of C in diamonds: a review. Appl. Geochemistry 6, 477–494. https://doi.org/10.1016/0883-2927(91)90048-T

Kiseeva, E.S., Litasov, K.D., Yaxley, G.M., Ohtani, E., Kamenetsky, V.S., 2013a. Melting and phase relations of carbonated eclogite at 9-21 GPa and the petrogenesis of alkali-rich melts in the deep mantle. J. Petrol. 54, 1555–1583. https://doi.org/10.1093/petrology/egt023

Kiseeva, E.S., Yaxley, G.M., Stepanov, A.S., Tkalčić, H., Litasov, K.D., Kamenetsky, V.S., 2013b. Metapyroxenite in the mantle transition zone revealed from majorite inclusions in diamonds. Geology 41, 883–886. https://doi.org/10.1130/G34311.1

Kobussen, A.F., Griffin, W.L., O'Reilly, S.Y., 2009. Cretaceous thermo-chemical modification of the Kaapvaal cratonic lithosphere, South Africa. Lithos 112, 886–895. https://doi.org/10.1016/j.lithos.2009.06.031

Kopylova, M.G., Rickard, R.S., Kleyenstueber, A., Taylor, W.R., Gurney, J.J., Daniels, L.R.M., 1997. First occurrence of strontian K-Cr-loparite and Cr-chevkinite in diamonds. Geol. I Geofiz. 38, 405–420.

Korenaga, J., 2020. Plate tectonics and surface environment: Role of the oceanic upper mantle. Earth-Science Rev. 205. https://doi.org/10.1016/j.earscirev.2020.103185

Kraus, W., Nolze, G., 1996. POWDER CELL - a program for the representation and manipulation of crystal structures and calculation of the resulting X-ray powder patterns. J. Appl. Crystallogr.

Krebs, M.Y., Pearson, D.G., Stachel, T., Laiginhas, F., Woodland, S., Chinn, I., Kong, J., 2019. A common parentage-low abundance trace element data of gem diamonds reveals similar fluids to fibrous diamonds. Lithos 324–325, 356–370. https://doi.org/10.1016/j.lithos.2018.11.025

Krivovichev, S. V., Chakhmouradian, A.R., Mitchell, R.H., Filatov, S.K., Chukanov, N. V, 2000. Crystal structure of isolueshite and its synthetic compositional analogue. Eur. J. Mineral. 12, 597–607.

Krogh, E.J., 1988. The garnet-clinopyroxene Fe-Mg geothermometer – a reinterpretation of existing experimental data. Contrib. to Mineral. Petrol. 99, 44–48. https://doi.org/10.1007/BF00399364

Kuritani, T., Xia, Q.K., Kimura, J.I., Liu, J., Shimizu, K., Ushikubo, T., Zhao, D., Nakagawa, M., Yoshimura, S., 2019. Buoyant hydrous mantle plume from the mantle transition zone. Sci. Rep. 9, 1–7. https://doi.org/10.1038/s41598-019-43103-y

Kushiro, I., Syono, Y., Akimoto, S.-I., 1968. Melting of peridotite nodule at high pressures and high water pressures. J Geophys. Res. 73, 6023–6029. https://doi.org/10.1029/jb073i018p06023

Labidi, J., Barry, P.H., Bekaert, D. V., Broadley, M.W., Marty, B., Giunta, T., Warr, O., Sherwood Lollar, B., Fischer, T.P., Avice, G., Caracausi, A., Ballentine, C.J., Halldórsson, S.A., Stefánsson, A., Kurz, M.D., Kohl, I.E., Young, E.D., 2020. Hydrothermal $^{15}N^{15}N$ abundances constrain the origins of mantle nitrogen. Nature 580, 367–371. https://doi.org/10.1038/s41586-020-2173-4

Lafuente, B., Downs, R.T., Yang, H., Stone, N., 2016. The power of databases: The RRUFF project, in: Armbruster, T., Danisi, R.M. (Eds.), Highlights in Mineralogical Crystallography. W. De Gruyter, pp. 1–29. https://doi.org/10.1515/9783110417104-003

Laves, F., 1962. The growing field of mineral structures, in: Ewald, P.P. (Ed.), Fifty Years of X-Ray Diffraction. Springer, Boston, M.A., pp. 174–189.

Lazarov, M., Brey, G.P., Weyer, S., 2012. Evolution of the South African mantle-a case study of garnet peridotites from the Finsch diamond mine (Kaapvaal craton); Part 2: Multiple depletion and re-enrichment processes. Lithos 154, 210–223. https://doi.org/10.1016/j.lithos.2012.07.013

Leahy, K., Taylor, W.R., 1997. The influence of the Glennie domain deep structure on the diamonds in Saskatchewan kimberlites. Geol. i Geofiz. 38, 451–460.

Li, K., Li, L., Pearson, D.G., Stachel, T., 2019. Diamond isotope compositions indicate altered igneous oceanic crust dominates deep carbon recycling. Earth Planet. Sci. Lett. 516, 190–201. https://doi.org/10.1016/j.epsl.2019.03.041

Li, L., Bebout, G.E., Idleman, B.D., 2007. Nitrogen concentration and $\delta^{15}N$ of altered oceanic crust obtained on ODP Legs 129 and 185: insights into alteration-related nitrogen enrichment and the nitrogen subduction budget. Geochim. Cosmochim. Acta 71, 2344–2360. https://doi.org/10.1016/j.gca.2007.02.001

Li, Y., Keppler, H., 2014. Nitrogen speciation in mantle and crustal fluids. Geochim. Cosmochim. Acta 129, 13–32. https://doi.org/10.1016/j.gca.2013.12.031

Litasov, K.D., Shatskiy, A., Ohtani, E., 2014. Melting and subsolidus phase relations in peridotite and eclogite systems with reduced COH fluid at 3-16 GPa. Earth Planet. Sci. Lett. 391, 87–99. https://doi.org/10.1016/j.epsl.2014.01.033

Liu, L.-G., 1986. Phase transformations in serpentine at high pressures and temperatures and implications for subducting lithosphere. Phys. Earth Planet. Inter. 42, 255–262. https://doi.org/10.1016/0031-9201(86)90028-2

Liu, L.-G., 1977. Mineralogy and chemistry of the Earth's mantle above 1000 km. Geophys. J. R. Astron. Soc. 48, 53–62.

Liu, L.-G., 1976a. The post-spinel phase of fosterite. Nature 262, 770–772.

Liu, L.-G., 1976b. Orthorhombic perovskite phases observed in olivine, pyroxene and garnet at high pressures and temperatures. Phys. Earth Planet. Inter. 11, 289–298. https://doi.org/10.1016/0031-9201(76)90016-9

Liu, Z., Ishii, T., Katsura, T., 2017. Rapid decrease of MgAlO2.5 component in bridgmanite with pressure. Geochemical Perspect. Lett. 5, 12–18. https://doi.org/10.7185/geochemlet.1739

Lord, O.T., Walter, M.J., Dasgupta, R., Walker, D., Clark, S.M., 2009. Melting in the Fe-C system to 70 GPa. Earth Planet. Sci. Lett. 284, 157–167. https://doi.org/10.1016/j.epsl.2009.04.017

Lowe, D.R., 1994. Accretionary history of the Archean Barberton Greenstone Belt (3.55-3.22 Ga), Southern Africa. Geology 22, 1099–1102. https://doi.org/10.1130/0091-7613(1994)022<1099:AHOTAB>2.3.CO;2

Lowry, D., Mattey, D.P., Harris, J.W., 1999. Oxygen isotope composition of syngenetic inclusions in diamond from the Finsch Mine, RSA. Geochim. Cosmochim. Acta 63, 1825–1836. https://doi.org/10.1016/S0016-7037(99)00120-9

Lummen, T.T.A., Leung, J., Kumar, A., Wu, X., Ren, Y., VanLeeuwen, B.K., Haislmaier, R.C., Holt, M., Lai, K., Kalinin, S. V., Gopalan, V., 2017. Emergent low-symmetry phases and large property enhancements in ferroelectric $KNbO_3$ bulk crystals. Adv. Mater. 29, 1–7. https://doi.org/10.1002/adma.201700530

Luth, R.., 1999. Carbon and carbonates in the mantle, in: Fei, Y., Bertka, C.M., Mysen, B.O. (Eds.), Mantle Petrology: Field Observations and High Pressure Experimentation (a Tribute to Francis R. (Joe) Boyd). The Geochemical Society, pp. 297–316.

Luth, R.W., 2003. Mantle Volatiles-Distribution and Consequences. Treatise on Geochemistry

2–9, 319–361. https://doi.org/10.1016/B0-08-043751-6/02124-1
Luth, R.W., Stachel, T., 2014. The buffering capacity of lithospheric mantle: implications for diamond formation. Contrib. to Mineral. Petrol. 168, 1–12. https://doi.org/10.1007/s00410-014-1083-6
Luth, R.W., Virgo, D., Boyd, F.R., Wood, B.J., 1990. Ferric iron in mantle-derived garnets – Implications for thermobarometry and for the oxidation state of the mantle. Contrib. to Mineral. Petrol. 104, 56–72. https://doi.org/10.1007/BF00310646
Malkovets, V., Taylor, L., Griffin, W., Reilly, S.O., Verichev, E., Golovin, N., Litasov, K., Valley, J., 2003. Eclogites from the Grib kimberlite pipe, Arkhangelsk, Russia, in: 8th International Kimberlite Conference. Victoria. https://doi.org/ISBN 978-1-55195-422-6
Mandarino, J.A., 1976. The Gladstone-Dale relationship - Part I: derivation of new constants. Can. Mineral. 14, 498–502.
Martinez, I., Chamorro Peréz, E.M., Matas, J., Gillet, P., Vidal, G., 1998. Experimental investigation of silicate-carbonate system at high pressure and high temperature. J. Geophys. Res. Solid Earth 103, 5143–5163. https://doi.org/10.1029/97jb03401
Martirosyan, N.S., Yoshino, T., Shatskiy, A., Chanyshev, A.D., Litasov, K.D., 2016. The CaCO3–Fe interaction: Kinetic approach for carbonate subduction to the deep Earth's mantle. Phys. Earth Planet. Inter. 259, 1–9. https://doi.org/10.1016/j.pepi.2016.08.008
Marty, B., 1995. Nitrogen content of the mantle inferred from N_2-Ar correlation in oceanic basalts. Nature 377, 326–329. https://doi.org/10.1038/377326a0
Mason, B.H., 1992. Victor Moritz Goldschmidt: Father of Modern Geochemistry. Geochemical Society, San Antonio.
Mather, K.A., Pearson, D.G., McKenzie, D., Kjarsgaard, B.A., Priestley, K., 2011. Constraints on the depth and thermal history of cratonic lithosphere from peridotite xenoliths, xenocrysts and seismology. Lithos 125, 729–742. https://doi.org/10.1016/j.lithos.2011.04.003
Mathez, E.A., Fogel, R.A., Hutcheon, I.D., Marshintsev, V.K., 1995. Carbon isotopic composition and origin of SiC from kimberlites of Yakutia, Russia. Geochim. Cosmochim. Acta 59, 781–791. https://doi.org/10.1016/0016-7037(95)00002-H
Matjuschkin, V., Woodland, A.B., Yaxley, G.M., 2019. Methane-bearing fluids in the upper mantle: an experimental approach. Contrib. to Mineral. Petrol. 174, 1–14. https://doi.org/10.1007/s00410-018-1536-4
Mattey, D., Lowry, D., Macpherson, C., 1994. Oxygen isotope composition of mantle peridotite. Earth Planet. Sci. Lett. 128, 231–241. https://doi.org/10.1016/0012-821X(94)90147-3
Mattey, D.P., Carr, R.H., Wright, I.P., Pillinger, C.T., 1984. Carbon isotopes in submarine basalts. Earth Planet. Sci. Lett. 70, 196–206. https://doi.org/10.1016/0012-821X(84)90005-0
McCammon, C.A., Stachel, T., Harris, J.W., 2004. Iron oxidation state in lower mantle mineral assemblages II. Inclusions in diamonds from Kankan, Guinea. Earth Planet. Sci. Lett. 222, 423–434. https://doi.org/10.1016/j.epsl.2004.03.019
McDonough, W.F., Rudnick, R.L., 1998. Mineralogy and composition of the upper mantle, in: Reviews in Mineralogy. Mineralogical Society of America, pp. 139–164.
McDonough, W.F., Sun, S., 1995. The composition of the Earth. Chem. Geol. 120, 223–253. https://doi.org/10.1016/0009-2541(94)00140-4
McKenzie, D., Bickle, M.J., 1988. The volume and composition of melt generated by extension of the lithosphere. J. Petrol. 29, 625–679. https://doi.org/10.1093/petrology/29.3.625

McKenzie, D., Jackson, J., Priestley, K., 2005. Thermal structure of oceanic and continental lithosphere. Earth Planet. Sci. Lett. 233, 337–349. https://doi.org/10.1016/j.epsl.2005.02.005

McKenzie, D., O'Nions, R.K., 1991. Partial melt distributions from inversion of rare earth element concentrations. J. Petrol. 23, 1021–1091. https://doi.org/10.1093/petrology/32.5.1021

Menzies, M.A., Hawkesworth, C.J. (Eds.), 1987. Mantle Metasomatism, Academic Press. Academic Press, London.

Menzies, M.A., Rogers, N., Tindle, A., Hawkesworth, C.J., 1987. Metasomatic and enrichment processes in lithospheric peridotites, an effect of asthenosphere-lithosphere interaction, in: Menzies, M.A., Hawkesworth, C.J. (Eds.), Mantle Metasomatism. Academic Press, London, pp. 313–361. https://doi.org/10.1210/er.2013-1115

Meyer, H.O.A., 1987. Inclusions in diamond, in: Nixon, P.H. (Ed.), Mantle Xenoliths. John Wiley & Sons, Inc., pp. 501–522.

Meyer, H.O.A., 1986. Genesis of diamond: a mantle saga. Am. Mineral. 71, 1259–1260.

Meyer, H.O.A., McCallister, R.H., 1984. Two-pyroxene megacrysts from South African kimberlites., Kimberlites II: The Mantle and Crust-Mantle Relationships. Elsevier Science Publishers B.V. https://doi.org/10.1016/b978-0-444-42274-3.50018-4

Meyer, N.A., Wenz, M.D., Walsh, J.P.S., Jacobsen, S.D., Locock, A.J., Harris, J.W., 2019. Goldschmidtite, (K,REE,Sr)(Nb,Cr)O_3: a new perovskite supergroup mineral found in diamond from Koffiefontein, South Africa. Am. Mineral. 104, 1345–1350. https://doi.org/10.2138/am-2019-6937

Mikhail, S., Guillermier, C., Franchi, I.A., Beard, A.D., Crispin, K., Verchovsky, A.B., Jones, A.P., Milledge, H.J., 2014a. Empirical evidence for the fractionation of carbon isotopes between diamond and iron carbide from the Earth's mantle. Geochemistry, Geophys. Geosystems 15, 855–866. https://doi.org/10.1002/2013GC005138

Mikhail, S., Sverjensky, D.A., 2014. Nitrogen speciation in upper mantle fluids and the origin of Earth's nitrogen-rich atmosphere. Nat. Geosci. 7, 816–819. https://doi.org/10.1038/ngeo2271

Mikhail, S., Verchovsky, A.B., Howell, D., Hutchison, M.T., Southworth, R., Thomson, A.R., Warburton, P., Jones, A.P., Milledge, H.J., 2014b. Constraining the internal variability of the stable isotopes of carbon and nitrogen within mantle diamonds. Chem. Geol. 366, 14–23. https://doi.org/10.1016/j.chemgeo.2013.12.014

Milledge, H.J., Mendelssohn, M.J., Seal, M., Rouse, J.E., Swart, P.K., Pillinger, C.T., 1983. Carbon isotopic variation in spectral type II diamonds. Nature 303, 791–792. https://doi.org/10.1038/303791a0

Mitchell, R.H., Choi, J.B., Hawthorne, F.C., Burns, P.C., 1998. Latrappite: a re-investigation. Can. Mineral. 36, 107–116.

Mitchell, R.H., Welch, M.D., Chakhmouradian, A.R., 2017. Nomenclature of the perovskite supergroup: A hierarchical system of classification based on crystal structure and composition. Mineral. Mag. 81, 411–461.

Moore, R.O., Gurney, J.J., 1985. Pyroxene solid solution in garnets included in diamond. Nature 318, 553–555. https://doi.org/10.1038/318553a0

Moore, R.O., Otter, M.L., Rickard, R.S., Harris, J.W., Gurney, J.J., 1986. The occurrence of moissanite and ferro-periclase as inclusions in diamond, in: 4th International Kimberlite Conference. Geological Society of Australia Incorporated, Perth, pp. 409–411.

Morimoto, N., 1988. Nomenclature of pyroxenes. Mineral. Petrol. 39, 55–76. https://doi.org/10.1007/BF01226262

Murakami, M., Hirose, K., Kawamura, K., Sata, N., Ohishi, Y., 2004. Post-Perovskite Phase Transition in $MgSiO_3$. Science 304, 855–858. https://doi.org/10.1126/science.1095932

Murakami, M., Ohishi, Y., Hirao, N., Hirose, K., 2012. A perovskitic lower mantle inferred from high-pressure, high-temperature sound velocity data. Nature 485, 90–94. https://doi.org/10.1038/nature11004

Naidoo, P., Stiefenhofer, J., Field, M., Dobbe, R., 2004. Recent advances in the geology of Koffiefontein Mine, Free State Province, South Africa. Lithos 76, 161–182. https://doi.org/10.1016/j.lithos.2004.04.032

Navon, O., Hutcheon, I.D., Rossman, G.R., Wasserburg, G.J., 1988. Mantle-derived fluids in diamond micro-inclusions. Nature 335, 784–789. https://doi.org/10.1038/335784a0

Nestola, F., Korolev, N., Kopylova, M., Rotiroti, N., Pearson, D.G., Pamato, M.G., Alvaro, M., Peruzzo, L., Gurney, J.J., Moore, A.E., Davidson, J., 2018. CaSiO3 perovskite in diamond indicates the recycling of oceanic crust into the lower mantle. Nature 555, 237–241. https://doi.org/10.1038/nature25972

Nickel, K.G., Green, D.H., 1985. Empirical geothermobarometry for garnet peridotites and implications for the nature of the lithosphere, kimberlites and diamonds. Earth Planet. Sci. Lett. 73, 158–170.

Nilsen, W.G., Skinner, J.G., 1968. Raman spectrum of strontium titanate. J. Chem. Phys. 48, 2240–2248.

Nimis, P., Grütter, H.S., 2010. Internally consistent geothermometers for garnet peridotites and pyroxenites. Contrib. to Mineral. Petrol. 159, 411–427. https://doi.org/10.1007/s00410-009-0455-9

Nimis, P., Taylor, W.R., 2000. Single clinopyroxene thermobarometry for garnet peridotites. Part I. Calibration and testing of a Cr-in-Cpx barometer and an enstatite-in-Cpx thermometer. Contrib. to Mineral. Petrol. 139, 541–554.

Nishizawa, M., Sano, Y., Ueno, Y., Maruyama, S., 2007. Speciation and isotope ratios of nitrogen in fluid inclusions from seafloor hydrothermal deposits at ~ 3.5 Ga. Earth Planet. Sci. Lett. 254, 332–344. https://doi.org/10.1016/j.epsl.2006.11.044

Nixon, P.H., Van Calsteren, P.W.C., Boyd, F.R., Hawkesworth, C.J., 1987. Harzburgites with garnets of diamond facies from southern African kimberlites, in: Nixon, P.H. (Ed.), Mantle Xenoliths. John Wiley & Sons, Inc., pp. 523–534.

O'Neill, H.S.C., Rubie, D.C., Canil, D., Geiger, C.A., Ross, C.R., Seifert, F.A., Woodland, A.B., 1993. Ferric iron in the upper mantle and in transition zone assemblages: implications for relative oxygen fugacities. Evol. Earth Planets 74, 73–88.

O'Neill, H.S.C., Wood, B.J., 1979. An experimental study of Fe-Mg partitioning between garnet and olivine and its calibration as a geothermometer. Contrib. to Mineral. Petrol. 70, 59–70. https://doi.org/10.1007/BF00371872

Ohtani, E., Shibata, T., Kubo, T., Kato, T., 1995. Stability of hydrous phases in the transition zone and the upper most part of the lower mantle. Geophys. Res. Lett. 22, 2553–2556. https://doi.org/10.1029/95GL02338

Palache, C., 1900. Notes on tellurides from Colorado. Am. J. Sci. 419–427.

Palot, M., Cartigny, P., Harris, J.W., Kaminsky, F. V., Stachel, T., 2012. Evidence for deep mantle convection and primordial heterogeneity from nitrogen and carbon stable isotopes in diamond. Earth Planet. Sci. Lett. 357–358, 179–193.

https://doi.org/10.1016/j.epsl.2012.09.015
Palot, M., Jacobsen, S.D., Townsend, J.P., Nestola, F., Marquardt, K., Miyajima, N., Harris, J.W., Stachel, T., McCammon, C.A., Pearson, D.G., 2016. Evidence for H_2O-bearing fluids in the lower mantle from diamond inclusion. Lithos 265, 237–243. https://doi.org/10.1016/j.lithos.2016.06.023
Palot, M., Pearson, D.G., Stern, R.A., Stachel, T., Harris, J.W., 2014. Isotopic constraints on the nature and circulation of deep mantle C-H-O-N fluids: carbon and nitrogen systematics within ultra-deep diamonds from Kankan (Guinea). Geochim. Cosmochim. Acta 139, 26–46. https://doi.org/10.1016/j.gca.2014.04.027
Palyanov, Y.N., Bataleva, Y. V., Sokol, A.G., Borzdov, Y.M., Kupriyanov, I.N., Reutsky, V.N., Sobolev, N. V., 2013. Mantle-slab interaction and redox mechanism of diamond formation. Proc. Natl. Acad. Sci. 110, 20408–20413. https://doi.org/10.1073/pnas.1313340110
Paton, C., Hellstrom, J., Paul, B., Woodhead, J., Hergt, J., 2011. Iolite: Freeware for the visualisation and processing of mass spectrometric data. J. Anal. At. Spectrom. 26, 2508–2518. https://doi.org/10.1039/c1ja10172b
Pattison, D.R.M., Bégin, N.J., 1994. Zoning patterns in orthopyroxene and garnet in granulites: implications for geothermometry. J. Metamorph. Geol. 12, 387–410. https://doi.org/10.1111/j.1525-1314.1994.tb00031.x
Peacock, M.A., 1940. Goldschmidtine identical with stephanite. Am. Mineral. 25, 372–373.
Peacock, M.A., 1939. Goldschmidtine, a newly recognized antimonide of silver. Am. Mineral. 24, 227–241.
Pearson, D.G., Brenker, F.E., Nestola, F., McNeill, J., Nasdala, L., Hutchison, M.T., Matveev, S., Mather, K.A., Silversmit, G., Schmitz, S., Vekemans, B., Vincze, L., 2014. Hydrous mantle transition zone indicated by ringwoodite included within diamond. Nature 507, 221–4. https://doi.org/10.1038/nature13080
Pearson, D.G., Shirey, S.B., Harris, J.W., Carlson, R.W., 1998. Sulphide inclusions in diamonds from the Koffiefontein kimberlite, S Africa: constraints on diamond ages and mantle Re-Os systematics. Earth Planet. Sci. Lett. 160, 311–326.
Pearson, D.G., Wittig, N., 2008. Formation of Archaean continental lithosphere and its diamonds: the root of the problem. J. Geol. Soc. London. 165, 895–914. https://doi.org/10.1144/0016-76492008-003
Pernet-Fisher, J.F., Howarth, G.H., Liu, Y., Barry, P.H., Carmody, L., Valley, J.W., Bodnar, R.J., Spetsius, Z. V., Taylor, L.A., 2014. Komsomolskaya diamondiferous eclogites: Evidence for oceanic crustal protoliths. Contrib. to Mineral. Petrol. 167, 1–17. https://doi.org/10.1007/s00410-014-0981-y
Petts, D.C., Chacko, T., Stachel, T., Stern, R.A., Heaman, L.M., 2015. A nitrogen isotope fractionation factor between diamond and its parental fluid derived from detailed SIMS analysis of a gem diamond and theoretical calculations. Chem. Geol. 410, 188–200. https://doi.org/10.1016/j.chemgeo.2015.06.020
Poli, S., Schmidt, M.W., 2002. Petrology of subducted slabs. Annu. Rev. Earth Planet. Sci. 30, 207–235. https://doi.org/10.1146/annurev.earth.30.091201.140550
Pollack, H.N., Chapman, D.S., 1977. On the regional variation of heat flow, geotherms, and lithospheric thickness. Tectonophysics 38, 279–296. https://doi.org/10.1016/0040-1951(77)90215-3
Poujol, M., Robb, L.J., Anhaeusser, C.R., Gericke, B., 2003. A review of the geochronological constraints on the evolution of the Kaapvaal Craton, South Africa. Precambrian Res. 127,

181–213. https://doi.org/10.1016/S0301-9268(03)00187-6
Ray, J.S., Ramesh, R., 2000. Rayleigh fractionation of stable isotopes from a multicomponent source. Geochim. Cosmochim. Acta 64, 299–306. https://doi.org/10.1016/S0016-7037(99)00181-7
Regier, M.E., 2020. Subduction and the genesis of mantle roots and diamonds. University of Alberta.
Regier, M.E., Mišković, A., Ickert, R.B., Pearson, D.G., Stachel, T., Stern, R.A., Kopylova, M., 2018. An oxygen isotope test for the origin of Archean mantle roots. Geochemical Perspect. Lett. 6–10. https://doi.org/10.7185/geochemlet.1830
Regier, M.E., Pearson, D.G., Stachel, T., Luth, R.W., Stern, R.A., Harris, J.W., 2020. The lithospheric-to-lower-mantle carbon cycle recorded in superdeep diamonds. Nature 585, 234–238. https://doi.org/10.1038/s41586-020-2676-z
Richardson, S.H., Gurney, J.J., Erlank, A.J., Harris, J.W., 1984. Origins of diamond in old enriched mantle. Nature 310, 198–202. https://doi.org/10.1038/311525a0
Riches, A.J.V., Ickert, R.B., Pearson, D.G., Stern, R.A., Jackson, S.E., Ishikawa, A., Kjarsgaard, B.A., Gurney, J.J., 2016. In situ oxygen-isotope, major-, and trace-element constraints on the metasomatic modification and crustal origin of a diamondiferous eclogite from Roberts Victor, Kaapvaal Craton. Geochim. Cosmochim. Acta 174, 345–359. https://doi.org/10.1016/j.gca.2015.11.028
Riches, A.J.V., Liu, Y., Day, J.M.D., Spetsius, Z. V., Taylor, L.A., 2010. Subducted oceanic crust as diamond hosts revealed by garnets of mantle xenoliths from Nyurbinskaya, Siberia. Lithos 120, 368–378. https://doi.org/10.1016/j.lithos.2010.09.006
Richet, P., Bottinga, Y., Javoy, M., 1977. A reivew of hydrogen, carbon, nitrogen, oxygen, sulphur, and chlorine stable isotope fractionation among gaseous molecules. Annu. Rev. Earth Planet. Sci. 5, 65–110.
Rickard, R.S., Harris, J.W., Gurney, J.J., Cardoso, P., 1989. Mineral inclusions in diamonds from Koffiefontein Mine, in: Kimberlites and Related Rocks. Blackwell Scientific Publications, Victoria, pp. 1054–1062.
Ringwood, A.E., 1991. Phase transformations and their bearing on the constitution and dynamics of the mantle. Geochim. Cosmochim. Acta 55, 2083–2110. https://doi.org/10.1016/0016-7037(91)90090-R
Ringwood, A.E., 1969. Composition of the crust and upper mantle, in: Hart, P.J. (Ed.), Geophysical Monograph Series. William Bryd Press, Richmond, pp. 1–17.
Ringwood, A.E., 1962a. A model for the upper mantle. J. Geophys. Res. 67, 4473–4478. https://doi.org/10.1029/JZ067i011p04473
Ringwood, A.E., 1962b. Mineralogical constitution of the deep mantle. J. Geophys. Res. 67, 4005. https://doi.org/10.1029/JZ067i010p04005
Ringwood, A.E., 1959. On the chemical evolution and densities of the planets. Geochim. Cosmochim. Acta 15, 257–283. https://doi.org/10.1016/0016-7037(59)90062-6
Ringwood, A.E., 1958. Olivine-spinel transition in fayalite. Bull. Geol. Soc. Am. 69, 129–130.
Ringwood, A.E., Green, D.H., 1966. An experimental investigation of the gabbro-eclogite transformation and some geophysical implications. Tectonophysics 3, 383–427. https://doi.org/10.1016/0040-1951(66)90009-6
Ringwood, A.E., Major, A., 1966. High-pressure transformations in pyroxenes. Earth Planet. Sci. Lett. 1, 351–357. https://doi.org/10.1016/0012-821X(66)90023-9
Rohrbach, A., Schmidt, M.W., 2011. Redox freezing and melting in the Earths deep mantle

resulting from carbon-iron redox coupling. Nature 472, 209–214. https://doi.org/10.1038/nature09899
Rollinson, H., 2019. Dunites in the mantle section of the Oman ophiolite - the boninite connection. Lithos 334–335, 1–7. https://doi.org/10.1016/j.lithos.2019.03.008
Rudnick, R.L., 1994. Northern Tanzanian peridotite xenoliths: a comparison with Kaapvaal peridotites and inferences on metasomatic interactions. Int. Kimberl. Conf. 336–353.
Rudnick, R.L., McDonough, W.F., Chappell, B.C., 1993. Carbonatite metasomatism in the northern Tanzanian mantle. Earth Planet. Sci. Lett. 114, 463–475.
Ryabchikov, I.D., Kaminsky, F. V., 2013. Oxygen potential of diamond formation in the lower mantle. Geol. Ore Depos. 55, 1–12. https://doi.org/10.1134/S1075701513010066
Saunders, A.D., Storey, M., Kent, R.W., Norry, M.J., 1992. Consequences of plume-lithosphere interactions. Geol. Soc. London, Spec. Publ. 68, 41–60. https://doi.org/10.1144/GSL.SP.1992.068.01.04
Schauble, E.A., Ghosh, P., Eiler, J.M., 2006. Preferential formation of ^{13}C-^{18}O bonds in carbonate minerals, estimated using first-principles lattice dynamics. Geochim. Cosmochim. Acta 70, 2510–2529. https://doi.org/10.1016/j.gca.2006.02.011
Schaufele, R.F., Weber, M.J., 1967. First- and second-order Raman scattering of $SrTiO_3$. J. Chem. Phys. 46, 2859–2861. https://doi.org/10.1063/1.1841140
Schidlowski, M., 2001. Carbon isotopes as biogeochemical recorders of life over 3.8 Ga of Earth history: Evolution of a concept. Precambrian Res. 106, 117–134. https://doi.org/10.1016/S0301-9268(00)00128-5
Schmidt, M.W., Gao, C., Golubkova, A., Rohrbach, A., Connolly, J.A., 2014. Natural moissanite (SiC) – a low temperature mineral formed from highly fractionated ultra-reducing COH-fluids. Prog. Earth Planet. Sci. 1, 1–14. https://doi.org/10.1186/s40645-014-0027-0
Schmidt, M.W., Poli, S., 1998. Experimentally based water budgets for dehydrating slabs and consequences for arc magma generation. Earth Planet. Sci. Lett. 163, 361–379. https://doi.org/10.1016/S0012-821X(98)00142-3
Schmitz, M.D., Bowring, S.A., de Wit, M.J., Gartz, V., 2004. Subduction and terrane collision stabilize the western Kaapvaal craton tectosphere 2.9 billion years ago. Earth Planet. Sci. Lett. 222, 363–376. https://doi.org/10.1016/j.epsl.2004.03.036
Schneider, M.E., Eggler, D.H., 1986. Fluids in equilibrium with peridotite minerals: implications for mantle metasomatism. Geochim. Cosmochim. Acta 50, 711–724. https://doi.org/10.1016/0016-7037(86)90347-9
Schrauder, M., Navon, O., 1994. Hydrous and carbonatitic mantle fluids in fibrous diamonds from Jwaneng, Botswana. Geochim. Cosmochim. Acta 58, 761–771. https://doi.org/10.1016/0016-7037(94)90504-5
Schrauder, M., Navon, O., 1993. Solid carbon dioxide in a natural diamond. Nature 365, 42–44.
Schulze, D.J., 1989. Constraints on the abundance of eclogite in the upper mantle. J. Geophys. Res. Solid Earth 94, 4205–4212. https://doi.org/10.1029/JB094iB04p04205
Schulze, D.J., Valley, J.W., Spicuzza, M.J., Channer, D.M.D.R., 2003. Oxygen isotope composition of eclogitic and peridotitic garnet xenocrysts from the la ceniza kimberlite, Guaniamo, Venezuela. Int. Geol. Rev. 45, 968–975. https://doi.org/10.2747/0020-6814.45.11.968
Scott Smith, B.H., Danchin, R.V., Harris, J.W., Stracke, K.J., 1984. Kimberlites Near Orroroo, South Australia. Dev. Petrol. 11, 121–142. https://doi.org/10.1016/B978-0-444-42273-6.50017-1

Scott Smith, B.H., Nowicki, T.E., Russell, J.K., Webb, K.J., Mitchell, R.H., Hetman, C.M., Harder, M., Skinner, E.M.W., Robey, J.A., 2013. Kimberlite Terminology and Classification, in: Proceedings of 10th International Kimberlite Conference. pp. 1–17. https://doi.org/10.1007/978-81-322-1173-0_1

Sephton, M.A., Verchovsky, A.B., Bland, P.A., Gilmour, I., Grady, M.M., Wright, I.P., 2003. Investigating the variations in carbon and nitrogen isotopes in carbonaceous chondrites. Geochim. Cosmochim. Acta 67, 2093–2108. https://doi.org/10.1016/S0016-7037(02)01320-0

Shilobreeva, S., Martinez, I., Busigny, V., Agrinier, P., Laverne, C., 2011. Insights into C and H storage in the altered oceanic crust: Results from ODP/IODP Hole 1256D. Geochim. Cosmochim. Acta 75, 2237–2255. https://doi.org/10.1016/j.gca.2010.11.027

Shimizu, N., Richardson, S.H., 1987. Trace element abundance patterns of garnet inclusions in peridotite-suite diamonds. Geochim. Cosmochim. Acta 51, 755–758. https://doi.org/10.1016/0016-7037(87)90085-8

Shimizu, N., Sobolev, N.N., 1995. Young peridotitic diamonds from the Mir kimberlite pipe. Nature 375, 394–397. https://doi.org/10.1038/375394a0

Shirey, S.B., Richardson, S.H., Harris, J.W., 2004a. Integrated models of diamond formation and craton evolution. Lithos 77, 923–944. https://doi.org/10.1016/j.lithos.2004.04.018

Shirey, S.B., Richardson, S.H., Harris, J.W., 2004b. Age, paragenesis and composition of diamonds and evolution of the Precambrian mantle lithosphere of southern Africa. South African J. Geol. 107, 91–106. https://doi.org/10.2113/107.1-2.91

Shu, Q., Brey, G.P., 2015. Ancient mantle metasomatism recorded in subcalcic garnet xenocrysts: temporal links between mantle metasomatism, diamond growth and crustal tectonomagmatism. Earth Planet. Sci. Lett. 418, 27–39. https://doi.org/10.1016/j.epsl.2015.02.038

Shu, Q., Brey, G.P., Gerdes, A., Hoefer, H.E., 2014. Mantle eclogites and garnet pyroxenites - the meaning of two-point isochrons, Sm-Nd and Lu-Hf closure temperatures and the cooling of the subcratonic mantle. Earth Planet. Sci. Lett. 389, 143–154. https://doi.org/10.1016/j.epsl.2013.12.028

Shu, Q., Brey, G.P., Gerdes, A., Hoefer, H.E., 2013. Geochronological and geochemical constraints on the formation and evolution of the mantle underneath the Kaapvaal craton: Lu-Hf and Sm-Nd systematics of subcalcic garnets from highly depleted peridotites. Geochim. Cosmochim. Acta 113, 1–20. https://doi.org/10.1016/j.gca.2013.03.010

Shu, Q., Brey, G.P., Pearson, D.G., 2018. Eclogites and garnet pyroxenites from Kimberley, Kaapvaal craton, South Africa: their diverse origins and complex metasomatic signatures. Mineral. Petrol. 112, 43–56. https://doi.org/10.1007/s00710-018-0595-6

Simon, N.S.C., Carlson, R.W., Pearson, D.G., Davies, G.R., 2007. The origin and evolution of the Kaapvaal cratonic lithospheric mantle. J. Petrol. 48, 589–625. https://doi.org/10.1093/petrology/egl074

Simon, N.S.C., Irvine, G.J., Davies, G.R., Pearson, D.G., Carlson, R.W., 2003. The origin of garnet and clinopyroxene in “depleted” Kaapvaal peridotites, Lithos. https://doi.org/10.1016/S0024-4937(03)00118-X

Skjærvø, S.L., Høydalsvik, K., Blichfeld, A.B., Einarsrud, M.-A., Grande, T., 2018. Thermal evolution of the crystal structure and phase transitions of KNbO3. R. Soc. Open Sci. 5, 180368. https://doi.org/10.1098/rsos.180368

Sleep, N.H., 2003. Geodynamic implications of xenolith geotherms. Geochemistry, Geophys.

Geosystems 4. https://doi.org/10.1029/2003GC000511
Smit, K. V., Stachel, T., Luth, R.W., Stern, R.A., 2019. Evaluating mechanisms for eclogitic diamond growth: An example from Zimmi Neoproterozoic diamonds (West African craton). Chem. Geol. 520, 21–32. https://doi.org/10.1016/j.chemgeo.2019.04.014
Smith, E.M., Kopylova, M.G., 2014. Implications of metallic iron for diamonds and nitrogen in the sublithospheric mantle. Can. J. Earth Sci. 51, 510–516. https://doi.org/10.1139/cjes-2013-0218
Smith, E.M., Shirey, S.B., Nestola, F., Bullock, E.S., Wang, J., Richardson, S.H., Wang, W., 2016. Large gem diamonds from metallic liquid in Earth's deep mantle. Science 354, 1403–1405. https://doi.org/10.1126/science.aal1303
Snyder, G.A., Taylor, L.A., Jerde, E.A., Clayton, R.N., Mayeda, T.K., Deines, P., Rossman, G.R., Sobolev, N. V., 1995. Archean mantle heterogeneity and the origin of diamondiferous eclogites, Siberia: evidence from stable isotopes and hydroxyl in garnet. Am. Mineral. 80, 799–809. https://doi.org/10.2138/am-1995-7-816
Sobolev, V.S., Sobolev, N. V., 1980. New proof on very deep subsidence of eclogitized crustal rocks. Dokl. Akad. Nauk SSSR 250, 683–685.
Sokol, A.G., Palyanov, Y.N., Tomilenko, A.A., Bul'bak, T.A., Palyanova, G.A., 2017. Carbon and nitrogen speciation in nitrogen-rich C–O–H–N fluids at 5.5–7.8 GPa. Earth Planet. Sci. Lett. 460, 234–243. https://doi.org/10.1016/j.epsl.2016.11.050
Sokol, A.G., Tomilenko, A.A., Bul'bak, T.A., Sokol, I.A., Zaikin, P.A., Sobolev, N. V., 2020. Composition of reduced mantle fluids: Evidence from modeling experiments and fluid inclusions in natural diamond. Russ. Geol. Geophys. 61, 663–674. https://doi.org/10.15372/RGG2020103
Sossi, P.A., Eggins, S.M., Nesbitt, R.W., Nebel, O., Hergt, J.M., Campbell, I.H., O'Neill, H.S.C., Kranendonk, M. Van, Rhodri Davies, D., 2016. Petrogenesis and geochemistry of Archean Komatiites. J. Petrol. 57, 147–184. https://doi.org/10.1093/petrology/egw004
Speelmanns, I.M., Schmidt, M.W., Liebske, C., 2019. The almost lithophile character of nitrogen during core formation. Earth Planet. Sci. Lett. 510, 186–197. https://doi.org/10.1016/j.epsl.2019.01.004
Spetsius, Z. V., Taylor, L.A., Valley, J.W., Deangelis, M.T., Spicuzza, M., Ivanov, A.S., Banzeruk, V.I., 2008. Diamondiferous xenoliths from crustal subduction: garnet oxygen isotopes from the Nyurbinskaya pipe, Yakutia. Eur. J. Mineral. 20, 375–385. https://doi.org/10.1127/0935-1221/2008/0020-1828
Stachel, T., 2014. Diamonds. Geol. Gem Depos. 1–28.
Stachel, T., Aulbach, S., Brey, G.P., Harris, J.W., Leost, I., Tappert, R., Viljoen, K.S., 2004a. The trace element composition of silicate inclusions in diamonds: a review. Lithos 77, 1–19. https://doi.org/10.1016/j.lithos.2004.03.027
Stachel, T., Brey, G.P., Harris, J.W., 2000a. Kankan diamonds (Guinea) I: from the lithosphere down to the transition zone. Contrib. to Mineral. Petrol. 140, 1–15. https://doi.org/10.1007/s004100000173
Stachel, T., Cartigny, P., Chacko, T., Pearson, D.G., 2021. Carbon and nitrogen of mantle-derived diamonds. Rev. Mineral. Geochemistry submitted.
Stachel, T., Chacko, T., Luth, R.W., 2017. Carbon isotope fractionation during diamond growth in depleted peridotite: counterintuitive insights from modelling water-maximum CHO fluids as multi-component systems. Earth Planet. Sci. Lett. 473, 44–51. https://doi.org/10.1016/j.epsl.2017.05.037

Stachel, T., Harris, J.W., 2009. Formation of diamond in the Earth's mantle. J. Phys. Condens. Matter 21, 364206. https://doi.org/10.1088/0953-8984/21/36/364206
Stachel, T., Harris, J.W., 2008. The origin of cratonic diamonds – constraints from mineral inclusions. Ore Geol. Rev. 34, 5–32. https://doi.org/10.1016/j.oregeorev.2007.05.002
Stachel, T., Harris, J.W., 1997. Diamond precipitation and mantle metasomatism - evidence from the trace element chemistry of silicate inclusions in diamonds from Akwatia, Ghana. Contrib. to Mineral. Petrol. 129, 143–154. https://doi.org/10.1007/s004100050328
Stachel, T., Harris, J.W., Aulbach, S., Deines, P., 2002. Kankan diamonds (Guinea) III: $\delta^{13}C$ and nitrogen characteristics of deep diamonds. Contrib. to Mineral. Petrol. 142, 465–475. https://doi.org/10.1007/s004100100297
Stachel, T., Harris, J.W., Brey, G.P., 1998a. Rare and unusual mineral inclusions in diamonds from Mwadui, Tanzania. Contrib. to Mineral. Petrol. 132, 34–47. https://doi.org/10.1007/s004100050403
Stachel, T., Harris, J.W., Brey, G.P., Joswig, W., 2000b. Kankan diamonds (Guinea) II: lower mantle inclusion parageneses. Contrib. to Mineral. Petrol. 140, 16–27. https://doi.org/10.1007/s004100000174
Stachel, T., Harris, J.W., Muehlenbachs, K., 2009. Sources of carbon in inclusion bearing diamonds. Lithos 112, 625–637. https://doi.org/10.1016/j.lithos.2009.04.017
Stachel, T., Luth, R.W., 2015. Diamond formation – where, when and how? Lithos 220–223, 200–220. https://doi.org/10.1016/j.lithos.2015.01.028
Stachel, T., Viljoen, K.S., Brey, G., Harris, J.W., 1998b. Metasomatic processes in lherzolitic and harzburgitic domains of diamondiferous lithospheric mantle: REE in garnets from xenoliths and inclusions in diamonds. Earth Planet. Sci. Lett. 159, 1–12. https://doi.org/10.1016/S0012-821X(98)00064-8
Stachel, T., Viljoen, K.S., McDade, P., Harris, J.W., 2004b. Diamondiferous lithospheric roots along the western margin of the Kalahari Craton - the peridotitic inclusion suite in diamonds from Orapa and Jwaneng. Contrib. to Mineral. Petrol. 147, 32–47. https://doi.org/10.1007/s00410-003-0535-1
Stagno, V., 2019. Carbon, carbides, carbonates and carbonatitic melts in the Earth's interior. J. Geol. Soc. London. 176, 375–387. https://doi.org/10.1144/jgs2018-095
Stagno, V., Tange, Y., Miyajima, N., McCammon, C.A., Irifune, T., Frost, D.J., 2011. The stability of magnesite in the transition zone and the lower mantle as function of oxygen fugacity. Geophys. Res. Lett. 38, 1–5. https://doi.org/10.1029/2011GL049560
Stern, R.A., Palot, M., Howell, D.H., Stachel, T., Pearson, D., Cartigny, P., Oh, A., 2014. Research Report 14-01: Methods and reference materials for SIMS diamond C- and N-isotope analysis.
Stixrude, L., Lithgow-Bertelloni, C., 2007. Influence of phase transformations on lateral heterogeneity and dynamics in Earth's mantle. Earth Planet. Sci. Lett. 263, 45–55. https://doi.org/10.1016/j.epsl.2007.08.027
Suess, H.E., 1988. V.M Goldschmidt and the origin of the elements. Appl. Geochemistry 3, 385–391.
Tappert, R., Stachel, T., Harris, J.W., Muehlenbachs, K., Ludwig, T., Brey, G.P., 2005a. Diamonds from Jagersfontein (South Africa): Messengers from the sublithospheric mantle. Contrib. to Mineral. Petrol. 150, 505–522. https://doi.org/10.1007/s00410-005-0035-6
Tappert, R., Stachel, T., Harris, J.W., Shimizu, N., Brey, G.P., 2005b. Mineral inclusions in diamonds from the Panda kimberlite, Slave Province, Canada. Eur. J. Mineral. 17, 423–440.

https://doi.org/10.1127/0935-1221/2005/0017-0423
Taylor, L.A., Anand, M., Promprated, P., Floss, C., Sobolev, N. V., 2003. The significance of mineral inclusions in large diamonds from Yakutia, Russia – Taylor et al. 88 (56): 912 – American Mineralogist. Am. Mineral. 88, 912–920.
Taylor, L.A., Spetsius, Z. V., Wiesli, R., Spicuzza, M., Valley, J.W., 2005. Diamondiferous peridotites from oceanic protoliths: Crustal signatures from yakutian kimberlites. Geol. i Geofiz. 46, 1198–1206.
Taylor, W.R., Green, D.H., 1988. Measurement of reduced peridotite-C-O-H solidus and implications for redox melting in the mantle. Nature 332, 349–352.
Taylor, W.R., Jaques, A.L., Ridd, M., 1990. Nitrogen-defect aggregation characteristics of some Australasian diamonds: time-temperature constraints on the source regions of pipe and alluvial diamonds. Am. Mineral. 75, 1290–1310.
Thomson, A.R., Kohn, S.C., Bulanova, G.P., Smith, C.B., Araujo, D., EIMF, Walter, M.J., 2014. Origin of sub-lithospheric diamonds from the Juina-5 kimberlite (Brazil): constraints from carbon isotopes and inclusion compositions. Contrib. to Mineral. Petrol. 168. https://doi.org/10.1007/s00410-014-1081-8
Thomson, A.R., Walter, M.J., Kohn, S.C., Brooker, R.A., 2016. Slab melting as a barrier to deep carbon subduction. Nature 529, 76–79. https://doi.org/10.1038/nature16174
Tilley, C.E., 1948. Victor Moritz Goldschmidt. Biogr. Mem. Fellows R. Soc. 6, 51–66.
Timmerman, S., Jaques, A.L., Weiss, Y., Harris, J.W., 2018. N-δ13C-inclusion profiles of cloudy diamonds from Koffiefontein: evidence for formation by continuous Rayleigh fractionation and multiple fluids. Chem. Geol. 483, 31–46. https://doi.org/10.1016/j.chemgeo.2018.02.024
Titkov, S.V., Krivovichev, S. V., Organova, N.I., 2012. Plastic deformation of natural diamonds by twinning: evidence from X-ray diffraction studies. Mineral. Mag. 76, 143–149. https://doi.org/10.1180/minmag.2012.076.1.143
Trønnes, R.G., Frost, D.J., 2002. Peridotite melting and mineral-melt partitioning of major and minor elements at 22-24.5 GPa. Earth Planet. Sci. Lett. 197, 117–131. https://doi.org/10.1016/S0012-821X(02)00466-1
Tschauner, O., Huang, S., Greenberg, E., Prakapenka, V.B., Ma, C., Rossman, G.R., Shen, A.H., Zhang, D., Newville, M., Lanzirotti, A., Tait, K., 2018. Ice-VII inclusions in diamonds: Evidence for aqueous fluid in Earth's deep mantle. Science 359, 1136–1139. https://doi.org/10.1126/science.aao3030
Tschauner, O., Ma, C., Beckett, J.R., Prescher, C., Prakapenka, V.B., Rossman, G.R., Chi, M., Beckett, J.R., Prescher, C., Prakapenka, V.B., Rossman, G.R., 2014. Discovery of bridgmanite, the most abundant mineral in Earth, in a shocked meteorite. Science 346, 1100–1102. https://doi.org/10.1126/science.1259369
Valley, J.W., Kinny, P.D., Schulze, D.J., Spicuzza, M.J., 1998. Zircon megacrysts from kimberlite: Oxygen isotope variability among mantle melts. Contrib. to Mineral. Petrol. 133, 1–11. https://doi.org/10.1007/s004100050432
Van Der Hilst, R.D., Widiyantoro, S., Engdahl, E.R., 1997. Evidence for deep mantle circulation from global tomography. Nature 386, 578–584. https://doi.org/10.1038/386578a0
Vance, E.R., Harris, J.W., Milledge, H.J., 1973. Possible origins of α-damage in diamonds from kimberlite and alluvial sources. Mineral. Mag. 39, 349–360. https://doi.org/10.1180/minmag.1973.039.303.12
Veizer, J., Hoefs, J., 1976. The nature of O^{18}/O^{16} and C^{13}/C^{12} secular trends in sedimentary

carbonate rocks. Geochim. Cosmochim. Acta 40, 1387–1395. https://doi.org/10.1016/0016-7037(76)90129-0

Viljoen, K.S., Smith, C.B., Sharp, Z.D., 1996. Stable and radiogenic isotope study of eclogite xenoliths from the Orapa kimberlite, Botswana. Chem. Geol. 131, 235–255. https://doi.org/10.1016/0009-2541(96)00018-6

Vlaar, N.J., van Keken, P.E., van den Berg, A.P., 1994. Cooling of the earth in the Archaean: consequences of pressure-release melting in a hotter mantle. Earth Planet. Sci. Lett. 121, 1–18. https://doi.org/10.1016/0012-821X(94)90028-0

Vorster, C.J., 2002. Simplified geology and diamond deposits South Africa, Lesotho and Swaziland [WWW Document]. Counc. Geosci. URL http://www.geoscience.org.za/images/Maps/diamond.gif (accessed 2.24.20).

Walraven, F., Armstrong, R.., Kruger, F.., 1990. A chronostratigraphic framework for the north-central Kaapvaal craton, the Bushveld Complex and the Vredefort structure. Tectonophysics 171, 23–48.

Walter, M.J., 1999. Melting residues of fertile peridotite and the origin of cratonic lithosphere, in: Fei, Y., Bertka, C.M., Mysen, B.O. (Eds.), Mantle Petrology: Field Observations and High Pressure Experimentation (a Tribute to Francis R. (Joe) Boyd). The Geochemical Society, pp. 225–239.

Walter, M.J., 1998. Melting of garnet peridotite and the origin of komatiite and depleted lithosphere. J. Petrol. 39, 29–60. https://doi.org/10.1093/petroj/39.1.29

Walter, M.J., Bulanova, G.P., Armstrong, L.S., Keshav, S., Blundy, J.D., Gudfinnsson, G., Lord, O.T., Lennie, A.R., Clark, S.M., Smith, C.B., Gobbo, L., 2008. Primary carbonatite melt from deeply subducted oceanic crust. Nature 454, 622–625. https://doi.org/10.1038/nature07132

Walter, M.J., Kohn, S.C., Araujo, D.P., Bulanova, G.P., Smith, C.B., Gaillou, E., Wang, J., Steele, A., Shirey, S.B., 2011. Deep Mantle Cycling of Oceanic Crust: Evidence from Diamonds and Their Mineral Inclusions. Science 334, 54–57. https://doi.org/10.1126/science.1209300

Weiss, Y., Griffin, W.L., Navon, O., 2013. Diamond-forming fluids in fibrous diamonds: the trace-element perspective. Earth Planet. Sci. Lett. 376, 110–125. https://doi.org/10.1016/j.epsl.2013.06.021

Weiss, Y., Kessel, R., Griffin, W.L., Kiflawi, I., Klein-BenDavid, O., Bell, D.R., Harris, J.W., Navon, O., 2009. A new model for the evolution of diamond-forming fluids: evidence from microinclusion-bearing diamonds from Kankan, Guinea. Lithos 112, 660–674. https://doi.org/10.1016/j.lithos.2009.05.038

Weiss, Y., Kiflawi, I., Navon, O., 2010. IR spectroscopy: quantitative determination of the mineralogy and bulk composition of fluid microinclusions in diamonds. Chem. Geol. 275, 26–34. https://doi.org/10.1016/j.chemgeo.2010.04.010

Weiss, Y., Navon, O., Goldstein, S.L., Harris, J.W., 2018. Inclusions in diamonds constrain thermo-chemical conditions during Mesozoic metasomatism of the Kaapvaal cratonic mantle. Earth Planet. Sci. Lett. 491, 134–147. https://doi.org/10.1016/j.epsl.2018.03.014

Wilding, M.C., 1990. A study of diamonds with syngenetic inclusions. University of Edinburgh.

Williams, H.M., Nielsen, S.G., Renac, C., Griffin, W.L., O'Reilly, S.Y., McCammon, C.A., Pearson, N., Viljoen, F., Alt, J.C., Halliday, A.N., 2009. Fractionation of oxygen and iron isotopes by partial melting processes: Implications for the interpretation of stable isotope signatures in mafic rocks. Earth Planet. Sci. Lett. 283, 156–166.

https://doi.org/10.1016/j.epsl.2009.04.011
Wilson, A.H., 2019. The Late-Paleoarchean ultra-depleted Commondale Komatiites: Earth's hottest lavas and consequences for eruption. J. Petrol. 60, 1575–1620. https://doi.org/10.1093/petrology/egz040
Wilson, A.H., 2003. A new class of silica enriched, highly depleted komatiites in the southern Kaapvaal Craton, South Africa. Precambrian Res. 127, 125–141. https://doi.org/10.1016/S0301-9268(03)00184-0
Wilson, A.H., Shirey, S.B., Carlson, R.W., 2003. Archaean ultra-depleted komatiites formed by hydrous melting of cratonic mantle. Nature 423, 858–861. https://doi.org/10.1038/nature01701
Wood, B.J., 2000. Phase transformations and partitioning relations in peridotite under lower mantle conditions. Earth Planet. Sci. Lett. 174, 341–354. https://doi.org/10.1016/S0012-821X(99)00273-3
Wood, B.J., Bryndzia, L.T., Johnson, K.E., 1990. Mantle oxidation state and its relationship to tectonic environment and fluid speciation. Science 248, 337–345. https://doi.org/10.1126/science.248.4953.337
Woods, G.S., 1986. Platelets and the infrared absorption of type Ia diamonds. Proc. R. Soc. London. A Math. Phys. Sci. 407, 219–238.
Wyllie, P.J., 1987a. Metasomatism and fluid generation in mantle xenoliths., in: Nixon, P.H. (Ed.), Mantle Xenoliths. John Wiley & Sons, Inc., pp. 609–622.
Wyllie, P.J., 1987b. Discussion of recent papers on carbonated peridotite, bearing on mantle metasomatism and magmatism. Earth Planet. Sci. Lett. 82, 391–397. https://doi.org/10.1016/0012-821X(87)90213-5
Wyllie, P.J., 1978. Mantle fluid compositions buffered in peridotite-CO2-H2O by carbonates, amphibole, and phlogopite. J. Geol. 86, 687–713. https://doi.org/10.1086/649737
Wyllie, P.J., Huang, W.-L., 1976. Carbonation and melting reactions in the system CaO-MgO-SiO2-CO2 at mantle pressures with geophysical and petrological applications. Contrib. to Mineral. Petrol. 54, 79–107.
Wyllie, P.J., Ryabchikov, I.D., 2000. Volatile Components, Magmas, and Critical Fluids in Upwelling Mantle. J. Petrol. 41, 1195–1206. https://doi.org/10.1093/petrology/41.7.1195
Zhang, H., Menzies, M.A., Gurney, J.J., Zhou, X., 2001. Cratonic peridotites and silica-rich melts: diopside-enstatite relationships in polymict xenoliths, Kaapvaal, South Africa. Geochim. Cosmochim. Acta 65, 3365–3377. https://doi.org/10.1016/S0016-7037(01)00675-5
Zheng, H., Csete de Györgyfalva, G.D.C., Quimby, R., Bagshaw, H., Ubic, R., Reaney, I.M., Yarwood, J., 2003. Raman spectroscopy of B-site order-disorder in $CaTiO_3$-based microwave ceramics. J. Eur. Ceram. Soc. 23, 2653–2659. https://doi.org/10.1016/S0955-2219(03)00149-3
Zheng, H., Reaney, I.M., Gyo, G.D.C.C. De, Ubic, R., Yarwood, J., Seabra, M.., Ferreira, V.M., 2004. Raman spectroscopy of CaTiO3-based perovskite. J. Mater. Res. 19, 488–495.
Zhu, F., Li, J., Liu, J., Dong, J., Liu, Z., 2019. Metallic iron limits silicate hydration in Earth's transition zone. Proc. Natl. Acad. Sci. U. S. A. 116, 22526–22530. https://doi.org/10.1073/pnas.1908716116
Ziberna, L., Nimis, P., Kuzmin, D., Malkovets, V.G., 2016. Error sources in single-clinopyroxene thermobarometry and a mantle geotherm for the Novinka kimberlite, Yakutia. Am. Mineral. 101, 2222–2232. https://doi.org/10.2138/am-2016-5540

Appendix A. Supplementary Data for Chapter 3

Table A1: Physical characteristics of Koffiefontein diamonds.
Table A2: Nitrogen concentration and aggregation of Koffiefontein diamonds as determined by FTIR. Mantle residence temperatures calculated for a time of 2 Gyr based on Leahy and Taylor (1996).
Table A3: Carbon and nitrogen isotopes and nitrogen concentration of selected diamond fragments. Numbered spots correspond to points in Figure A1.

Figure A4: Cathodoluminescence figures of Koffiefontein diamond fragments. Numbers indicate spot number listed in Table A3.

Table A1: Summary of physical characteristics of Koffiefontein diamonds. Samples are divided into suite: P – peridotitic, W – websteritic, and E – eclogitic. Colours are grouped into colourless, yellow, and brown and vl or l for very light or lights, respectively. For diamond shape that is transitional (e.g., octa/dodec, dodec/octa), the fist shape is the most prominent. Growth refers to ocahedral growth plates and PD for plastic deformation. Resorption features are listed for each shape. Octahedral resorption: shield lam – shield-shaped laminae; N flat tri – negative flat-bottomed trigons, N ter tri – negative terraced trigons, P raised tri – positive raised trigons; dodecahedra resorption: T – terraces, ED hil – elongates drop-shaped hillocks, Pyr hil – pyramidal hillocks. Overall resorption

Sample #	Suite	Colour	Shape	Growth	PD	Octa. Resorption	Dodec. Resorption	Overall Resorption	Comments
1/02	P	colourless	octa/dodec	-	-	-	T, ED hil	weak	-
1/04	P	colourless	irregular	-	-	hexagons	-	moderate	-
1/05	P	colourless	irregular	-	-	-	T, ED hil	moderate	-
2/01	P	colourless	twin; octa/dodec	-	-	N flat tri	ED hil	moderate	macle
2/02	P	lyellow	twin	-	-	-	terraces	strong	macle, rounded; ruts
2/03	P	colourless	twin; octa/dodec	-	-	N flat tri	ED hil	weak	macle
2/04	P	colourless	twin	Y	-	shield lam	-	weak	macle
2/05	P	colourless	twin	-	-	-	T, ED hil	strong	macle, rounded
3/01	P	vl yellow	dodec	-	-	-	-	moderate	-
3/02	P	colourless	dodec	-	-	-	T, ED hil	moderate	-
3/03	P	colourless	dodec	-	-	-	-	moderate	-
4/02	P	vl brown	dodec/octa	-	-	shield lam	ED hil	moderate	-
4/03	P	colourless	octahedra	-	-	shield lam, N flat tri	-	moderate	-
5/01	P	colourless	octahedra	Y	-	shield lam, N flat tri	-	weak	-
5/02	P	colourless	octahedra	Y	-	N flat tri	-	minor	-
5/03	P	lbrown	octahedra	-	-	N flat tri	-	weak	-
5/04	P	colourless	octahedra	-	-	P raised tri	-	weak	-
6/01	P	lbrown	twin	-	striations x2	N ter tri	-	strong	macle, rounded
6/02	P	colourless	twin	-	-	N flat tri	-	moderate	macle
6/03	P	colourless	twin	-	line of trigons	-	ED hil	strong	macle
6/04	P	colourless	twin	-	-	-	ED hil	moderate	macle

Table A1: continued

Sample #	Suite	Colour	Shape	Growth	PD	Octa. Resorption	Dodec. Resorption	Overall Resorption	Comments
6/05	P	colourless	twin; octa/dodec	-	-	shield lam, N flat tri	ED hil	moderate	macle
6/06	P	colourless	twin; octa/dodec	Y	-	-	ED hil	strong	macle, slightly rounded
6/07	P	colourless	twin; octa/dodec	Y	-	N flat tri	T, ED hil	weak	macle
6/08	P	colourless	twin; octa/dodec	-	-	shield lam, N flat tri	ED hil	weak	macle
6/09	P	colourless	twin	-	-	shield lam, N ter tri	-	weak	macle
6/10	P	lbrown	twin	-	-	-	-	none	macle
7/01	P	colourless	twin	-	-	-	-	strong	macle, elongate; ruts
7/02	P	colourless	irregular	-	-	-	-	strong	elongate, rounded
7/03	P	lbrown	twin	-	coarse PD	-	T, ED hil	strong	macle
7/04	P	colourless	dodec	-	-	-	ED hil	moderate	-
7/05	P	colourless	octahedra	Y	-	-	-	none	-
7/06	P	colourless	twin; dodec/octa	-	-	shield lam, N ter tri	ED hil	moderate	macle; pseudohemimorphic
7/07	P	colourless	octahedra	Y	-	N ter tri	-	weak	flattened
7/08	P	colourless	dodec/octa	-	-	shield lam, N ter tri	T, ED hil	moderate	-
7/09	P	colourless	twin	-	-	N flat tri	-	minor	macle
7/10	P	brown	octa/dodec	-	Y	shield lam, N flat tri	ED hil	weak	-
7/11	P	colourless	octahedra	-	-	shield lam	-	weak	-
7/12	P	colourless	octahedra	Y	-	N flat tri	-	weak	-
7/13	P	vl yellow	octahedra	Y	-	N flat tri	-	minor	-
7/14	P	colourless	twin	Y	-	-	ED hil	pseudohemi morphic	re-entrant?
7/15	P	colourless	twin	-	-	hexagons	-	moderate	macle
7/16	P	colourless	dodec	-	-	-	-	moderate	-
7/17	P	colourless	dodec	-	-	-	-	moderate	-
7/18	P	colourless	dodec	-	-	-	T, ED hil	strong	-
7/19	P	colourless	twin	-	-	-	T, ED hil	moderate	contact

Table A1: continued

Sample #	Suite	Colour	Shape	Growth	PD	Octa. Resorption	Dodec. Resorption	Overall Resorption	Comments
8/01	P	colourless	irregular	-	-	-	-	moderate	-
8/02	P	colourless	twin	-	-	-	ED hil	moderate	contact
8/03	P	colourless	octahedra	Y	-	Shield lam	-	minor	-
8/04	P	colourless	irregular	-	-	flat hexagon	-	moderate	-
8/05	P	colourless	dodec	-	-	-	T, ED hil	strong	flattened; ruts
8/06	P	colourless	dodec	-	-	-	ED hil	strong	flattened; ruts
8/07	P	colourless	dodec/octa	-	-	N flat tri	ED hil	strong	flattened
8/08	P	colourless	dodec	-	-	shield lam, N flat tri	ED hil	moderate	-
8/09	P	colourless	octa/dodec	-	-	shield lam, N flat tri	ED hil	weak	ruts
8/10	P	colourless	twin	-	-	-	ED hil	moderate	-
8/11	P	colourless	dodec/octa	-	-	shield lam, N flat tri	T, ED hil	moderate	ruts
8/12	P	colourless	dodec	-	-	-	T, ED hil	weak	-
8/13	P	colourless	twin	-	-	-	ED hil	moderate	ruts
8/14	P	colourless	irregular	-	-	-	ED hil	weak	knobbles from fast growth
8/15	P	colourless	dodec	-	-	-	T, ED hil	moderate	slightly rounded
8/16	P	colourless	twin	-	-	-	T, ED hil	moderate	-
8/17	P	colourless	octahedra	Y	-	shield lam	-	weak	-
8/18	P	lbrown	twin	-	-	N flat tri	-	minor	macle
8/19	P	colourless	twin	-	-	-	-	minor	macle
8/20	P	colourless	octa/dodec	-	-	shield lam, N flat tri	ED hil	weak	ruts
8/21	P	colourless	octa/dodec	-	coarse PD	shield lam, N flat tri	ED hil	weak	-
8/22	P	colourless	twin	-	coarse PD	-	T, ED hil	n	macle; flattened
8/23	P	colourless	octa/dodec	Y	n	hexagon	ED hil	moderate	-
8/24	P	colourless	twin	-	coarse PD	-	ED hil	moderate	macle; elongate
8/25	P	colourless	octahedra	Y	-	-	-	weak	-

Table A1: continued

Sample #	Suite	Colour	Shape	Growth	PD	Octa. Resorption	Dodec. Resorption	Overall Resorption	Comments
8/26	P	colourless	dodec	-	striations x1	ED hil	strong	slightly rounded	
8/27	P	colourless	octahedra	Y	-	N flat tri	-	none	-
8/28	P	colourless	twin	-	-	-	Pry hil	moderate	complicated
9/01	P	colourless	irregular	-	-	-	ED hil	weak	-
9/02	P	colourless	octa/dodec	Y	-	N flat tri	ED hil	weak	-
40/14	P	colourless	frag	-	-	hexagons	-	slightly rounded	-
10/01	P	colourless	dodec	-	striations x1	-	ED hil	moderate	-
10/02	P	vl brown	dodec	-	-	-	T, ED hil	strong	-
10/03	P	vl yellow	dodec	-	-	-	T, ED hil	moderate	-
10/04	P	colourless	twin	-	-	-	T, ED hil	moderate	re-entrant
10/05	P	colourless	twin	-	-	-	T, ED hil	moderate	macle; ruts
10/06	P	colourless	irregular	-	-	-		moderate	ruts
10/07	P	colourless	dodec	-	-	-	ED hil	moderate	-
10/08	P	colourless	twin	-	-	-	T, ED hil	moderate	ruts
10/09	P	vl yellow	twin	-	-	-	ED hil	moderate	re-entrant
10/10	P	colourless	irregular	-	-	-	ED hil	moderate	ruts
10/11	P	colourless	dodec	-	-	-	T, ED hil	strong	-
10/12	P	colourless	dodec	-	-	-	T, ED hil	strong	-
10/13	P	colourless	octa/dodec	-	-	shield lam, N flat tri	ED hil	weak	-
10/14	P	yellow	dodec	-	-	-	-	strong	rounded
10/15	P	colourless	twin	-	-	N flat tri	-	none	macle
10/16	P	colourless	octahedra	-	-	-	ED hil	moderate	-
10/17	P	colourless	octa/dodec	-	-	-	T, ED hil	n	-
10/18	P	colourless	twin	-	-	-	T, ED hil	strong	-
10/19	P	lyellow	octa/dodec	-	-	shield lam, N flat tri	ED hil	moderate	-

Table A1: continued

Sample #	Suite	Colour	Shape	Growth	PD	Octa. Resorption	Dodec. Resorption	Overall Resorption	Comments
10/20	P	lyellow	twin	-	striations x1	N flat tri	-	moderate	aggregated twin
11/01	P	vl brown	irregular	-	-	-	ED hil	weak	-
11/02	P	colourless	twin	-	-	-	-	moderate	aggregated twin
11/03	P	colourless	octahedra	Y	-	-	T	minor	-
12/06	P	lbrown	octahedra	Y	-	N raised tri	T	minor	surface undulating
16/01	P	lbrown	dodec	-	coarse PD	-	ED hil	strong	rounded
16/02	P	colourless	dodec	-	-	-	ED hil	moderate	-
16/03	P	colourless	octa/dodec	-	-	-	ED hil	moderate	-
20/01	P	lbrown	twin	Y	-	N flat tri	T	weak	octahedra
21/02	P	colourless	twin	Y	-	-	T	minor	-
23/02	P	lbrown	irregular	-	-	N flat tri	ED hil	moderate	-
39/01	P	colourless	octahedra	Y	-	-	-	n	-
39/02	P	colourless	dodec	-	-	N flat tri	ED hil	moderate	flattened
12/03	W	colourless	dodec	-	-	-	ED hil	n	flattened
12/02	W	colourless	dodec	-	-	-	ED hil	strong	-
14/03	W	colourless	twin	-	-	-	ED hil	moderate	re-entrant; ruts
1/01	E	lyellow	irregular	-	-	-	-	weak	flattened; ruts
12/01	E	colourless	irregular	-	-	-	ED hil	na	-
12/04	E	lbrown	twin	-	-	-	ED hil	na	-
12/05	E	colourless	dodec	-	-	-	ED hil	moderate	-
12/07	E	colourless	octa/dodec	-	-	shield lam, N flat tri	ED hil	weak	-
12/08	E	vl brown	irregular	-	-	-	-	n	-
12/09	E	colourless	irregular	-	coarse PD	-	T, ED hil	moderate	-
12/10	E	colourless	irregular	-	-	-	T, ED hil	moderate	ruts
12/11	E	colourless	dodec	-	striations x1	-	T, ED hil	moderate	ruts
12/12	E	colourless	frag	-	-	-	ED hil	na	-

Table A1: continued

Sample #	Suite	Colour	Shape	Growth	PD	Octa. Resorption	Dodec. Resorption	Overall Resorption	Comments
12/13	E	colourless	dodec	-	striations x1	-	T, ED hil	strong	-
12/14	E	colourless	dodec	-	-	-	T, ED hil	moderate	-
12/15	E	colourless	dodec	-	-	-	ED hil	strong	flattened; ruts
12/16	E	colourless	twin	Y	-	-	-	minor	parallel integrowth
12/17	E	colourless	dodec	-	coarse PD	-	T, ED hil	strong	-
1/03	E	colourless	irregular	-	-	-	T, ED hil	moderate	-
4/01	E	colourless	dodec	-	-	-	ED hil	strong	flattened
13/01	E	colourless	dodec	-	-	-	ED hil	strong	-
13/02	E	vl yellow	irregular	-	-	-	T, ED hil	strong	flattened
14/01	E	lyellow	dodec	-	-	-	ED hil	pseudohemi morphic	-
14/02	E	colourless	twin	Y	-	N flat tri	-	minor	octahedra; ruts
14/04	E	vl yellow	dodec	-	-	-	T, ED hil	strong	-
14/05	E	colourless	irregular	-	-	-	-	-	-
14/06	E	colourless	dodec	-	-	-	ED hil	strong	flattened
14/07	E	colourless	dodec	-	-	-	T, ED hil	strong	ruts
14/08	E	colourless	dodec	-	striations x1	N flat tri	-	moderate	flattened
14/09	E	colourless	irregular	-	-	-	ED hil	strong	surface is undulating
14/10	E	colourless	dodec	-	-	-	ED hil	flattened	flattened; ruts
14/11	E	colourless	dodec	-	-	-	ED hil	strong	-
14/12	E	colourless	dodec	-	striations x1	-	T, ED hil	strong	corrosion
14/13	E	colourless	dodec	-	-	-	T, ED hil	strong	flattened
14/14	E	colourless	dodec	-	-	-	T, ED hil	moderate	flattened
15/01	E	colourless	dodec	-	-	-	T, ED hil	strong	flattened
15/02	E	colourless	dodec/octa	-	-	N flat tri	T, ED hil	strong	flattened
15/03	E	colourless	dodec	-	coarse PD	-	ED hil	strong	-

Table A1: continued

Sample #	Suite	Colour	Shape	Growth	PD	Octa. Resorption	Dodec. Resorption	Overall Resorption	Comments
15/04	E	colourless	dodec	-	-	-	T, ED hil	strong	-
22/01	E	colourless	dodec	-	-	-	ED hil	moderate	ruts
36/01	E	colourless	irregular	-	Y	-	-	-	flattened
26/01	Sul_E	colourless	dodec	-	-	-	ED hil	-	-
26/02	Sul_E	colourless	dodec	-	-	-	ED hil	slightly rounded	-
26/03	Sul_E	colourless	dodec	-	-	N flat tri	-	-	remant octahedra faces with trigons
26/04	Sul_E	vl brown	dodec	-	-	-	T	-	-
27/01	Sul_E	vl brown	dodec	-	-	-	-	-	-
27/02	Sul_E	colourless	octahedra	-	-	-	ED hil	slightly rounded	-
28/01	Sul_E	colourless	dodec	-	coarse PD	-	ED hil	-	flattened
28/02	Sul_E	colourless	dodec	-	-	-	ED hil	-	-
29/01	Sul_E	colourless	dodec	-	-	-	ED hil	-	-
30/01	Sul_E	colourless	dodec	-	-	-	T	well rounded	-
31/01	Sul_E	colourless	dodec	-	-	-	T	-	flattened
31/02	Sul_E	vl brown	dodec	-	striations x1	-	ED hil	-	-
32/01	Sul_E	colourless	twin	-	striations x2	-	T	well rounded	flattened
33/01	Sul_E	brown	dodec	-	striations x2	-	T, ED hil	-	-
34/01	Sul_E	colourless	dodec	-	-	-	ED hil	-	Interesting texture "scratch"
34/02	Sul_E	colourless	dodec	-	-	-	T	-	remant octahedra faces
35/01	Sul_E	colourless	twin	-	-	-	ED hil	-	macle
36/02	Sul_E	colourless	octahedra	Y	-	-	T	-	-

Table A1: continued

Sample #	Suite	Colour	Shape	Growth	PD	Octa. Resorption	Dodec. Resorption	Overall Resorption	Comments
40/01	Sul_E	colourless	dodec	-	-	-	-	-	elongated
40/02	Sul_E	colourless	dodec	-	-	-	-	-	multiple conchoidal fractures
40/03	Sul_E	colourless	octahedra	-	-	-	T	slightly rounded	-
40/04	Sul_E	colourless	dodec	-	-	-	ED hil		-
40/05	Sul_E	colourless	octahedra	-	-	-	T	-	-
40/06	Sul_E	colourless	dodec	-	-	-	ED hil	-	flattened
40/07	Sul_E	vl yellow	dodec	-	-	N flat tri	-	-	remant octahedra faces with trigons
40/08	Sul_E	colourless	dodec	-	-	-	T	-	flattened
40/09	Sul_E	vl yellow	octa/dodec	-	-	N flat tri	T	-	-
40/10	Sul_E	colourless	twin	-	-	-	ED hil	-	macle; flattened
40/11	Sul_E	colourless	dodec	-	-	-	T, ED hil	-	flattened
40/12	Sul_E	colourless	twin	Y	-	-	-	-	parallel integrowth
40/13	Sul_E	lbrown	dodec/octa	-	-	-	T, ED hil	-	-
40/15	Sul_E	colourless	dodec	-	-	-	-	-	-
40/16	Sul_E	colourless	dodec	-	-	-	T	-	-
40/17	Sul_E	colourless	irregular	-	-	-	T, ED hil	-	flattened
40/18	Sul_E	colourless	dodec	-	-	-	T, ED hil	-	flattened; undulated resorption on surface?
40/19	Sul_E	colourless	dodec	-	-	-	T	-	-
40/20	Sul_E	lyellow	dodec	-	-	-	T, ED hil	rounded	-
40/21	Sul_E	colourless	dodec	-	-	-	ED hil	-	elongated
41/01	Sul_E	colourless	dodec	-	-	-	ED hil	-	-

Table A2: Nitrogen concentration and aggregation of diamond by Fourier Transform infrared spectrometry (FTIR). Diamonds classified based on nitrogen concentration and aggregation as Type II, IaA, IaAB, or IaA (cut-off for [N] is 10 at.ppm). Where diamond fragments were analysed, separate outside and inside analysis points are listed, otherwise a whole diamond was analysed. Mantle residence temperature (T) calculated for 2 Gyr residence time and where %B is <5 % or >95 %, a %B of 5 % and 95 %, respectively, was used. Abbreviations: P – peridotitic, W – websteritic, E – eclogitic, Sulp E – sulphide-only eclogitic. Cracked diamonds indicated with *.

			Outside					**Inside**					**Whole**					
#	**Suite**	**Type**	**N_A** (ppm)	**N_B** (ppm)	**Total** (ppm)	**%B** %	**I(B')** cm^{-1}	**N_A** (ppm)	**N_B** (ppm)	**Total** (ppm)	**%B** %	**I(B')** cm^{-1}	**N_A** (ppm)	**N_B** (ppm)	**Total** (ppm)	**%B** %	**I(B')** cm^{-1}	**T @ 2Ga** (°C)
1/02	P*	Iab											107	17	123	13	3.5	1127
1/04	P*	Ia	577	40	617	7	19.1	663	25	688	4	28.6						1063
1/05	P*	II											1	4	6	78	0.0	na
2/01	P*	II	7	1	9	15	0.3	8	0	8	0	0.0						na
2/02	P*	II																na
2/03	P*	II																na
2/04	P*	Iab	434	395	829	48	261.2	456	432	888	49	279.2						1124
2/05	P*	Iab	45	17	62	27	17.0	17	25	42	60	0.0						1190
3/01	P*	Iab	433	450	883	51	288.0	422	487	909	54	307.4						1127
3/02	P*	Ib	0	396	396	100	8.9	0	527	527	100	5.8						1411
3/03	P*	Iab											16	12	29	43	6.0	1205
4/02	P	Ia	503	8	511	2	34.5	309	29	337	9	10.7						1067
4/03	P	Ib											0	254	254	100	65.0	1432
5/01	P*	Ib	48	285	333	86	129.3	22	247	268	92	108.6						1206
5/02	P*	Ia	216	16	232	7	13.9	190	0	190	0	0.0						1029
5/03	P	Ia											28	0	28	0	0.0	998
5/04	P	Iab											410	336	746	45	172.2	1124
6/01	P*	Iab	19	111	129	86	12.7											1220
6/02	P*	Iab	52	8	60	13	4.4											1145
6/03	P*	Iab						16	35	50	69	11.6						1219
6/04	P*	Iab	156	101	258	39	46.7	0	363	363	100	0.0						1282
6/05	P*	Iab	28	21	49	43	5.2											1191
6/06	P*	Iab	59	0	59	0	0.0	98	0	98	0	12.7						979
6/07	P*	Iab	129	65	195	34	42.5	197	55	252	22	31.1						1135
6/08	P*	Iab	178	88	266	33	52.0	35	8	43	19	13.4						1150
6/09	P*	Iab											51	53	104	51	40.2	1179
6/10	P*	Iab	241	52	293	18	26.7	150	0	150	0	13.1						1040

Table A2: Continued

#	Suite	Type	Outside N_A (ppm)	Outside N_B (ppm)	Outside Total (ppm)	Outside %B %	Outside I(B') cm^{-1}	Inside N_A (ppm)	Inside N_B (ppm)	Inside Total (ppm)	Inside %B %	Inside I(B') cm^{-1}	Whole N_A (ppm)	Whole N_B (ppm)	Whole Total (ppm)	Whole %B %	Whole I(B') cm^{-1}	T @ 2Ga (°C)
7/01	P*	II																na
7/02	P*	Iab	225	62	286	21	29.7											1121
7/03	P*	Ib	6	58	64	90	7.2	0	209	209	100	24.1						1345
7/04	P*	Ia	44	0	44	0	6.2	67	37	104	36	26.6						1076
7/05	P	Iab											80	274	354	77	148.5	1178
7/06	P	II											7	0	7	0	0.0	na
7/07	P	Iab											71	46	117	39	29.6	1164
7/08	P	Iab											36	34	70	49	23.2	1187
7/09	P	Iab	228	135	363	37	82.8	102	11	112	9	5.4						1127
7/10	P	Ia	64	0	64	0	1.9	102	4	106	4	3.7						1040
7/11	P	Iab	332	177	508	35	99.2	368	238	606	39	135.3						1123
7/12	P	Iab											17	17	34	50	6.1	1208
7/13	P	Iab	202	355	558	64	209.9	232	471	703	67	262.7						1149
7/14	P	II																na
7/15	P	II											6	0	6	0	0.0	na
7/16	P	Iab											10	3	13	23	0.0	1201
7/17	P	Ib											0	342	342	100	0.0	1421
7/18	P	Iab											48	32	80	40	18.3	1174
7/19	P	Iab											45	49	94	52	29.2	1183
8/01	P*	II											12	0	12	0	0.0	1017
8/02	P*	II																na
8/03	P*	Iab	17	3	20	15	1.7	15	0	15	0	1.5						1094
8/04	P*	II																na
8/05	P*	Ia	17	0	17	0	0.0	15	0	15	0	1.0						1010
8/06	P*	II											0	3	3	100	0.0	na
8/07	P*	II											3	0	3	0	0.0	na
8/08	P*	II											3	0	3	0	0.0	na
8/09	P*	Iab	80	93	173	54	62.6	157	208	365	57	159.1						1161
8/10	P*	II																na
8/11	P*	Iab	195	35	229	15	21.8	210	63	273	23	36.3						1120
8/12	P*	Iab	32	21	52	40	14.1	199	49	248	20	47.3						1153
8/13	P*	Ib						0	440	440	100	0.0						1398
8/14	P*	Iab	5	5	10	52	1.5	3	38	41	93	1.2						1259

Table A2: Continued

#	Suite	Type	Outside N_A (ppm)	Outside N_B (ppm)	Outside Total (ppm)	Outside %B %	Outside I(B') cm^{-1}	Inside N_A (ppm)	Inside N_B (ppm)	Inside Total (ppm)	Inside %B %	Inside I(B') cm^{-1}	Whole N_A (ppm)	Whole N_B (ppm)	Whole Total (ppm)	Whole %B %	Whole I(B') cm^{-1}	T @ 2Ga (°C)
8/15	P*	Iab	39	21	60	35	7.3	80	187	266	70	97.9						1176
8/16	P*	II																na
8/17	P*	Iab	61	0	61	0	3.8	48	42	90	47	12.4						1081
8/18	P*	Iab	45	26	71	37	14.0	33	25	57	43	12.4						1180
8/19	P*	Iab						111	26	138	19	18.3						1135
8/20	P	Iab											24	4	28	13	2.4	1163
8/21	P	Iab	359	263	622	42	144.1	300	250	550	45	131.4						1129
8/22	P	II																na
8/23	P	Iab	64	76	140	54	52.6	19	17	36	47	10.8						1189
8/24	P	II																na
8/25	P	Iab	29	6	34	16	8.9	28	29	58	51	21.9						1179
8/26	P	Ib											3	33	37	91	0.0	1272
8/27	P	Iab											49	207	256	81	119.7	1192
8/28	P	II																na
9/01	P*	II																na
9/02	P*	Ib	32	330	362	91	211.4	28	377	406	93	213.4						1209
40/14	P	na																na
10/01	P*	Ia	795	77	872	9	22.9	1082	63	1145	5	0.0						1062
10/02	P*	Iab											99	100	199	50	62.3	1162
10/03	P*	II											6	0	6	0	0.0	na
10/04	P*	Ia											19	0	19	0	1.4	1006
10/05	P*	Ia											52	0	52	0	8.4	986
10/06	P*	II	8	0	8	0	0.0	178	0	178	0	0.0						993
10/07	P*	Ib	14	147	161	91	53.7	30	112	141	79	44.4						1218
10/08	P*	II																na
10/09	P*	II																na
10/10	P*	II																na
10/11	P*	Iab	24	61	86	72	29.6	0	377	377	100	212.1						1313
10/12	P*	Ia	19	0	19	0	0.0	12	0	12	0	0.0						1011
10/13	P*	Iab	117	81	198	41	49.2	32	0	32	0	0.0						1074
10/14	P*	II																na
10/15	P*	Iab	30	14	43	32	6.9	24	0	24	0	4.1						1091
10/16	P*	II	4	9	13	71	0.0	4	0	4	0	0.0						1150

Table A2: Continued

#	Suite	Type	Outside N_A (ppm)	Outside N_B (ppm)	Outside Total (ppm)	Outside %B %	Outside I(B') cm^{-1}	Inside N_A (ppm)	Inside N_B (ppm)	Inside Total (ppm)	Inside %B %	Inside I(B') cm^{-1}	Whole N_A (ppm)	Whole N_B (ppm)	Whole Total (ppm)	Whole %B %	Whole I(B') cm^{-1}	T @ 2Ga (°C)
10/17	P	Iab	47	47	94	50	36.5	18	0	18	0	1.5						1094
10/18	P*	II																na
10/19	P	Iab	13	11	24	46	3.5	0	383	383	100	167.8						1315
10/20	P	Iab											297	476	773	62	354.8	1140
11/01	P*	Iab	67	20	87	23	4.4	81	46	127	36	0.0						1156
11/02	P*	Iab	254	144	398	36	70.7	96	47	143	33	22.9						1141
11/03	P*	Iab	535	117	652	18	50.3	218	24	242	10	0.0						1100
12/06	P	Iab	14	111	125	89	11.8	16	68	83	81	6.4						1226
16/01	P*	Iab											307	196	503	39	103.4	1128
16/02	P*	Iab	579	133	712	19	69.1	549	91	640	14	60.5						1093
16/03	P	Ia											33	0	33	0	0.0	995
20/01	P*	Iab											162	21	183	12	15.0	1114
21/02	P*	Iab											21	16	37	43	6.0	1197
23/02	P	Ib											26	17	43	39	0.0	1189
39/01	P*	Iab											290	75	365	21	46.1	1114
39/02	P*	II																na
12/02	W*	II																1024
12/03	W*	Ia	281	0	281	0	13.7	394	55	449	12	34.5						na
14/03	W*	II																na
1/01	E*	Iab	20	14	34	42	6.0	31	48	79	61	8.5						1198
12/01	E*	Ia	27	0	27	0	0.7	46	0	46	0	1.3						994
12/04	E*	Ia											260	15	275	5	11.4	1085
12/05	E*	Iab											144	56	200	28	23.3	1138
12/07	E*	Iab	60	61	121	51	31.9	63	24	87	27	26.0						1167
12/08	E*	Ia	187	0	187	0	5.5	179	0	179	0	2.2						962
12/09	E	Iab	41	0	41	0	4.5	41	17	59	30	10.9						1081
12/10	E	na																na
12/11	E	Iab	237	233	470	50	97.4	172	150	321	47	42.4						1143
12/12	E	Iab											76	122	198	61	52.1	1174
12/13	E	na																na
12/14	E	Iab											158	419	577	73	256.2	1159
12/15	E	Ia											404	39	443	9	11.2	1086
12/16	E	Ia	173	0	173	0	6.6	153	0	153	0	0.0						965

Table A2: Continued

#	Suite	Type	Outside N_A (ppm)	Outside N_B (ppm)	Outside Total (ppm)	Outside %B %	Outside I(B') cm^{-1}	Inside N_A (ppm)	Inside N_B (ppm)	Inside Total (ppm)	Inside %B %	Inside I(B') cm^{-1}	Whole N_A (ppm)	Whole N_B (ppm)	Whole Total (ppm)	Whole %B %	Whole I(B') cm^{-1}	T @ 2Ga (°C)
12/17	E	Iab											36	136	172	79	60.9	1200
1/03	E*	Iab											118	320	438	73	143.6	1167
4/01	E*	Iab	362	218	580	38	132.9	108	31	139	22	25.0						1131
13/01	E*	Ia	71	0	71	0	0.0	73	0	73	0	0.0						980
13/02	E*	Iab	182	404	586	69	206.1	85	641	725	88	320.9						1167
14/01	E*	na																na
14/02	E*	Iab											81	511	592	86	313.4	1181
14/04	E	Iab	189	36	225	16	21.5	133	0	133	0	0.0						1043
14/05	E*	II											5	0	5	0	0.0	1034
14/06	E*	Ia											70	0	70	0	0.0	981
14/07	E*	Iab											100	160	260	62	92.1	1167
14/08	E	Iab	203	448	652	69	272.4	175	327	502	65	193.4						1153
14/09	E	Iab											171	393	565	70	171.5	1156
14/10	E	II											10	0	10	0	0.0	864
14/11	E	Iab											231	159	390	41	38.2	1136
14/12	E	Iab											145	282	427	66	167.9	1159
14/13	E	Iab	142	223	365	61	112.3	168	338	506	67	192.1						1157
14/14	E	Iab											32	16	48	33	4.5	1180
15/01	E	Iab											71	315	387	82	180.2	1183
15/02	E	Iab											338	264	602	44	157.8	1128
15/03	E	Iab											34	23	56	40	5.3	1184
15/04	E	II																na
36/01	E	II																na
22/01	E	Iab											344	53	397	13	29.9	1100
26/01	Sul E	Ia											446	0	446	0	0.0	956
26/02	Sul E	Iab											347	167	513	32	99.9	1120
26/03	Sul E	Ia											1155	79	1234	6	0.0	1056
26/04	Sul E	Iab											462	119	581	20	60.5	1103
27/01	Sul E	Iab											248	318	565	56	214.6	1142
27/02	Sul E	Iab											288	68	356	19	35.3	1112
28/01	Sul E	Ia											363	8	371	2	3.5	1057
28/02	Sul E	na																na
29/01	Sul E	na																na

Table A2: Continued

#	Suite	Type	Outside N_A (ppm)	Outside N_B (ppm)	Outside Total (ppm)	Outside %B %	Outside I(B') cm^{-1}	Inside N_A (ppm)	Inside N_B (ppm)	Inside Total (ppm)	Inside %B %	Inside I(B') cm^{-1}	Whole N_A (ppm)	Whole N_B (ppm)	Whole Total (ppm)	Whole %B %	Whole I(B') cm^{-1}	T @ 2Ga (°C)
30/01	Sul E	Iab											220	183	403	45	96.9	1139
31/01	Sul E	Iab											184	292	477	61	155.4	1151
31/02	Sul E	Iab											54	271	325	83	142.2	1190
32/01	Sul E	Iab											52	160	212	76	79.2	1189
32/02	Sul E	Iab											222	174	396	44	44.2	1138
33/01	Sul E	Ia											197	13	209	6	0.0	1094
34/01	Sul E	Iab											249	79	328	24	42.0	1121
34/02	Sul E	Iab											164	368	532	69	197.1	1157
35/01	Sul E	Iab											330	79	409	19	86.8	1109
36/02	Sul E	Iab											199	342	541	63	178.7	1150
40/01	Sul E	Ia											204	19	223	9	0.0	1102
40/02	Sul E	Ia											205	12	217	6	0.0	1091
40/03	Sul E	Iab											169	268	438	61	105.9	1153
40/04	Sul E	Iab											345	136	481	28	60.2	1117
40/05	Sul E*	Iab											420	112	531	21	40.6	1105
40/06	Sul E	na																na
40/07	Sul E*	Iab											273	441	714	62	213.7	1142
40/08	Sul E*	Iab											206	371	577	64	170.7	1150
40/09	Sul E	Iab											104	346	450	77	166.5	1172
40/10	Sul E	Ia											85	0	85	0	0.0	977
40/11	Sul E	Ia											331	64	394	16	0.0	1105
40/12	Sul E	Iab											174	268	442	61	0.0	1152
40/13	Sul E	Iab											120	143	263	54	54.0	1159
40/15	Sul E	Iab											341	370	710	52	152.7	1132
40/16	Sul E	Iab											157	250	408	61	141.1	1155
40/17	Sul E*	na																na
40/18	Sul E	Ia											323	57	380	15	26.4	1104
40/19	Sul E	Iab											454	273	727	38	21.8	1117
40/20	Sul E	Iab											281	277	558	50	135.0	1136
40/21	Sul E	Iab											418	328	746	44	30.8	1123

Table A3: Carbon and nitrogen isotope ratios, as well as nitrogen concentrations of Koffiefontein diamonds. Isotopic values are given in ‰, while nitrogen concentrations (N) are reported as ppm. Multiple analysis points per diamond are listed after sample number. Abbreviations: na – not analysed, P – peridotitic, W – websteritic, E – eclogitic, E_sulp – sulphide-only, LM – lower mantle. Functional limit of detection for [N] of diamond is 0.1 at.ppm

Sample #	Suite	$\delta^{13}C$ (VPDB)	2σ (‰)	[N] at ppm	2σ (ppm)	$\delta^{15}N$ (AIR)	2σ (‰)
1/02_1	P	-10.58	0.17	33.6	1.3	na	na
1/02_2	P	-10.37	0.16	35.4	1.4	na	na
1/02_3	P	-10.62	0.17	37.0	1.4	na	na
1/04_1	P	-5.08	0.16	716.1	21.9	-5.43	0.95
1/04_2	P	-5.28	0.16	713.6	21.8	-6.41	0.81
1/05_1	P	-6.99	0.16	9.1	0.5	na	na
1/05_2	P	-6.93	0.17	55.2	2.0	na	na
1/05_3	P	-6.94	0.17	5.9	0.4	na	na
2/01_1	P	na	na	10.0	0.5	na	na
2/01_2	P	-6.27	0.18	15.1	1.4	na	na
2/01_3	P	-5.73	0.17	13.2	0.6	na	na
2/02_1	P	-6.08	0.18	6.2	0.4	na	na
2/02_2	P	-5.76	0.17	5.9	0.5	na	na
2/03_1	P	-5.95	0.18	12.2	0.6	na	na
2/03_2	P	-6.04	0.16	11.2	0.6	na	na
2/03_3	P	-6.19	0.17	8.9	0.6	na	na
2/04_1	P	-5.81	0.17	799.9	25.4	-10.02	0.84
2/04_2	P	-5.77	0.17	901.4	27.5	-11.02	0.86
2/05_1	P	-8.50	0.17	2096.2	65.1	-4.44	0.51
2/05_2	P	-4.65	0.18	6.0	0.4	na	na
3/01_1	P	-5.58	0.17	1267.0	38.4	-9.61	0.66
3/01_2	P	-4.32	0.17	916.0	27.9	-9.23	0.84
3/01_3	P	-4.83	0.16	970.4	30.2	-9.97	0.71
3/02_1	P	-6.85	0.17	813.5	24.8	-1.30	0.75
3/02_2	P	-6.68	0.17	466.5	15.1	-0.62	0.98
3/02_3	P	-6.92	0.17	832.0	27.1	-1.60	0.76
3/03_1	P	-5.14	0.16	83.6	3.0	na	na
3/03_2	P	-5.62	0.17	68.7	2.8	na	na
4/02_1	P	-5.24	0.18	1012.8	30.8	-8.70	0.71
4/02_2	P	-6.86	0.16	813.2	24.8	-4.84	0.76
4/02_3	P	-6.88	0.16	839.8	25.6	-4.39	0.81
5/01_1	P	-5.27	0.17	290.5	9.1	-10.05	1.23
5/01_2	P	-5.26	0.17	4.4	0.3	na	na
5/01_3	P	-6.01	0.18	321.4	10.1	-9.46	1.37
5/02_1	P	-5.98	0.18	23.2	1.3	na	na
5/02_2	P	-6.52	0.18	847.8	25.9	-5.81	0.80
5/02_3	P	-6.08	0.19	14.7	0.7	na	na
6/01_1	P	-18.01	0.20	109.6	4.6	8.84	1.98
6/01_2	P	-17.49	0.18	122.8	4.1	10.31	1.93
6/01_3	P	-16.20	0.19	221.5	7.1	12.62	1.51
6/02_1	P	-6.79	0.18	74.4	2.6	12.65	2.42
6/02_2	P	-5.53	0.17	100.7	3.4	10.77	2.13
6/02_3	P	-7.00	0.16	80.6	2.8	13.24	2.37
6/03_1	P	-4.34	0.18	7.9	0.7	na	na
6/03_2	P	-4.41	0.17	6.8	0.4	na	na
6/03_3	P	-4.40	0.16	6.1	0.4	na	na

Table A3: Continued

Sample #	Suite	$\delta^{13}C$ (VPDB)	2σ (‰)	[N] at ppm	2σ (ppm)	$\delta^{15}N$ (AIR)	2σ (‰)
6/04_1	P	-5.24	0.18	556.5	17.5	-3.88	0.94
6/04_2	P	-4.96	0.16	60.8	2.2	na	na
6/04_3	P	na	na	451.2	14.0	-4.21	1.07
6/05_1	P	-4.81	0.16	4.6	0.4	na	na
6/05_2	P	-4.62	0.16	2.2	0.2	na	na
6/05_3	P	-4.60	0.18	32.1	1.4	na	na
6/06_1	P	-7.41	0.18	454.0	14.3	-8.44	1.24
6/06_2	P	-6.82	0.17	104.1	3.5	8.70	2.18
6/06_3	P	-7.45	0.17	77.2	2.7	7.82	2.72
6/07_1	P	-4.71	0.16	216.7	7.0	na	na
6/07_2	P	-5.69	0.17	31.5	1.2	na	na
6/07_3	P	-6.15	0.18	28.3	1.3	na	na
6/08_1	P	-5.24	0.18	64.8	2.3	na	na
6/08_2	P	-5.07	0.18	153.2	5.2	5.04	1.77
6/08_3	P	-4.59	0.16	86.0	2.9	6.33	2.34
6/08_4	P	-4.05	0.20	20.4	0.9	na	na
6/09_1	P	-4.10	0.17	28.3	1.5	na	na
6/09_2	P	-4.20	0.17	12.5	0.6	na	na
6/10_1	P	-6.25	0.16	308.2	9.6	9.76	1.29
6/10_2	P	-6.05	0.17	317.3	9.9	8.24	1.18
6/10_3	P	-5.97	0.16	331.0	10.7	8.76	1.28
7/01_1	P	-5.21	0.17	3.6	0.3	na	na
7/01_2	P	-5.40	0.19	4.7	0.3	na	na
7/01_3	P	-5.33	0.17	5.6	0.3	na	na
7/02_1	P	-6.49	0.17	12.1	0.6	na	na
7/02_2	P	-6.56	0.17	9.5	0.6	na	na
7/02_3	P	-6.88	0.17	3.5	0.3	na	na
7/02_4	P	-6.80	0.16	440.8	13.6	8.52	1.03
7/03_1	P	-6.97	0.16	5.9	0.4	na	na
7/03_2	P	-6.93	0.17	10.8	0.5	na	na
7/03_3	P	-7.38	0.17	1343.5	40.7	2.78	0.61
7/04_1	P	-6.06	0.18	20.3	0.9	na	na
7/04_2	P	-5.34	0.18	11.9	0.6	na	na
7/04_3	P	-5.76	0.18	34.2	1.5	na	na
7/04_4	P	-5.77	0.18	37.2	1.4	na	na
8/01_1	P	-5.17	0.17	7.2	0.4	na	na
8/01_2	P	-5.18	0.17	7.2	0.4	na	na
8/02_1	P	-5.48	0.17	5.9	0.3	na	na
8/02_2	P	-5.45	0.16	7.0	0.5	na	na
8/02_3	P	-6.38	0.16	7.0	0.5	na	na
8/03_1	P	-4.24	0.18	43.4	1.6	na	na
8/03_2	P	-4.59	0.17	6.3	0.4	na	na
8/03_3	P	-4.29	0.16	13.4	0.7	na	na
8/04_1	P	-6.44	0.20	8.7	0.5	na	na
8/04_2	P	-6.51	0.16	7.3	0.6	na	na
8/04_3	P	-6.63	0.19	6.1	0.4	na	na
8/05_1	P	-5.85	0.18	16.3	0.9	na	na
8/05_2	P	-6.21	0.17	43.0	1.7	na	na
8/05_3	P	-5.69	0.18	15.6	0.9	na	na
8/06_1	P	-5.65	0.19	3.8	0.3	na	na
8/06_2	P	-5.56	0.18	4.9	0.3	na	na
8/06_3	P	-5.44	0.17	3.8	0.3	na	na

Table A3: Continued

Sample #	Suite	$\delta^{13}C$ (VPDB)	2σ (‰)	[N] at ppm	2σ (ppm)	$\delta^{15}N$ (AIR)	2σ (‰)
8/07_1	P	-4.96	0.19	358.9	11.2	na	na
8/07_2	P	-2.93	0.18	7.8	0.5	na	na
8/07_3	P	-4.50	0.18	3.6	0.3	na	na
8/07_4	P	-6.42	0.17	94.4	3.2	-9.50	2.13
8/08_1	P	-3.99	0.18	7.4	0.6	na	na
8/08_2	P	-3.99	0.17	10.0	0.5	na	na
8/08_3	P	-4.06	0.17	4.8	0.3	na	na
8/09_1	P	-3.33	0.18	25.7	1.1	na	na
8/09_2	P	-4.97	0.17	560.2	17.3	-2.93	0.90
8/09_3	P	-5.35	0.16	165.3	5.3	-7.65	1.62
8/10_1	P	-7.27	0.18	8.7	0.5	na	na
8/10_2	P	-6.69	0.17	6.2	0.4	na	na
8/10_3	P	na	na	6.0	0.4	na	na
8/11_1	P	-4.49	0.18	253.9	8.0	3.68	1.34
8/11_2	P	-4.66	0.17	187.3	6.0	3.61	1.68
8/11_3	P	-5.43	0.16	160.2	5.2	8.31	1.70
8/12_1	P	-4.67	0.18	26.1	1.1	na	na
8/12_2	P	-5.03	0.17	157.5	5.5	-3.32	1.15
8/12_3	P	-4.69	0.17	815.3	25.5	-1.61	0.76
8/13_1	P	-3.87	0.16	9.6	0.8	na	na
8/13_2	P	-2.08	0.17	534.6	17.1	-5.76	0.93
8/13_3	P	-3.91	0.17	9.8	0.6	na	na
8/14_1	P	-3.36	0.17	42.0	1.8	na	na
8/14_2	P	-4.19	0.18	22.2	1.0	na	na
8/14_3	P	-4.73	0.16	19.0	0.8	na	na
8/15_1	P	-5.05	0.18	31.8	1.4	na	na
8/15_2	P	-5.80	0.16	57.6	2.1	na	na
8/15_3	P	-5.53	0.19	17.1	0.8	na	na
8/16_1	P	-6.29	0.17	3.8	0.3	na	na
8/16_2	P	-6.24	0.16	4.7	0.3	na	na
8/17_1	P	-5.73	0.16	113.5	3.8	6.18	2.23
8/17_2	P	-4.82	0.17	22.9	1.0	na	na
8/17_3	P	-5.29	0.17	31.1	1.2	na	na
8/18_1	P	-3.42	0.17	3.2	0.2	na	na
8/18_2	P	-3.81	0.16	110.8	3.7	6.99	2.03
8/18_3	P	-3.98	0.17	2.4	0.2	na	na
8/19_1	P	-5.32	0.19	5.9	0.4	na	na
8/19_2	P	-4.96	0.16	5.9	0.4	na	na
9/01_1	P	-5.90	0.17	6.3	0.4	na	na
9/01_2	P	-5.82	0.17	5.2	0.3	na	na
9/01_3	P	-6.07	0.18	5.7	0.4	na	na
9/02_1	P	-5.22	0.17	10.8	0.6	na	na
9/02_2	P	-5.40	0.16	22.7	1.0	na	na
9/02_3	P	-5.30	0.17	8.7	0.5	na	na
10/01_1	P	-6.66	0.19	914.5	27.9	-2.85	0.74
10/01_2	P	-6.55	0.17	870.4	26.7	-2.54	0.73
10/01_3	P	-6.83	0.16	1204.4	36.6	-1.94	0.64
10/02_1	P	-3.04	0.17	13.5	0.6	na	na
10/02_2	P	-4.83	0.17	111.6	3.7	7.28	2.14
10/02_3	P	-5.33	0.20	51.2	1.9	na	na
10/03_1	P	-5.02	0.17	13.2	0.7	na	na
10/03_2	P	-4.99	0.17	9.7	0.5	na	na

Table A3: Continued

Sample #	Suite	$\delta^{13}C$ (VPDB)	2σ (‰)	[N] at ppm	2σ (ppm)	$\delta^{15}N$ (AIR)	2σ (‰)
10/04_1	P	-4.60	0.19	51.0	2.2	na	na
10/04_2	P	-4.81	0.17	18.0	0.8	na	na
10/04_3	P	-4.88	0.18	21.8	0.9	na	na
10/05_1	P	-4.86	0.16	30.7	1.2	na	na
10/05_2	P	-4.27	0.18	5.8	0.5	na	na
10/05_3	P	-4.23	0.18	9.3	0.5	na	na
10/06_1	P	-7.84	0.18	4.9	0.3	na	na
10/06_2	P	-8.16	0.18	3.3	0.3	na	na
10/06_3	P	-7.72	0.17	7.3	0.5	na	na
10/07_1	P	-4.03	0.17	491.1	15.3	-25.64	1.03
10/07_2	P	-4.95	0.19	5.0	0.4	na	na
10/07_3	P	-3.98	0.22	478.5	14.8	-25.58	1.00
10/08_1	P	-5.75	0.17	5.0	0.3	na	na
10/08_2	P	-4.72	0.17	2.9	0.3	na	na
10/08_3	P	-6.52	0.18	2.5	0.2	na	na
10/09_1	P	-6.58	0.20	7.0	0.4	na	na
10/09_2	P	-6.76	0.17	9.8	0.5	na	na
10/09_3	P	-6.57	0.18	5.6	0.4	na	na
10/10_1	P	-6.05	0.18	15.9	0.7	na	na
10/10_2	P	-6.25	0.17	4.6	0.3	na	na
10/10_3	P	-6.16	0.17	3.3	0.2	na	na
10/10_4	P	-5.96	0.18	2.2	0.2	na	na
10/11_1	P	-7.23	0.19	245.7	7.8	-7.33	1.37
10/11_2	P	-5.93	0.19	7.6	1.3	na	na
10/11_3	P	-7.39	0.17	5.2	0.3	na	na
10/12_1	P	-4.89	0.19	12.2	0.6	na	na
10/12_2	P	-4.76	0.18	10.0	0.7	na	na
10/12_3	P	-3.11	0.17	14.3	0.7	na	na
10/12_4	P	-5.31	0.18	12.3	0.8	na	na
10/13_1	P	-3.74	0.19	26.7	1.2	na	na
10/13_2	P	-3.87	0.20	47.7	1.7	na	na
10/13_3	P	-3.59	0.18	49.7	2.0	na	na
10/14_1	P	-5.51	0.18	3.1	0.2	na	na
10/14_2	P	-6.03	0.16	7.7	0.6	na	na
10/14_3	P	-6.11	0.22	5.8	0.4	na	na
10/15_1	P	-5.59	0.17	62.1	2.2	na	na
10/15_2	P	-5.12	0.17	7.8	0.5	na	na
10/15_3	P	-3.69	0.18	12.6	0.6	na	na
10/16_1	P	-6.02	0.18	38.9	1.5	na	na
10/16_2	P	-6.22	0.19	4.1	0.5	na	na
10/16_3	P	-6.59	0.17	5.2	0.3	na	na
10/17_1	P	-5.11	0.17	8.1	0.4	na	na
10/17_2	P	-4.53	0.17	672.8	22.6	-3.14	0.80
10/17_3	P	-5.61	0.16	323.3	11.3	11.22	1.27
10/18_1	P	-5.51	0.18	3.5	0.3	na	na
10/18_2	P	-5.51	0.16	12.2	0.9	na	na
10/18_3	P	-5.58	0.18	3.6	0.3	na	na
11/01_1	P	-7.29	0.20	282.5	8.9	6.89	1.19
11/01_2	P	-7.59	0.16	52.0	1.9	na	na
11/01_3	P	-7.05	0.17	40.8	1.5	na	na

Table A3: Continued

Sample #	Suite	$\delta^{13}C$ (VPDB)	2σ (‰)	[N] at ppm	2σ (ppm)	$\delta^{15}N$ (AIR)	2σ (‰)
11/02_1	P	-6.01	0.18	647.9	19.9	1.73	0.86
11/02_2	P	-6.26	0.17	400.1	12.4	5.13	1.10
11/02_3	P	-2.09	0.17	9.8	0.6	na	na
11/03_1	P	-6.36	0.17	819.1	25.1	0.60	0.76
11/03_2	P	-5.63	0.19	450.6	13.9	1.01	1.09
11/03_3	P	-5.17	0.17	20.6	1.1	na	na
16/01_1	P	-6.45	0.20	586.2	18.2	0.48	0.89
16/01_2	P	-5.12	0.18	42.6	1.6	na	na
16/01_3	P	-5.50	0.18	210.9	6.8	3.04	1.29
16/02_1	P	-4.73	0.18	582.9	17.9	6.25	0.98
16/02_2	P	-5.60	0.16	665.3	20.5	9.55	0.87
16/02_3	P	-5.64	0.17	671.4	20.6	8.22	0.84
12/06_1	P	-15.35	0.19	84.0	3.1	na	na
12/06_2	P	-15.05	0.17	64.7	2.3	na	na
12/06_3	P	-15.14	0.19	49.1	1.8	na	na
20/01_1	P	-5.05	0.13	65.2	2.4	-7.17	2.97
20/01_2	P	-5.05	0.14	500.7	15.6	-5.50	1.27
20/01_3	P	-4.73	0.13	57.1	2.2	na	na
21/02_1	P	-4.60	0.15	5.8	0.4	na	na
21/02_2	P	-3.25	0.13	5.3	0.4	na	na
21/02_3	P	-3.46	0.14	326.8	11.2	na	na
39/01_1	P	-2.69	0.13	437.1	13.7	-3.93	1.10
39/01_2	P	-2.82	0.14	460.7	14.4	-4.80	1.08
39/01_3	P	-2.66	0.12	386.8	12.3	-5.08	1.17
39/02_1	P	-6.45	0.13	1.1	0.1	na	na
39/02_2	P	-5.89	0.12	5.7	0.4	na	na
39/02_4	P	-5.84	0.13	1.8	0.2	na	na
14/03_1	W	-6.63	0.17	2.5	0.2	na	na
14/03_2	W	-6.82	0.19	2.4	0.2	na	na
14/03_3	W	-7.17	0.17	2.7	0.2	na	na
12/02_1	W	-3.61	0.18	15.0	0.8	na	na
12/02_2	W	-2.39	0.16	181.6	6.2	3.93	1.50
12/02_3	W	-2.03	0.19	81.2	2.9	-0.03	2.04
12/02_4	W	-2.05	0.17	150.1	4.9	-15.23	1.92
12/02_5	W	-2.09	0.16	35.5	1.4	na	na
12/02_6	W	-2.02	0.17	69.2	2.5	-12.98	2.98
12/02A_1	W	-3.77	0.16	204.9	7.2	9.38	1.43
12/02A_2	W	-3.83	0.18	251.1	7.9	8.36	1.30
12/02B_1	W	-3.19	0.17	5.3	0.3	na	na
12/02B_2	W	-3.42	0.17	62.1	2.4	na	na
12/03_1	W	-8.98	0.16	232.1	7.4	-0.86	1.47
12/03_2	W	-9.01	0.17	235.1	7.4	0.83	1.39
12/03_3	W	-9.07	0.16	444.6	14.0	1.32	1.09
1/01_1	E	-4.27	0.17	14.8	0.9	na	na
1/01_2	E	-3.95	0.16	127.1	4.2	12.59	1.81
1/01_3	E	-3.95	0.17	76.1	2.6	9.17	2.19
1/03_1	E	-5.30	0.17	291.7	9.1	-0.42	1.21
1/03_2	E	-5.98	0.18	231.9	7.3	0.33	1.33
1/03_3	E	-5.33	0.16	184.7	6.1	-3.75	1.52
4/01_1	E	-11.72	0.19	89.5	3.6	0.75	2.57
4/01_2	E	-12.05	0.18	120.8	4.0	-0.27	1.94
4/01_3	E	-11.95	0.18	41.3	1.5	na	na

Table A3: Continued

Sample #	Suite	$\delta^{13}C$ (VPDB)	2σ (‰)	[N] at ppm	2σ (ppm)	$\delta^{15}N$ (AIR)	2σ (‰)
12/01_1	E	-5.22	0.18	27.2	1.1	na	na
12/01_2	E	-5.56	0.16	71.4	2.5	2.33	2.46
12/01_3	E	-5.56	0.17	135.5	4.4	4.63	1.71
12/01_4	E	-5.09	0.17	32.1	1.3	na	na
12/04_1	E	-4.97	0.17	806.9	25.0	7.25	0.88
12/04_2	E	-5.51	0.18	246.8	7.8	8.56	1.56
12/04_3	E	-5.74	0.18	6.4	0.5	na	na
12/05_1	E	-10.74	0.17	70.9	2.5	8.45	2.21
12/05_2	E	-8.97	0.18	576.9	17.9	-1.69	0.90
12/05_3	E	-10.43	0.16	46.3	1.7	na	na
12/07_1	E	-5.80	0.18	20.1	1.0	na	na
12/07_2	E	-6.14	0.21	9.6	0.7	na	na
12/07_3	E	-6.27	0.19	60.1	2.6	na	na
12/08_1	E	-5.38	0.17	192.1	6.2	-4.07	1.63
12/08_2	E	-5.53	0.17	58.0	2.1	na	na
12/08_3	E	-5.84	0.16	48.4	1.8	na	na
12/09_1	E	-4.49	0.13	1.1	0.1	na	na
12/09_2	E	-4.46	0.12	16.1	0.9	na	na
12/09_3	E	-4.48	0.14	31.7	1.3	na	na
12/09_4	E	-4.73	0.12	30.6	1.3	na	na
13/01_1	E	-6.44	0.17	914.8	27.9	-8.03	0.74
13/01_2	E	-6.01	0.18	14.5	0.7	na	na
13/01_3	E	-5.82	0.19	249.7	7.9	-8.38	1.33
13/02_1	E	-12.04	0.16	1426.5	43.2	1.67	0.59
13/02_2	E	-9.49	0.16	533.7	17.1	2.91	0.84
13/02_3	E	-9.74	0.18	937.2	28.5	2.90	0.83
14/01_1	E	-5.24	0.19	1311.3	40.4	1.04	0.61
14/01_2	E	-5.24	0.16	1349.2	40.9	-0.89	0.60
14/01_3	E	na	na	1196.5	36.3	-0.30	0.67
14/02_1	E	-6.06	0.16	1162.8	35.3	-7.01	0.65
14/02_2	E	-6.37	0.16	232.7	7.4	-3.29	1.28
14/02_3	E	-6.79	0.18	275.7	8.7	2.33	1.28
14/04_1	E	-6.25	0.17	101.7	3.8	1.62	2.40
14/04_2	E	-5.84	0.18	71.5	2.5	-0.69	2.51
14/04_3	E	-5.99	0.17	115.6	3.8	-1.96	2.13
14/05_1	E	-6.18	0.17	7.0	0.4	na	na
14/05_2	E	-6.11	0.18	4.8	0.4	na	na
14/05_3	E	-6.43	0.16	8.5	0.5	na	na
14/06_1	E	-7.17	0.17	82.0	3.0	-1.06	2.37
14/06_2	E	-7.24	0.16	76.6	2.8	4.86	2.50
14/06_3	E	-7.26	0.16	76.0	2.6	6.15	2.37
14/07_1	E	-5.63	0.16	1104.8	34.5	-0.63	0.68
14/07_2	E	-5.75	0.17	1095.3	33.3	-0.19	0.68
14/07_3	E	-6.03	0.17	327.8	10.4	0.22	1.33
14/08_1	E	-4.59	0.17	119.2	4.0	-2.51	1.96
14/08_2	E	-5.85	0.16	2.7	0.2	na	na
14/08_3	E	-5.70	0.16	583.3	19.0	0.15	0.90
22/01_1	E	-4.52	0.14	501.0	16.6	-2.39	1.04
22/01_2	E	-4.34	0.12	461.4	14.8	-3.78	1.10
22/01_3	E	-4.36	0.12	326.2	11.2	-4.91	1.28

Table A3: Continued

Sample #	Suite	$\delta^{13}C$ (VPDB)	2σ (‰)	[N] at ppm	2σ (ppm)	$\delta^{15}N$ (AIR)	2σ (‰)
24/01_1	E	-5.06	0.14	741.0	22.8	-3.63	0.86
24/01_2	E	-4.96	0.13	683.1	21.2	-3.13	0.90
24/01_3	E	-4.76	0.13	771.2	23.7	-2.95	0.90
40/05_1	Sul_E	-5.31	0.13	906.9	28.0	-2.97	0.79
40/05_2	Sul_E	-4.66	0.13	478.9	15.1	-3.66	1.05
40/05_3	Sul_E	-4.30	0.13	225.8	7.3	-5.00	1.54
40/05_4	Sul_E	-4.44	0.16	195.9	6.8	-2.93	1.64
40/07_1	Sul_E	-4.50	0.13	903.9	27.9	-2.68	0.77
40/07_2	Sul_E	-4.45	0.16	937.9	29.0	-3.83	0.81
40/07_3	Sul_E	-3.50	0.12	2056.1	63.7	0.37	0.55
40/07_4	Sul_E	-4.11	0.14	755.9	24.7	-2.07	0.86
40/07_5	Sul_E	-4.29	0.13	1265.2	38.8	-4.25	0.71
40/08_1	Sul_E	-4.47	0.15	803.3	24.7	-2.09	0.84
40/08_2	Sul_E	-4.43	0.14	1049.4	33.3	-4.08	0.77
40/08_3	Sul_E	-3.60	0.14	750.1	23.1	-3.08	0.85
40/08_4	Sul_E	-3.35	0.13	2169.0	66.2	-1.30	0.52
40/15_1	Sul_E	-5.20	0.13	996.2	32.0	-7.85	0.83
40/15_2	Sul_E	-5.34	0.13	749.2	23.9	-8.64	0.86
40/15_3	Sul_E	-5.38	0.12	1138.2	34.7	-7.61	0.69
40/15_4	Sul_E	-5.55	0.13	1124.7	34.3	-7.82	0.69
40/15_5	Sul_E	-5.38	0.16	1066.4	32.6	-7.97	0.72
40/17_1	Sul_E	-3.32	0.13	765.4	23.8	-2.94	0.87
40/17_2	Sul_E	-3.43	0.14	729.4	22.6	-3.52	0.91
40/17_3	Sul_E	-3.49	0.12	799.2	25.4	-3.52	0.93
40/17_4	Sul_E	-3.20	0.12	749.7	23.1	-3.44	0.85
21/01_1	LM	-5.74	0.14	2.1	0.2	na	na
21/01_2	LM	-6.25	0.12	2.5	0.4	na	na
21/01_3	LM	-5.82	0.14	9.4	0.5	na	na
21/01_4	LM	-5.89	0.13	7.2	0.4	na	na
23/01_1	LM	-4.73	0.12	1.1	0.2	na	na
23/01_2	LM	-4.58	0.13	3.8	0.4	na	na
23/01_3	LM	-5.62	0.13	78.2	2.8	-14.09	2.71
23/01_4	LM	-5.86	0.15	1.2	0.1	na	na
25/01_1	LM	-4.59	0.14	6.8	0.5	na	na
25/01_2	LM	-3.40	0.13	127.0	4.5	-14.82	2.37
25/01_3	LM	-3.47	0.12	45.7	1.9	na	na
25/01_4	LM	-4.86	0.12	6.1	0.4	na	na

Figure A1: Cathodoluminescence images of Koffiefontein diamond fragments. Data for analytical pots (numbered on each fragment) are listed in Table A3. Red line indicates the outer edge of the diamond and dashed line is an inferred edge.

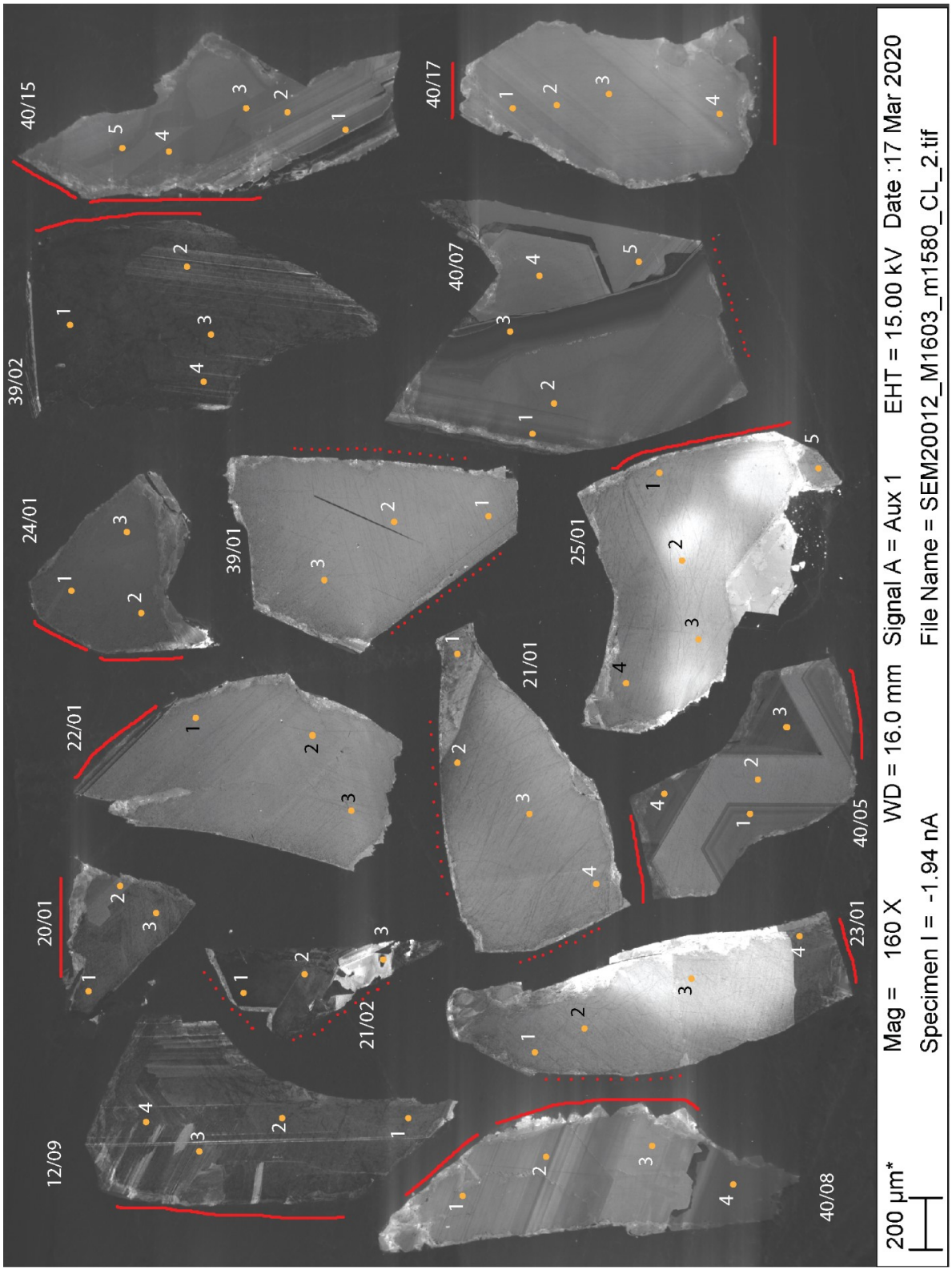

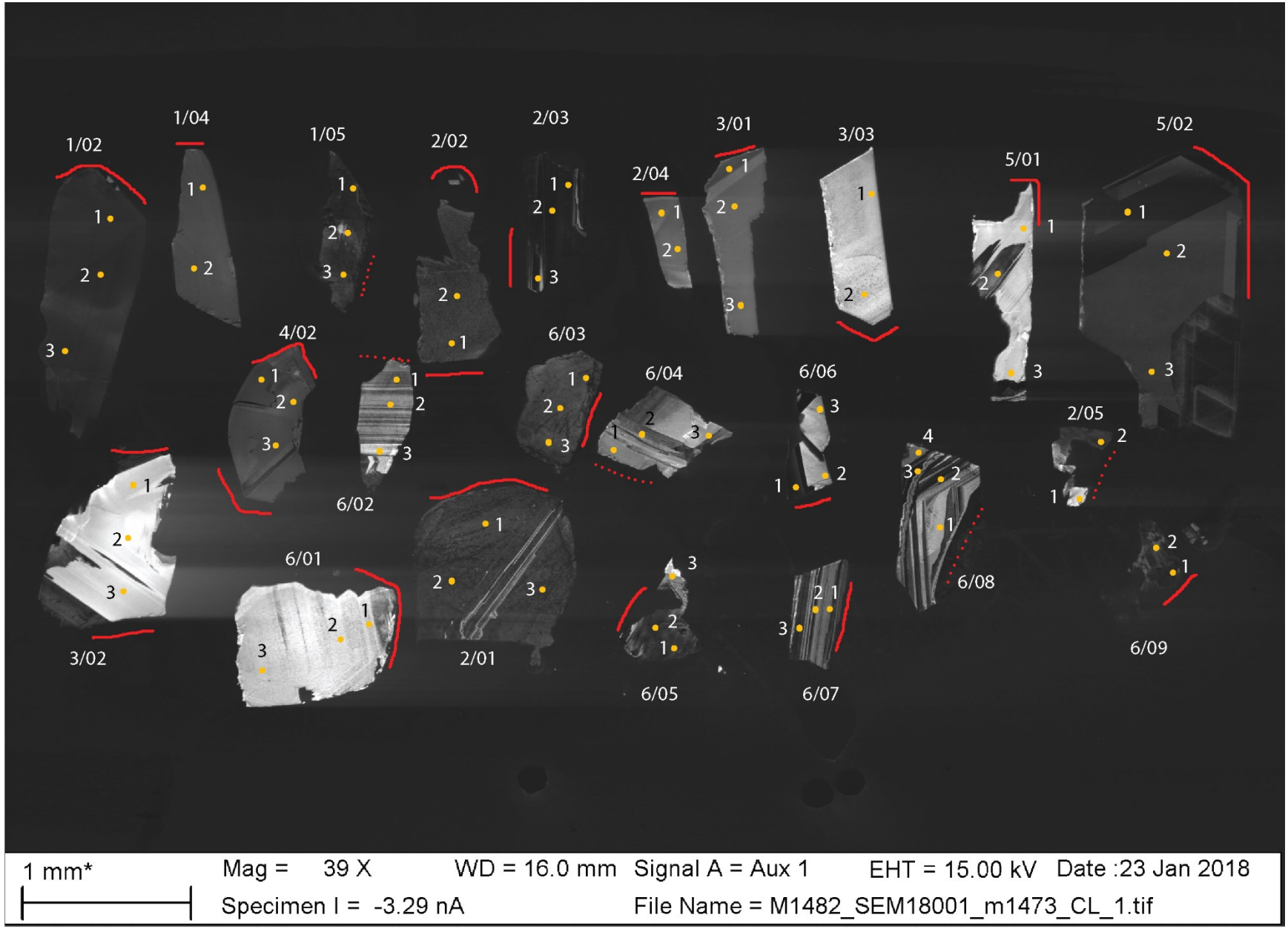
1/02
1/04
1/05
2/02
2/03
2/04
3/01
3/03
5/01
5/02
4/02
6/03
6/04
6/06
2/05
6/02
6/01
2/01
6/05
6/07
6/08
6/09
3/02
1 mm*
Mag = 39 X
WD = 16.0 mm
Signal A = Aux 1
EHT = 15.00 kV
Date :23 Jan 2018
Specimen I = -3.29 nA
File Name = M1482_SEM18001_m1473_CL_1.tif

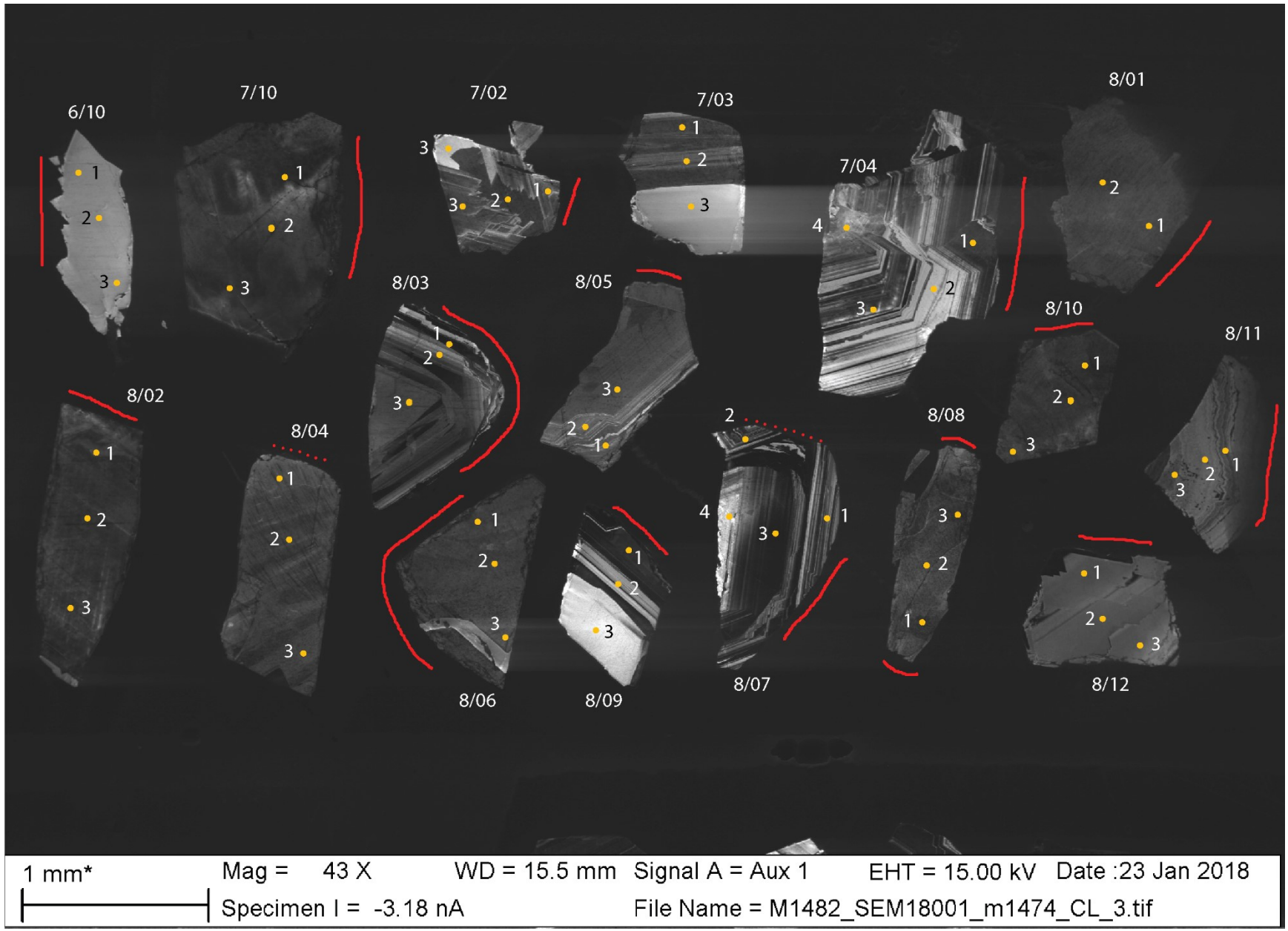
6/10
7/10
7/02
7/03
7/04
8/01
8/02
8/03
8/04
8/05
8/06
8/07
8/08
8/09
8/10
8/11
8/12
1 mm*
Mag = 43 X
WD = 15.5 mm
Signal A = Aux 1
EHT = 15.00 kV
Date :23 Jan 2018
Specimen I = -3.18 nA
File Name = M1482_SEM18001_m1474_CL_3.tif

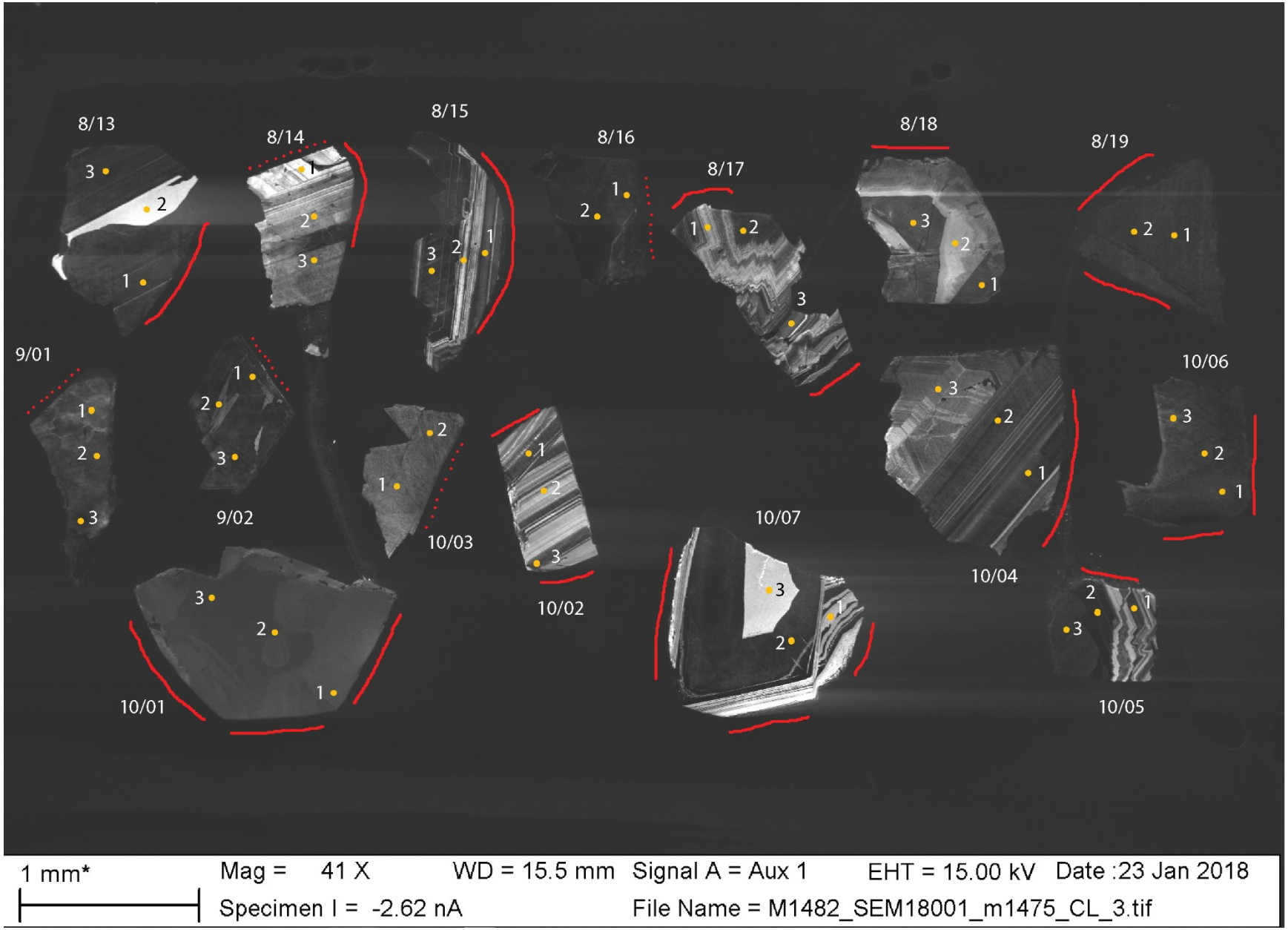
8/13
8/14
8/15
8/16
8/17
8/18
8/19
9/01
9/02
10/01
10/02
10/03
10/04
10/05
10/06
10/07
1 mm*
Mag = 41 X
WD = 15.5 mm
Signal A = Aux 1
EHT = 15.00 kV
Date :23 Jan 2018
Specimen I = -2.62 nA
File Name = M1482_SEM18001_m1475_CL_3.tif

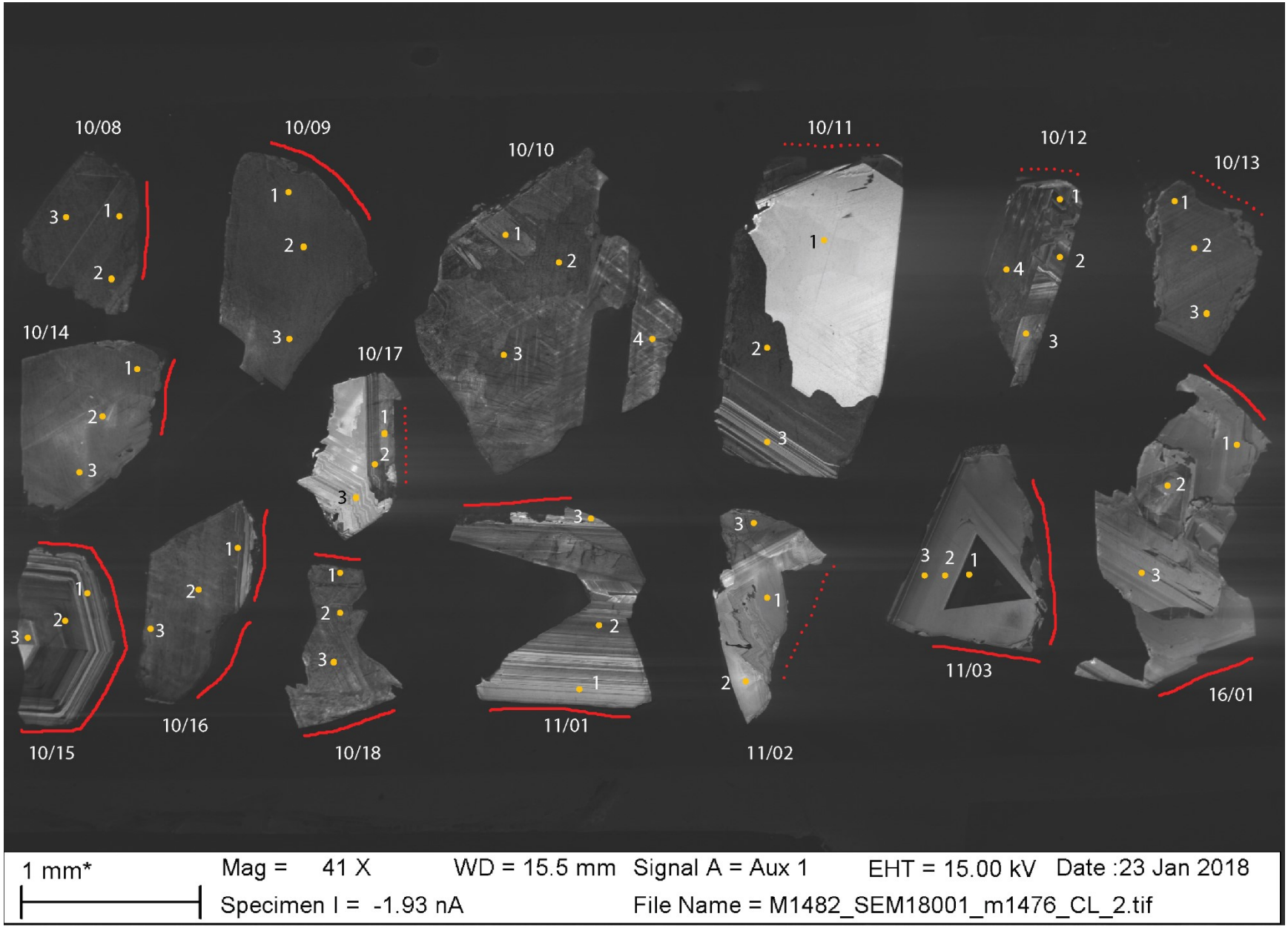
10/08
10/09
10/10
10/11
10/12
10/13
10/14
10/17
10/15
10/16
10/18
11/01
11/02
11/03
16/01
1 mm*
Mag = 41 X
WD = 15.5 mm
Signal A = Aux 1
EHT = 15.00 kV
Date :23 Jan 2018
Specimen I = -1.93 nA
File Name = M1482_SEM18001_m1476_CL_2.tif

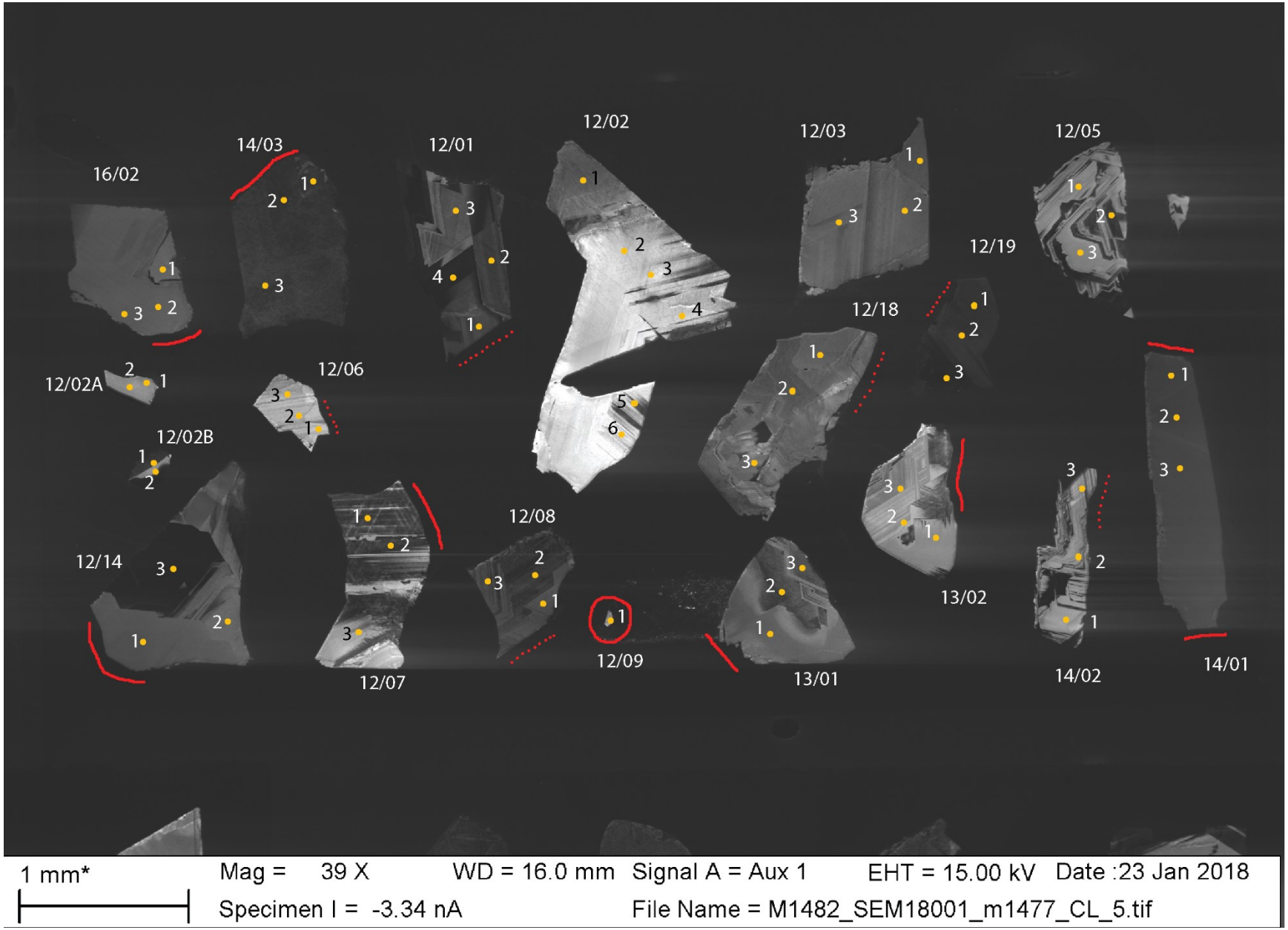
16/02
14/03
12/01
12/02
12/03
12/05
12/19
12/18
12/02A
12/06
12/02B
12/14
12/08
12/09
13/02
12/07
13/01
14/02
14/01
1 mm*
Mag = 39 X
WD = 16.0 mm
Signal A = Aux 1
EHT = 15.00 kV
Date :23 Jan 2018
Specimen I = -3.34 nA
File Name = M1482_SEM18001_m1477_CL_5.tif

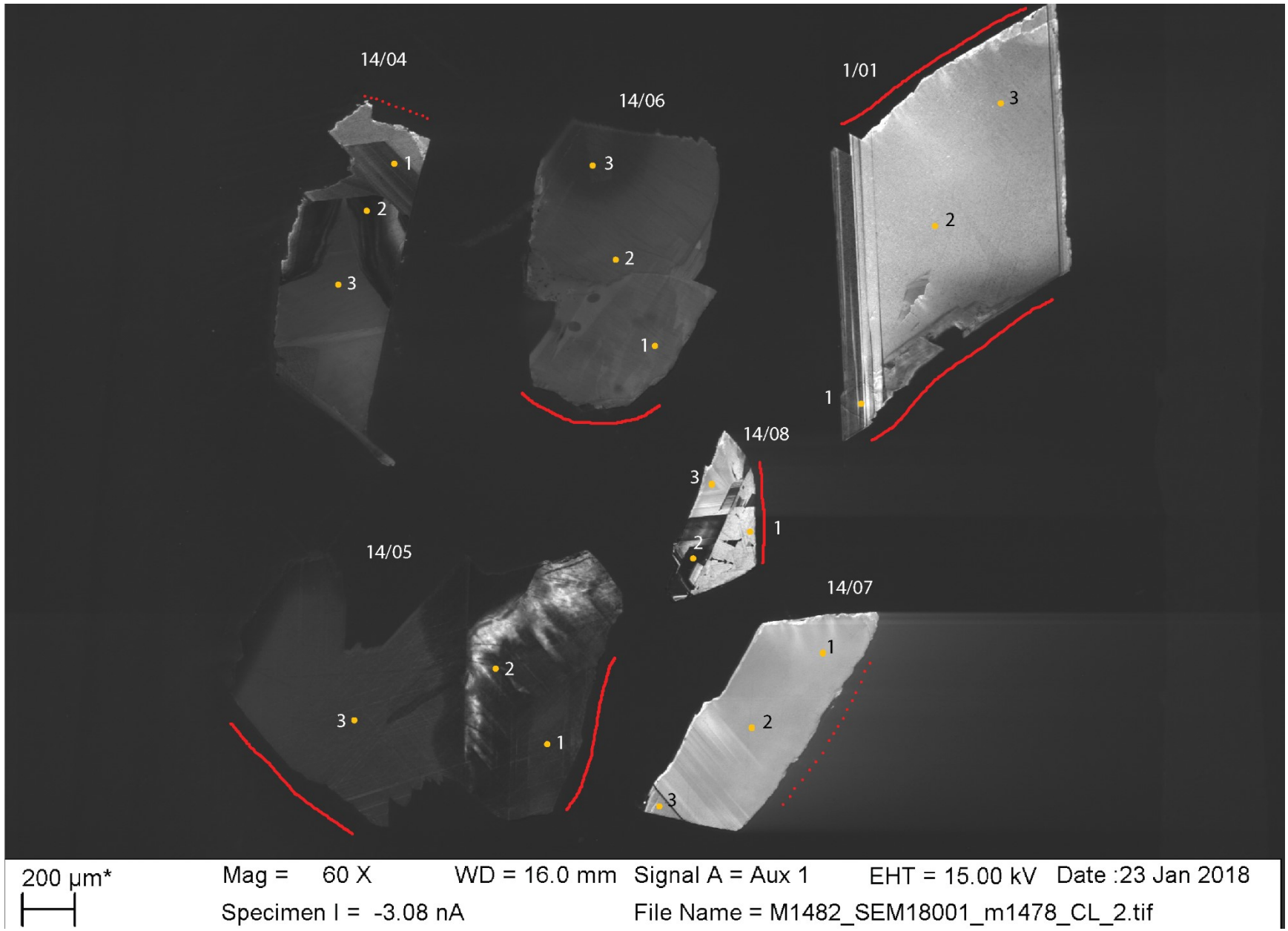
14/04
1
2
3
14/06
3
2
1
1/01
3
2
1
14/08
3
1
2
14/05
2
3
1
14/07
1
2
3
200 µm*
Mag = 60 X
WD = 16.0 mm
Signal A = Aux 1
EHT = 15.00 kV
Date :23 Jan 2018
Specimen I = -3.08 nA
File Name = M1482_SEM18001_m1478_CL_2.tif

Appendix B. Supplementary Data for Chapter 4

Table B1: Average major-element compositions of minerals from Koffiefontein diamonds, reported as oxide wt%
Table B2: Trace element concentration of olivine determined by electron probe microanalysis
Table B3: Laser ablation inductively coupled mass spectrometry
Table B4: Geothermobarometry of mineral inclusions in Koffiefontein diamonds.
Table B5: Temperature calculated for Ni in peridotitic garnet based on the geothermometer of Canil (1999).

Table B1: Average major-element compositions of minerals from Koffiefontein diamonds, reported as oxide wt%. Cations are calculated on the basis of oxygen, listed in table. All iron is reported as FeO. Highest detection limit (in wt%) recorded for each element based on all analyses is shown. Samples are grouped by suite as described in text: P – peridotitic, W – websteritic, and E – eclogitic. Abbreviations: en – enstatite, ol – olivine, grt – garnet, sic – moissanite, diop – diopside, chr – chromite, cc – calcite, omp – omphacite.

Sample #	**Detection**	**1/04A**	**1/05B**	**2/01B**	**2/01C**	**2/01E**	**2/02B**	**2/02C**
Suite	**Limit**	P	P	P	P	P	P	P
Mineral		EN	OL	OL	EN	EN	OL	OL
N		3	2	3	1	1	3	2
SiO_2	0.020	58.39	43.17	41.08	58.49	58.36	41.67	41.42
TiO_2	0.012	bdl	bdl	bdl	bdl	bdl	bdl	bdl
ZnO	0.024	na	na	na	na	na	na	na
Al_2O_3	0.023	0.43	0.00	0.02	0.63	0.67	0.02	0.01
V_2O_3	0.021	0.01	bdl	bdl	bdl	bdl	bdl	bdl
Cr_2O_3	0.016	0.21	0.03	0.03	0.24	0.24	0.03	0.02
FeO	0.016	4.48	6.53	6.39	3.77	3.78	6.01	5.89
NiO	0.017	0.12	0.39	0.39	0.12	0.12	0.37	0.38
MnO	0.015	0.10	0.09	0.08	0.08	0.10	0.08	0.07
MgO	0.015	35.85	50.35	51.04	36.31	36.20	51.12	51.72
CaO	0.013	0.57	0.04	0.04	0.55	0.54	0.03	0.03
Na_2O	0.037	0.06	0.01	0.00	0.02	0.02	0.00	bdl
K_2O	0.012	0.00	bdl	bdl	bdl	bdl	bdl	bdl
P_2O_5	0.012	0.01	0.03	0.01	bdl	bdl	0.00	bdl
Sum		100.24	100.67	99.09	100.22	100.02	99.35	99.55
# Ox		6	4	4	6	6	4	4
Si		1.992	1.032	1.001	1.989	1.989	1.010	1.002
Ti		-	-	-	-	-	-	-
Zn		-	-	-	-	-	-	-
Al		0.017	0.000	0.001	0.025	0.027	0.000	0.000
V		0.000	-	-	-	-	-	-
Cr		0.006	0.001	0.001	0.006	0.006	0.001	0.000
Fe		0.128	0.131	0.130	0.107	0.108	0.122	0.119
Ni		0.003	0.008	0.008	0.003	0.003	0.007	0.007
Mn		0.003	0.002	0.002	0.002	0.003	0.002	0.001
Mg		1.823	1.794	1.855	1.841	1.839	1.847	1.866
Ca		0.021	0.001	0.001	0.020	0.020	0.001	0.001
Na		0.004	0.000	0.000	0.001	0.001	0.000	-
K		0.000	-	-	-	-	-	-
P		0.000	0.000	0.000	-	-	0.000	0.000
Sum		3.998	2.968	2.998	3.995	3.995	2.990	2.997
Mg#		93.4	93.2	93.4	94.5	94.5	93.8	94.0

Table B1: Continued

Sample #	**2/02D**	**2/03A**	**2/03B**	**2/04A**	**2/04C**	**2/05B**	**2/05C**	**2/05E**
Suite	P	P	P	P	P	P	P	P
Mineral	OL	OL	OL	OL	OL	OL	EN	EN
N	3	3	1	2	1	2	4	3
SiO_2	41.98	41.39	43.03	41.22	41.07	41.14	59.56	58.27
TiO_2	bdl	bdl	bdl	bdl	bdl	bdl	bdl	bdl
ZnO	na	na	na	na	na	na	na	na
Al_2O_3	0.01	0.01	0.01	0.01	0.01	0.02	0.69	0.67
V_2O_3	bdl	bdl	bdl	bdl	bdl	bdl	0.01	bdl
Cr_2O_3	0.03	0.06	0.05	0.06	0.06	0.02	0.24	0.26
FeO	6.15	6.01	6.23	5.62	5.37	5.37	2.99	3.23
NiO	0.37	0.36	0.36	0.35	0.36	0.38	0.13	0.13
MnO	0.08	0.08	0.09	0.07	0.07	0.08	0.07	0.07
MgO	50.45	51.60	49.43	51.67	52.08	52.10	35.62	36.60
CaO	0.03	0.03	0.02	0.03	0.02	0.02	0.21	0.23
Na_2O	bdl	bdl	bdl	0.01	bdl	0.01	0.02	0.01
K_2O	0.00	0.00	bdl	bdl	bdl	0.00	0.00	bdl
P_2O_5	0.01	0.00	bdl	0.01	0.04	bdl	0.01	bdl
Sum	99.12	99.57	99.24	99.05	99.09	99.13	99.56	99.49
# Ox	4	4	4	4	4	4	6	6
Si	1.019	1.002	1.040	1.001	0.997	0.998	2.023	1.990
Ti	-	-	-	-	-	-	-	-
Zn	-	-	-	-	-	-	-	-
Al	0.000	0.000	0.000	0.000	0.000	0.000	0.028	0.027
V	-	-	-	-	-	-	0.000	-
Cr	0.001	0.001	0.001	0.001	0.001	0.000	0.006	0.007
Fe	0.125	0.122	0.126	0.114	0.109	0.109	0.085	0.092
Ni	0.007	0.007	0.007	0.007	0.007	0.007	0.004	0.004
Mn	0.002	0.002	0.002	0.002	0.002	0.002	0.002	0.002
Mg	1.826	1.862	1.782	1.871	1.885	1.884	1.804	1.863
Ca	0.001	0.001	0.001	0.001	0.000	0.000	0.008	0.008
Na	-	-	-	0.000	-	0.000	0.001	0.001
K	0.000	0.000	-	-	-	0.000	0.000	-
P	0.000	0.000	-	0.000	0.000	-	0.000	-
Sum	2.980	2.997	2.959	2.998	3.002	3.002	3.961	3.994
Mg#	93.6	93.9	93.4	94.3	94.5	94.5	95.5	95.3

Table B1: Continued

Sample #	**2/05F**	**3/01A**	**3/02A**	**3/02B**	**3/02D**	**3/02E**	**3/03A**	**5/01A**
Suite	P	P	P	P	P	P	P	P
Mineral	SiC	OL	OL	OL	OL	OL	OL	OL
N	1	3	1	2	1	3	2	1
SiO_2	69.10	41.90	40.66	40.94	42.73	41.05	42.48	42.57
TiO_2	bdl	bdl	bdl	bdl	bdl	bdl	0.01	bdl
ZnO	na	na	na	na	na	na	na	na
Al_2O_3	bdl	0.01	0.03	0.02	0.02	0.02	0.01	bdl
V_2O_3	bdl	bdl	bdl	bdl	bdl	0.01	bdl	bdl
Cr_2O_3	bdl	0.03	0.04	0.05	0.04	0.03	0.05	0.04
FeO	bdl	5.51	6.75	6.66	6.60	6.64	5.73	6.17
NiO	bdl	0.37	0.40	0.41	0.39	0.41	0.37	0.37
MnO	0.01	0.06	0.08	0.08	0.07	0.09	0.07	0.08
MgO	bdl	50.90	50.54	51.19	50.61	50.82	50.87	51.66
CaO	bdl	0.00	0.04	0.03	0.04	0.04	0.02	0.01
Na_2O	bdl	0.00	0.01	bdl	bdl	bdl	0.01	bdl
K_2O	bdl	bdl	bdl	bdl	bdl	bdl	bdl	bdl
P_2O_5	bdl	0.01	bdl	0.01	0.04	0.02	0.03	bdl
Sum	69.13	98.83	98.57	99.38	100.54	99.14	99.64	100.93
# Ox		4	4	4	4	4	4	4
Si	-	1.017	0.999	0.997	1.024	1.002	1.023	1.015
Ti	-	-	-	-	-	-	0.000	-
Zn	-	-	-	-	-	-	-	-
Al	-	0.000	0.001	0.001	0.001	0.001	0.000	-
V	-	-	-	-	-	0.000	0.000	-
Cr	-	0.001	0.001	0.001	0.001	0.001	0.001	0.001
Fe	-	0.112	0.139	0.136	0.132	0.135	0.115	0.123
Ni	-	0.007	0.008	0.008	0.007	0.008	0.007	0.007
Mn	-	0.001	0.002	0.002	0.001	0.002	0.001	0.002
Mg	-	1.842	1.851	1.858	1.807	1.848	1.826	1.836
Ca	-	0.000	0.001	0.001	0.001	0.001	0.000	0.000
Na	-	0.000	0.001	-	-	-	0.000	-
K	-	-	-	-	-	-	-	-
P	-	0.000	-	0.000	0.000	0.000	0.000	-
Sum	-	2.982	3.001	3.002	2.975	2.998	2.976	2.984
Mg#	-	94.3	93.0	93.2	93.2	93.2	94.1	93.7

Table B1: Continued

Sample #	**5/02A**	**6/01A**	**6/01C**	**6/02A**	**6/02B**	**6/02C**	**6/03A**	**6/03B**
Suite	P	P	P	P	P	P	P	P
Mineral	OL	OL	OL	OL	OL	OL	OL	OL
N	3	4	4	3	2	1	2	2
SiO_2	41.57	40.34	41.42	41.62	41.25	40.95	40.88	41.57
TiO_2	0.00	0.00	0.00	bdl	bdl	bdl	bdl	0.01
ZnO	na	na	na	na	na	na	na	na
Al_2O_3	0.01	0.02	0.01	0.00	0.01	bdl	0.01	0.01
V_2O_3	bdl	0.00	bdl	0.01	bdl	bdl	bdl	bdl
Cr_2O_3	0.02	0.08	0.08	0.08	0.09	0.06	0.05	0.05
FeO	5.06	7.74	7.77	4.98	4.98	4.95	6.90	6.76
NiO	0.42	0.37	0.37	0.37	0.38	0.36	0.34	0.33
MnO	0.06	0.10	0.11	0.07	0.07	0.07	0.09	0.08
MgO	52.35	50.84	49.18	52.71	52.06	52.27	50.45	50.51
CaO	0.02	0.04	0.04	0.00	0.01	bdl	0.04	0.03
Na_2O	0.00	0.01	0.02	0.00	bdl	bdl	0.02	0.02
K_2O	0.00	bdl	0.00	bdl	bdl	bdl	bdl	bdl
P_2O_5	0.00	0.01	0.02	0.01	0.01	0.02	0.01	bdl
Sum	99.52	99.57	99.03	99.88	98.86	98.70	98.80	99.37
# Ox	4	4	4	4	4	4	4	4
Si	1.002	0.987	1.015	1.000	1.001	0.996	1.002	1.010
Ti	0.000	0.000	0.000	-	-	-	-	0.000
Zn	-	-	-	-	-	-	-	-
Al	0.000	0.000	0.000	0.000	0.000	0.000	0.000	0.000
V	-	0.000	-	0.000	-	-	-	-
Cr	0.000	0.002	0.002	0.001	0.002	0.001	0.001	0.001
Fe	0.102	0.158	0.159	0.100	0.101	0.101	0.141	0.137
Ni	0.008	0.007	0.007	0.007	0.007	0.007	0.007	0.006
Mn	0.001	0.002	0.002	0.001	0.001	0.001	0.002	0.002
Mg	1.882	1.854	1.796	1.888	1.884	1.896	1.843	1.830
Ca	0.000	0.001	0.001	0.000	0.000	-	0.001	0.001
Na	0.000	0.001	0.001	0.000	-	-	0.001	0.001
K	0.000	-	0.000	-	-	-	-	-
P	0.000	0.000	0.000	0.000	0.000	0.000	0.000	-
Sum	2.997	3.012	2.984	2.999	2.998	3.003	2.998	2.989
Mg#	94.9	92.1	91.9	95.0	94.9	95.0	92.9	93.0

Table B1: Continued

Sample #	**6/04A**	**6/05A**	**6/05B**	**6/05C**	**6/05D**	**6/07A**	**6/08A**	**6/08B**
Suite	P	P	P	P	P	P	P	P
Mineral	OL	OL	OL	EN	OL	DIOP	EN	EN
N	3	3	4	1	4	4	2	5
SiO_2	41.22	41.90	41.05	58.84	42.04	55.48	59.65	59.55
TiO_2	bdl	bdl	0.00	bdl	0.00	0.28	bdl	0.00
ZnO	na	na	na	na	na	na	na	na
Al_2O_3	0.01	0.02	bdl	0.28	0.01	2.72	0.48	0.46
V_2O_3	bdl	bdl	bdl	bdl	bdl	0.04	bdl	bdl
Cr_2O_3	0.04	0.04	0.05	0.18	0.05	0.67	0.28	0.28
FeO	6.45	5.88	5.86	3.43	5.64	1.57	2.95	3.07
NiO	0.40	0.36	0.36	0.12	0.35	0.04	0.14	0.15
MnO	0.07	0.07	0.08	0.07	0.07	0.07	0.07	0.07
MgO	51.22	51.54	51.74	37.43	50.27	15.70	36.26	36.56
CaO	0.05	0.01	0.01	0.12	0.00	22.05	0.12	0.11
Na_2O	bdl	0.00	bdl	0.01	bdl	1.39	0.02	0.00
K_2O	bdl	bdl	bdl	bdl	bdl	0.01	0.00	0.00
P_2O_5	0.01	0.00	0.01	bdl	bdl	0.02	bdl	0.01
Sum	99.46	99.85	99.15	100.48	99.77	100.04	99.97	100.27
# Ox	4	4	4	6	4	6	6	6
Si	1.001	1.010	0.998	1.991	1.024	1.995	2.018	2.011
Ti	-	-	0.000	-	0.000	0.008	-	0.000
Zn	-	-	-	-	-	-	-	-
Al	0.000	0.000	-	0.011	0.000	0.115	0.019	0.018
V	-	-	-	-	-	0.001	-	-
Cr	0.001	0.001	0.001	0.005	0.001	0.019	0.008	0.007
Fe	0.131	0.119	0.119	0.097	0.115	0.047	0.084	0.087
Ni	0.008	0.007	0.007	0.003	0.007	0.001	0.004	0.004
Mn	0.002	0.002	0.002	0.002	0.002	0.002	0.002	0.002
Mg	1.855	1.851	1.875	1.888	1.826	0.842	1.829	1.841
Ca	0.001	0.000	0.000	0.004	0.000	0.850	0.004	0.004
Na	-	0.000	-	0.001	-	0.097	0.001	0.000
K	-	-	-	-	-	0.000	0.000	0.000
P	0.000	0.000	0.000	-	-	0.000	-	0.000
Sum	2.998	2.990	3.002	4.002	2.975	3.978	3.969	3.976
Mg#	93.4	94.0	94.0	95.1	94.1	94.7	95.6	95.5

Table B1: Continued

Sample #	**6/08C**	**6/08D**	**6/09A**	**6/09C**	**6/09D**	**6/10A**	**6/10B**	**7/01A**
Suite	P	P	P	P	P	P	P	P
Mineral	EN	EN	OL	OL	OL	OL	OL	GRT
N	3	4	3	3	2	3	3	1
SiO_2	59.44	59.34	41.44	41.65	41.22	41.36	40.90	41.77
TiO_2	bdl	bdl	bdl	bdl	0.01	bdl	bdl	0.02
ZnO	na	na	na	na	na	na	na	na
Al_2O_3	0.46	0.46	bdl	bdl	0.02	bdl	0.01	20.92
V_2O_3	bdl	bdl	bdl	0.01	bdl	0.01	bdl	0.07
Cr_2O_3	0.28	0.28	0.05	0.06	0.04	0.08	0.08	4.15
FeO	3.07	2.96	6.43	6.30	6.27	7.21	7.20	5.29
NiO	0.15	0.15	0.36	0.37	0.35	0.39	0.39	0.01
MnO	0.07	0.07	0.08	0.08	0.08	0.10	0.10	0.22
MgO	36.73	35.79	51.81	52.19	51.52	51.20	50.49	23.63
CaO	0.11	0.11	0.01	0.01	0.01	0.05	0.05	2.78
Na_2O	0.00	0.01	bdl	bdl	bdl	bdl	bdl	bdl
K_2O	0.00	0.00	0.00	bdl	bdl	bdl	bdl	bdl
P_2O_5	0.01	0.00	bdl	bdl	bdl	bdl	0.01	bdl
Sum	100.34	99.53	100.19	100.68	99.52	100.39	99.22	98.84
# Ox	6	6	4	4	4	4	4	12
Si	2.007	2.023	0.999	0.999	1.000	0.999	1.000	2.977
Ti	-	-	-	-	0.000	-	-	0.001
Zn	-	-	-	-	-	-	-	-
Al	0.018	0.019	-	-	0.001	0.000	0.000	1.757
V	-	-	-	0.000	-	0.000	-	0.004
Cr	0.008	0.008	0.001	0.001	0.001	0.001	0.001	0.234
Fe	0.087	0.084	0.130	0.126	0.127	0.146	0.147	0.315
Ni	0.004	0.004	0.007	0.007	0.007	0.008	0.008	0.001
Mn	0.002	0.002	0.002	0.002	0.002	0.002	0.002	0.013
Mg	1.849	1.819	1.862	1.865	1.863	1.843	1.840	2.511
Ca	0.004	0.004	0.000	0.000	0.000	0.001	0.001	0.212
Na	0.000	0.001	-	-	-	-	-	-
K	0.000	0.000	0.000	-	-	-	-	-
P	0.000	0.000	-	-	-	-	0.000	0.000
Sum	3.980	3.964	3.000	3.001	3.000	3.000	2.999	8.025
Mg#	95.5	95.6	93.5	93.7	93.6	92.7	92.6	88.8

Table B1: Continued

Sample #	**7/01B**	**7/01C**	**7/01D**	**7/01E**	**7/01F**	**7/02A**	**7/02B**	**7/02C**
Suite	P	P	P	P	P	P	P	P
Mineral	GRT	GRT	EN	GRT	EN	GRT	GRT	GRT
N	2	2	3	3	3	2	2	3
SiO_2	42.16	42.40	58.43	42.54	58.46	42.22	42.24	42.00
TiO_2	bdl	0.02	0.01	0.02	bdl	0.02	0.02	0.02
ZnO	na	na	na	na	na	na	na	na
Al_2O_3	21.06	21.22	0.53	21.26	0.52	21.28	21.34	21.29
V_2O_3	0.05	0.05	bdl	0.05	bdl	0.04	0.04	0.04
Cr_2O_3	4.13	4.07	0.18	4.12	0.18	3.11	3.16	3.12
FeO	5.31	5.27	3.81	5.29	3.82	5.52	5.53	5.59
NiO	0.02	0.02	0.12	0.01	0.13	0.02	bdl	0.01
MnO	0.21	0.21	0.08	0.21	0.09	0.20	0.22	0.21
MgO	23.80	23.91	36.80	24.05	36.60	22.70	22.64	22.70
CaO	2.74	2.72	0.53	2.77	0.52	4.19	4.17	4.17
Na_2O	bdl	bdl	bdl	bdl	0.00	bdl	bdl	0.01
K_2O	bdl	bdl	bdl	bdl	0.00	bdl	bdl	bdl
P_2O_5	0.01	bdl	bdl	0.01	0.01	0.02	0.01	0.02
Sum	99.49	99.88	100.49	100.33	100.33	99.33	99.37	99.17
# Ox	12	12	6	12	6	12	12	12
Si	2.984	2.986	1.983	2.984	1.987	2.998	2.998	2.989
Ti	0.000	0.001	0.000	0.001	-	0.001	0.001	0.001
Zn	-	-	-	-	-	-	-	-
Al	1.757	1.761	0.021	1.757	0.021	1.781	1.785	1.786
V	0.003	0.003	0.000	0.003	-	0.002	0.002	0.002
Cr	0.231	0.227	0.005	0.228	0.005	0.175	0.177	0.176
Fe	0.314	0.311	0.108	0.310	0.108	0.328	0.328	0.333
Ni	0.001	0.001	0.003	0.000	0.004	0.001	-	0.000
Mn	0.013	0.013	0.002	0.013	0.003	0.012	0.013	0.013
Mg	2.511	2.510	1.862	2.515	1.854	2.403	2.396	2.408
Ca	0.208	0.205	0.019	0.209	0.019	0.319	0.317	0.318
Na	-	-	-	-	0.000	-	-	0.001
K	-	-	-	-	0.000	-	-	-
P	0.000	-	-	0.000	0.000	0.000	0.000	0.000
Sum	8.021	8.018	4.004	8.021	4.000	8.021	8.018	8.027
Mg#	88.9	89.0	94.5	89.0	94.5	88.0	88.0	87.9

Table B1: Continued

Sample #	**7/02D**	**7/03A**	**7/04A**	**7/04B**	**8/01A**	**8/01B**	**8/02A**	**8/02B**
Suite	P	P	P	P	P	P	P	P
Mineral	GRT	GRT	GRT	EN	EN	GRT	GRT	GRT
N	2	7	3	3	3	4	2	3
SiO_2	41.99	42.31	41.95	58.50	58.22	42.22	42.10	41.99
TiO_2	0.03	0.01	bdl	bdl	bdl	0.02	0.01	bdl
ZnO	na	na	na	na	na	na	na	na
Al_2O_3	21.18	19.29	18.26	0.55	0.56	20.72	19.17	19.84
V_2O_3	0.04	0.03	0.04	0.01	bdl	0.03	0.04	0.05
Cr_2O_3	3.13	6.87	7.37	0.31	0.21	4.34	5.70	5.71
FeO	5.50	5.34	5.42	3.76	3.60	4.77	5.32	5.10
NiO	bdl	0.01	0.01	0.16	0.12	0.01	0.02	0.01
MnO	0.21	0.27	0.23	0.08	0.09	0.21	0.23	0.22
MgO	22.57	25.02	24.07	36.82	36.13	24.72	23.58	23.58
CaO	4.19	0.91	2.04	0.31	0.39	2.01	2.73	2.58
Na_2O	0.01	bdl	bdl	bdl	0.03	0.05	0.01	0.00
K_2O	bdl	bdl	bdl	0.00	bdl	0.01	bdl	0.00
P_2O_5	0.01	0.02	0.02	0.01	bdl	0.04	bdl	bdl
Sum	98.86	100.07	99.43	100.52	99.34	99.14	98.90	99.10
# Ox	12	12	12	6	6	12	12	12
Si	2.996	2.988	3.000	1.984	1.994	2.988	3.014	2.995
Ti	0.001	0.000	-	-	-	0.001	0.001	-
Zn	-	-	-	-	-	-	-	-
Al	1.781	1.606	1.539	0.022	0.023	1.728	1.617	1.668
V	0.002	0.002	0.002	0.000	0.000	0.002	0.002	0.003
Cr	0.176	0.384	0.417	0.008	0.006	0.243	0.322	0.322
Fe	0.328	0.315	0.324	0.107	0.103	0.282	0.318	0.304
Ni	-	0.000	0.001	0.004	0.003	0.001	0.001	0.001
Mn	0.013	0.016	0.014	0.002	0.003	0.012	0.014	0.013
Mg	2.401	2.634	2.566	1.861	1.845	2.608	2.516	2.506
Ca	0.321	0.069	0.156	0.011	0.014	0.153	0.210	0.197
Na	0.002	-	-	-	0.002	0.006	0.001	0.001
K	-	-	-	0.000	-	0.001	-	0.000
P	0.000	0.001	0.001	0.000	-	0.001	-	-
Sum	8.023	8.015	8.020	4.001	3.992	8.026	8.015	8.010
Mg#	88.0	89.3	88.8	94.6	94.7	90.2	88.8	89.2

Table B1: Continued

Sample #	**8/02C**	**8/02D**	**8/03A**	**8/03B**	**8/03C**	**8/03D**	**8/03E**	**8/04B**
Suite	P	P	P	P	P	P	P	P
Mineral	OL	OL	GRT	EN	GRT	OL	SiO_2	OL
N	2	3	1	1	2	1	4	2
SiO_2	40.85	41.57	42.38	57.54	42.04	41.04	99.76	41.23
TiO_2	bdl	bdl	0.23	0.08	0.23	bdl	bdl	bdl
ZnO	na	na	na	na	na	na	na	na
Al_2O_3	0.01	0.02	19.44	0.56	19.10	0.05	bdl	0.01
V_2O_3	bdl	bdl	0.08	bdl	0.08	bdl	bdl	bdl
Cr_2O_3	0.06	0.07	5.82	0.34	5.81	0.09	bdl	0.02
FeO	6.46	6.81	5.73	3.74	5.72	5.80	bdl	7.06
NiO	0.40	0.39	bdl	0.10	0.02	0.33	bdl	0.38
MnO	0.08	0.10	0.24	0.08	0.25	0.08	0.00	0.09
MgO	50.59	50.54	24.68	36.15	24.43	51.49	0.01	49.89
CaO	0.03	0.03	1.14	0.12	1.14	0.01	0.01	0.04
Na_2O	bdl	0.00	bdl	0.03	bdl	bdl	bdl	0.01
K_2O	bdl	0.00	bdl	bdl	0.00	bdl	bdl	0.00
P_2O_5	0.02	0.01	0.02	bdl	0.02	0.01	bdl	bdl
Sum	98.53	99.55	99.77	98.73	98.84	98.89	99.80	98.73
# Ox	4	4	12	6	12	4		4
Si	1.002	1.009	3.000	1.985	3.006	1.000	-	1.011
Ti	-	-	0.012	0.002	0.012	-	-	-
Zn	-	-	-	-	-	-	-	-
Al	0.000	0.000	1.622	0.023	1.609	0.001	-	0.000
V	-	-	0.004	-	0.004	-	-	-
Cr	0.001	0.001	0.326	0.009	0.329	0.002	-	0.000
Fe	0.133	0.138	0.339	0.108	0.342	0.118	-	0.145
Ni	0.008	0.008	-	0.003	0.001	0.007	-	0.007
Mn	0.002	0.002	0.015	0.002	0.015	0.002	-	0.002
Mg	1.850	1.829	2.605	1.860	2.603	1.870	-	1.823
Ca	0.001	0.001	0.086	0.004	0.088	0.000	-	0.001
Na	-	0.000	-	0.002	-	-	-	0.000
K	-	0.000	-	-	0.000	-	-	0.000
P	0.000	0.000	0.001	-	0.001	0.000	-	-
Sum	2.997	2.990	8.010	3.998	8.010	2.999	-	2.989
Mg#	93.3	93.0	88.5	94.5	88.4	94.1	-	92.6

Table B1: Continued

Sample #	**8/06A**	**8/06B**	**8/06D**	**8/07A**	**8/07B**	**8/07C**	**8/07D**	**8/07E**
Suite	P	P	P	P	P	P	P	P
Mineral	EN	EN	OL	GRT	GRT	OL	OL	OL
N	3	2	4	3	2	2	1	3
SiO_2	58.32	58.28	41.99	42.07	42.19	41.26	41.32	41.47
TiO_2	bdl	bdl	0.00	0.01	0.01	bdl	bdl	bdl
ZnO	na	na	na	na	na	na	na	na
Al_2O_3	0.44	0.42	0.00	18.69	19.05	bdl	0.02	0.01
V_2O_3	bdl	bdl	bdl	0.03	0.03	bdl	bdl	bdl
Cr_2O_3	0.12	0.13	0.02	7.04	7.16	0.06	0.06	0.04
FeO	3.45	3.45	6.10	5.31	5.06	5.59	5.77	6.25
NiO	0.13	0.12	0.39	bdl	bdl	0.34	0.37	0.32
MnO	0.08	0.09	0.07	0.25	0.23	0.08	0.09	0.08
MgO	36.40	35.74	51.38	24.92	25.31	51.52	51.09	51.93
CaO	0.44	0.44	0.02	0.74	0.67	0.01	0.01	0.01
Na_2O	0.02	0.01	0.01	bdl	bdl	bdl	bdl	bdl
K_2O	bdl	bdl	bdl	0.01	bdl	bdl	bdl	0.00
P_2O_5	0.00	0.02	0.01	0.01	0.04	0.02	bdl	0.00
Sum	99.41	98.71	100.01	99.10	99.76	98.90	98.76	100.12
# Ox	6	6	4	12	12	4	4	4
Si	1.995	2.006	1.011	3.002	2.986	1.003	1.007	0.999
Ti	-	-	0.000	0.000	0.001	-	-	-
Zn	-	-	-	-	-	-	-	-
Al	0.018	0.017	0.000	1.571	1.590	-	0.001	0.000
V	-	-	-	0.002	0.002	-	-	-
Cr	0.003	0.004	0.000	0.397	0.401	0.001	0.001	0.001
Fe	0.099	0.099	0.123	0.317	0.300	0.114	0.118	0.126
Ni	0.004	0.003	0.008	-	-	0.007	0.007	0.006
Mn	0.002	0.003	0.001	0.015	0.014	0.002	0.002	0.002
Mg	1.857	1.834	1.844	2.650	2.670	1.868	1.856	1.865
Ca	0.016	0.016	0.001	0.056	0.051	0.000	0.000	0.000
Na	0.001	0.000	0.000	-	-	-	-	-
K	-	-	-	0.000	-	-	-	0.000
P	0.000	0.000	0.000	0.000	0.001	0.000	-	0.000
Sum	3.995	3.983	2.989	8.012	8.015	2.996	2.992	3.000
Mg#	95.0	94.9	93.8	89.3	89.9	94.3	94.0	93.7

Table B1: Continued

Sample #	**8/08A**	**8/08B**	**8/08C**	**8/08E**	**8/08F**	**8/08H**	**8/08I**	**8/09A**
Suite	P	P	P	P	P	P	P	P
Mineral	OL	OL	OL	GRT	GRT	GRT	GRT	GRT
N	3	4	1	3	1	1	1	3
SiO_2	40.99	41.72	40.73	41.05	41.32	41.36	41.62	41.60
TiO_2	bdl	bdl	bdl	0.11	0.14	0.12	0.01	bdl
ZnO	na	na	na	na	na	na	na	na
Al_2O_3	0.01	0.01	0.01	16.35	16.38	17.34	18.39	18.50
V_2O_3	bdl	bdl	bdl	0.04	0.05	0.04	0.06	0.08
Cr_2O_3	0.06	0.04	0.04	8.56	8.69	8.41	6.90	6.83
FeO	6.54	6.76	6.51	5.73	5.77	5.47	6.12	6.26
NiO	0.33	0.32	0.33	0.00	0.01	0.02	bdl	bdl
MnO	0.09	0.09	0.08	0.27	0.29	0.26	0.31	0.31
MgO	50.78	51.17	50.71	21.49	21.78	21.90	23.31	23.41
CaO	0.03	0.03	0.03	4.32	4.33	4.04	2.01	2.01
Na_2O	0.01	0.01	0.12	0.03	0.03	0.02	bdl	bdl
K_2O	bdl	bdl	bdl	bdl	bdl	bdl	bdl	bdl
P_2O_5	0.01	0.00	bdl	0.02	0.01	bdl	0.06	0.07
Sum	98.86	100.16	98.58	97.98	98.79	98.99	98.80	99.07
# Ox	4	4	4	12	12	12	12	12
Si	1.002	1.006	0.999	3.020	3.016	3.001	3.002	2.994
Ti	-	-	-	0.006	0.008	0.006	0.001	-
Zn	-	-	-	-	-	-	-	-
Al	0.000	0.000	0.000	1.418	1.409	1.483	1.564	1.569
V	-	-	-	0.002	0.003	0.002	0.004	0.004
Cr	0.001	0.001	0.001	0.498	0.502	0.482	0.393	0.389
Fe	0.134	0.136	0.134	0.353	0.352	0.332	0.369	0.377
Ni	0.007	0.006	0.006	0.000	0.001	0.001	-	-
Mn	0.002	0.002	0.002	0.017	0.018	0.016	0.019	0.019
Mg	1.851	1.840	1.855	2.357	2.371	2.369	2.506	2.512
Ca	0.001	0.001	0.001	0.340	0.339	0.314	0.155	0.155
Na	0.001	0.000	0.006	0.004	0.004	0.003	-	-
K	-	-	-	-	-	-	-	-
P	0.000	0.000	-	0.000	0.000	-	0.002	0.002
Sum	2.997	2.993	3.003	8.016	8.021	8.010	8.014	8.021
Mg#	93.3	93.1	93.3	87.0	87.1	87.7	87.2	87.0

Table B1: Continued

Sample #	**8/09C**	**8/09D**	**8/09F**	**8/09G**	**8/09I**	**8/10B**	**8/10C**	**8/10D**
Suite	P	P	P	P	P	P	P	P
Mineral	GRT	OL	OL	GRT	GRT	EN	GRT	GRT
N	3	3	1	1	3	2	2	1
SiO_2	41.70	40.93	40.63	41.74	41.65	57.84	41.92	41.84
TiO_2	0.00	bdl	bdl	bdl	0.02	bdl	bdl	bdl
ZnO	na	na	na	na	na	na	na	na
Al_2O_3	18.91	0.01	bdl	18.24	18.41	0.69	20.99	20.03
V_2O_3	0.09	bdl	bdl	0.07	0.06	bdl	0.04	0.02
Cr_2O_3	6.76	0.01	0.03	6.84	6.88	0.25	4.41	4.49
FeO	5.92	6.19	6.06	6.22	6.19	4.09	5.25	5.28
NiO	bdl	0.40	0.39	0.02	0.01	0.12	bdl	bdl
MnO	0.30	0.08	0.08	0.30	0.31	0.11	0.23	0.22
MgO	23.45	51.31	51.37	23.09	23.43	35.53	22.37	21.96
CaO	1.91	0.01	0.01	2.00	1.99	0.62	4.54	4.74
Na_2O	bdl	bdl	bdl	bdl	bdl	0.05	0.02	0.01
K_2O	bdl	bdl	bdl	bdl	bdl	0.01	bdl	bdl
P_2O_5	0.07	0.01	bdl	0.07	0.06	bdl	0.01	0.02
Sum	99.11	98.97	98.60	98.60	99.04	99.32	99.80	98.63
# Ox	12	4	4	12	12	6	12	12
Si	2.992	0.998	0.995	3.016	2.998	1.989	2.975	3.008
Ti	0.000	-	-	-	0.001	-	-	-
Zn	-	-	-	-	-	-	-	-
Al	1.599	0.000	-	1.554	1.562	0.028	1.756	1.698
V	0.005	-	-	0.004	0.003	0.000	0.002	0.001
Cr	0.383	0.000	0.001	0.391	0.392	0.007	0.248	0.255
Fe	0.355	0.126	0.124	0.376	0.373	0.118	0.312	0.317
Ni	-	0.008	0.008	0.001	0.001	0.003	-	-
Mn	0.018	0.002	0.002	0.018	0.019	0.003	0.014	0.013
Mg	2.509	1.866	1.875	2.487	2.514	1.821	2.368	2.354
Ca	0.147	0.000	0.000	0.155	0.154	0.023	0.345	0.365
Na	-	-	-	-	-	0.003	0.003	0.001
K	-	-	-	-	-	0.000	-	-
P	0.002	0.000	-	0.002	0.002	-	0.000	0.001
Sum	8.011	3.001	3.005	8.006	8.019	3.995	8.023	8.014
Mg#	87.6	93.7	93.8	86.9	87.1	93.9	88.4	88.1

Table B1: Continued

Sample #	**8/10E**	**8/11B***	**8/11B***	**8/12A**	**8/12B**	**8/12C**	**8/12D**	**8/12E**
Suite	P	P	P	P	P	P	P	P
Mineral	GRT	EN	GRT	GRT	GRT	EN	EN	EN
N	3	1	2	3	2	6	3	4
SiO_2	41.73	58.70	42.60	41.74	41.38	59.30	59.23	59.39
TiO_2	bdl	bdl	0.01	0.01	0.01	bdl	bdl	0.00
ZnO	na	na	na	na	na	na	na	na
Al_2O_3	20.76	0.55	21.75	16.73	17.04	0.45	0.47	0.46
V_2O_3	0.03	bdl	0.03	0.03	0.03	0.00	bdl	bdl
Cr_2O_3	4.43	0.19	3.16	9.95	9.99	0.31	0.30	0.31
FeO	5.29	1.87	3.06	4.47	4.29	2.81	2.85	2.82
NiO	0.00	0.16	0.01	bdl	0.02	0.11	0.13	0.12
MnO	0.23	0.04	0.13	0.22	0.20	0.07	0.07	0.06
MgO	22.34	37.90	27.00	25.48	25.43	36.41	36.87	36.92
CaO	4.54	0.05	0.47	0.44	0.40	0.05	0.06	0.06
Na_2O	0.03	0.03	bdl	bdl	bdl	bdl	bdl	0.08
K_2O	bdl	bdl	bdl	bdl	bdl	0.00	bdl	0.00
P_2O_5	0.01	bdl	0.03	0.02	0.05	0.01	bdl	bdl
Sum	99.41	99.49	98.27	99.09	98.84	99.55	99.99	100.24
# Ox	12	6	12	12	12	6	6	6
Si	2.976	1.991	2.991	2.994	2.975	2.014	2.005	2.006
Ti	-	-	0.001	0.001	0.001	-	-	0.000
Zn	-	-	-	-	-	-	-	-
Al	1.745	0.022	1.800	1.414	1.444	0.018	0.019	0.018
V	0.002	-	0.002	0.002	0.001	0.000	-	-
Cr	0.250	0.005	0.176	0.564	0.568	0.008	0.008	0.008
Fe	0.316	0.053	0.180	0.268	0.258	0.080	0.081	0.080
Ni	0.000	0.004	0.001	-	0.001	0.003	0.004	0.003
Mn	0.014	0.001	0.008	0.013	0.012	0.002	0.002	0.002
Mg	2.375	1.916	2.826	2.724	2.725	1.844	1.861	1.859
Ca	0.347	0.002	0.036	0.034	0.031	0.002	0.002	0.002
Na	0.004	0.002	-	-	-	-	-	0.005
K	-	-	-	-	-	0.000	-	0.000
P	0.000	-	0.001	0.001	0.001	0.000	-	-
Sum	8.028	3.996	8.019	8.014	8.016	3.972	3.981	3.983
Mg#	88.3	97.3	94.0	91.0	91.4	95.8	95.8	95.9

Table B1: Continued

Sample #	**8/12F**	**8/13A**	**8/13B**	**8/14A**	**8/14B**	**8/15A**	**8/15B**	**8/16A**
Suite	P	P	P	P	P	P	P	P
Mineral	EN	GRT	EN	GRT	EN	GRT	GRT	GRT
N	2	3	2	4	3	2	3	3
SiO_2	58.01	42.66	58.18	42.35	58.06	41.68	42.16	42.27
TiO_2	bdl	0.04	0.01	0.00	0.01	bdl	bdl	0.01
ZnO	na	na	na	na	na	na	na	na
Al_2O_3	0.46	18.81	0.51	18.93	0.50	18.75	18.95	20.63
V_2O_3	0.01	0.07	0.01	0.03	0.01	0.04	0.04	0.05
Cr_2O_3	0.32	7.53	0.35	6.95	0.51	7.11	7.09	5.15
FeO	2.86	5.56	3.50	5.37	4.04	5.47	5.44	5.34
NiO	0.12	bdl	0.08	0.00	0.09	bdl	bdl	0.01
MnO	0.06	0.27	0.08	0.26	0.09	0.24	0.23	0.22
MgO	37.13	24.24	35.73	24.73	36.06	24.03	24.36	23.94
CaO	0.06	1.32	0.13	1.21	0.42	1.78	1.78	2.62
Na_2O	bdl	0.01	0.03	bdl	0.13	bdl	bdl	bdl
K_2O	0.00	bdl	bdl	bdl	bdl	bdl	bdl	bdl
P_2O_5	bdl	0.01	bdl	0.02	0.00	0.04	0.02	0.01
Sum	99.03	100.53	98.63	99.86	99.93	99.14	100.10	100.24
# Ox	6	12	6	12	6	12	12	12
Si	1.987	3.010	2.004	3.001	1.985	2.986	2.989	2.977
Ti	-	0.002	0.000	0.000	0.000	-	-	0.000
Zn	-	-	-	-	-	-	-	-
Al	0.019	1.564	0.021	1.581	0.020	1.583	1.583	1.713
V	0.000	0.004	0.000	0.002	0.000	0.002	0.002	0.003
Cr	0.009	0.420	0.010	0.389	0.014	0.403	0.397	0.287
Fe	0.082	0.328	0.101	0.318	0.116	0.328	0.323	0.315
Ni	0.003	-	0.002	0.000	0.003	-	-	0.000
Mn	0.002	0.016	0.002	0.016	0.003	0.015	0.014	0.013
Mg	1.896	2.550	1.835	2.612	1.838	2.565	2.574	2.514
Ca	0.002	0.100	0.005	0.092	0.015	0.137	0.135	0.198
Na	-	0.002	0.002	-	0.009	-	-	-
K	0.000	-	-	-	-	-	-	-
P	-	0.000	-	0.001	0.000	0.001	0.001	0.000
Sum	4.000	7.995	3.982	8.012	4.002	8.019	8.019	8.020
Mg#	95.9	88.6	94.8	89.1	94.1	88.7	88.9	88.9

Table B1: Continued

Sample #	**8/16B**	**8/16C**	**8/17A**	**8/17B**	**8/18A**	**8/18B**	**8/18C**	**8/18D**
Suite	P	P	P	P	P	P	P	P
Mineral	GRT	EN	GRT	GRT	GRT	GRT	GRT	GRT
N	3	3	3	3	3	3	4	3
SiO_2	42.11	57.97	41.91	41.90	42.24	43.14	42.61	42.65
TiO_2	0.01	0.00	0.03	0.02	0.01	0.01	0.02	0.01
ZnO	na	na	na	na	na	na	na	na
Al_2O_3	20.11	0.84	16.84	16.84	20.37	20.59	20.45	20.81
V_2O_3	0.05	bdl	0.05	0.05	0.03	0.01	0.02	0.01
Cr_2O_3	5.12	0.36	10.19	10.10	4.75	4.78	4.83	4.79
FeO	5.25	3.95	4.59	4.58	5.47	5.42	5.37	5.43
NiO	0.01	0.13	0.01	0.01	0.01	0.02	0.01	0.01
MnO	0.22	0.10	0.21	0.21	0.24	0.23	0.23	0.23
MgO	23.68	36.51	24.40	24.28	24.37	24.76	24.65	24.65
CaO	2.70	0.47	2.13	2.12	1.78	1.77	1.69	1.76
Na_2O	bdl	0.01	bdl	bdl	bdl	bdl	bdl	bdl
K_2O	bdl	0.00	bdl	bdl	bdl	bdl	bdl	bdl
P_2O_5	0.02	bdl	0.01	0.02	0.00	bdl	0.00	bdl
Sum	99.28	100.33	100.36	100.12	99.26	100.73	99.90	100.35
# Ox	12	6	12	12	12	12	12	12
Si	2.995	1.973	2.985	2.990	2.996	3.011	3.000	2.990
Ti	0.001	0.000	0.002	0.001	0.000	0.001	0.001	0.001
Zn	-	-	-	-	-	-	-	-
Al	1.686	0.034	1.414	1.416	1.703	1.694	1.697	1.719
V	0.003	-	0.003	0.003	0.002	0.001	0.001	0.000
Cr	0.288	0.010	0.574	0.570	0.266	0.264	0.269	0.266
Fe	0.312	0.112	0.273	0.274	0.324	0.316	0.316	0.318
Ni	0.001	0.004	0.001	0.000	0.000	0.001	0.001	0.000
Mn	0.014	0.003	0.012	0.013	0.014	0.014	0.013	0.014
Mg	2.511	1.853	2.591	2.583	2.576	2.576	2.587	2.577
Ca	0.205	0.017	0.162	0.162	0.135	0.132	0.128	0.133
Na	-	0.000	-	-	-	-	-	-
K	-	0.000	-	-	-	-	-	-
P	0.001	-	0.000	0.001	0.000	-	0.000	-
Sum	8.015	4.005	8.017	8.013	8.018	8.009	8.015	8.017
Mg#	88.9	94.3	90.5	90.4	88.8	89.1	89.1	89.0

Table B1: Continued

Sample #	**8/19A**	**9/01A**	**9/01B**	**9/01C**	**9/01D**	**9/01E**	**9/01F**	**9/02A**
Suite	P	P	P	P	P	P	P	P
Mineral	GRT	GRT	OL	GRT	EN	GRT	D	GRT
N	2	3	3	3	4	3	4	2
SiO_2	41.76	42.72	41.32	42.64	58.32	42.20	64.34	42.01
TiO_2	0.02	bdl	bdl	bdl	0.00	0.01	0.07	0.02
ZnO	na	na	na	na	na	na	na	na
Al_2O_3	20.91	21.16	0.01	20.71	0.51	20.93	0.20	19.86
V_2O_3	0.03	0.04	bdl	0.04	bdl	0.06	bdl	0.05
Cr_2O_3	4.40	4.95	0.02	4.69	0.21	4.81	0.18	5.16
FeO	4.90	5.30	6.53	5.16	3.84	5.37	2.88	5.19
NiO	0.01	0.00	0.39	0.01	0.13	0.01	0.10	0.01
MnO	0.21	0.22	0.09	0.22	0.09	0.22	0.03	0.21
MgO	24.38	24.68	52.03	24.64	37.01	24.40	18.16	24.86
CaO	2.01	2.04	0.03	2.15	0.34	2.02	0.03	1.53
Na_2O	bdl	bdl	bdl	bdl	bdl	bdl	0.09	bdl
K_2O	bdl	bdl	0.00	bdl	bdl	bdl	0.39	bdl
P_2O_5	bdl	0.01	0.00	0.02	0.00	bdl	0.01	0.02
Sum	98.63	101.12	100.42	100.28	100.46	100.03	86.50	98.91
# Ox	12	12	4	12	6	12		12
Si	2.973	2.974	0.995	2.991	1.980	2.971	-	2.990
Ti	0.001	-	-	-	0.000	0.000	-	0.001
Zn	-	-	-	-	-	-	-	-
Al	1.754	1.736	0.000	1.712	0.020	1.737	-	1.666
V	0.002	0.002	-	0.002	-	0.003	-	0.003
Cr	0.247	0.272	0.000	0.260	0.006	0.268	-	0.290
Fe	0.292	0.309	0.131	0.302	0.109	0.316	-	0.309
Ni	0.001	0.000	0.007	0.001	0.004	0.000	-	0.001
Mn	0.012	0.013	0.002	0.013	0.003	0.013	-	0.013
Mg	2.588	2.561	1.867	2.577	1.873	2.562	-	2.638
Ca	0.153	0.152	0.001	0.162	0.013	0.152	-	0.117
Na	-	-	-	-	-	-	-	-
K	-	-	0.000	-	-	-	-	-
P	-	0.000	0.000	0.000	0.000	-	-	0.001
Sum	8.024	8.020	3.005	8.021	4.007	8.024	-	8.028
Mg#	89.9	89.2	93.4	89.5	94.5	89.0	-	89.5

Table B1: Continued

Sample #	**9/02B**	**10/01A**	**10/01B**	**10/02A***	**10/02A***	**10/03A**	**10/04A**	**10/04C**
Suite	P	P	P	P	P	P	P	P
Mineral	EN	GRT	GRT	EN	GRT	GRT	GRT	OL
N	3	3	2	3	3	3	3	1
SiO_2	57.96	42.26	42.23	58.98	42.45	42.80	42.93	41.58
TiO_2	bdl	0.01	bdl	bdl	0.05	0.01	bdl	bdl
ZnO	na	na	na	na	na	na	na	na
Al_2O_3	0.82	21.17	21.42	0.65	19.81	21.10	19.59	0.02
V_2O_3	0.01	0.04	0.04	bdl	0.07	0.05	0.06	bdl
Cr_2O_3	0.32	3.82	3.84	0.53	5.78	4.80	5.55	0.05
FeO	3.87	5.84	5.81	3.93	5.95	5.32	5.57	6.61
NiO	0.13	0.02	0.01	0.09	0.02	0.01	0.01	0.36
MnO	0.09	0.27	0.28	0.10	0.28	0.22	0.23	0.08
MgO	36.63	21.65	21.22	34.30	23.58	24.08	23.43	51.91
CaO	0.42	4.53	4.51	0.25	1.86	1.86	2.33	0.03
Na_2O	bdl	0.00	0.01	0.24	0.05	bdl	bdl	bdl
K_2O	bdl	bdl	bdl	bdl	bdl	bdl	bdl	bdl
P_2O_5	0.01	0.05	0.02	bdl	0.08	0.01	0.01	bdl
Sum	100.26	99.67	99.40	99.08	99.99	100.26	99.73	100.66
# Ox	6	12	12	6	12	12	12	4
Si	1.973	3.003	3.007	2.024	3.006	3.000	3.040	0.999
Ti	-	0.000	-	-	0.003	0.000	-	-
Zn	-	-	-	-	-	-	-	-
Al	0.033	1.773	1.798	0.026	1.653	1.743	1.635	0.001
V	0.000	0.003	0.002	-	0.004	0.003	0.003	-
Cr	0.009	0.215	0.216	0.014	0.324	0.266	0.311	0.001
Fe	0.110	0.347	0.346	0.113	0.352	0.312	0.330	0.133
Ni	0.004	0.001	0.000	0.002	0.001	0.000	0.000	0.007
Mn	0.003	0.016	0.017	0.003	0.017	0.013	0.014	0.002
Mg	1.859	2.294	2.253	1.755	2.490	2.516	2.474	1.858
Ca	0.015	0.345	0.344	0.009	0.141	0.140	0.177	0.001
Na	-	0.001	0.001	0.016	0.007	-	-	-
K	-	-	-	-	-	-	-	-
P	0.000	0.001	0.000	0.000	0.002	0.000	0.000	-
Sum	4.006	7.999	7.985	3.963	8.000	7.993	7.985	3.001
Mg#	94.4	86.9	86.7	94.0	87.6	89.0	88.2	93.3

Table B1: Continued

Sample #	**10/04D**	**10/05A**	**10/06B**	**10/07A**	**10/08A**	**10/09B**	**10/10A**	**10/11A**
Suite	P	P	P	P	P	P	P	P
Mineral	SiO_2	GRT	GRT	GRT	GRT	GRT	GRT	GRT
N	1	3	3	1	3	1	3	3
SiO_2	99.97	41.89	42.11	42.59	42.35	42.14	42.50	41.98
TiO_2	0.02	0.04	0.07	0.02	0.01	0.02	bdl	bdl
ZnO	na	na	na	na	na	na	na	na
Al_2O_3	0.13	15.30	20.78	19.89	21.17	21.11	19.83	19.18
V_2O_3	bdl	0.07	0.07	0.03	0.04	0.04	0.03	0.05
Cr_2O_3	bdl	11.27	3.73	5.32	4.46	4.09	6.18	6.55
FeO	bdl	5.96	6.16	4.13	5.34	4.93	4.94	5.76
NiO	bdl	0.00	0.01	bdl	0.01	bdl	bdl	bdl
MnO	bdl	0.31	0.22	0.20	0.23	0.21	0.22	0.28
MgO	0.02	22.61	21.14	26.18	23.89	24.21	23.98	24.44
CaO	0.01	2.16	5.16	0.31	2.88	2.45	2.33	0.99
Na_2O	0.02	0.01	0.00	bdl	bdl	bdl	bdl	0.03
K_2O	0.04	bdl	bdl	bdl	bdl	bdl	bdl	0.00
P_2O_5	bdl	0.01	0.12	bdl	0.04	0.03	0.02	0.10
Sum	100.21	99.64	99.58	98.68	100.42	99.23	100.04	99.35
# Ox		12	12	12	12	12	12	12
Si	-	3.035	3.006	3.012	2.973	2.982	3.000	2.992
Ti	-	0.002	0.004	0.001	0.001	0.001	-	-
Zn	-	-	-	-	-	-	-	-
Al	-	1.307	1.748	1.658	1.752	1.761	1.650	1.611
V	-	0.004	0.004	0.002	0.002	0.003	0.002	0.003
Cr	-	0.645	0.211	0.298	0.248	0.229	0.345	0.369
Fe	-	0.361	0.368	0.244	0.313	0.292	0.292	0.343
Ni	-	0.000	0.001	-	0.001	-	-	-
Mn	-	0.019	0.013	0.012	0.014	0.012	0.013	0.017
Mg	-	2.442	2.250	2.760	2.501	2.553	2.523	2.597
Ca	-	0.167	0.395	0.024	0.217	0.186	0.176	0.075
Na	-	0.001	0.001	-	-	-	-	0.004
K	-	-	-	-	-	-	-	0.000
P	-	0.000	0.004	-	0.001	0.001	0.001	0.003
Sum	-	7.984	8.004	8.009	8.023	8.020	8.001	8.014
Mg#	-	87.1	85.9	91.9	88.9	89.7	89.6	88.3

Table B1: Continued

Sample #	**10/12A**	**10/13A**	**10/14A**	**10/15A**	**10/15B**	**10/16A**	**10/18A**	**10/18B**
Suite	P	P	P	P	P	P	P	P
Mineral	GRT	GRT	GRT	GRT	GRT	GRT	GRT	GRT
N	1	5	3	3	2	3	2	3
SiO_2	41.17	42.20	42.60	40.69	40.44	41.94	42.46	42.34
TiO_2	0.01	0.01	0.01	0.04	0.04	0.01	0.01	0.01
ZnO	na	na	na	na	na	na	na	na
Al_2O_3	15.85	20.11	22.35	15.25	14.94	19.48	20.86	20.80
V_2O_3	0.09	0.04	0.03	0.08	0.09	0.08	0.01	0.02
Cr_2O_3	10.74	5.21	2.73	10.50	10.58	6.62	4.54	4.25
FeO	6.02	5.29	5.36	7.69	7.81	5.96	4.97	4.77
NiO	bdl	?	0.01	??	0.01	??	0.01	0.02
MnO	0.31	0.25	0.22	0.45	0.47	0.26	0.21	0.20
MgO	23.70	23.78	24.30	19.63	19.55	24.11	24.73	24.66
CaO	0.98	2.64	2.48	4.79	4.79	1.53	1.98	1.92
Na_2O	bdl	bdl	bdl	0.04	0.04	bdl	bdl	bdl
K_2O	bdl	bdl	bdl	bdl	bdl	bdl	bdl	bdl
P_2O_5	bdl	0.01	bdl	0.06	0.05	0.01	0.01	bdl
Sum	98.88	99.54	100.10	99.21	98.80	100.01	99.79	98.99
# Ox	12	12	12	12	12	12	12	12
Si	2.996	2.990	2.980	3.010	3.008	2.977	2.987	2.977
Ti	0.001			0.002	0.002			0.001
Zn	-							
Al	1.360	1.682	1.842	1.329	1.310	1.629	1.730	1.736
V	0.005	0.002	0.002	0.004	0.005	0.004	0.001	0.001
Cr	0.618	0.269	0.151	0.614	0.622	0.372	0.252	0.238
Fe	0.366	0.318	0.313	0.476	0.486	0.354	0.293	0.282
Ni	-				0.001		0.001	0.001
Mn	0.019	0.015	0.013	0.028	0.029	0.016	0.012	0.012
Mg	2.571	2.514	2.534	2.164	2.168	2.551	2.595	2.602
Ca	0.076	0.201	0.186	0.380	0.382	0.117	0.150	0.146
Na	-	-	0.001	0.006	0.005	-	-	-
K	-	-	-	-	-	-	-	-
P	-	-	-	0.002	0.002	0.000	0.000	-
Sum	8.012	8.020	8.022	8.015	8.021	8.020	8.020	8.015
Mg#	87.5	88.8	89.0	82.0	81.0	87.8	89.9	90.2

Table B1: Continued

Sample #	**11/01A**	**11/02A**	**11/03A**	**11/03B**	**11/03C**	**12/06A**	**16/01A**	**16/02A**
Suite	P	P	P	P	P	P	P	P
Mineral	CHR	CHR	CHR	CHR	CHR	AUGITE	DIOP	DIOP
N	3	3	3	3	3	2	4	3
SiO_2	0.06	0.02	0.10	0.11	0.06	56.70	55.54	54.07
TiO_2	0.15	0.07	0.14	0.14	0.15	0.06	0.05	0.08
ZnO	na	na	na	na	na	na	na	na
Al_2O_3	8.59	8.01	8.59	8.40	8.59	1.00	1.78	0.62
V_2O_3	0.14	0.15	0.15	0.12	0.14	0.01	0.04	bdl
Cr_2O_3	63.78	63.37	63.71	63.20	63.78	0.94	2.31	1.77
FeO	11.78	11.64	11.61	11.60	11.78	3.78	2.05	1.83
NiO	0.08	0.10	0.09	0.08	0.08	0.08	0.05	0.06
MnO	0.17	0.14	0.16	0.15	0.17	0.14	0.08	0.08
MgO	15.12	15.33	15.00	15.08	15.12	23.07	17.97	17.80
CaO	bdl	bdl	0.01	bdl	bdl	13.77	18.42	21.59
Na_2O	0.01	0.01	bdl	0.01	0.01	1.02	1.89	0.84
K_2O	bdl	0.01	bdl	bdl	bdl	0.04	0.15	0.18
P_2O_5	0.00	bdl	bdl	0.00	0.00	0.03	0.02	0.02
Sum	99.89	98.84	99.55	98.90	99.89	100.64	100.34	98.93
# Ox	4	4	4	4	4	6	6	6
Si	0.002	0.001	0.003	0.003	0.002	2.002	1.991	1.982
Ti	0.004	0.002	0.003	0.003	0.004	0.002	0.001	0.002
Zn	-	-	-	-	-	-	-	-
Al	0.327	0.308	0.328	0.323	0.327	0.041	0.075	0.027
V	0.004	0.004	0.004	0.003	0.004	0.000	0.001	-
Cr	1.627	1.637	1.630	1.628	1.627	0.026	0.065	0.051
Fe	0.318	0.318	0.314	0.316	0.318	0.112	0.061	0.056
Ni	0.002	0.003	0.002	0.002	0.002	0.002	0.001	0.002
Mn	0.005	0.004	0.004	0.004	0.005	0.004	0.003	0.003
Mg	0.727	0.747	0.724	0.732	0.727	1.215	0.960	0.973
Ca	-	-	0.000	-	-	0.521	0.707	0.848
Na	0.001	0.001	-	0.000	0.001	0.070	0.131	0.060
K	-	0.000	-	-	-	0.002	0.007	0.009
P	0.000	-	-	0.000	0.000	0.000	0.000	0.000
Sum	3.016	3.024	3.013	3.016	3.016	3.997	4.006	4.011
Mg#	83.3	84.1	83.3	83.5	83.3	91.6	94.0	94.5

Table B1: Continued

Sample #	**39/01A**	**39/01B**	**39/01C**	**39/01D**	**39/01E**	**39/02A**	**39/02B**	**39/02C**
Suite	P	P	P	P	P	P	P	P
Mineral	GRT	GRT	GRT	OL	OL	OL	OL	CC
N	7	7	7	7	6	7	6	3
SiO_2	39.88	40.92	40.72	41.32	40.99	40.78	41.56	bdl
TiO_2	0.06	0.05	0.06	bdl	0.00	0.00	0.00	bdl
ZnO	0.00	0.00	0.00	0.01	0.01	0.01	0.00	0.02
Al_2O_3	13.19	13.60	13.40	bdl	bdl	bdl	bdl	0.01
V_2O_3	0.09	0.09	0.09	bdl	bdl	0.00	0.01	bdl
Cr_2O_3	12.87	12.89	12.82	0.07	0.07	0.05	0.06	bdl
FeO	6.37	6.42	6.40	8.35	8.17	7.25	7.20	bdl
NiO	0.01	0.01	0.01	0.39	0.38	0.37	0.36	bdl
MnO	0.28	0.29	0.29	0.11	0.11	0.09	0.09	bdl
MgO	17.44	18.05	17.96	50.11	49.46	49.92	51.12	0.07
CaO	8.39	8.38	8.37	0.07	0.07	0.03	0.02	57.03
Na_2O	bdl	bdl	bdl	bdl	bdl	bdl	bdl	0.02
K_2O	0.00	0.00	0.00	bdl	0.00	bdl	0.00	bdl
P_2O_5	bdl	bdl	bdl	bdl	bdl	bdl	bdl	bdl
Sum	98.58	100.72	100.14	100.44	99.28	98.50	100.42	57.14
# Ox	12	12	12	4	4	4	4	
Si	3.008	3.015	3.018	1.002	1.005	1.004	1.002	-
Ti	0.003	0.003	0.003	-	0.000	0.000	0.000	-
Zn	-	-	-	-	-	-	-	-
Al	1.173	1.181	1.170	-	-	-	-	-
V	0.005	0.005	0.005	-	-	0.000	0.000	-
Cr	0.767	0.751	0.751	0.001	0.001	0.001	0.001	-
Fe	0.402	0.396	0.397	0.169	0.168	0.149	0.145	-
Ni	0.001	0.001	0.001	0.008	0.008	0.007	0.007	-
Mn	0.018	0.018	0.018	0.002	0.002	0.002	0.002	-
Mg	1.961	1.983	1.985	1.812	1.808	1.832	1.838	-
Ca	0.678	0.661	0.665	0.002	0.002	0.001	0.001	-
Na	-	-	-	-	-	-	-	-
K	0.000	0.000	0.000	-	0.000	-	0.000	-
P	-	-	-	-	-	-	-	-
Sum	8.016	8.014	8.015	2.997	2.994	2.995	2.997	-
Mg#	83.0	83.4	83.3	91.4	91.5	92.5	92.7	-

Table B1: Continued

Sample #	**39/02D**	**12/02C**	**12/03A**	**12/03B**	**14/03A**	**1/01A**	**1/03A**	**1/03C**
Suite	P	W	W	W	W	E	E	E
Mineral	OL	AUGITE	AUGITE	AUGITE	GRT	Corundum	OMP	OMP
N	4	2	3	3	3	2	2	2
SiO_2	40.78	54.40	54.68	55.44	41.41	0.01	54.65	54.61
TiO_2	bdl	0.07	0.07	0.07	0.54	1.53	0.63	0.70
ZnO	0.01	na	na	na	na	na	na	na
Al_2O_3	bdl	1.60	1.58	1.59	21.54	100.95	10.05	10.18
V_2O_3	0.01	bdl	0.03	0.02	0.03	bdl	0.04	0.03
Cr_2O_3	0.06	1.20	1.21	1.19	1.35	bdl	0.04	0.04
FeO	7.11	4.86	4.78	4.76	13.02	bdl	5.59	5.21
NiO	0.35	0.09	0.09	0.08	0.01	0.01	0.02	0.03
MnO	0.09	0.18	0.16	0.17	0.31	bdl	0.06	0.06
MgO	50.29	16.85	16.85	17.12	17.53	0.02	9.26	9.27
CaO	0.02	18.46	18.62	18.45	4.20	bdl	14.96	14.96
Na_2O	bdl	1.01	0.99	1.00	0.08	bdl	3.84	3.82
K_2O	bdl	0.51	0.50	0.51	bdl	bdl	0.08	0.06
P_2O_5	bdl	0.03	0.02	0.02	0.09	0.00	0.01	0.02
Sum	98.72	99.24	99.58	100.42	100.10	102.51	99.22	99.01
# Ox	4	6	6	6	12		6	6
Si	1.001	1.994	1.997	2.004	3.006	-	1.970	1.969
Ti	-	0.002	0.002	0.002	0.029	-	0.017	0.019
Zn	-	-	-	-	-	-	-	-
Al	-	0.069	0.068	0.068	1.843	-	0.427	0.433
V	0.000	-	0.001	0.001	0.001	-	0.001	0.001
Cr	0.001	0.035	0.035	0.034	0.078	-	0.001	0.001
Fe	0.146	0.149	0.146	0.144	0.790	-	0.169	0.157
Ni	0.007	0.003	0.003	0.002	0.001	-	0.001	0.001
Mn	0.002	0.006	0.005	0.005	0.019	-	0.002	0.002
Mg	1.840	0.921	0.917	0.922	1.897	-	0.498	0.498
Ca	0.001	0.725	0.729	0.714	0.326	-	0.578	0.578
Na	-	0.072	0.070	0.070	0.011	-	0.268	0.267
K	-	0.024	0.023	0.024	-	-	0.003	0.003
P	-	0.000	0.000	0.000	0.003	-	0.000	0.000
Sum	2.998	3.999	3.996	3.990	8.005	-	3.934	3.929
Mg#	92.7	86.1	86.3	86.5	70.6	-	74.7	76.0

Table B1: Continued

Sample #	**1/03D**	**4/01A**	**4/01B**	**12/01A**	**12/01B**	**12/01C**	**12/01D**	**12/01E**
Suite	E	E	E	E	E	E	E	E
Mineral	OMP	OMP	OMP	OMP	OMP	OMP	OMP	OMP
N	3	3	2	2	3	3	3	2
SiO_2	53.49	54.75	55.25	53.99	54.78	54.17	54.41	53.99
TiO_2	0.59	0.34	0.35	0.22	0.22	0.23	0.23	0.22
ZnO	na	na	na	na	na	na	na	na
Al_2O_3	9.84	6.93	7.21	5.12	5.18	5.07	5.13	5.06
V_2O_3	0.05	0.05	0.06	0.01	0.04	0.03	0.03	0.03
Cr_2O_3	0.05	0.10	0.07	0.13	0.16	0.15	0.14	0.14
FeO	5.47	7.30	7.20	9.78	9.68	9.75	9.72	9.78
NiO	0.01	0.06	0.06	0.06	0.06	0.06	0.06	0.07
MnO	0.06	0.14	0.14	0.15	0.16	0.17	0.16	0.16
MgO	9.18	12.47	12.37	13.56	13.55	13.52	13.52	13.47
CaO	15.76	13.11	12.43	12.37	12.37	12.35	12.32	12.33
Na_2O	4.37	4.20	3.70	3.40	3.52	3.46	3.36	3.42
K_2O	0.08	0.08	0.08	0.18	0.18	0.19	0.18	0.18
P_2O_5	0.01	0.01	bdl	0.01	0.01	0.03	0.02	0.01
Sum	98.99	99.53	98.93	98.98	99.90	99.17	99.29	98.85
# Ox	6	6	6	6	6	6	6	6
Si	1.946	1.985	2.003	1.990	1.997	1.993	1.997	1.993
Ti	0.016	0.009	0.010	0.006	0.006	0.006	0.006	0.006
Zn	-	-	-	-	-	-	-	-
Al	0.422	0.296	0.308	0.223	0.222	0.220	0.222	0.220
V	0.001	0.001	0.002	0.000	0.001	0.001	0.001	0.001
Cr	0.002	0.003	0.002	0.004	0.005	0.004	0.004	0.004
Fe	0.167	0.221	0.218	0.301	0.295	0.300	0.298	0.302
Ni	0.000	0.002	0.002	0.002	0.002	0.002	0.002	0.002
Mn	0.002	0.004	0.004	0.005	0.005	0.005	0.005	0.005
Mg	0.498	0.674	0.668	0.745	0.737	0.741	0.739	0.741
Ca	0.615	0.509	0.483	0.489	0.483	0.487	0.484	0.488
Na	0.308	0.295	0.260	0.243	0.249	0.246	0.239	0.245
K	0.004	0.004	0.003	0.009	0.008	0.009	0.009	0.009
P	0.000	0.000	-	0.000	0.000	0.000	0.000	0.000
Sum	3.981	4.005	3.964	4.016	4.011	4.015	4.007	4.015
Mg#	74.9	75.3	75.4	71.2	71.4	71.2	71.3	71.1

Table B1: Continued

Sample #	**12/04A**	**12/05A**	**12/05B**	**12/07A**	**12/07B**	**12/08A**	**12/08B**	**13/01A**
Suite	E	E	E	E	E	E	E	E
Mineral	CC	OMP	OMP	OMP	OMP	OMP	OMP	OMP
N	2	3	3	3	3	3	3	3
SiO_2	bdl	55.12	55.51	55.10	54.74	55.74	55.58	54.95
TiO_2	bdl	0.33	0.34	0.50	0.52	0.42	0.42	0.23
ZnO	na	na	na	na	na	na	na	na
Al_2O_3	bdl	5.84	5.91	10.52	10.53	10.12	10.10	4.56
V_2O_3	0.01	0.04	0.04	0.03	0.04	0.03	0.04	0.03
Cr_2O_3	bdl	0.20	0.20	0.06	0.08	0.17	0.16	0.16
FeO	0.01	7.34	7.33	6.13	6.19	4.00	4.06	5.03
NiO	bdl	0.06	0.07	0.04	0.03	0.05	0.05	0.09
MnO	bdl	0.14	0.14	0.07	0.07	0.05	0.05	0.13
MgO	0.50	15.59	15.65	8.92	8.98	10.27	10.29	15.49
CaO	57.20	11.17	11.21	11.92	11.91	14.18	14.09	15.72
Na_2O	0.01	3.25	3.36	5.73	5.79	5.07	5.37	2.98
K_2O	bdl	0.21	0.22	0.08	0.08	0.19	0.19	0.14
P_2O_5	0.04	0.01	0.00	0.03	0.03	0.02	0.03	0.03
Sum	57.78	99.33	99.97	99.14	99.00	100.31	100.44	99.54
# Ox		6	6	6	6	6	6	6
Si	-	1.990	1.991	1.985	1.977	1.976	1.971	1.988
Ti	-	0.009	0.009	0.013	0.014	0.011	0.011	0.006
Zn	-	-	-	-	-	-	-	-
Al	-	0.248	0.250	0.447	0.448	0.423	0.422	0.194
V	-	0.001	0.001	0.001	0.001	0.001	0.001	0.001
Cr	-	0.006	0.006	0.002	0.002	0.005	0.004	0.005
Fe	-	0.222	0.220	0.185	0.187	0.119	0.120	0.152
Ni	-	0.002	0.002	0.001	0.001	0.001	0.001	0.003
Mn	-	0.004	0.004	0.002	0.002	0.001	0.002	0.004
Mg	-	0.839	0.836	0.479	0.484	0.543	0.544	0.835
Ca	-	0.432	0.431	0.460	0.461	0.539	0.535	0.609
Na	-	0.228	0.234	0.400	0.405	0.348	0.369	0.209
K	-	0.010	0.010	0.004	0.004	0.008	0.009	0.006
P	-	0.000	0.000	0.000	0.000	0.000	0.000	0.000
Sum	-	3.991	3.993	3.979	3.987	3.976	3.992	4.013
Mg#	-	79.1	79.2	72.2	72.1	82.1	81.9	84.6

Table B1: Continued

Sample #	**13/01B**	**13/01C**	**13/01D**	**13/02A**	**13/02B**	**14/01A**	**14/02A**	**14/05A**
Suite	E	E	E	E	E	E	E	E
Mineral	OMP	GRT	OMP	GRT	OMP	GRT	GRT	GRT
N	3	1	3	2	3	2	2	2
SiO_2	54.88	41.52	55.46	39.82	54.30	40.76	40.87	40.60
TiO_2	0.23	0.25	0.22	1.01	0.63	0.23	0.58	0.45
ZnO	na	na	na	na	na	na	na	na
Al_2O_3	4.49	22.74	4.59	21.62	10.12	22.46	22.07	22.48
V_2O_3	0.03	bdl	0.03	0.04	0.04	bdl	0.03	0.01
Cr_2O_3	0.17	0.22	0.17	0.06	0.04	0.16	0.16	0.14
FeO	5.08	12.00	5.03	13.45	5.16	16.95	14.50	15.81
NiO	0.09	bdl	0.08	bdl	0.02	0.01	bdl	0.01
MnO	0.13	0.39	0.13	0.30	0.07	0.34	0.32	0.30
MgO	15.34	18.23	15.67	10.13	9.84	15.32	13.52	16.45
CaO	15.81	3.54	15.77	12.57	15.56	2.76	7.69	2.76
Na_2O	2.80	0.05	2.93	0.21	4.02	0.09	0.13	0.09
K_2O	0.13	bdl	0.14	bdl	0.08	bdl	bdl	bdl
P_2O_5	0.01	0.05	0.02	0.11	0.03	0.04	0.04	0.03
Sum	99.19	99.00	100.23	99.32	99.90	99.13	99.90	99.14
# Ox	6	12	6	12	6	12	12	12
Si	1.992	3.014	1.990	2.988	1.948	3.016	3.012	2.991
Ti	0.006	0.014	0.006	0.057	0.017	0.013	0.032	0.025
Zn	-	-	-	-	-	-	-	-
Al	0.192	1.945	0.194	1.913	0.428	1.959	1.917	1.952
V	0.001	-	0.001	0.003	0.001	-	0.002	0.000
Cr	0.005	0.013	0.005	0.003	0.001	0.010	0.009	0.008
Fe	0.154	0.728	0.151	0.844	0.155	1.049	0.894	0.974
Ni	0.003	-	0.002	-	0.001	0.001	-	0.001
Mn	0.004	0.024	0.004	0.019	0.002	0.021	0.020	0.019
Mg	0.830	1.972	0.838	1.133	0.526	1.690	1.486	1.807
Ca	0.615	0.276	0.606	1.011	0.598	0.219	0.608	0.218
Na	0.197	0.008	0.204	0.031	0.280	0.013	0.018	0.012
K	0.006	-	0.006	-	0.004	-	-	-
P	0.000	0.002	0.000	0.004	0.000	0.001	0.001	0.001
Sum	4.004	7.995	4.009	8.006	3.961	7.991	7.999	8.009
Mg#	84.3	73.0	84.7	57.3	77.3	61.7	62.4	65.0

Table B1: Continued

Sample #	**14/05B**	**14/06A**	**14/07A**	**20/01A**	**22/01A**
Suite	E	E	E	E	E
Mineral	GRT	GRT	GRT	?	OMP
N	3	3	3	6	8
SiO_2	41.20	40.82	40.75	41.98	54.38
TiO_2	0.45	0.40	0.50	0.04	0.60
ZnO	na	na	na	0.12	0.01
Al_2O_3	22.62	22.33	22.12	1.87	8.37
V_2O_3	0.01	0.01	0.03	0.07	0.05
Cr_2O_3	0.11	0.13	0.16	bdl	0.14
FeO	14.85	17.82	16.80	18.39	6.26
NiO	0.01	0.00	0.01	9.11	0.05
MnO	0.30	0.43	0.31	0.10	0.08
MgO	16.83	13.83	14.29	14.92	10.98
CaO	2.83	4.26	4.40	2.95	12.23
Na_2O	0.09	0.09	0.14	1.38	4.77
K_2O	bdl	bdl	bdl	0.34	0.23
P_2O_5	0.02	0.05	0.02	bdl	bdl
Sum	99.32	100.17	99.55	91.26	98.17
# Ox	12	12	12		6
Si	3.012	3.015	3.017	-	1.986
Ti	0.025	0.022	0.028	-	0.017
Zn	-	-	-	-	-
Al	1.950	1.944	1.930	-	0.360
V	0.001	0.001	0.002	-	0.001
Cr	0.007	0.007	0.010	-	0.004
Fe	0.908	1.100	1.040	-	0.191
Ni	0.001	0.000	0.001	-	0.001
Mn	0.019	0.027	0.019	-	0.003
Mg	1.834	1.523	1.577	-	0.598
Ca	0.221	0.337	0.349	-	0.479
Na	0.013	0.013	0.020	-	0.338
K	-	-	-	-	0.011
P	0.001	0.002	0.001	-	-
Sum	7.990	7.991	7.993	-	3.988
Mg#	66.9	58.1	60.3	-	75.7

Table B2: Trace element concentration of olivine determined by electron probe microanalysis.

Sample #	Al (ppm)	Cr (ppm)	Ca (ppm)
Detection limit	7.9	5.6	6.0
2/01B	101	261	283
2/02B	75	204	235
2/02C	80	202	242
2/02D	135	200	271
2/03A	77	294	210
2/03B	93	289	202
2/04A	63	384	186
2/05B	101	297	128
3/01A	65	202	42
3/02A	91	333	315
3/02B	84	308	241
3/03A	68	238	155
5/01A	65	271	96
5/02A	31	133	98
6/01A	104	544	292
6/01C	110	546	281
6/02A	11	504	16
6/02B	13	524	66
6/02C	na	503	17
6/03A	63	356	291
6/03B	61	332	243
6/04A	52	362	401
6/05A	64	309	74
6/05B	49	278	52
6/05D	51	277	50
6/09A	35	336	93
6/09D	54	359	193
6/10A	121	517	334
6/10B	123	516	336
8/02C	103	336	225
8/02D	90	345	225
8/03D	61	305	96
8/04B	70	163	340
8/06D	41	139	152
8/07C	84	358	256
8/07D	61	383	56
8/08A	45	343	202
8/08B	47	333	239
8/08C	50	357	237
8/09D	41	150	89
8/09F	24	134	110
9/01B	58	155	220

Table B3: Laser ablation inductively coupled mass spectrometry in ppm. Spot size of analysis point in μm. Abbreviations: P-GRT – peridotitic garnet, E-GRT – eclogitic garnet, E-CPX – eclogitic clinopyroxene; OPX – orthopyroxene, OL – olivine, not analysed – na, below detection – bd.

Sample #	**LOD**	**LOD**	**LOD**	**LOD**	**8/01B**	**8/02A**	**8/08I**	**8/09A**	**8/11B**	**8/12A**	**8/14B**	**8/15B**
Mineral	NIST612	NIST612	NIST612	NIST612	P-GRT	P-GRT	P-GRT	P-GRT	P-GRT	P-GRT	P-GRT	P-GRT
Spot size	130	90	75	50	75	75	75	75	75	75	50	50
Li	0.109	-	-	-	na	na	na	na	na	na	na	na
Na	0.26	0.81			na	na	na	na	na	na	na	na
Al	0.3				na	na	na	na	na	na	na	na
Ca	6	14	19	42	12410	15920	12250	12430	1650	2737	24720	10560
Sc	0.008	0.020	0.023	0.055	na	na	na	na	na	na	na	na
Ti	0.04	0.09	0.45	0.60	132	54.3	22.9	24.8	44.8	29.6	510.1	29.5
V	0.003	-	-	-	na	na	na	na	na	na	na	na
Ni	0.155	0.370	0.501	0.994	115.6	123.8	73.6	70.71	527	78.81	52.6	83.8
Rb	0.0032	0.0079	-	-	na	na	na	na	na	na	na	na
Sr	0.0019	0.0048	0.0012	0.0191	0.944	2.582	4.569	4.886	2.249	0.955	6.79	0.95
Y	0.0008	0.0019	0.0037	0.0059	0.772	0.139	0.059	0.0639	0.138	0.0931	1.484	0.09
Zr	0.0011	0.0027	0.0067	0.0109	2.757	0.163	0.679	0.662	1.91	1.163	16.11	0.213
Nb	0.0007	0.0015	0.0022	0.0054	na	na	na	na	na	na	na	na
Ba	0.0049	0.0097	0.0141	0.0289	0	0.267	bd	bd	0.111	bd	bd	3.2
La	0.0003	0.0007	0.0007	0.0016	0.0796	0.447	0.1458	0.159	0.173	0.057	0.288	0.279
Ce	0.0003	0.0007	0.0010	0.0016	1.105	3.649	2.116	2.194	1.23	0.846	4.564	1.6
Pr	0.0002	0.0005	0.0008	0.0014	0.2288	0.492	0.837	0.855	0.228	0.2294	1.456	0.391
Nd	0.0015	0.0034	0.0038	0.0056	1.191	0.993	7.42	7.64	1.08	1.461	9.35	2.17
Sm	0.0015	0.0033	0.0037	0.0071	0.319	0.0132	2.498	2.598	0.182	0.344	1.89	0.279
Eu	0.0016	0.0012	0.0015	0.0027	0.1009	0.0031	0.425	0.433	0.0395	0.0762	0.499	0.0356
Gd	0.0005	0.0037	0.0088	0.0147	0.317	bd	0.46	0.46	0.09	0.155	1.226	0.047
Tb	0.0009	0.0005	0.0010	0.0017	0.0368	0.002	0.0083	0.0074	0.008	0.008	0.1107	0.0044
Dy	0.0004	0.0022	0.0028	0.0050	0.186	0.0122	0.0106	0.013	0.0338	0.0179	0.466	0.0143
Ho	0.0006	0.0006	0.0006	0.0012	0.0289	0.0048	0.0023	0.00184	0.0054	0.00276	0.0652	bd
Er	0.0003	0.0015	0.0020	0.0033	0.0712	0.0216	0.0086	0.0092	0.0102	0.0122	0.116	0.0099
Tm	0.0009	0.0005	0.0008	0.0014	0.0128	0.0075	0.0031	0.00313	0.00247	0.0035	0.0154	bd
Yb	0.0004	0.0028	0.0031	0.0057	0.137	0.088	0.0473	0.0446	0.021	0.0212	0.104	0.04
Lu	0.00006	0.0005	0.0010	0.0017	0.0294	0.0264	0.0189	0.0171	0.006	0.009	0.0203	0.0146
Hf	0.0006	-	0.0019	0.0018	0.0389	0.0033	0.0039	0.0053	0.038	0.02	0.325	na

Table B3: Continued

Sample #	8/16A	8/17A	8/18A	9/01E	9/02A	10/03A	10/04A	10/06B	10/07A	10/08A	10/10A	10/12A
Mineral	P-GRT	P-GRT	P-GRT	P-GRT	P-GRT	P-GRT	P-GRT	P-GRT	P-GRT	P-GRT	P-GRT	P-GRT
Spot Size	50	75	50	75	50	75	75	75	50	75	75	75
Li	na	na	na	na	na	na	na	na	na	na	na	na
Na	na	na	na	na	na	na	na	na	na	na	na	na
Al	na	na	na	na	na	na	na	na	na	na	na	na
Ca	15420	13380	10110	12740	9490	11840	15040	33010	1870	17830	14690	5807
Sc	na	na	na	84.95	82.1	na	na	na	na	na	na	na
Ti	38.4	117.7	75.8	22.9	88	12	11.8	371.7	105.5	83.9	47.7	101
V	na	na	na	na	na	na	na	na	na	na	na	na
Ni	100.5	91.9	96.7	84.13	115.6	62.46	113.5	132.3	93.8	86.4	89.1	46.23
Rb	na	na	na	na	na	na	na	na	na	na	na	na
Sr	7.16	0.676	0.229	5.059	1.83	3.048	0.329	5.292	1.567	1.734	3.984	12.33
Y	0.162	2.469	0.399	0.0493	0.501	0.106	0.1201	4.66	0.078	0.451	0.149	0.149
Zr	0.391	4.66	0.525	0.105	4.09	0.82	0.515	8.86	3.295	0.931	0.296	0.596
Nb	na	na	na	0.394	0.335	na	na	na	na	na	na	na
Ba	bd	bd	bd	bd	bd	bd	bd	bd	bd	0.036	bd	bd
La	0.619	0.1497	0.1696	0.277	0.154	0.5562	0.0441	0.2727	0.1465	0.3738	0.2781	0.4474
Ce	7.98	1.736	0.488	4.697	1.944	3.989	0.772	7.162	4.677	2.482	5.885	17.1
Pr	1.633	0.344	0.0323	1.219	0.48	0.425	0.253	2.982	0.642	0.4173	1.622	0.2655
Nd	1.523	1.674	0.185	3.856	2.39	1.129	1.801	24.3	0.99	2.432	6.58	0.987
Sm	0.105	0.464	0.061	0.055	0.387	0.114	0.504	8.36	0.191	0.504	0.197	0.11
Eu	0.0194	0.1643	0.0189	0.0084	0.087	0.0257	0.1443	2.118	0.0506	0.1039	0.0282	0.0303
Gd	0.038	0.551	0.069	0.013	0.232	0.053	0.375	5.55	0.108	0.211	0.065	0.057
Tb	0.0031	0.0773	0.0124	bd	0.0261	0.0061	0.0262	0.469	0.0095	0.0127	0.007	0.0052
Dy	0.018	0.465	0.069	bd	0.122	0.0274	0.0498	1.5	0.0219	0.0544	0.0378	0.0287
Ho	0.0044	0.0966	0.0133	0.00216	0.0218	0.003	0.0047	0.163	0.0025	0.0139	0.0054	0.005
Er	0.0294	0.275	0.0499	0.013	0.0466	0.008	0.0224	0.306	0.01	0.0763	0.0195	0.0165
Tm	0.0078	0.0371	0.0093	0.0046	0.0064	0.0047	0.0089	0.0371	0.002	0.0204	0.0039	0.00273
Yb	0.108	0.267	0.096	0.078	0.072	0.0437	0.12	0.285	0.0303	0.274	0.0639	0.0296
Lu	0.0321	0.0437	0.0215	0.0239	0.0195	0.0143	0.0359	0.0571	0.0108	0.061	0.0139	0.0086
Hf	0.0055	0.09	0.0152	bd	na	0.0086	0.0133	0.166	0.056	0.0189	na	na

Table B3: Continued

Sample #	10/14A	10/15B	10/16A	39/01B	13/01C	13/02A	14/01A	14/02A	14/03A	14/05A	14/06A	16/01A
Mineral	P-GRT	P-GRT	P-GRT	P-GRT	E-GRT	E-GRT	E-GRT	E-GRT	E-GRT	E-GRT	E-GRT	P-CPX
Spot Size	75	75	75	75	50	75	75	50	75	50	75	50
Li	na	na	na	na	na	na	na	na	na	na	na	na
Na	na	na	na	na	na	na	na	na	na	na	na	na
Al	na	na	na	na	na	na	na	na	na	na	na	na
Ca	14890	30320	9660	55530	22500	79450	17040	46350	26240	16970	27000	105200
Sc	na	na	na	230.4	na	na	na	na	na	na	na	6.6
Ti	23.8	261.3	4.4	353	1449.5	5519	1270	3081	3039	2427	2284	238
V	na	na	na	na	na	na	na	na	na	na	na	na
Ni	70.57	36.58	61	101.7	103.8	44.51	57.02	61.6	88.46	100.2	48.85	337
Rb	na	na	na	na	na	na	na	na	na	na	na	na
Sr	1.679	0.0626	7.5	1.371	0.4435	2.9	1.298	0.81	0.081	0.285	0.554	100.6
Y	0.256	0.608	0.417	0.47	39.11	31.31	26.16	24.57	34.93	21.97	34.6	0.282
Zr	0.147	46.96	3.591	0.49	36.39	39.76	3.402	10.82	103.22	14.06	14.34	1.64
Nb	na	na	na	1.136	na	na	na	na	na	na	na	0.33
Ba	bd	bd	bd	bd	0.064	bd	bd	bd	bd	bd	0.059	2.92
La	0.2937	0.0643	0.474	2.101	0.0369	0.0727	0.0128	0.0208	0.0464	bd	0.0224	1.58
Ce	1.432	0.783	5.341	5.595	0.3135	0.687	0.1317	0.1318	1.011	0.0149	0.268	3.91
Pr	0.2092	0.3151	0.555	0.355	0.09425	0.2746	0.0644	0.0532	0.524	0.0103	0.0976	0.67
Nd	1.05	2.877	1.357	0.451	0.872	2.828	0.953	0.474	6.01	0.209	1.009	3.23
Sm	0.206	1.291	0.177	0.0257	0.848	2.066	1.116	0.481	4.61	0.367	0.913	0.55
Eu	0.0397	0.34	0.0411	0.007	0.3875	0.992	0.594	0.285	1.617	0.279	0.45	0.23
Gd	0.071	0.665	0.121	0.025	2.292	3.683	2.316	1.381	6.662	1.291	2.345	0.35
Tb	0.00324	0.0537	0.0132	0.005	0.6235	0.719	0.495	0.384	1.111	0.35	0.577	0.015
Dy	0.0193	0.181	0.0773	0.0403	5.495	5.239	3.889	3.42	6.69	3.102	4.972	0.118
Ho	0.0075	0.0226	0.0169	0.0164	1.3975	1.204	0.969	0.923	1.296	0.826	1.301	bd
Er	0.0589	0.0518	0.0389	0.0892	4.765	3.613	3.128	3.069	3.375	2.716	4.382	0.012
Tm	0.0192	0.0063	0.0053	0.0206	0.742	0.518	0.478	0.46	0.425	0.436	0.668	bd
Yb	0.227	0.068	0.06	0.291	5.455	3.715	3.632	3.47	2.553	3.15	4.89	bd
Lu	0.0479	0.0162	0.0171	0.0735	0.8685	0.537	0.576	0.551	0.338	0.496	0.761	bd
Hf	na	0.618	0.065	na	0.722	0.884	0.054	0.256	2.159	0.237	0.187	na

Table B3: Continued

Sample #	12/01A	12/02C	12/05B	1/03C	4/01A	13/01B	6/08B	6/08C	22/01A	2/05E	8/06B	2/01B
Mineral	E-CPX	E-CPX	E-CPX	E-CPX	E-CPX	E-CPX	OPX	OPX	E-CPX	OPX	OPX	OL
Spot Size	75	50	75	50	50	75	130	90	50	90	90	130
Li	na	na	na	na	na	na	na	na	na	na	na	0.972
Na	na	na	na	na	na	na	46.39	29.8	na	68.70	bd	32.18
Al	na	na	na	na	na	na	na	na	na	na	na	99.29
Ca	85160	124900	79740	100900	82400	105130	795	737	81200	1457	3270	228
Sc	15.95	18.41	15.89	16.96	15.86	14.38	1.125	1.051	15.29	0.976	0.14	0.502
Ti	1317	407.8	2038	4221	1969	1307	18.86	19.73	3488	12.52	bd	1.37
V	na	na	na	na	na	na	na	na	na	na	na	5.084
Ni	525	762.3	542.8	193.7	468.5	700.4	1278.3	1227.7	351.6	1026.6	681	3081
Rb	na	na	na	na	na	na	0.0091	0	na	0.0131	0.07	na
Sr	240.3	195.8	264.9	71.35	52.45	244	1.37	1.154	322.8	1.415	2.63	0.025
Y	7.21	3.516	7.17	1.907	1.139	9.05	bd	bd	5.26	bd	bd	0
Zr	21.72	1.018	8.12	12.82	5.86	31.57	0.0071	bd	29.1	bd	0.16	0.00084
Nb	0.312	0.0233	0.048	0.0369	0.201	0.425	0.0366	0.0159	0.051	0.0274	bd	0.0085
Ba	2.5	6.97	0.396	0.056	0.53	1.089	0.112	bd	0.167	0.55	0.9	0.066
La	8.71	7.376	1.074	0.196	0.327	6.977	0.0161	0.00085	1.238	0.0570	bd	0.00314
Ce	26.83	18.92	4.197	0.878	1.155	22.18	0.0405	0.0066	4.77	0.0910	0.035	0.0058
Pr	3.752	2.383	0.948	0.214	0.208	3.036	0.00575	0.00148	1.195	0.00187	bd	bd
Nd	16.32	8.86	6.78	1.522	1.046	12.84	0.0198	0.0103	7.95	bd	bd	0.00177
Sm	3.17	1.304	2.655	0.638	0.28	2.941	0.0022	bd	2.78	bd	bd	bd
Eu	0.779	0.361	0.894	0.251	0.103	0.819	0.00061	bd	0.881	bd	0.016	bd
Gd	2.582	1.162	2.607	0.763	0.262	3.008	bd	bd	2.53	bd	bd	bd
Tb	0.339	0.1545	0.346	0.0904	0.038	0.4272	bd	bd	0.309	bd	0.004	bd
Dy	1.719	0.804	1.778	0.484	0.219	2.21	bd	bd	1.474	bd	bd	bd
Ho	0.291	0.149	0.296	0.0866	0.0484	0.366	bd	bd	0.216	bd	bd	bd
Er	0.629	0.351	0.652	0.191	0.119	0.797	bd	bd	0.452	bd	bd	bd
Tm	0.0636	0.0429	0.0736	0.0198	0.0161	0.0893	bd	bd	0.0467	bd	bd	bd
Yb	0.371	0.247	0.379	0.118	0.103	0.446	bd	bd	0.222	bd	bd	bd
Lu	0.042	0.0354	0.0443	0.0143	0.0155	0.0501	bd	bd	0.0308	bd	bd	bd
Hf	bd	bd	bd	bd	bd	bd	bd	bd	bd	bd	bd	0.0037

Table B3: Continued

Sample #	2/02C	6/10B	8/02D	8/07D	10/04C	39/02A
Mineral	OL	OL	OL	OL	OL	OL
Spot Size	130	130	130	130	130	130
Li	1.038	1.532	1.099	0.817	0.98	0.927
Na	26.4	40.49	33.94	13.13	228	62.44
Al	79.08	136.17	93.63	56.65	67.6	34.5
Ca	202	311	203	41.4	280	149
Sc	0.408	0.92	0.639	0.508	0.45	0.509
Ti	0.6	2.91	1.35	1.82	4.7	25.6
V	4.562	8.051	6.219	6.176	4.83	7.451
Ni	3079	3028	3117	2817	2070	2877
Rb	na	na	na	na	na	na
Sr	0.041	0.0092	0.0026	0.121	0.072	0.0117
Y	0.00026	bd	bd	0	bd	bd
Zr	0.00059	bd	bd	0.0204	bd	0.0219
Nb	0.0349	0.0013	bd	0.0293	0.124	0.0132
Ba	0.121	bd	bd	0.407	0.42	bd
La	0.0085	0.00033	bd	0.0145	0.028	bd
Ce	0.0116	0.00033	bd	0.0265	0.037	0.00047
Pr	0.00017	bd	bd	0.00221	0.0073	bd
Nd	0.0011	bd	bd	0.0062	bd	bd
Sm	bd	bd	bd	bd	bd	bd
Eu	0.0016	bd	bd	bd	bd	bd
Gd	0.00002	bd	bd	bd	bd	bd
Tb	bd	bd	bd	bd	bd	bd
Dy	0.00005	bd	bd	bd	bd	bd
Ho	bd	bd	bd	bd	bd	bd
Er	bd	bd	bd	bd	0.0007	bd
Tm	bd	bd	bd	bd	bd	bd
Yb	bd	bd	bd	bd	bd	bd
Lu	bd	bd	bd	bd	bd	bd
Hf	0.0024	bd	bd	0.00126	0.017	bd

Table B4: Geothermobarometry of mineral inclusions in Koffiefontein diamonds.

Sample #	Al-in-olivine/38mW		Cr-in-garnet
	T (°C)	P (kbar)	P (kbar)
1/05	978	44.7	
2/01	1297	64.8	
2/02	1280	63.7	
2/03	1258	62.3	
2/04	1169	56.7	
2/05	1297	64.8	
3/01	1200	58.6	
3/02	1279	63.7	
3/03	1208	59.1	
5/01	1199	58.5	
5/02	1034	48.2	
6/01	1311	65.7	
6/02	805	34.0	
6/03	1187	57.8	
6/04	1149	55.4	
6/05	1157	55.9	
6/07			
6/09	1108	52.8	
6/10	1341	67.6	
7/01	1285	68.4	30.3
7/02			24.4
7/03			46.3
7/04	1233	65.9	44.5
8/01			32.9
8/02	1288	64.2	36.4
8/03	1184	57.6	41.9
8/04	1216	59.6	
8/06	1096	52.0	
8/07	1185	57.7	47.6
8/08	1126	53.9	42
8/09	1035	48.2	42.9
8/10			27.9
8/11			32.1
8/12			57.7
8/13			47.1
8/14			45.6
8/15			44.4
8/16			34.3
8/17			53.3
8/18			35.4
9/01	1172	56.9	34.6
9/02			37.6
10/01			26.1
10/02			39.1
10/03			35.1
10/04	1330	66.9	36.7
10/05			56.6
10/06			25.0
10/07			43.1
10/08			31.2
10/09			30.8
10/10			39.1
10/11			45.0
10/12			58.5
10/13			34.6
10/14			25.6
10/15			46.5
10/16			43.6
10/18			33.2
39/01			43.0
39/02	1056	49.6	

Sample #	Krogh88/38mW	
	T (°C)	P (kbar)
13/01	1160	56.1
13/02	1563	82.1

Table B5: Temperature calculated for Ni in garnet for peridotitic assemblages based on the geothermometer of Canil (1999).

Sample #	Ni in garnet (ppm)	Ni in olivine (ppm)	Temperature (°C)
8/01B	116	3700	1190
8/02A	124	4000*	1188
8/08I	74	3300*	1112
8/09A	71	4000*	1063
8/11B	527	3700	1686
8/12A	79	3700	1102
8/14B	53	3700	1020
8/15B	84	3700	1115
8/16A	101	3700	1157
8/17A	92	3700	1136
8/18A	97	3700	1148
10/03A	62	3700	1054
10/04A	114	3700	1186
10/06B	132	3700	1224
10/07A	94	3700	1141
10/08A	86	3700	1122
10/10A	89	3700	1129
10/12A	46	3700	996
10/14A	71	3700	1079
10/15B	37	3700	954
10/16A	61	3700	1049

* Actual values determined from coexisting olivine by EPMA